OPTIMIZATION OF THE AXIAL CRUSHING BEHAVIOR OF CLOSED-CELL ALUMINUM FOAM FILLED WELDED 1050 AL SQUARE-CROSS SECTION CRASH BOXES

A Thesis Submitted to
the Graduate School of Engineering and Sciences of
İzmir Institute of Technology
in Partial Fulfillment of the Requirements for the Degree of

DOCTOR OF PHILOSOPHY

In Mechanical Engineering

by
Ahmet Kaan TOKSOY

November 2009
İZMİR

We approve the thesis of **Ahmet Kaan TOKSOY**

Prof. Dr. Mustafa GÜDEN
Supervisor

Prof. Dr. Ramazan KARAKUZU
Committee Member

Assoc. Prof. Dr. Serhan ÖZDEMİR
Committee Member

Assoc. Prof. Dr. Hasan YILDIZ
Committee Member

Asst. Prof. Dr. Alper TAŞDEMİRCİ
Committee Member

06 November 2009

Prof. Dr. Metin TANOĞLU
Head of the Department of
Mechanical Engineering

Assoc.Prof Dr. Talat YALÇIN
Dean of the Graduate School of Engineering
and Sciences

ACKNOWLEDGEMENTS

My PhD quest has been started since 2003. At the beginning, I was just considered scientific progress. First question in my mind was How? What kind of methodology was the best for scientific progress? These questions kept me busy and I was continuously looking for answers. I gained extensive experience on planning of experimental testing but I wish to improve way of scientific thinking on special topics. I have to admit that most of my success on scientific research study belongs to only one person, Prof. Dr. Mustafa GUDEN, who supports me most of the time and supplied proper environment for conducting highly extensive scientific work of mine. Without his patience, guidance and friendship, I could have lost both my desire on scientific education and all the way to end of the PhD journey.

I would like to thank TUBITAK research project 106M186 for financial support to this PhD study. Further, I would like thank stuff of central mechanical atelier for their helps on sample preparing and further mechanical processing during the experimental procedure of the study.

Lastly, and in my heart the most important, I would express my feelings to my wife, Sultan Eylem TOKSOY. Most of the time, she supplied warm and full of tranquility environment at home. Without her love and emotional support, this thesis would have never been reality. She gave me a special gift during the completion of my doctoral thesis, my son Efe. I would also dedicate part of the success to my lovely child. I believe that a wonderful life waits us.

ABSTRACT

OPTIMIZATION OF THE AXIAL CRUSHING BEHAVIOR OF CLOSED-CELL ALUMINUM FOAM FILLED WELDED 1050 AL SQUARE-CROSS SECTION CRASH BOXES

The crushing behavior of partially Al closed-cell foam (Alulight AlSi10) filled 1050H14 Al crash boxes was investigated at quasi-static and dynamic deformation velocities. The quasi-static crushing of empty and filled boxes was further simulated using LS-DYNA. Finally, the crushing of partially foam filled 1050H14 crash boxes was optimized using the response surface methodology. The used optimization methodology was also applied to the boxes made of a stronger Al alloy, 6061T4 Al, and filled with a higher strength Al foam, Hydro Al closed cell foam, in order to clarify the effect of box material and foam filler strength on the crushing behavior of the filled boxes. Within the investigated tube thickness and foam relative density range, the energy absorption of 1050H14 boxes was optimized at 3 mm wall thickness and 0.1114 (Alulight) and 0.0508 (Hydro foam) foam filler relative density. The increase in specific energy absorption of 1050H14 crash box was 5.6% with Alulight and 21.9% for Hydro foam filling. The SEA values of empty, partially and fully foam filled boxes were predicted as function of box wall thickness between 1 and 3 mm and foam filler relative density between 0 and 0.2, using the analytical equations developed for the mean crushing loads. The analysis indicated that both fully and partially foam filled boxes were energetically more efficient than empty boxes above a critical foam filler relative density. Partial foam filling however decreased the critical foam filler density at increasing box wall thicknesses.

ÖZET

KAPALI HÜCRELİ ALUMİNYUM KÖPÜK DOLDURULMUŞ KAYNAKLI 1050 AL KARE KESİTLİ EZİLME KUTULARININ OPTİMİZASYONU

Bu çalışmada kısmi olarak aluminyum kapalı hücreli köpük (Alulight AlSi10) ile doldurulmuş 1050H14 Al ezilme kutularının ezilme davranışlarını quasi-statik ve dinamik deformasyon hızlarında incelenmiştir. Boş ve dolu ezilme kutularının quasi-statik ezilme davranışları LS-DYNA kullanılarak simule edilmiştir. Tezin son kısmında kısmi dolu 1050H14 Al ezilme kutularının ezilmeleri Cevap Yüzeyi Metodolojisi kullanılarak optimize edilmiştir. Uygulanan optimizasyon metodunda, ezilme kutusu ana malzemesi için daha kuvvetli aluminyum alaşımı 6061T4 ve dolgu malzemesi için yine daha yüksek mukavemete sahip Hydro Al kapalı hücreli köpük, ana malzeme ve dolgu malzemesinin dayanımının dolu tüplerin ezilme davranışlarına olan etkilerinin açık bir şekilde belirlenebilmesi için kullanılmışlardır. Araştırılan tüp kalınlığı ve nispi köpük yoğunluğu aralığında, 1050H14 Al kutuları 3 mm kalınlıkta ve 0.1114 (Alulight) ve 0.0508 (Hydro) köpük nispi yoğunluğunda optimize edilmişlerdir. 1050H14 ezilme kutusunun spesifik enerji absorbsiyonu artış oranı Alulight köpükler için %5.6 Hydro köpükler %21.9 olarak hesaplanmıştır. Boş, kısmi ve tam köpük dolu kutuların SEA değerlerinin tahminlenmesinde 1 ve 3mm aralığındaki kutu kesit kalınlığı ve 0 ile 0.2 aralıklarındaki nispi köpük yoğunluğunun fonksiyonu olan ortalama ezilme yükleri için geliştirilmiş analitik denklemler kullanılmışlardır. Analizler belirli kritik köpük dolgu yoğunluğunun üstünde kısmi ve tam köpük dolu ezilme kutularının boş kutulardan enerji açısından daha verimli olduklarını göstermiştir. Kısmi köpük doldurma işlemi kutu kesitinin artırılması durumunda kritik köpük yoğunluğunun düşmesine neden olduğu tespit edilmiştir.

TABLE OF CONTENTS

LIST OF FIGURES

LIST OF TABLES

CHAPTER 1

INTRODUCTION

The recent economical global crisis and the continuing unstable prices of oil and raw materials have tended the manufacturer to reduce the weight of automobiles and increase the efficiencies of engines, transmission and active and passive safety systems. Other restrictions on the automobile weight come from the legal regulations of air pollution. USA (EPA 2000) and European union (EC 1998) have announced new regulations on the gas emission levels separately. These regulations aim to decline CO and NO_x ratios in the exhaust gas emission. It is therefore expected that the weight saving possibilities in automobiles will be seriously considered and investigated by the automobile manufacturer as the new regulations appear in coming years.

Since the end of 1980s, the number of parts made from aluminum has been continuously increasing. According to European Aluminum Association, the total weight of aluminum use in automobile bodies will reach approximately 160 kg in the year of 2010 (EAA 2008). This corresponds to approximately 10% reduction in the total weight of an average European car. The recent European project entitled "Super Light Car" achieved 32% total weight reduction in the body in white of automobile using the combination of various kinds of materials including high strength steels, aluminum sheet/extrusions and casting, magnesium castings and carbon fiber reinforced plastics (Figure 1.1) (Duwe and Kopp 2009).

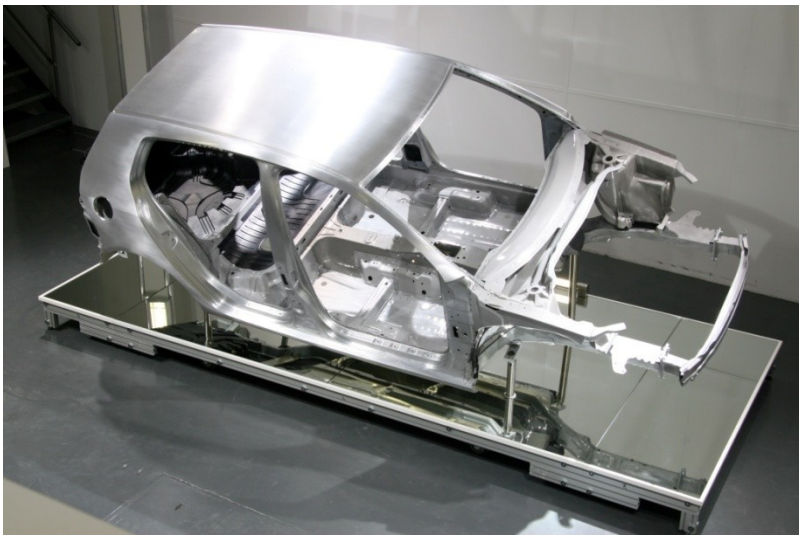

Figure 1. 1. The body in white structure of Super Light Car, with approximately 32% reduction in weight,(Source: Duwe and Kopp 2009).

The fuel economy bears an important aspect in Turkey because Turkey has the shortage of the adequate domestic supply of crude oil. A high tax ratio has been always subjected when a certain engine capacity and total weight are exceeded. Since Turkey is in a statute of the candidate country of EU membership, the EU regulations on exhaust emission is also valid in Turkey. Moreover, according to Turkish Statistical Institute, the number of automobiles in Turkey increased 6% per year on the average between 2002 and 2007, (TUIK 2007). In parallel with this, the number of crash accidents annually increased by 14%. Therefore, the weight savings and crash safety are received much more attention by the automobile buyers of Turkey.

A crash element should transform the kinetic energy into the deformation energy in a controllable manner, retain sufficient survival space for the protected components and keep the forces and accelerations on the crash element at possible minimum levels (Meguid, et al. 2004a). Figure 1.2 shows the percentages of the occurrences of the site crashes in the automobiles and the percentage of the occurrence of the frontal crashes is shown to be about 70% including direct and offset frontal crashes (Wallentowitz and Adam 1996). In the United States, for example, about 79% of the injuries are caused by the offset frontal crashes (Peden, et al. 2004). As parallel with the high probability of the occurrence of the frontal zone crashes, the passive crash elements used in these areas have been under constant improvement by the use crash elements made in various geometries of different materials.

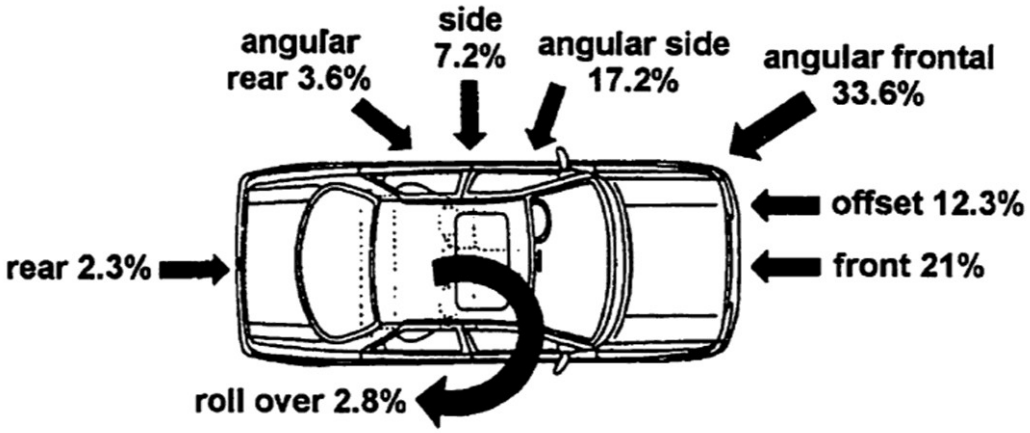

Figure 1. 2. The probability of the collision occurrence in a passenger car. (Source: Wallentowitz and Adam 1996)

A crash box is an element which is used in the frontal crash zones, generally inserted between chassis and bumper as shown in Figure 1.3. Crash boxes absorb the total crash energy at velocities approximately up to 30 km/h and protect the overall integrity of chassis and transmit less amount of energy to the rest of the front safety zones at velocities higher than 30km/h.

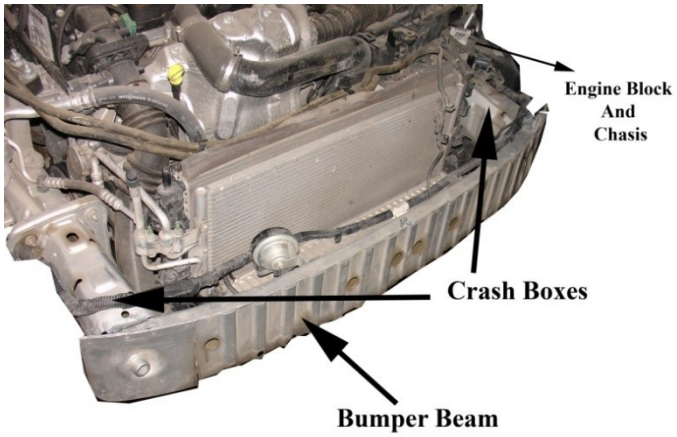

Figure 1. 3. Bumper, crash box, engine and chassis positions in a 2009 model Ford Mondeo.

Figure 1. 4. Commercial crash boxes in various geometries.

Two methodologies have been recently applied to improve the energy absorption performances of crash boxes. These are the use of multiple-cell structure and filling the crash boxes with a with light-weight metallic foam. Aluminum foam filling particularly has received much interest from both academia and industry since they have relatively very low density as compared with the foams of other metals. Unlike polymeric counterparts, aluminum foams are nonflammable and absorb much more energy under increasingly high deformation loads. In addition, aluminum foams have capabilities for the attenuating noise and vibration. The gear wheel noise emissions were reported to be reduced up to 10 dB (A), with the use of Al foam filling, at the full transmission of torque and turning speed with a 25% weight saving (Stöbener and Rausch 2009). Aluminum foams have recently been considered as the candidate materials for the crash safety applications. Despite many studies on Al foam filling of the columns in the literature, which are reviewed in Chapter 3 of this thesis, there has been no extensive study on Al foam filling of commercial crash boxes experimentally and numerically. The motivations of the present thesis include (a) assessing the effect of Al foam filling on the crash performance of a commercial crash box, (ii) modeling the associated crushing behavior of the filled boxes and verifying the model results with experiments and (iii) optimization of the filled crash boxes made of different materials and alloys. It is believed that with the results of this thesis, many aspects of the Al foam filling of commercially available crash boxes will be clarified and the limits of foam filling in terms crash performance and cost will be determined. In Chapter 2 of the thesis, the production methods and mechanical behavior of Al closed cell metal foams are reviewed. Chapter 3 reviews the crash behavior of circular and rectangular cross-

sectioned empty and foam filled crash box structures along with the used crash analysis methodologies and terminologies. The motivations for the research conducted in this thesis are given in Chapter 4. Chapter 5 includes the experimental methods of mechanical testing of the used Al foam filler and the crash box material, 1050H14 aluminum alloy and the production steps of empty and foam filled crash boxes. The details of the numerical simulations are outlined in Chapter 6. The results of experimental and simulation studies are given in Chapter 7 and 8, respectively. The results of optimization of partially aluminum foam filled boxes with Response Surface Methodology are analyzed in Chapter 9. Chapter 10 discusses the crash efficiencies of partially foam filled crash boxes. Conclusions are drawn in Chapter 10 along with suggested future studies.

CHAPTER 2

AL CLOSED CELL FOAMS: PROCESSING AND CRUSHING BEHAVIOR

2.1. Introduction

The mechanical and physical properties and the application fields of metal foams are outlined in Figure 2.1, (Banhart 2005). Metal foams have relatively low densities as compared with the metals from which they are made, very long plateau stress region extending to 50-60% strains and relatively good damping properties. Therefore, they have great potentials to be used in the construction of light weight, energy absorbing structures, as well as in the structures involved acoustic and thermal insulation management. Currently, on the research basis, metal foams made of various metals such as steel (Park and Nutt 2002), magnesium(Wen, et al. 2004), zinc(Kitazono and Takiguchi 2006) and Al(Song, et al. 2001) haven been investigated, while only Al closed cell foams are commercially produced for the structural applications.

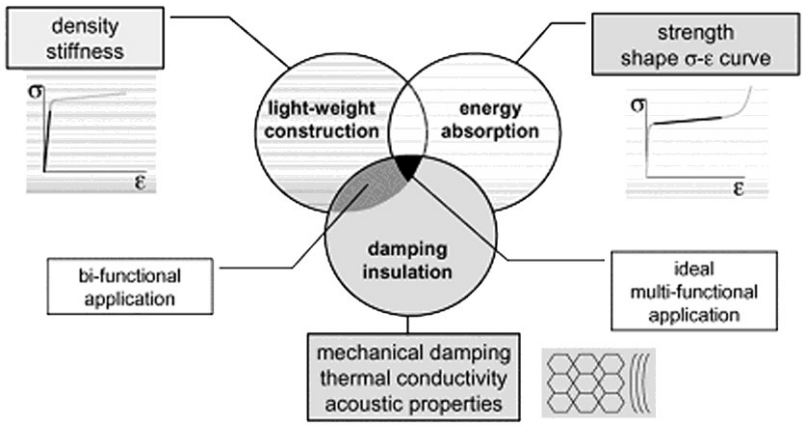

Figure 2. 1. General application areas of metal foams.
(Source: Banhart 2005)

In automobiles, the use Al foams improves the crash safety by increasing the energy absorbing capacity of crash boxes and the stiffness of specific areas of A/B pillars and by supporting the rail on chassis. They are also prominent materials, as being very light, for the space applications. An example of space applications, Ariene 5 rocket cone Al foam structure, was shown by Scwingel et al.(Schwingel, et al.). The mechanical properties of Al closed-cell foam have been extensively studied including uniaxial stress-strain response (McCullough, et al. 1999b), strain rate sensitivity (Hall, et al. 2000), energy absorption (Song and Nutt 2005), drop weight impact (Rajendran, et al. 2009a), fracture toughness (McCullough, et al. 1999a) and internal reinforcing with steel netting (Solorzano, et al. 2007).

2.2. Processing of Al Closed Cell Foams

A cellular solid is one made up of an interconnected network of solid struts or plates which form the edges and faces of cell(Gibson and Ashby 1997). In this definition, strut stands for the cell edge and plate for the cell face. Note that, an open cell foam is solely made of struts (Figure 2.2(a)) and a closed-cell foam is made of struts and plates (Figure 2.2(b)). As noted in Figures 2.2 (b), the cell faces are thinner than cell edges.

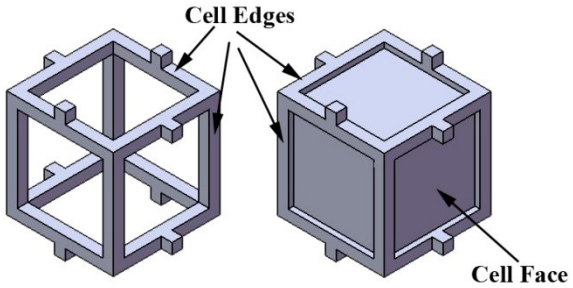

(a) (b)

Figure 2. 2. Schematic representation of a) an open and b) an closed cell cellular structure (Source :Gibson and Ashby 1997).

The processing methods and mechanical and physico-chemical properties of cellular metals or foamed metals, including Al, nickel, copper, magnesium, steel and production have been widely studied for more than 30 years (Gibson 2000). The production methodologies of cellular metallic materials are classified based on the starting metal as liquid metal, powdered metal, metal vapour or gaseous compounds and metal ion solution (Banhart 2001, Wood 1997) (Figure 2.3). Closed Al foams are however currently manufactured based on liquid metal and powder metal, which will be elaborated in the next section.

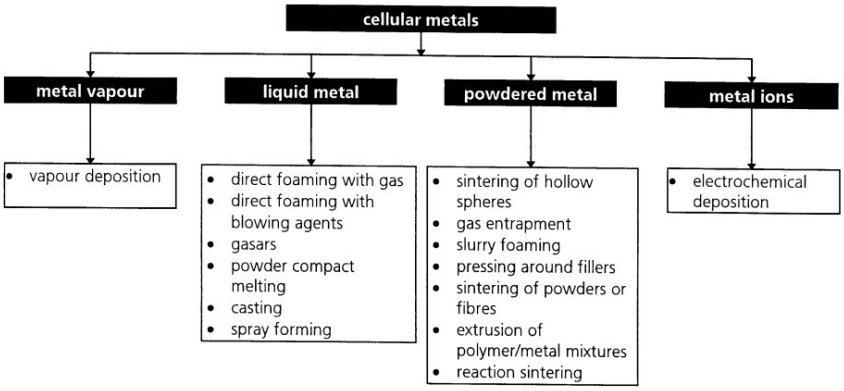

Figure 2. 3. The production methods of cellular metallic structures.
(Source :Wood 1997)

2.1.1. Foaming Melts by Gas Injection (Alcan/Cymat or Hydro Process)

Gas injection into molten metal process was developed coincidently and independently by Cymat/Alcan(Wood 1997) and Norsk Hydro(Asholt 1999). During foaming process, a gas is continuously injected by the help of a rotating shaft in liquid metal (Figure 2.4), (Ashby, et al. 2000). Including air, carbon dioxide, nitrogen and argon can be used as the injecting gas. Because of quick bursting of gas bubbles in the liquid metal, pure liquid metal cannot be easily foamed and therefore small insoluble or dissolving particles such as aluminum oxide or silicon carbide are added into liquid metal in order to stabilize the gas bubbles and increase the viscosity of liquid metal. The

stabilized gas bubbles rise to the surface of the liquid where the liquid foam is collected and then subsequently solidified.

Particle size and volume fraction have very important in the stabilization of foam structure. High particle volume fractions lead to high liquid metal viscosity, leading to very low foaming in liquid metal, Figure 2.5 (Prakash, et al. 1997). While very large particles settle in the liquid, hindering the foam stabilization. Generally, the preferred volume fraction of the reinforcing particles typically ranges from 10 to 20%, and the mean particle size from 5 to 20 μm for an efficient foaming (Banhart 2007). The other parameters effective in this foaming process are the gas flow rate and pressure, orifice geometry of injection system and orifice immersion depth (Deqing and Chengxin 2008).

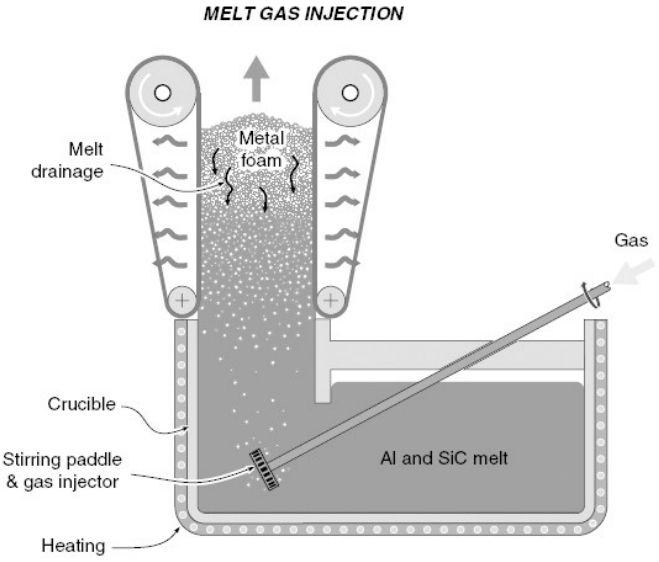

Figure 2. 4. Foaming melts by gas injection.
(Source :Ashby, et al. 2000)

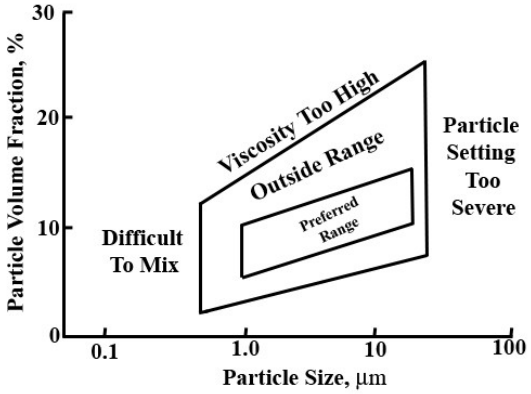

Figure 2. 5 The preferred particle volume fraction and particle size for the stabilization of Al-SiC foam,(Source: Parkash et al. 1997).

The production cost of foaming by gas injection into molten metal is relatively lower. The relative density of Al foams produced by this method ranges between 0.03 and 0.1(Ashby, et al. 2000). The presence of hard particles in the metal matrix; however, makes these foams relatively brittle and reduces the machinability (Kavi 2004).

2.1.2. Gas Releasing Particle Decomposition in the Melts (Alporas Process)

The foaming by gas releasing particle decomposition, also known as Alporas foaming process, comprises three sequential steps. These are thickening the molten metal, foaming the molten metal by adding TiH_2 foaming agent and cooling the liquid foam ,Figure 2.6 (Degischer 2002). In the thickening, calcium (Ca) particles are added into molten Al at 680 °C and the molten Al is aggressively stirred (T. Miyoshi 2000). The formation of calcium oxide (CaO) and calcium-Al oxide (CaAl2O4) thickens the liquid metal (Banhart 2000). The viscosity of liquid metal is a function stirring duration (Banhart 2000, Ma and Song 1998) and the molten metal viscosity increase up to five times is possible at longer stirring times as shown in Figure 2.7. The thickened liquid metal is then poured into a casting mold and stirred again with the addition of 1.6 wt% TiH_2 at 680 °C. The addition of TiH_2 foaming agent releases hydrogen gas into the hot viscous liquid according to the following reaction:

$$TiH_2\,(s) \rightarrow Ti\,(s) + H_2\,(g) \qquad (2.1)$$

It takes approximately 15 minutes for molten metal to expand and fill up the mold following the stirring. Then the foamed molten metal is cooled in the mold with a powerful blower. Typical cellular structure of Alporas closed cell Al foam is shown in Figure 2.8, (Miyoshi, et al. 1999). Typical density of Al foams produced by this method ranges between 0.2 and 0.3 g cm^{-3}

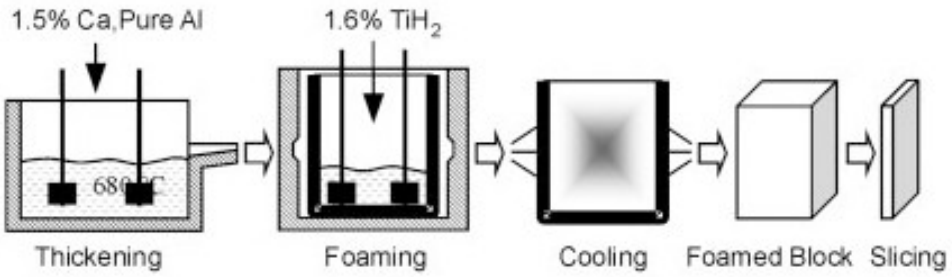

Figure 2. 6. Alporas foaming process.
(Source : Degischer 2002)

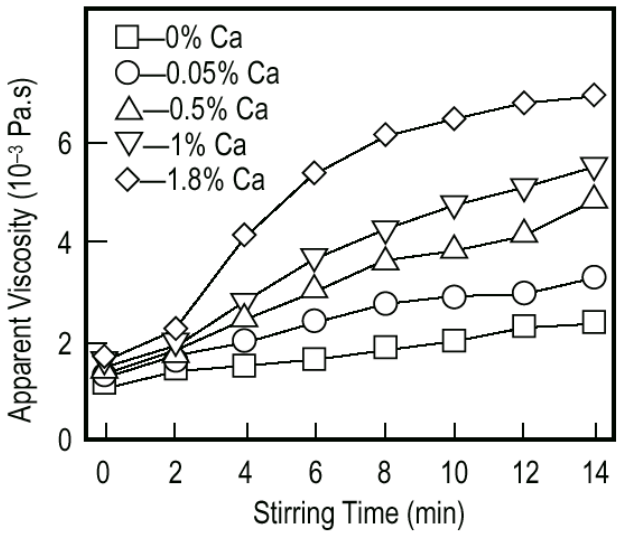

Figure 2. 7. Variation of viscosity with stirring time in Alporas foaming process.
(Source : Banhart 2000)

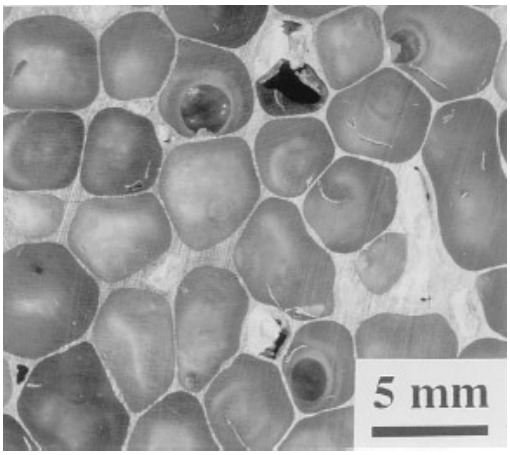

Figure 2. 8. Typical cellular structure of Alporas foam.
(Source : Miyoshi, et al. 1999)

2.1.3. Gas Releasing Particle Decomposition in Semi-Solids (Fraunhofer and the Alulight Process)

Gas releasing particle decomposition in semi-solid method is also known as foaming powder compacts process (Degischer 2002). The foaming process starting with a metal powder (typically Al and its alloys) and a foaming agent in powder form (typically TiH_2 and ZrH_2) was patented for the first time by Allen et. al. (Allen, et al. 1963) in 1963. The process sequences are shown in Figure 2.9 and begin with mixing metal powder with a foaming agent. Titanium hydride is the most widely used blowing/foaming agent for Al foaming since its decomposition temperature (465 °C) is near and lower than Al and Al alloy melting temperature range (550-650 °C). Several different methodologies including the preheating Al and TiH_2 mixture and Ni-coating of TiH_2 were previously investigated to increase the decomposition temperature of TiH_2 in order to prolong the foaming process duration(Proa-Flores and Drew 2008). The powder mixture is compacted to a density over 98%. Various mechanical forming processes including cold or hot uniaxial pressing, extrusion and rolling can be used to prepare dense powder compacts (foamable precursors) (Asavavisithchai and Kennedy 2006).The lubrication of the pressing die and the use of double compaction were found to increase the powder compact foaming effectiveness (Bonaccorsi and Proverbio 2006).

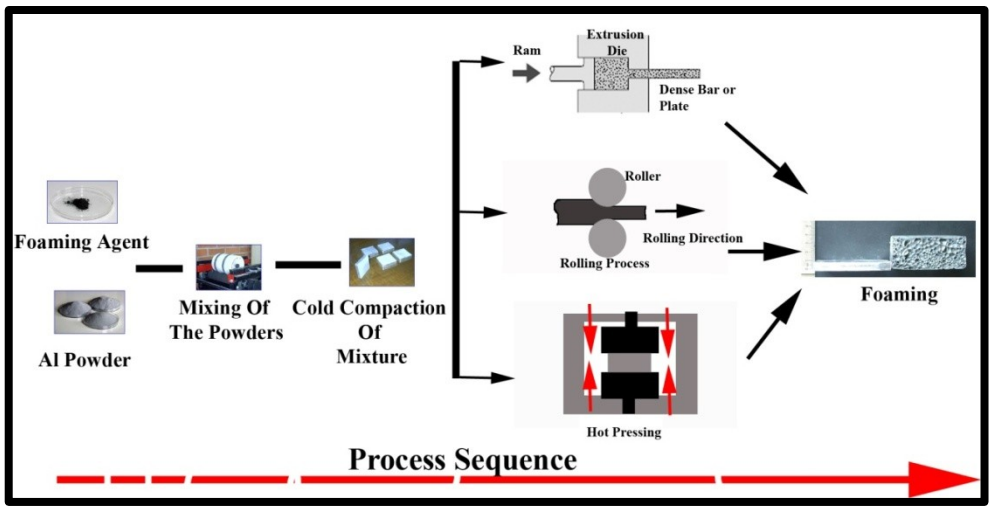

Figure 2. 9. Schematic of the foaming powder compact process.

Two factors affect the foaming cost: the production volume and production cost (Maine and Ashby 2000). No matter how high is the volume production of powder metallurgical processing of Al foam, the batch or continuous production methods cannot reach the liquid state production cost at increasing volumes as shown in Figure 2.10. Higher production cost of foaming powder compacts process is caused by the higher number of production steps involved and the more expensive powder form of Al used in the process. However, foaming powder compacts process has an important advantage over the liquid based foaming processes. In the foaming powder compacts process, the foam can be produced in near net shape with a naturally occurring dense skin layer to which various kinds of finishing processes such as sand blasting and polishing can be easily applied. This may compensate its higher cost at high volume productions when the shaped products are required by the customers. The other advantages of the method include its flexibility in alloy selection, the availability of manufacturing composite structures, no need for particle stabilization and possibility of reinforcement with ceramics or fiber (Baumgärtner, et al. 2000).

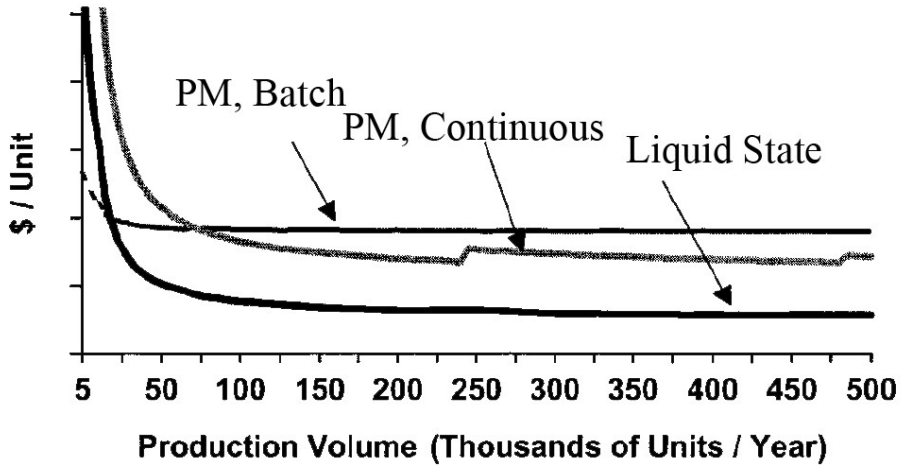

Figure 2. 10. Manufacturing cost of three methods of Al foam processing based on the production volume (Source : Maine and Ashby 2000)

2.1.4. Accumulative Roll-Bonding

In accumulative roll-bonding (ARB) process, two metal strips are rolled together with a blowing agent in between them as shown in Figure 2.11 (Kitazono, et al. 2004). The prepared strip is then rolled by 50% reduction and cut into two. These two strips are stacked together and then rolled again. After several repetitions of stacking and rolling and then cutting the blowing agent particles are homogeneously dispersed in metal matrix (Figure 2.11). The rolled composite metal is used as a foamable precursor in the following high temperature foaming process.

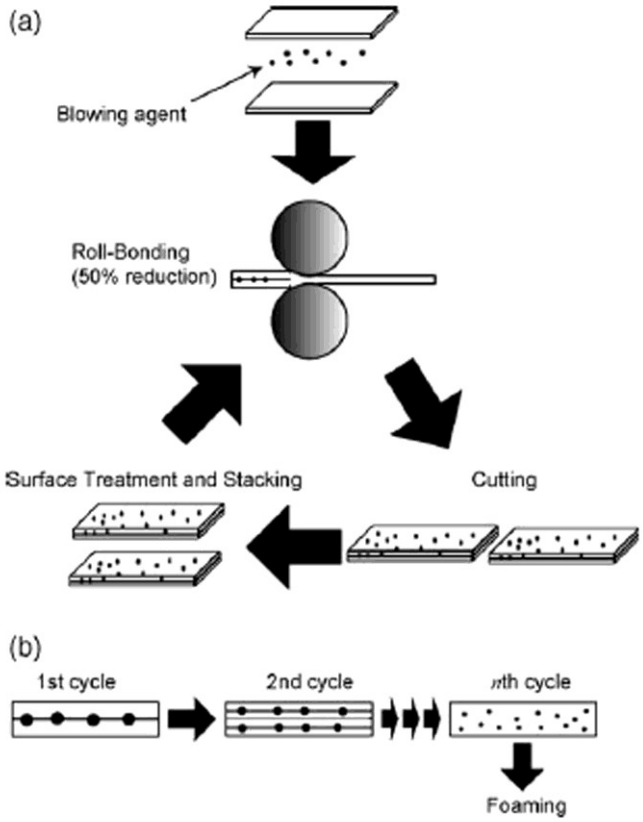

Figure 2. 11. (a) Schematic of foamable precursor preparation in ARB process and (b) gradual dispersion of blowing agent particles in the rolling cycles (Source :Kitazono, et al. 2004)

2.1.5. Laser Assisted Foaming

Laser assisted foaming is a relatively new technique of Al foam production. It is the same with foaming powder compact process except the foamable precursor is heated up to its melting points by high power laser beam irradiation as depicted in Figure 2.12. The foaming AlSi7 Al foaming using Nd-YAG and CO_2 laser was widely investigated (Kathuria 2001a, Kathuria 2001b, Kathuria 2003a, Kathuria 2003b). The expansion of the compact during foaming occurred predominantly local and unidirectional with the direction of laser irradiation.

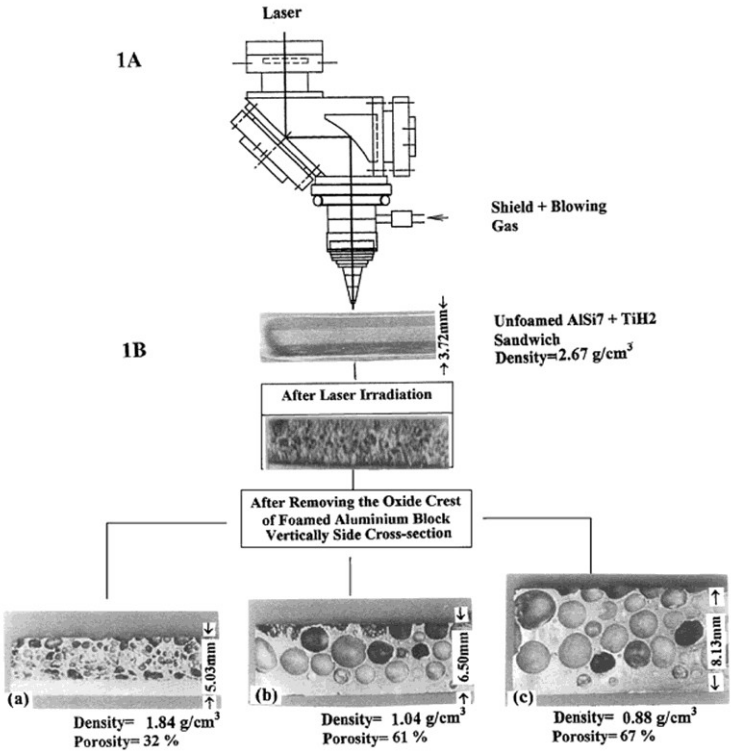

Figure 2. 12. Laser assisted foamed Al; (a) side cross-section of laser heating and (b) foamed Al compacts: Laser: cw CO2. Processing parameters: P = 5kW; Ar = 30 l/min; Processing speed (V) = (B-a): 2 m/min; (B-b): 0.8 m/min; (B-c): 0.4 m/min (Source :Kathuria, 2003b)

2.3. Mechanical Behavior of Closed Cell Foams

Under uniaxial compressive loads, metal foams show three distinct deformation regions in the stress-strain curves: linear elastic, plateau and densification regions as shown in Figure 2.13(Gibson and Ashby 1997). In linear elastic region, the foam deformation involves cell edge bending in an open cell foam and cell edge bending and/or cell face stretching in a closed cell foam. In plateau region, the deformation proceeds at a nearly constant stress resulting from continuous cell edge/cell wall collapse/crushing. When all the cells collapse, further deformation presses the opposing cell walls against each other, resulting in sharp increase in stress values. The region of sharply increased stress is called densification region.

Deshpande and Fleck (Deshpande and Fleck 2000a) studied the quasi-static and high strain rate compressive behavior of Alulight (Al-Mg0.6-Si0.3) closed cell and Duocell (Al6101-T6) open cell foams. The high strain rate tests were performed using a

split Hopkinson pressure bar and a direct impact test system. The tested Alulight and Duocell Al foams did not show any strain rate dependency (Figure 2.14), the plateau stresses and densification strains were shown to be independent of the strain rate. The number of oscillations observed in the stress values of Alulight foam in the plateau region was approximately equal to the number of crush bands formed.

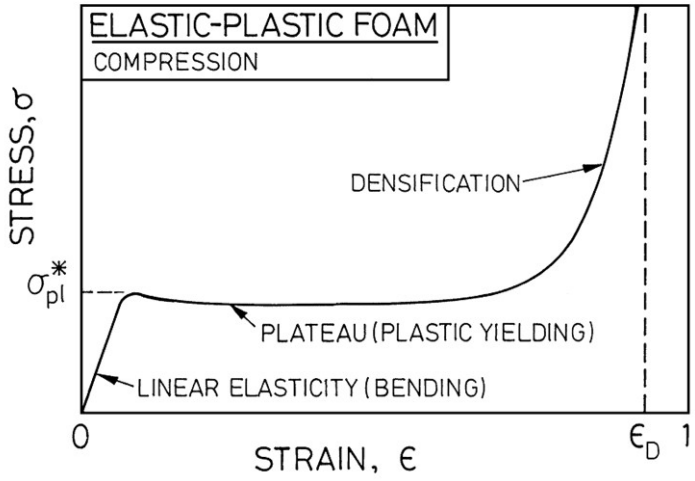

Figure 2. 13 Typical uniaxial compression stress-strain curve of a foam showing the linear elastic, stress plateau and densification regions (Source :Gibson and Ashby, 1997)

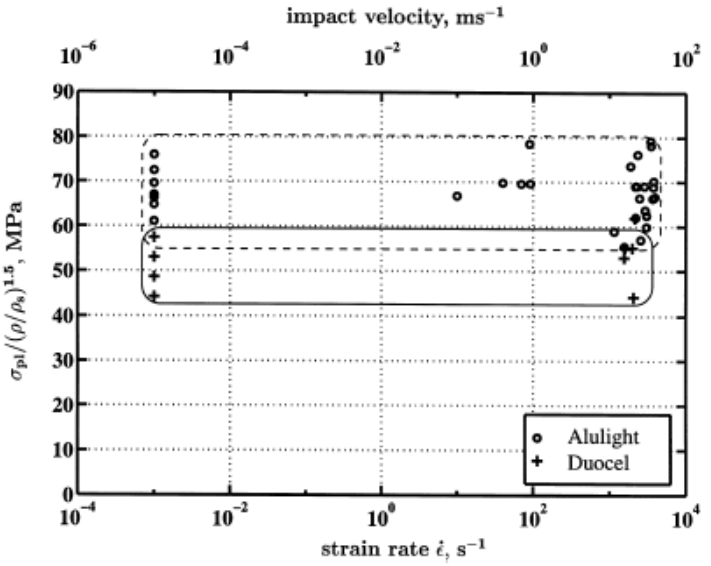

Figure 2. 14. Variation of plateau stress, σ_{pl} , with strain rate, $\dot{\varepsilon}$, for Alulight and Duocel foams, (Source :Deshpande and Fleck, 2000a).

Deshpande and Fleck (Deshpande and Fleck 2000b) proposed self similar and differential hardening models. In Deshpande and Fleck's foam model, the yield function is defined as,

$$\Phi \equiv \hat{\sigma} - Y \leq 0 \tag{2.2}$$

where, $\hat{\sigma}$ and Y are the equivalent stress and yield stress, respectively. The equivalent stress is given by the following,

$$\hat{\sigma}^2 \equiv \frac{1}{[1+(\alpha/3)^2]}[\sigma_e^2 + \alpha^2\sigma_m^2] \tag{2.3}$$

where σ_e and σ_m are the von Mises effective stress and the mean stress, respectively. α defines the shape of the yield surface. The yield stress is defined as (Hanssen, et al. 2002);

$$Y = \sigma_p + \gamma\frac{\hat{\varepsilon}}{\varepsilon_D} + \alpha_2 ln\left(\frac{1}{1-(\hat{\varepsilon}/\varepsilon_D)^\beta}\right) \tag{2.4}$$

where, σ_p is the foam plateau stress and ε_D is the densification strain given as,

$$\varepsilon_D = -\frac{9+\alpha^2}{3\alpha^2} ln\left(\rho_f/\rho_{fo}\right) \tag{2.5}$$

where, ρ_f and ρ_{fo} are the foam and foam base material density, respectively. The second term in Equation 2.4 is called linear strain hardening term, i.e. the slope of the linear section of strain stress curve. The last term represents the non-linear strain hardening,

densification region. α_2 and β are the coefficients of non-linear strain hardening. Miller proposed a continuum plasticity foam model in which the yield surface is defined as (Miller 2000),

$$\Phi = \sigma_e - \gamma\sigma_m + \frac{\alpha}{d}{\sigma_m}^2 - d \tag{2.6}$$

where, d corresponds to uniaxial strength of the foam material and γ and α are the yield surface parameters. In uniaxial compression, where (σ_c), $\sigma_e = \sigma_c$ and $\sigma_m = \sigma_c/3$ and for $\Phi = 0$, the compressive yield stress becomes;

$$\sigma_c = \frac{2d}{1-\gamma/3+\sqrt{\left(1-(\gamma/3)\right)^2+4\alpha/9}} \tag{2.7}$$

Similarly, in uniaxial tension, where σ_t, $\sigma_e = \sigma_t$and $\sigma_m = -\sigma_t/3$, the tensile yield strength becomes;

$$\sigma_c = \frac{2d}{1+\gamma/3+\sqrt{\left(1+(\gamma/3)\right)^2+4\alpha/9}} \tag{2.8}$$

The proposed model was used to simulate the indentation behavior of foam metal cored sandwich panels. Various geometric and material parameters affecting the load-displacement curves of the structure were determined. The foam material model accurately captured the behavior of sandwich panel under indentation. Sridhar and Fleck (Sridhar and Fleck 2005) studied the multiaxial yield behavior of Alulight Al foam.

Similar to uniaxial compression of Al foam, pressure vs. volumetric strain response of hydrostatic compression shows three distinct regimes; linear elastic, hardening plastic and densification. The strain hardening in hydrostatic compression is however higher than that in uniaxial compression as depicted in Figure 2.15,

The specimen size effects on the mechanical behavior of Alporas closed cell and Duocell open cell Al foams were determined by Andrews et al. (Andrews, et al. 2001, Onck, et al. 2001) . It was reported that Young's modulus and plastic collapse strength of both foams increased with increasing the ratio of specimen size to cell size, L/d. It was also detected that the decrease in Young's modulus and strength values with decreasing the ratio of specimen size to cell size in open cell foams was more rapid than in closed cell foams, mainly due to the lack of cell faces in open cell foam. The size effect on the shear strength was found to disappear for the specimens with a thickness at last twice the cell size as shown in Figure 2.16.

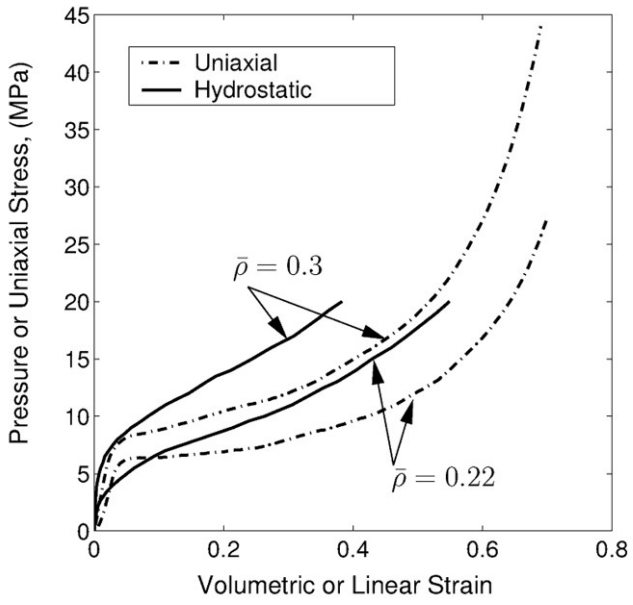

Figure 2. 15. .The uniaxial and hydrostatic stress-strain curves of Alulight foams. (Source: Shridhar and Fleck 2005)

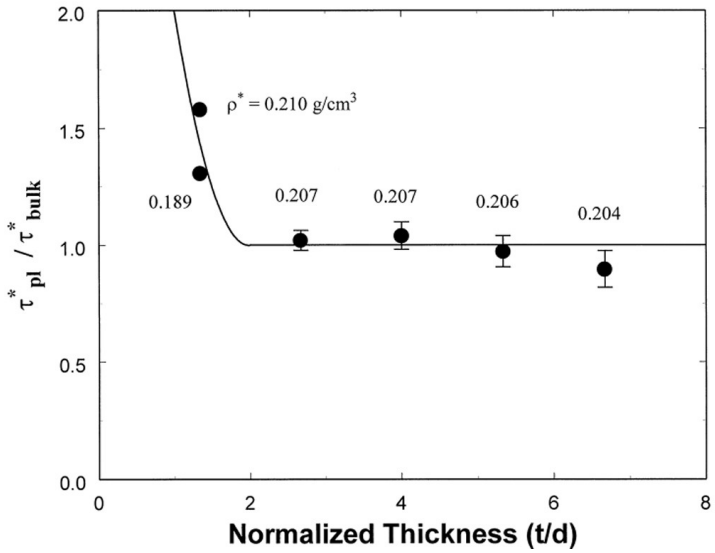

Figure 2.16. Shear strength, normalized by the bulk value, against the ratio of specimen thickness, t, to the cell size, d, for Alporas closed-cell foam (Source: Andrews, et al. 2001).

The effect of foam cell structure parameters on the compression behavior of Al foam was investigated by Dequing et. al. (Deqing, et al. 2005). With increasing foam cell size, foam density (Figure 2.17(a)) and cell wall and node size (Figure 2.17(a)) decreased. It was further postulated that the collapse plastic stress and energy absorption ability could be improved by the smaller cell size. Similar results were also found by Miyoshi et. al. (Miyoshi, et al. 1999). By reducing the cell edge length of conventional Alporas Al foams from ~2.68 mm to ~1.91 mm, the energy absorption per volume increased by 40% .

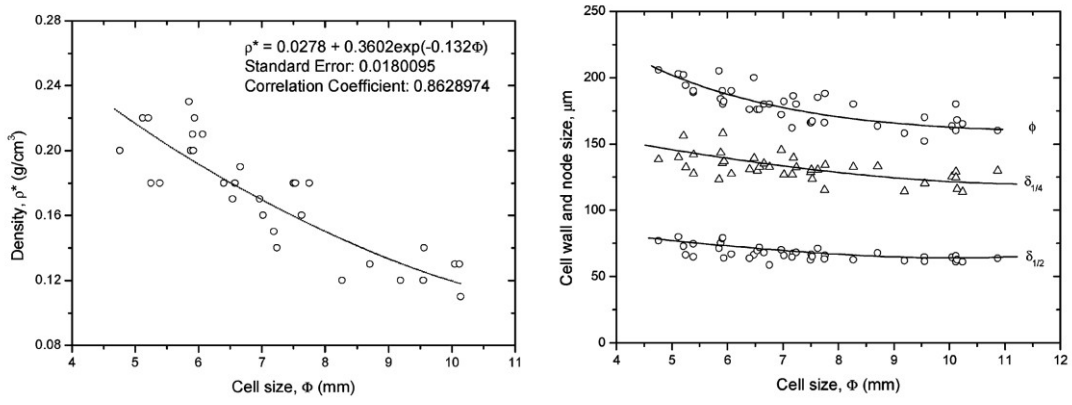

(a) (b)

Figure 2. 17. Variation of a) foam density and b) foam cell wall and node size with foam cell size of Al foam (Source: Deqing, et al. 2005).

The creep and plateau stress-temperature behavior of Al foams was previously studied by few researchers (Andrews, et al. 1999a, Andrews, et al. 1999b, Haag, et al. 2003). The secondary creep strain rate and the time to failure of Alporas closed cell Al foam were determined (Andrews, et al. 2001). Al foam showed comparable creep activation and power law exponent values with those of pure Al under relatively low stresses and at low temperatures. However, at high stresses, higher activation energy and power law number were found. This behavior was attributed to the cell wall breakage at very high creep rates due to the high local stresses caused by the inhomogeneous cell microstructure. The plateau stresses of Al closed cell foams decreased with increasing ,Figure 2.18 (Haag, et al. 2003).

The energy absorbing capacity and the plateau stresses of pure Al and solution hardened Al-10% magnesium alloy (AlMg10) foams were previously compared (Han, et al. 1998). The solution treated AlMg10 foam showed less number of load oscillations than untreated foams. This behavior was explained by β phase of Al and Mg compound partially or wholly dissolved in α phase by solution treatment. However, as-cast AlMg10 foams showed higher plateau stresses and energy absorption than pure Al and solution treated AlMg10 foams (Figure 2.19).

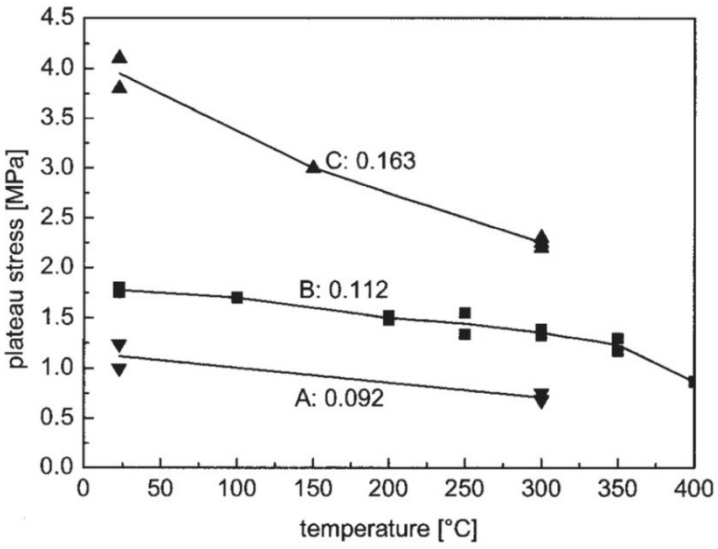

Figure 2. 18. Plateau stress vs. temperature at a strain rate of 3.4 X 10^{-4} s^{-1}.
(Source: Haag, et al. 2003)

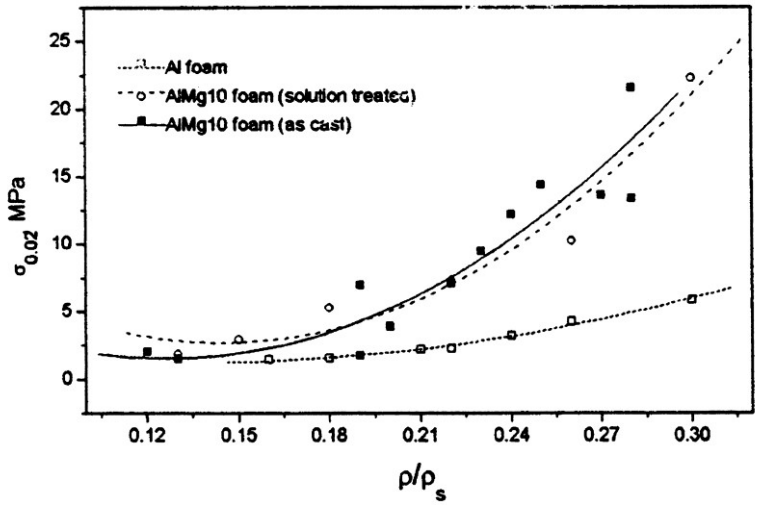

Figure 2. 19. Yield strength *vs.* relative density of pure Al, AlMg10 and solution treated AlMg10 foam (Source: Han, et al. 1998)

One of the earliest metal foam modeling studies using an unit cell geometry was performed by Santosa and Wierzbicki (Santosa and Wierzbicki 1998b). The unit cell geometry was a truncated cube comprising cruciform web and pyramidal sections. The crushing of truncated cube unit cell model was progressive folding initiated at the cruciform section and followed by plastic collapse in the pyramidal section. Good agreements between the simulation, analytical modeling and experimental uniaxial compression of HYDRO and IFAM Al closed-cell foam were found (Figure 2.20). However, CYMAT and ALCAN foams showed experimentally much lower crushing strength than the predicted values. This was attributed to the differences in the foam morphological structures between the investigated Al foams, leading to the difference in the crushing strengths.

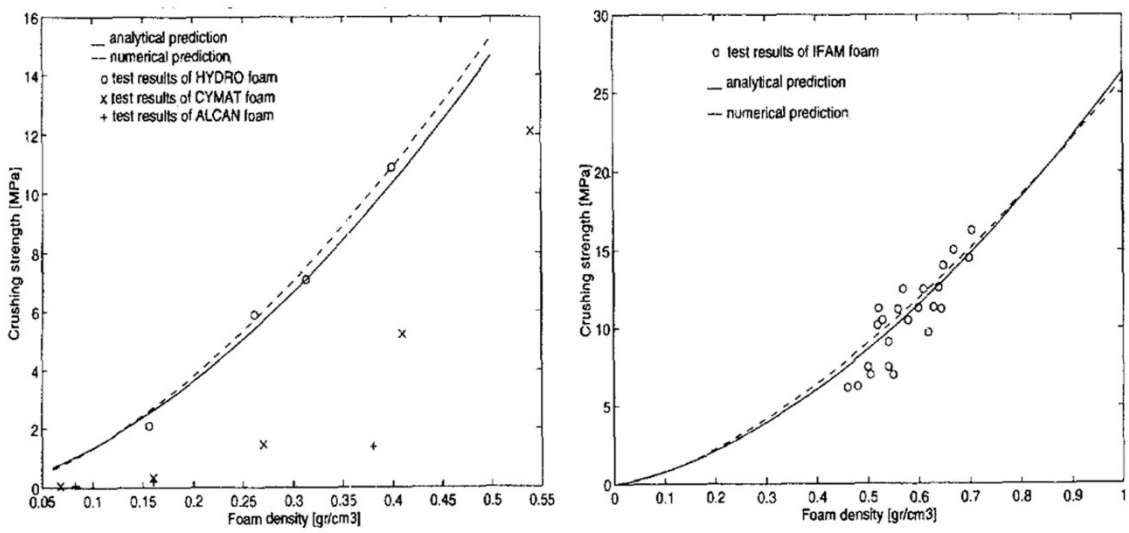

(a) (b)

Figure 2. 20. Crushing strength vs. foam density: a)Al-SiC and b)AlCu4 alloy closed cell foam, (Source: Santosa and Wierzbicki 1998b).

Compression behavior of Al foams was simulated by using a unit cell geometry consists of two hemispheres and five layered multi-cell structure, Figure 2.21(Meguid, et al. 2002). Experimental density measurements showed certain density variations through the in-plane and transverse directions. In the simulations, the layer density was altered by varying the unit cell wall thickness. The crush behavior and load vs. deformation curves of the simulations and the experiments showed good agreement for both directions, transverse and in plane. The deformation behavior of a uniform density multiple cell model was also examined in the same study. In this case, the model could not accurately capture the localization behavior of the foam, and the resulting nominal stress–strain curves showed unrealistic numerical oscillations.

Czekanski et al. (Czekanski, et al. 2005b) proposed a 3D unit cell geometry for modeling the deformation behavior of Al closed-cell foams. Proposed unit cell combined the ellipsoid small and pseudo-octagonal large cells as shown in Figures 2.22(a) and (b). Multi-cell finite element models were used to study the effect of individual cell size shape and the foam density on the collapse load and energy absorption. Simulation results showed geometrical parameters of multi-cell foam model had insignificant effects on the overall behavior of Al foam (Czekanski, et al. 2005a, Czekanski, et al. 2005b).

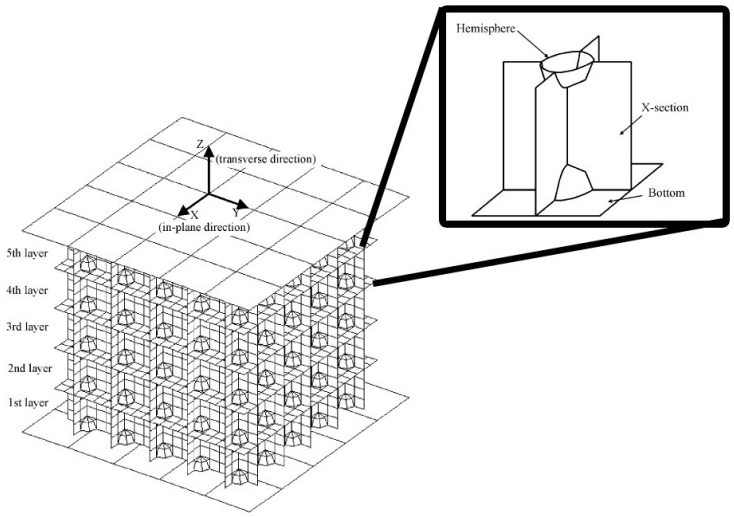

Figure 2. 21. Unit cell geometry and layered structure of Al foam simulation. (Source: Meguid, et al. 2002)

The mechanical behavior of an Al foam was investigated at quasi-static and high strain rates under hydrostatic compression and tension,(Peroni, et al. 2008). Dynamic tests were performed using Taylor impact tester and Split-Hopkinson pressure bar. It was reported that yield stress values at quasi-static and dynamic uniaxial compression over a vast range of relative densities showed no dependence on the strain rate (Figure 2.23).

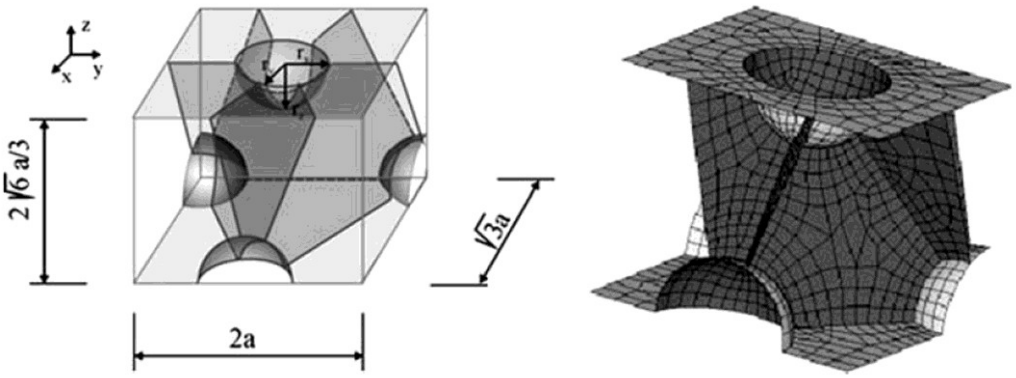

Figure 2. 22. Unit-cell model: (a) graphical representation, and (b) 3D discredited geometry of representative unit-cell, (Source: Czekanski, et al. 2005b).

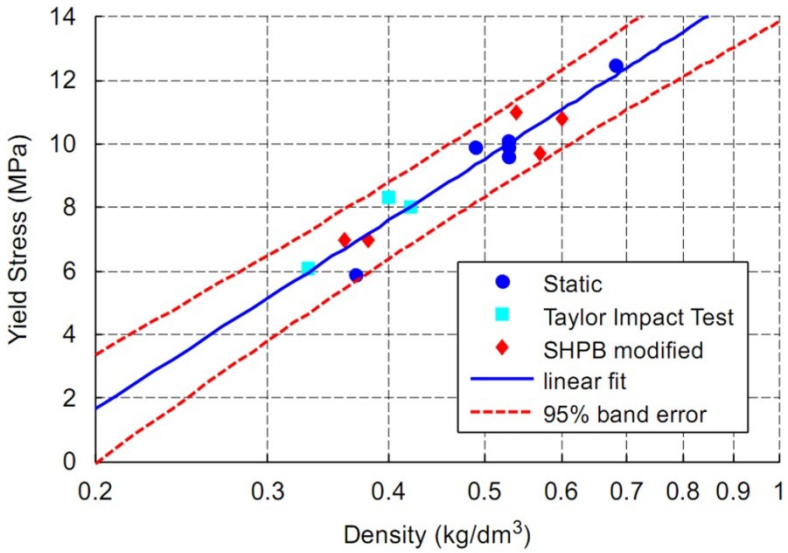

Figure 2.23. Yield stress vs. foam density and deformation energy vs. foam density in compression testing of an Al foam using different testing methods (Source Peroni, et al. 2008).

The effect of Al alloy type (AlSi7, 6061 and 7075 Al) on the microstructure and crushing behavior of Al foams were further investigated (Campana and Pilone 2008). The cell microstructure of AlSi7 foam was found to be more inhomogeneous than that of 6061 and 7075 Al foam. AlSi7 foam contained a higher number of small and large voids distributed anisotropically. Microscopic analysis showed the presence of intermetallic particles $(Fe,Cr)_3SiAl_{12}$ in the cells of 6061 and 7075 Al foams. The randomly distributed Ti particles surrounded by Si-Ti phase in the cell walls of AlSi7 Al foam proved the inefficient foaming of the alloy. AlSi7 foam showed a ductile deformation mode without the initial peak load and a distinctive hardening in the uniaxial compression, while 7075 Al foam showed an initial peak load and load oscillations (Figure 2.24), which was attributed to the presence of intermetallic compounds on the cell walls.

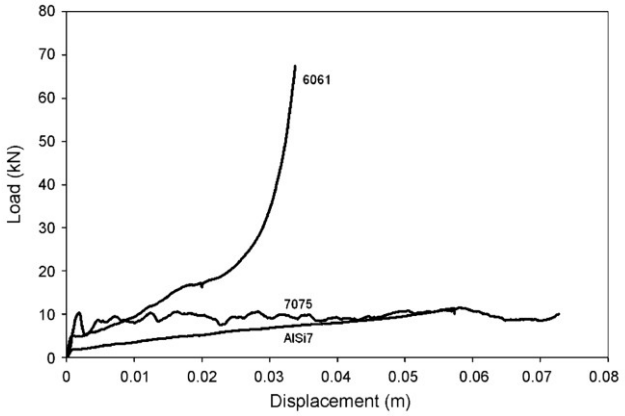

Figure 2. 24. Load–displacement curves of 6061, 7075 and AlSi7 alloy foams .(Source: Campana and Pilone 2008)

The strain rate sensitivity of Al foams produced by powder metallurgy route (IFAM) and gas injection process (CYMAT) was investigated (Zhao, et al. 2006). Although, IFAM foams showed strain rate enhancement in the mean flow stress by 15%, brittle CYMAT Al foam showed no strain rate sensitivity (Zhao, et al. 2007, Zhao, et al. 2006). The progressive folding of cell walls was observed in the deformed IFAM foam (Figure 2.25(a)), while the cells cracked multiply in CYMAT foam (Figure 2.25(b)). The rate sensitivity was proposed to be resulted from the micro inertia of progressive folding. In the compression testing, the deformation started at the weakest region in CYMAT foam (Ruan, et al. 2002). Following the densification in the weakest region, the deformation continued to another weakest region as shown in Figure 2.26.

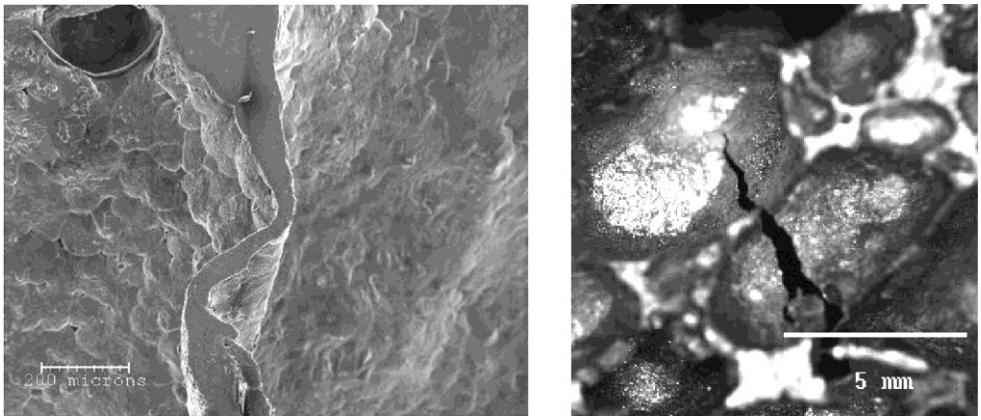

(a) (b)

Figure 2. 25. a) Progressive cell wall folding in IFAM foam and b) the cell wall fracture in CYMAT foam (Source: Zhao, et al. 2006).

The energy absorption of an Alporas Al foam was shown to increase approximately 50% at dynamic strain rates (Paul and Ramamurty 2000). The effect of strain rate on the deformation of Alporas Al foams was further studied by Mukai and his colleagues (Mukai, et al. 1999, Mukai, et al. 2006). The increase in the aspect ratio of cell wall thickness to the cell edge length was shown to result in higher cell face resistance to the cell wall stretching. The strain rate sensitivity of open and closed 6061 Al foams was investigated by Dannemann and Lankford (Dannemann and Lankford 2000). The strain rate dependency of the studied foams was explained by the change of cell shape at increasing foam densities from polyhedral to spheroidal. Ma and his colleagues studied the strain rate effect on the crushing behavior of metallic cellular materials,(Ma, et al. 2009). Voronoi mesoscale model was implemented to resemble closed cell foam structure in the numerical study (Figure 2.27). Both strain rate insensitive and sensitive material model were implemented to differentiate the inertial affects from the strain rate effects. Voronoi and the classical continuum models with strain rate insensitive material model showed the increases in the crushing stresses at increasing strain rates, proving the inertial effects on the stress enhancement at high strain rates.

The energy absorption characteristics of closed cell foam were investigated at varying impact velocities (Lopatnikov, et al. 2007, Lopatnikov, et al. 2004). The impact of a rigid plate on a metal foam is considered in four different deformation regimes. The first regime is the supersonic impact velocities, which is beyond the virtually all practical applications. In the second regime, the shock compaction occurs, the elastic wave propagation is neglected. In the third regime, both shock wave and elastic wave propagation occur. In the fourth regime, the wave propagation is neglected; the deformation is considered as quasi-static. The energy efficiency in regime 2 depends on the density of foam and base material, and the mass of the impacted plate. The energy efficiency in regime 3 depends on the Mach number and the critical stress and strain of foam.

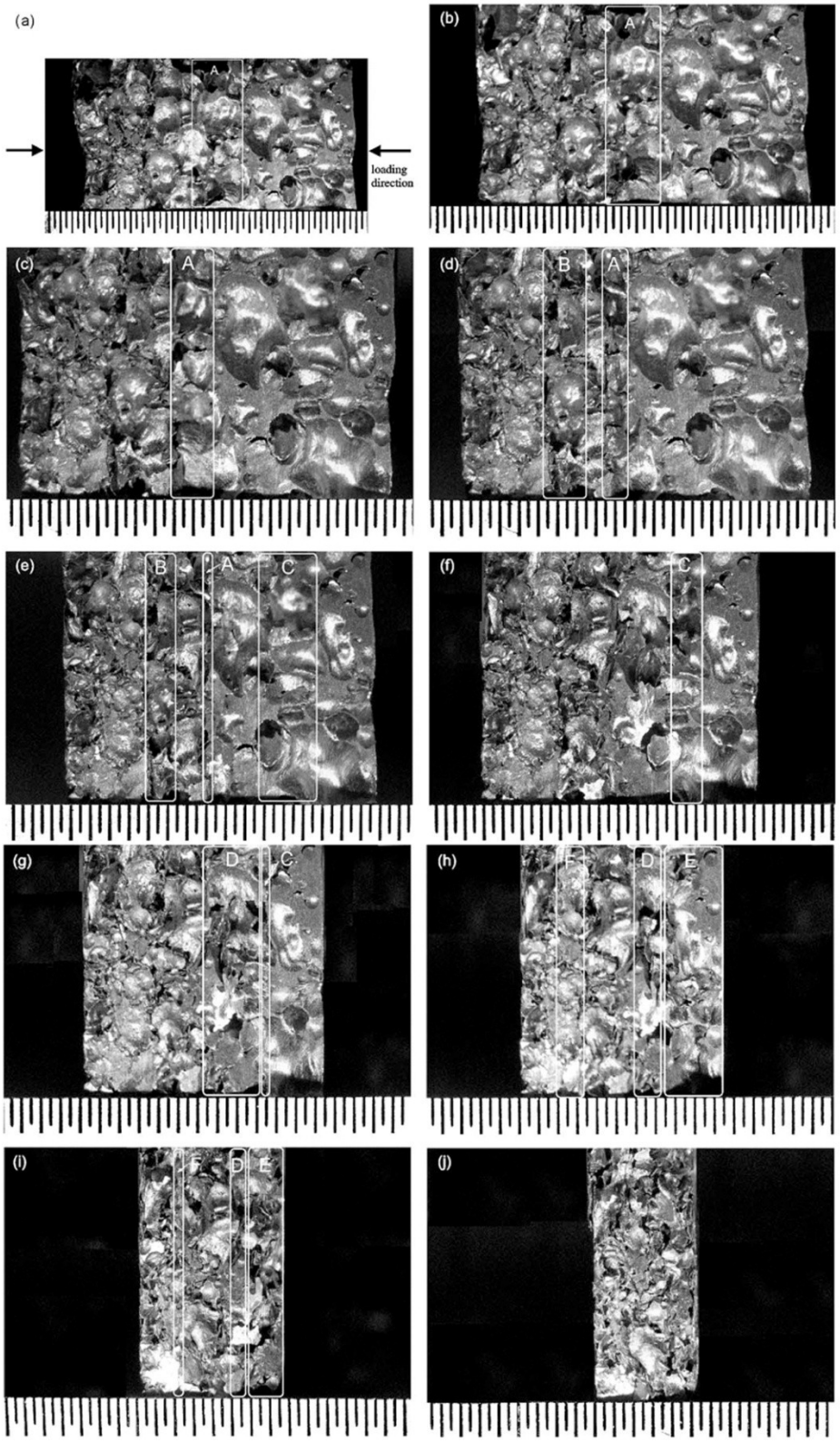

Figure 2. 26. The photographs of a compressed CYMAT foam, each interval approximately 1.5 mm (Source: Ruan, et al. 2002).

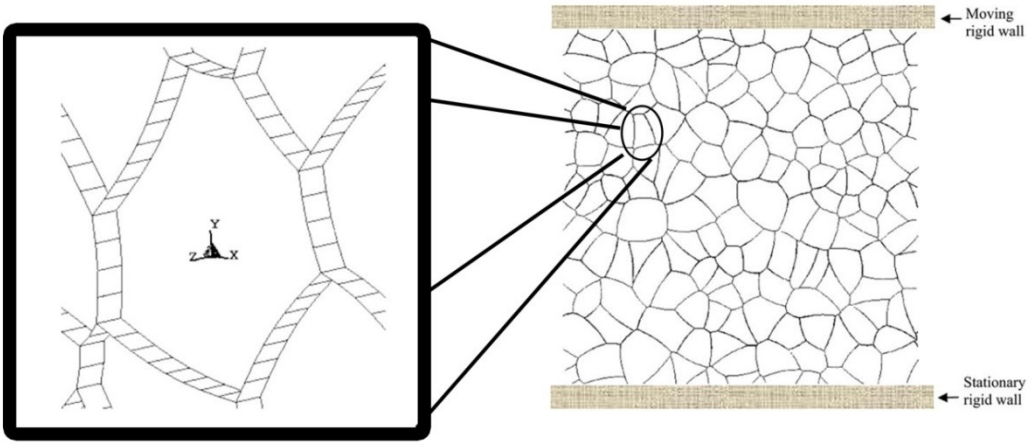

Figure 2. 27. Voronoi foam model (x–y plane).
(Source: Ma, et al. 2009)

Two ideal deformation scenarios, homogenous and progressive collapse, were used to characterize the energy absorbing capacity of metallic foams under quasi-static axial compression in regime 4 (Lopatnikov, et al. 2007). These collapse scenarios were compared with elastic-plastic-rigid (EPR) and elastic -perfectly plastic-rigid (EPPR) foam models (Figure 2.28). The developed theoretical models based on the deformation scenarios predicted the same energy absorption values with EPRS foam.

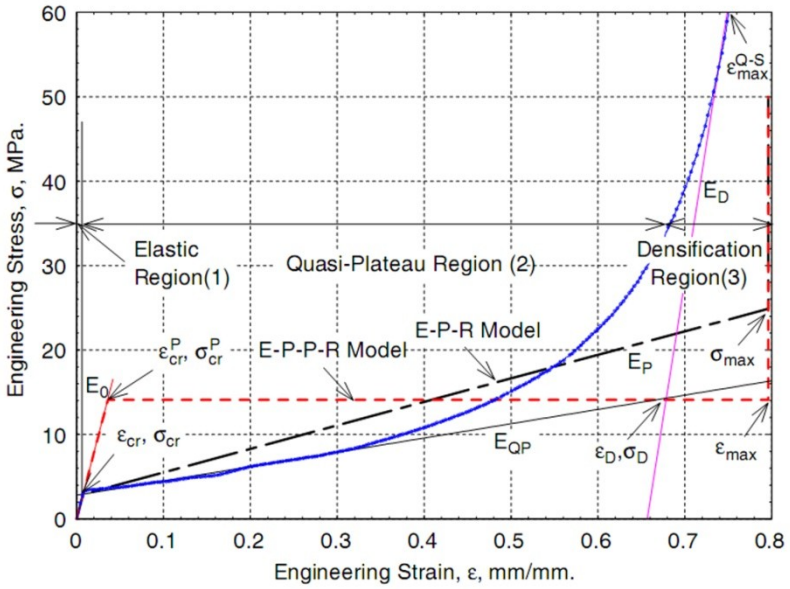

Figure 2. 28. Quasi-static compression behavior of metal foams and model definitions.
(Source: Lopatnikov, et al. 2007)

CHAPTER 3

CRUSHING BEHAVIOR OF TUBULAR STRUCTURES UNDER AXIAL DEFORMATIONS

3.1.Introduction

Tubular forms of crash elements are widely used in transportation industry especially in automobiles, trains and airplanes. Several different cross-sectional geometries including circular (Gameiro and Cirne 2007, Singace and Elsobky 2000, Wang and Lu 2002), square and rectangular (Abedrabbo, et al. 2009, Langseth and Hopperstad 1997, Qiao, et al. 2006) cross-sections have been extensively investigated because of their low cost of manufacturing such as extruding, welding and bending. Besides the cross-sectional geometries, the base material type determines the crash energy absorbing capabilities of tubular structures. Conventional structural steels (DiPaolo, et al. 2004, Peroni, et al. 2009, Talonen and Hanninen 2006) and aluminum alloys (Baccouche and Wagner 2001, Mamalis, et al. 2005, Tasdemirci 2008) and carbon fiber reinforced composites (Chirwa, et al. 2003, Mamalis, et al. 2002, Mamalis, et al. 2006) are among the most investigated base material types of the tubular structures. In recent years, lightweight polymeric (Mamalis, et al. 2003a, Toksoy 2003, Toksoy and Güden 2005) and metallic foams (Hall, et al. 2001, Hall, et al. 2002, Mamalis, et al. 2009, Rajendran, et al. 2009b) have been considered as fillers for both metallic and composite tubular structures. One of the most important motivations of foam filling is to maximize the energy absorption during the crash event. Extensive theoretical studies have also been conducted to predict the crushing behavior of empty and filled crash structures (Wang, et al. 2006).

3.2. Crushing Behavior of Empty Circular Tubes

Andrews et. al. (Andrews, et al. 1983) determined the deformation modes of empty aluminum cylindrical tubes with various lengths to diameter D/t and L/t and wall thickness to diameter ratios. The deformation modes associated with geometrical parameters of cylindrical tubes are graphically shown in Figure 3. 1. The common deformation modes are classifies as;

- Diamond: Progressive asymmetric folding of circular tubes, Figure 3.2., (Marsolek and Reimerdes 2004).
- Concertina: Progressive axisymmetric folding of circular tubes, Figure 3.3., (Huang 2003)
- Mixed: Axisymmetric folding followed diamond mode of folding , Figure 3.4., (Toksoy 2003)
- Axisymmetric deformation (single or multiple barreling): Simultaneous collapse along the length of the tube, Figure 3.5., (Kavi 2004)
- Global Bending (Euler): Tube buckling, Figure 3.6., (Seitzberger, et al. 1997).

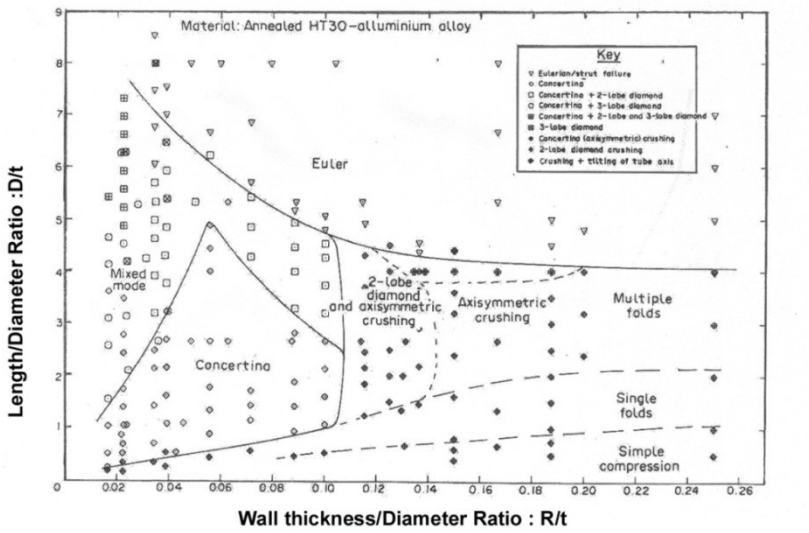

Figure 3.1. Crushing modes of HT30 Al tubes as functions of D/t and L/t.
(Source: Andrews, et al. 1983)

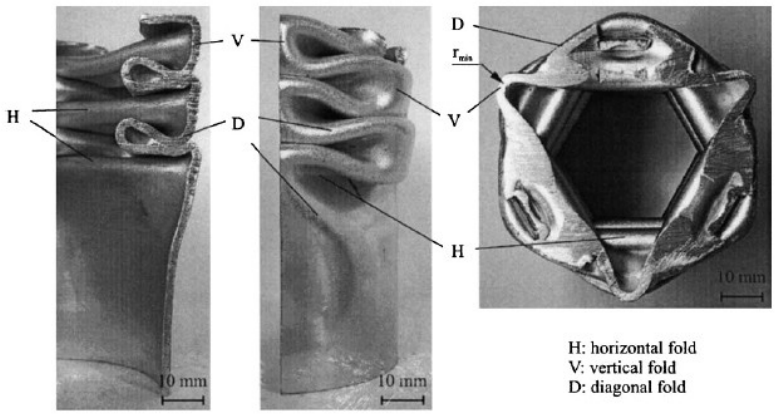

Figure 3.2. Diamond deformation mode of circular tubes.
(Source: Marsolek and Reimerdes 2004)

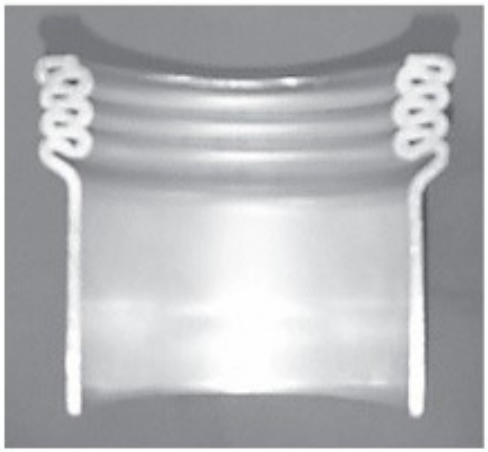

Figure 3.3. Concertina mode of 6060T5 circular aluminum tubes.
(Source: Huang 2003)

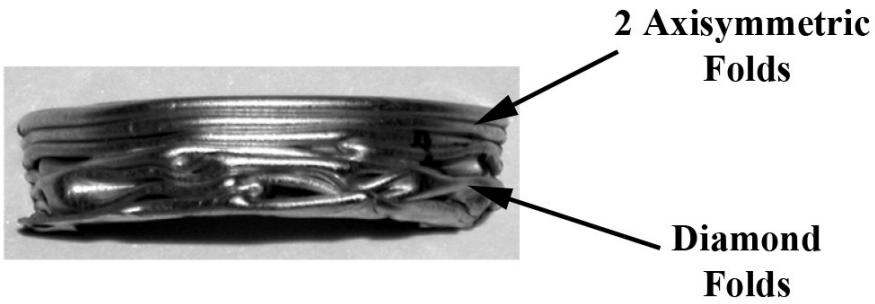

Figure 3.4. Mixed deformation mode.
(Source: Toksoy 2003)

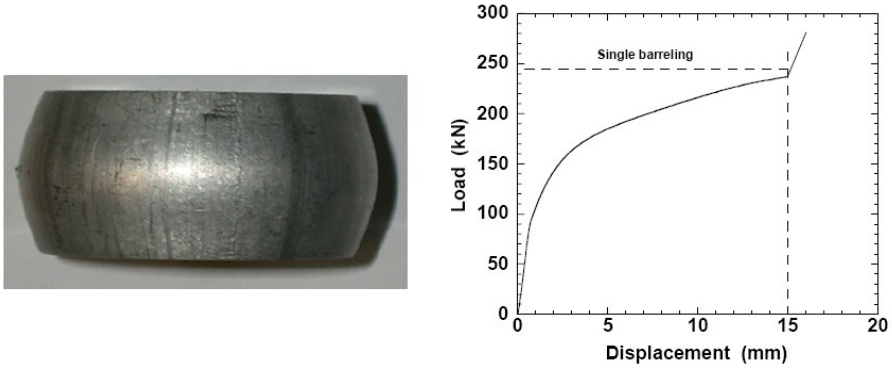

(a)

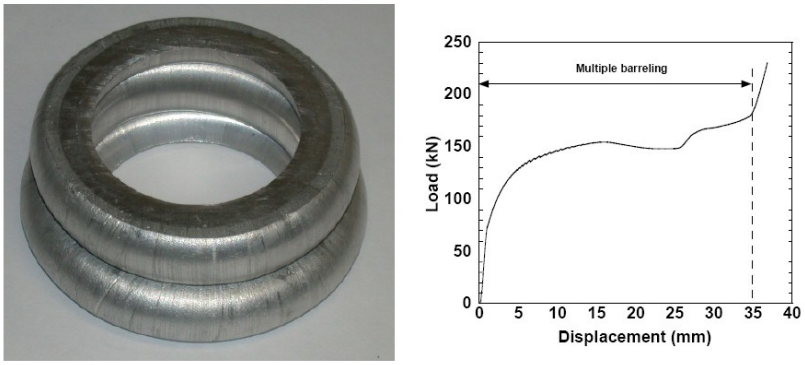

(b)

Figure 3.5. a) Single and b) multiple barreling of circular sections.
(Source: Kavi 2004)

Figure 3.6. Global bending (Euler) deformation mode.
(Source: Seitzberger, et al. 1997)

The first analytical study on the crushing behavior of circular tubes was made by Alexander in 1960 (Alexander 1960). The mean crushing load (P_m) of concertina mode of deformation was analytically determined based on the plastic work required for bending and stretching of extensible thin cylinder and is given as

$$P_m = \sigma_0 t^2 \left[5.983 \left(\frac{D}{t}\right)^{1/2} + 1.814\right] \tag{3.1}$$

where, D and t are the diameter and thickness of tube, respectively. σ_0 is the mean plastic flow stress and expressed as

$$\sigma_0 = \left(\frac{\sigma_{0.2} + \sigma_u}{2}\right) \tag{3.2}$$

$\sigma_{0.2}$ and σ_u in Equation 3.2 are the material proof and ultimate yield stress, respectively. Pugsley and Macaulay (Pugsley and Macaulay 1960) investigated the diamond mode of deformation of thin cylindrical columns with large D/t ratios. The deformation energy was assumed to be absorbed by plastic bending and shear of the diamond deformation pattern. The following equation was proposed for the average crushing load of diamond mode of deformation,

$$P_m = \sigma_0 t(10.05t + 0.38D) \tag{3.3}$$

Abramowicz and Jones (Abramowicz and Jones 1986, Abramowicz and Jones 1984) modified Alexander's model and proposed the following equations for the concertina mode of deformation,

$$P_m = \sigma_0 t\left[6(Dt)^{1/2} + 3.44t\right] \tag{3.4}$$

Wierzbicki et al. (Wierzbicki, et al. 1992) proposed the following equation for the concertina mode of deformation,

$$P_m = 7.933\sigma_0 t^2 \left(\frac{D}{t}\right)^2 \tag{3.5}$$

The concertina mode proceeds with two characteristic movements: outward and inward folding (Singace and Elsobky 1996). Outward fold length over total length of deformation fold is called as eccentricity factor. The eccentricity factor was proposed to be 0.65, but experimentally determined values of the eccentricity factors were found to be less than this value (Singace, et al. 1995). It was also proposed that if continuous zone or curved elements were used to represent the folding elements, a better agreement between the theory and the experimental results was expected. Singace's analytical approach of mean crushing force is given as,

$$P_m = \sigma_0 t^2 \left[5.567\left(\frac{D}{t}\right)^{1/2} + 1.408\right] \tag{3.6}$$

Kormi et. al (Kormi, et al. 1993) investigated empty cylindrical tubes under uniaxial and torsional deformation loads. The load carrying level of cylinder tubes under combined axial and torsion loading was found to be equal to the sum of the deformation load levels of only axial compression and only torsional loading. The axisymmetric progressive crushing behavior of circular tubes under axial compression was studied by Bardi et al.(Bardi, et al. 2003). Carbon Steel (CS-1020) and two different aluminum alloys (6061T6, 6260T4) circular tubes with different D/t ratios and L/t ratios were quasi-statically compression tested and the compression tests were simulated using ABAQUS. Experimental and simulation results were further compared with those of analytical models developed for circular tubes. It was reported that

deformation mode transition from axisymmetric to non-symmetric depended on tube D/t ratio and the hardening characteristics of the tube material. The simulation deformation modes and the load-deformation curves of the tubes were found to be in good agreement with those of experiments. The analytical model proposed by Wierzbicki et al. (Wierzbicki, et al. 1992) for circular tube plastic hinge deformation showed the highest correlation with the experiments. Pipkorn and Haland (Pipkorn and Hayland 2005) studied the crash performance of tubes with smooth and variable diameter and with internal pressure. Experimental and numeric results showed that increasing internal pressure increased the absorb energy. Energy efficiency increased up to 60% and 70% in smooth and variable diameter circular tubes, respectively.

Finite element simulation of square and circular tube inversion under static and dynamic loading was performed by Webb et al.(Webb, et al. 2001). The tube wall thickness was taken as variable. The simulations gave similar results with experiments. Singace and El-Sobky (Singace and Elsobky 2000) investigated the deformation modes of circular tubes and reported that concertina mode of deformation resulted in higher mean load values, while mixed mode of deformation showed higher energy absorption values than concertina mode. The crushing behavior of a 6060T5 circular aluminum tube was investigated experimentally and numerically by Huang and Lu (Huang 2003). A new theoretical model was used to predict the mean crushing force using a total work of membrane energy dissipation in deformation zones and the required bending energy of plastic hinges. The model could not predict the peak load values accurately, while the mean load and the half fold length calculations showed good agreement with those of experiments and simulations. Galib and Limam performed extensive study on the static and dynamic crushing behavior of empty 6060T5 aluminum circular tubes, (Galib and Limam 2004). It was found that the deformation velocity had no effect on the deformation load capacity and deformation mode of 6060T5 circular tubes within the strain rate range between 91 and 114 s^{-1}. The dynamic mean load values were found 10% higher than those of quasi-static tests. The increase in the mean load values was attributed to micro inertial effects (the lateral movement of circular structure at the initial stage of impact). The simulations showed that increasing the ratio of amplitude of the surface imperfection to thickness (a/t) reverted the mixed mode of deformation of tube into diamond mode (Figure 3.7), reducing the absorbed energy.

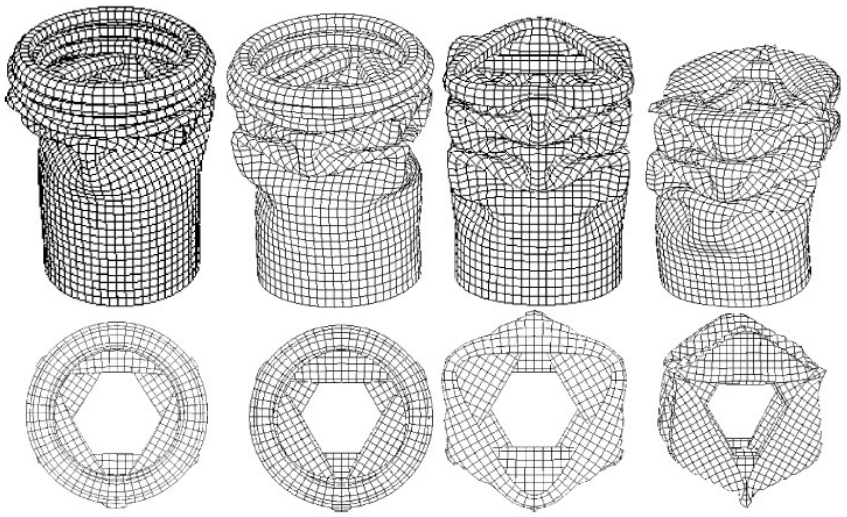

(a) (b) (c) (d)

Figure 3.7. Simulations of the deformation mode of circular tubes with circumferential imperfections; a/t ratios a) 5%, b)10%, c)50% and d)100% (Source: Galip and Liman 2004).

The static and dynamic crushing behavior of thin walled circular stainless steel, mild steel and Al alloy tubes were investigated (Hsu and Jones 2004). Energy efficiency factor was defined as total elastic and plastic strain energy absorbed by a structural member divided by the energy absorbed in the same volume of material up to the failure in tension for evaluating the crashworthiness level of structure. It was reported that stainless steel circular tubes absorbed the highest energy among the tested tubes (Figure 3.8). However, calculated energy efficiency factor of stainless steel circular tube was found the lowest for both the quasi-static and impact loading. The critical specimen length for the transition from the efficient progressive buckling to the catastrophic global bending for quasi-static loading was found to be similar for three tubes. The critical tube length of the transition was shown to increase with increasing impact velocity.

The crushing behavior of circular CR 1018 steel tubes with groove patterns was studied experimentally and numerically,(Mamalis, et al. 2003c). Model and simulations showed similar deformation modes (Figure 3.9(a) and (b)). The initial peak load value of grooved tube was found to be lower than that of non-grooved tube (Figure 3.9(c)). The number of grooves was found not to affect the peak load values in both experiments and simulations, while the number of load peaks and the values of mean load decreased with increasing number of grooves (Figure 3.9 (d)).

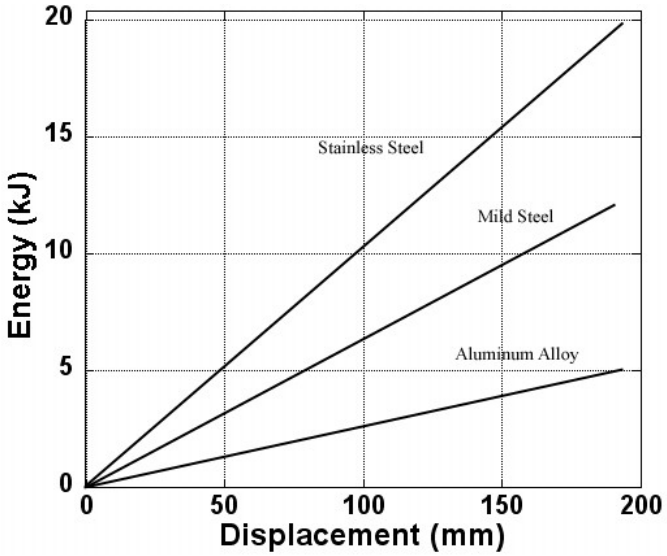

Figure 3.8. Energy absorption of quasi-statically loaded of stainless steel, mild steel and Al alloy tubes, L=250 mm (Source: Hsu and Jones 2004).

Energy absorption of aluminum (AlMgSi0.5) cylindrical tubes with the induced non-axisymmetric folding patterns was studied by Marsolek and Reimeders (Marsolek and Reimerdes 2004). Special apparatus was designed to initiate diamond mode with three and four circumferential waves. During the deformation of circular tubes, the designed apparatus induced local loads and caused the deformation mode change from concertina to diamond mode (Figure 3.10(a) and (b)). Non-axisymmetric folding patterns also decreased the initial peak loads. Particularly, circular tube with 3 circumferential waves (Figure 3.10(c)) showed lower deformation loads than both concertina mode and diamond deformation mode of deformation with 4 circumferential waves (Figure 3.10(c)).

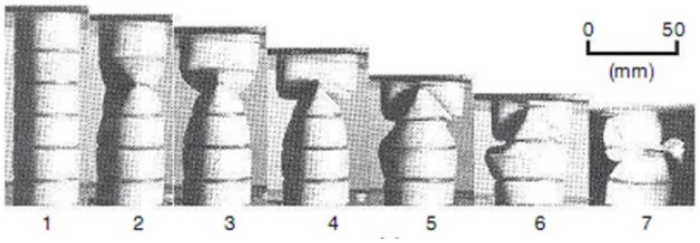

(a)

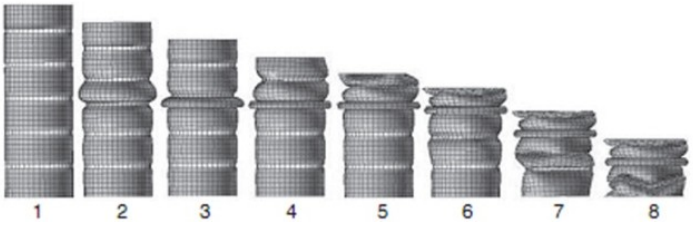

(b)

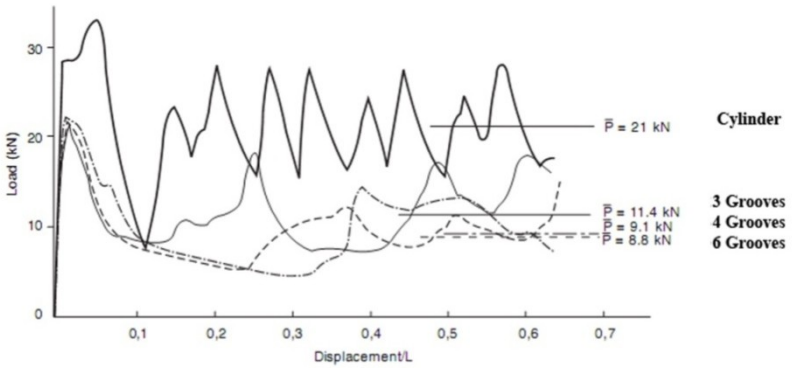

(c)

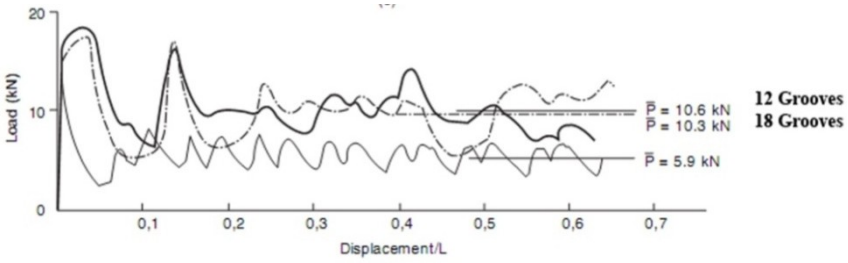

(d)

Figure 3.9. a) Experimental and b) numerical deformation behavior of circular tubes with 6 grooves and comparison of load-deformation graphs of circular tubes with c) non-grooved, 3,4 and 6 grooves, d) 12 and 18 grooves (Source Mamalis, et al. 2003b).

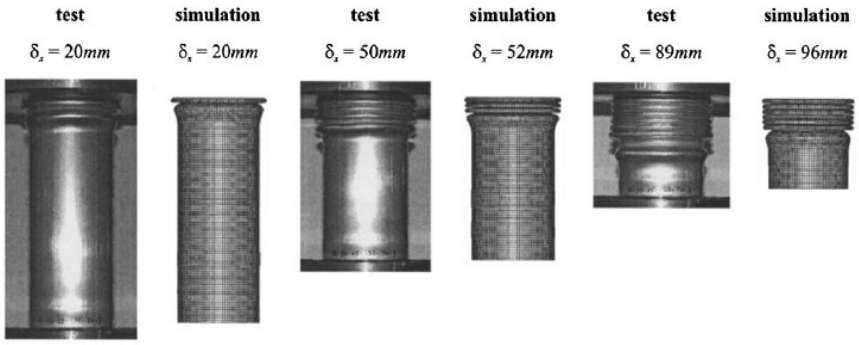

(a)

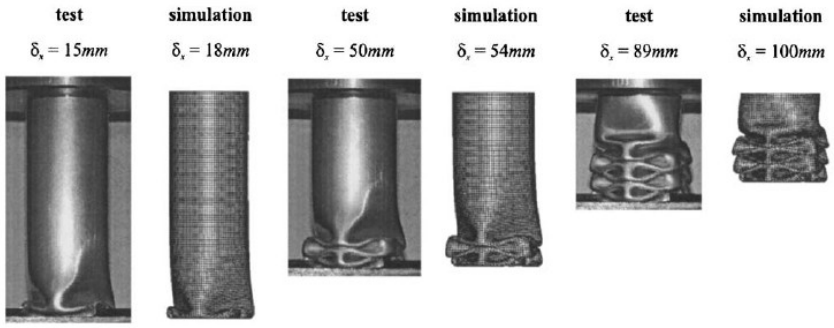

(b)

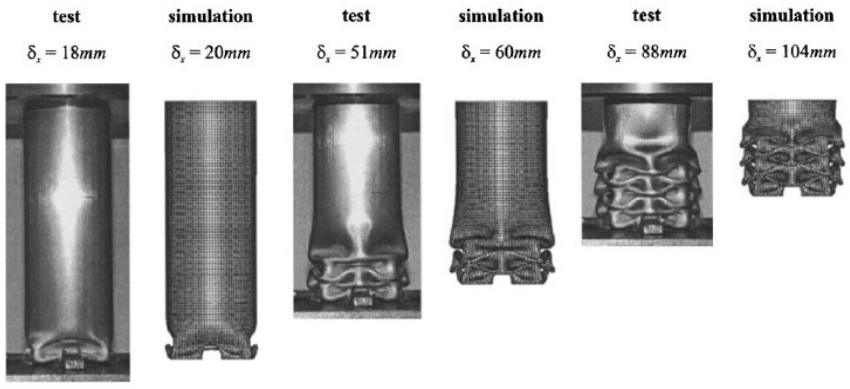

(c)

Figure 3.10. Deformation mode of a) concertina and diamond b) with 3 circumferential waves and c) 4 circumferential waves, (Source: Marsolek and Reminerdes 2004).

3.3. Crushing Behavior of Empty Square and Rectangular Tubes

Two common folding modes of square tubes, inextensional and extensional deformation mode are shown schematically in Figure 3.11(a) and (b), respectively. In inextensional deformation mode, two outwards folds form on the opposite sites of the tube, and the remaining two sides fold inwardly as shown in Figure 3.11(a). In extensional deformation mode, folds form outwardly (Figure 3.11(b)).

An analytical model predicting the mean crushing load of square empty tubes was developed by Wierzbcki and Abramowicz (Wierzbicki and Abramowicz 1983). The analytical formulation is expressed as,

$$P_m = 9.56\,\sigma_0 b^{1/3} t^{5/3} \tag{3.7}$$

where, σ_0, b, t are the flow stress of tube material and width and thickness of the tube. Later, Abramowicz and Jones simplified the Eq (3.7) as (Abramowicz and Jones 1986),

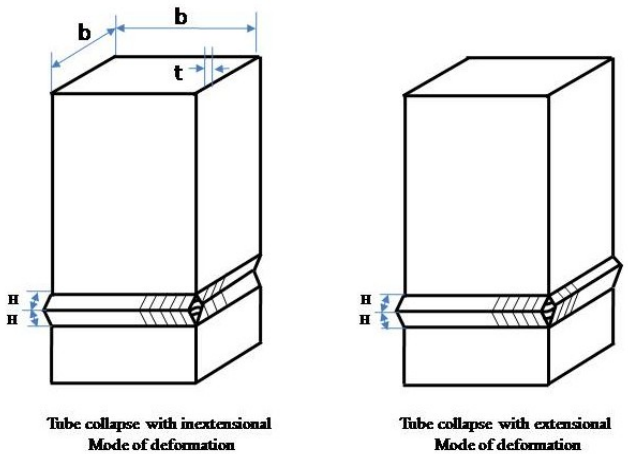

(a) (b)

Figure 3.11. Axial progressive collapse of square cross-section tubes, a) inextensional and b) extensional mode.

$$P_m = K\,\sigma_0 b^{1/3} t^{5/3} \tag{3.8}$$

where, K is a dimensionless constant. The values of K for the square sections was found 13.06 (Abramowicz and Jones 1986), 11.3 (Hanssen, et al. 1999) and 14 (Santosa and Wierzbicki 1998a). Jones proposed the following equation for the prediction of mean load in square tubes as (Jones 1989),

$$P_m = C_0\,\varphi^{2/3}\sigma_0 A_0 \tag{3.9}$$

here, C_0 is the cross-section dependent dimensionless constant and φ is the solidity ratio which is calculated from the solid cross-section area, A_0, divided by the inner area of the tube. Equation 3.8 and 3.9 were further found to be adequate to predict the mean crushing loads of square empty and foam filled tubes (Kavi, et al. 2006, Toksoy, et al. 2004).

The axial quasi-static crushing of longitudinally welded square tubes made of various kinds of steels , ASTM A36, ASTM 513 AISI 316 and AISI 304, were investigated (DiPaolo and Tom 2006). During quasi-static compression testing, end caps were used to constrain the side walls of the top and bottom of the tubes in order to form stable progressive crash behavior. Grooves (trigger mechanism) were machined on the each surface of the square tubes. In all steel tubes, the folding mode was found the same, symmetric axial crashing mode (Figure 3.12). The fold lengths were shown to be higher in higher strength steel tubes.

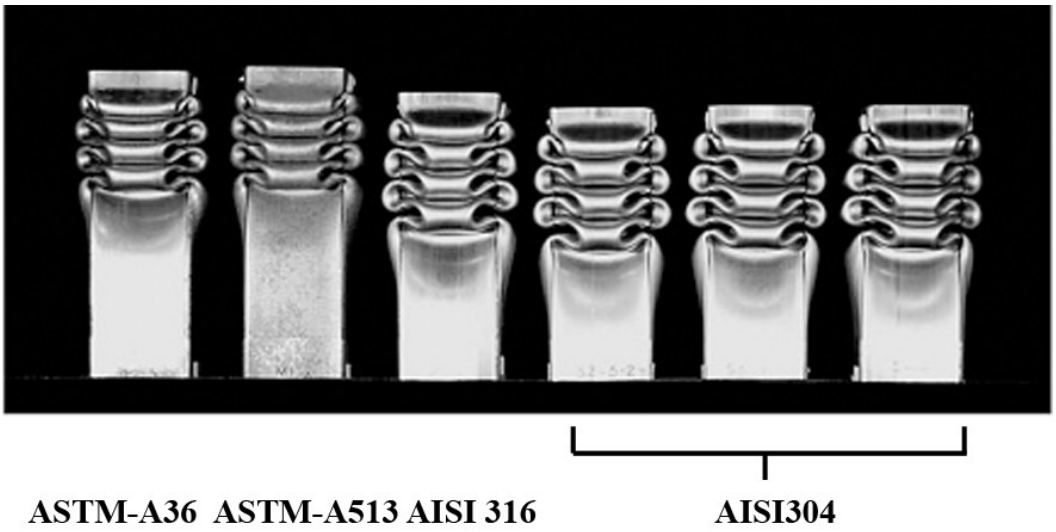

Figure 3.12. Folding in square tubes of ASTM A36, A513, AISI 316 and 304 (Source: DiPaolo and Tom 2006)

Impact energy absorption of extruded 6061 Al tubes with different cross-sections were investigated by Dong-Kuk Kim and Sunghak Lee (Kim and Lee 1999). The tubes with rectangular and circular cross-section were tested with and without welded top and bottom plate. SEA values of the impacted tubes of both geometries increased with increasing thickness to width and thickness to diameter ratios. The number of symmetric folds tended to increased with increasing thickness to width and thickness to diameter ratios, in both tube geometries. It was noted that circular specimens showed higher specific energy absorption than rectangular ones due to higher tendency of circular tubes for symmetric fold formation. In addition, the edge tip radius was found to be effective on the deformation load values of rectangular tubes. When the edge tip radius was very small, compressive load was concentrated on the edges and caused an early crack opening. The cracks propagated quickly and resulted in considerably lower values of energy absorption.

Experimental and numerical energy absorption of an axially crushed square 6063T5 tube were determined with a buckling initiator (Figure 3.13(a)) by Zhang et al.(Zhang, et al. 2009). During the impact test, a striker impinged the pre-hit column and forced the steel strip to pull the opposite tube walls inwards. The folding initiated when the striker contacted with the top edges of tube itself. Adopted folding initiator resulted in 30% reduction in the initial buckling load level without effecting the subsequent progressive crushing mode (Figure 3.12(b)).

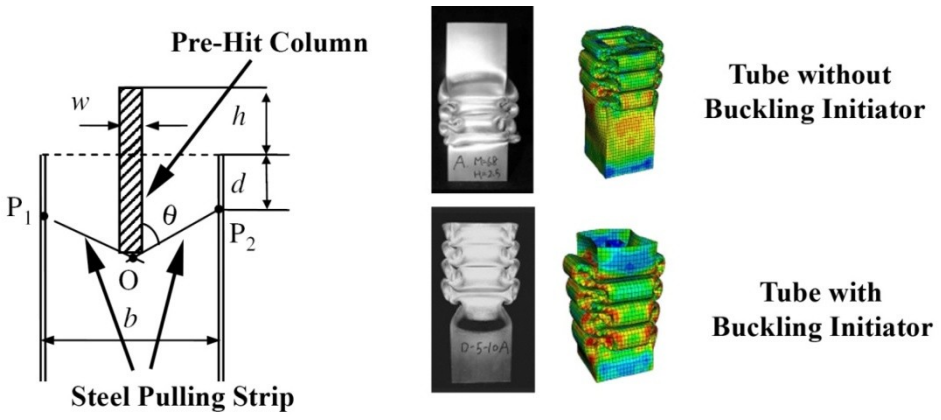

(a) (b)

Figure 3.13. a) Schematic of the buckling initiator and b) experimental and simulation deformation of the tube with and without buckling initiator (Source: Zhang, et al. 2009).

Bambach et al.(Bambach, et al. 2009) studied the dynamic crushing of thin walled composite steel-carbon fiber reinforced plastics (CFRP) square tubes. Carbon fiber layers were braided in two different combinations on the same sample: one transverse and one longitudinal layer (1T1L), and two transverse and two longitudinal layers (2T2L). Two deformation modes, ductile stable progressive deformation without and with partial delamination, were observed (Figure 3.14). It was reported that CFRP braiding of steel square tubes increased the dynamic mean crushing load by 82%. SEA values of composite steel-CFRP square tubes were found 52% higher than those of steel square tubes and 94% higher than those of CFRP square tubes.

The effect of damage parameters on the axial crushing behavior of 6060T5 thin-walled aluminum square extruded tubes was investigated (Galib, et al. 2006). Tensile tests on five different geometries of 6060T5 Al tube material were performed to identify the damage parameters of Lemaitre's damage model. Simulation results were compared with those of experimental impact tests. It was noted that experiments showed negative loads on the deformation history (Figure 3.15(a) arrows). This was attributed to the restriction of the vertical differential displacements of the constraints in the simulation. Numerical absorbed energy values agreed with those of experiments (Figure 3.15(b)). The used damage model also well represented the failed sections of the tested square 6060T5 square tubes (Figure 3.15(c)).

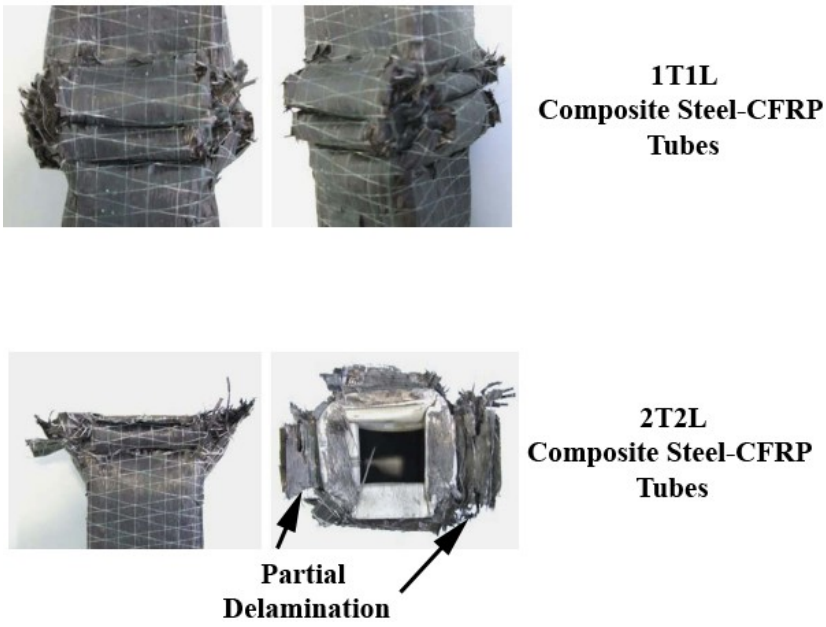

Figure 3.14. Deformed shape of 1T1L and 2l2T steel-CFRP square tubes.
(Source: Bambach, et al. 2009)

Jensen and colleagues investigated experimentally and numerically the deformation mode transition from progressive to global buckling of 6060T6 Al square tubes, (Jensen, et al. 2005, Jensen, et al. 2004). Global buckling was found to absorb less energy than progressive buckling. The transition from progressive folding to global buckling occurred after a certain time (Figure 3.16). It was also noted that the transition was delayed at increasing impact velocities due to the inertia forces.

The effect of trigger on the energy absorption capacity of square Al tubes with full and half dent shapes on the surface were also investigated (Lee, et al. 1999). Half and full multiple dent tubes showed lower energy absorption than the tubes without dent.

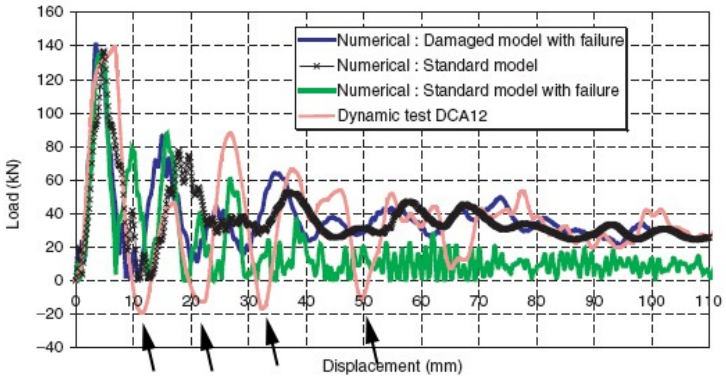

(a)

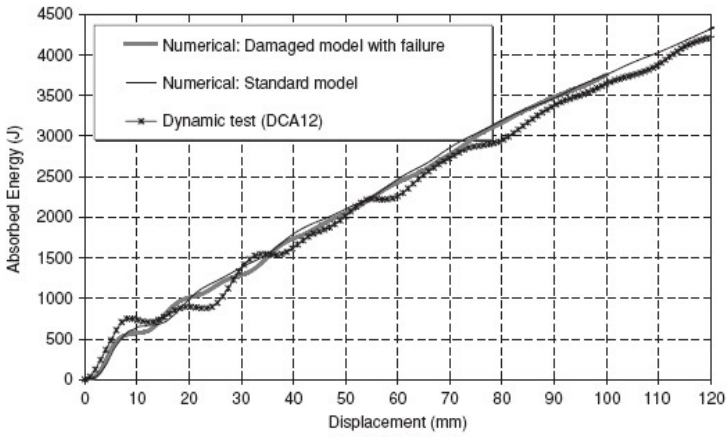

(b)

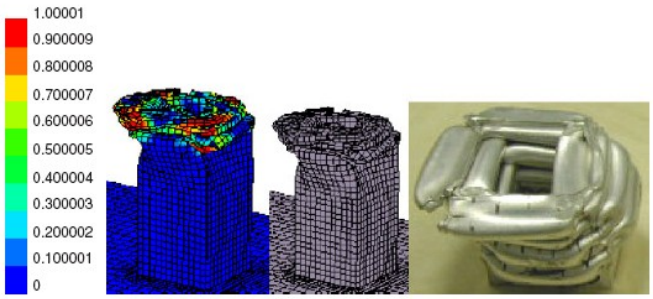

(c)

Figure 3.15. a) Load-displacement curve, b) absorbed energy-displacement curves and c) simulation and experimental deformed shapes of 6060T5 Al square tubes (Source: Galip, et al. 2006).

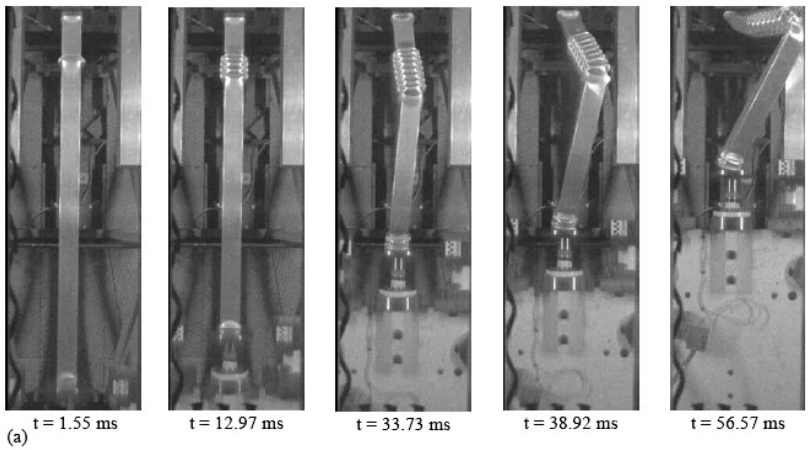

(a)

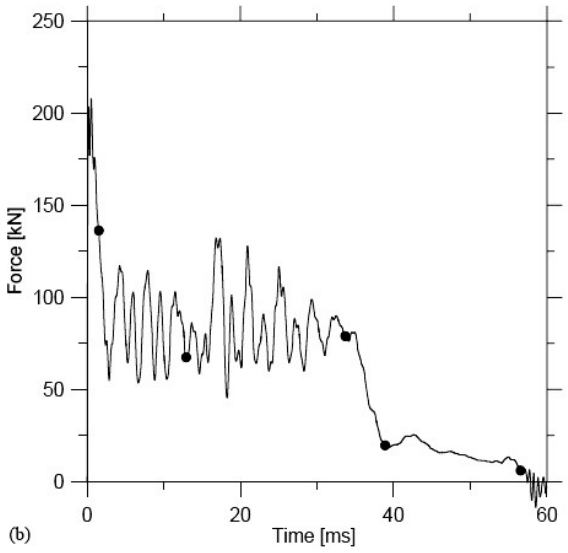

(b)

Figure 3. 16 (a) Transition from progressive to global buckling in 6060T6 Al square tubes and b) typical force vs. time history (Source: Jensen, et al. 2004)

3.4. Crushing Behavior of Foam Filled Tubes

Axial compression behavior of aluminum foam filled square and circular steel tubes were investigated by Seitzberger et al. (Seitzberger, et al. 1997). It was shown that the interaction between foam filler and tube wall increased the absorbed energy and changed the deformation mode tubes in foam filled tubes. The effect of aluminum foam filling on the crushing behavior of AA6060 T4 Al square tubes under dynamic and

static load were determined by Langseth et. al.(Langseth, et al. 1998). It was reported that increasing foam density and tube wall thickness increased SEA values. The use of adhesive between filler and tube wall was found to be effective in increasing energy absorption of filled tube.

Analytical and numerical analysis of the energy absorption in Al honeycomb and foam filled Al square tubes were performed by Santosa and Wierzbicki(Santosa and Wierzbicki 1998a). Al honeycomb filling was shown more weight efficient than aluminum foam filling in the direction of stronger axis of honeycomb. However, it was noted that aluminum foam filling could be better crash element for which it resisted the combination of compressive and bending forces. Results also showed that Al honeycomb and foam filling were more efficient than wall thickening after a critical mass as depicted in Figure 3.17. The same researchers were proposed the following equation for the mean crushing of honeycomb and foam filled square tubes,

$$P_{m,Honeycombfilled} = P_{m,empty} + b^2\sigma_h \tag{3.10}$$

and

$$P_{m,Foamfilled} = P_{m,empty} + 2b^2\sigma_f \tag{3.11}$$

where σ_h and σ_f are the honeycomb and foam crushing strength respectively.

Singace and El-Sobky investigated the deformation modes of empty and sawdust wood chips filled cylindrical polyvinylchloride (PVC) tubes under compression loads,(Singace 2000, Singace and Elsobky 2000). Deformation mode shift from multi-lobe to concertina was observed when PVC tube was densely filled with sawdust wood chips. After a critical of wood chip density, the filler was found to act as a solid wood and resulted in an inefficient mode of collapse.

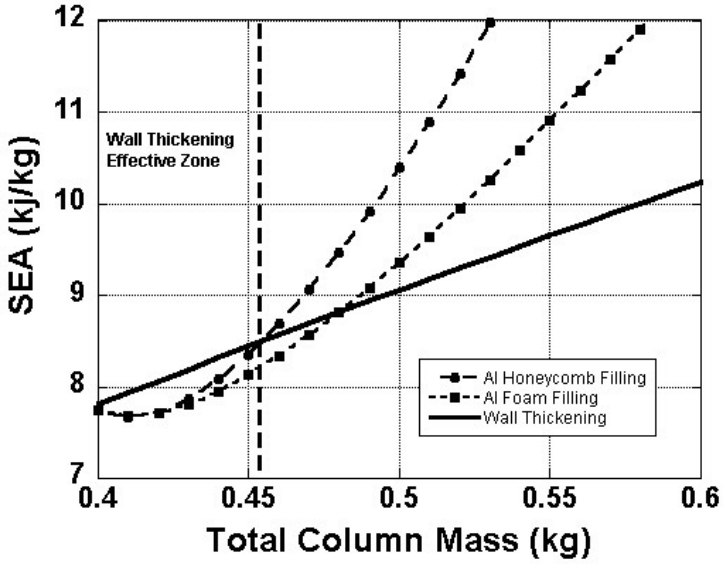

Figure 3.17. SEA vs. column mass for filled and wall thickened Al tubes.
(Source: Singace and Elsobky 2000)

Static and dynamic crash force efficiency (A_E), total efficiency (T_E) and stroke efficiency (S_E) of empty and foam filled tubes aluminum square and circular cross-sections were investigated by Hanssen and co-workers (Hanssen, et al. 2001a, Hanssen, et al. 1999, Hanssen, et al. 2000a, Hanssen, et al. 2000b, Hanssen, et al. 2001b). A_E is the ratio between mean load (P_m) and maximum force (P_{max}) and given as

$$A_E = \frac{P_m(d)}{P_{max}(d)} = \frac{E(d)}{P_{max}(d) * d} \tag{3.12}$$

T_E is the total absorbed energy divided by the product of P_{max} (d) and total length of deformation element (L),

$$T_E = \frac{E(d)}{P_{max}(d) * L} \tag{3.13}$$

S_E is the ratio between the point at which the total efficiency has its maximum value (d_{max}) and total length of the crash element,

$$S_E = \frac{d_{max}}{L} \tag{3.14}$$

For a crush element, the variations of above parameters with displacement are shown in Figure 3.18. Because of the foam lateral movement constraint effect on tube side walls, the stroke efficiency of foam filled structures was found to be lower than that of empty circular and square tubes and decreased with increasing foam relative density (Hanssen, et al. 2000a, Hanssen, et al. 2000b). Unlike stroke efficiency, the crash force efficiency and total efficiency increased with increasing with aluminum foam filler relative density. This behavior was explained by the interaction effect between foam and tube wall. Foam filled tube absorbed more energy than the sum of the energy absorption of foam alone and tube alone due to the interaction effect. The mean crushing load of filled tubes is given as

$$P_{m,Foamfilled} = P_{m,empty} + b^2\sigma_f + C_{avg}\sqrt{\sigma_f \sigma_0}\, bt \tag{3.17}$$

where, C_{avg} is the dimensionless interaction coefficient. At 50% deformation of foam filled structure, C_{avg} was calculated 2.68 for circular (Hanssen, et al. 2000a) and 5.5 for square tubes (Hanssen, et al. 2000b). Similarly, Jones (Jones 1989) found the value of C_{avg} 0.9 for circular and 1.4 for square tubes. Although the interaction of square cross-section filled tubes was found to be higher than that of circular filled tubes, higher energy absorption were found in circular foam filled extrusions at similar weights (Hanssen, et al. 2001a).

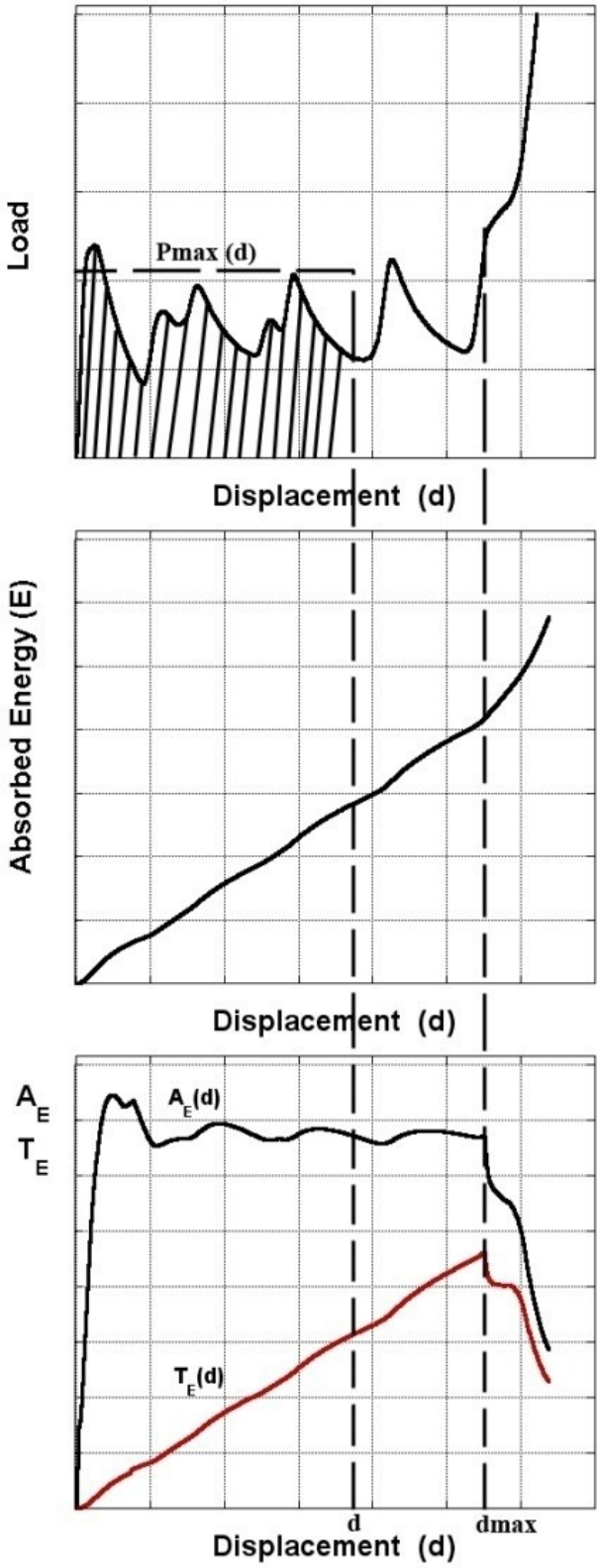

Figure 3.18. The crush terminology.
(Source: Hanssen, et al. 1999)

The crushing behavior of a bumper system with a foam filled square crash box was experimentally and numerically investigated (Hanssen, et al. 2000c). During the experimental test program, crash boxes without fixing part were also tested under the similar conditions. In addition, the bumper system was tested both symmetric loading and 40% overlap loading. The initial maximum load of single crash box was shown to be higher than that of the complete bumper system as shown in Figure 3.19. The decline in the initial maximum load with using the fixing part was attributed partly to gradual deformation of the box with fixing part and partly to the softened heat affected zones (HAZ) in the top and bottom of the crash box.

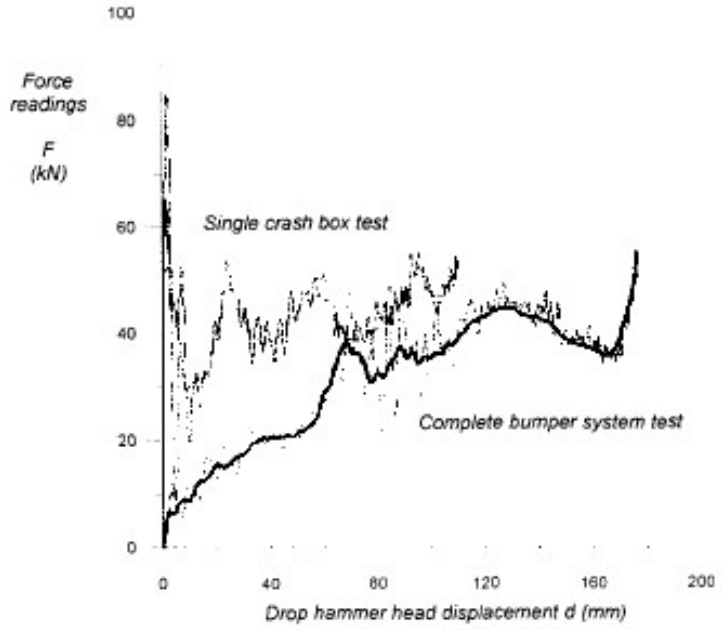

Figure 3.19. Deformation load -drop hammer displacement curves of a single and complete bumper system (Source: Hannsen, et al. 2000c)

Santosa et al. (Santosa, et al. 2000) investigated the crash behavior of Hydro aluminum foam filled 6060T4 and 6082T4 Al square tubes experimentally and numerically. The effect of adhesive, used to bond the foam filler to tube inner surface, on the crash behavior was also determined in the same study. The simulations were implemented using PAM CRASH 97 non linear finite element code. The mass density of the column structure was scaled down by a factor of 1000 at a deformation velocity of 2 m s^{-1}, in order to simulate the quasi-static crushing behavior. Empty tubes deformed in asymmetric (quasi-inextensional) mode forming five folds, while foam

filled unbounded tubes formed 8 folds. However, the use of adhesive transformed the deformation mode into a mixed quasi-inextensional and extensional folding mode (Figures 3.20(a) and (b)). The mean force values of bounded filled tubes were higher than those of unbounded filled tubes. The following equations were sequentially proposed for the mean load of foam-filled square tubes without and with adhesive,

$$P_{m,Foamfilled} = P_{m,empty} + 1.8b^2\sigma_f \tag{3.18}$$

and

$$P_{m,Foamfilled} = P_{m,empty} + 2.8b^2\sigma_f \tag{3.19}$$

Both equations showed well estimates of the mean load of filled tubes as compared with experimental and numerical mean load values.

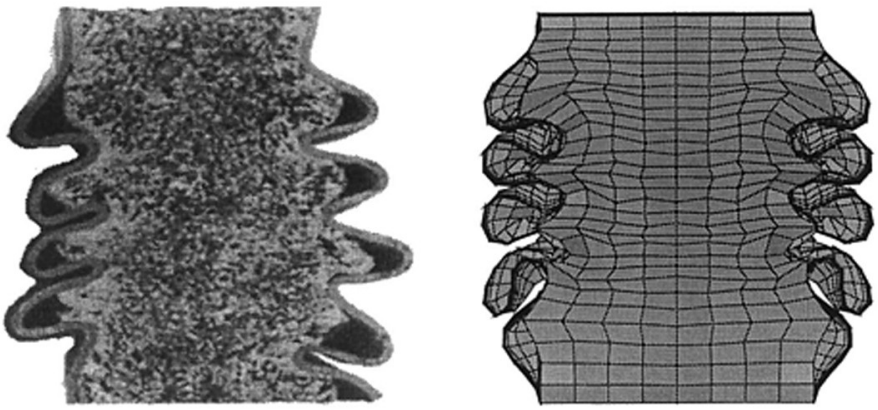

(a) (b)

Figure 3.20. Deformation pattern of foam-filled square tube, a) experiment and b) simulation (Source: Santosa, et al. 2000).

The quasi-static compression behavior of empty and polyurethane foam-filled 6060T5 Al circular tubes was investigated by Guillow et al. (Guillow, et al. 2001). Tubes having different diameter to thickness ratio (D/t) were tested to determine the deformation mode of 6060T5 Al circular tubes as function of D/t. Polyurethane foam filling resulted in higher mean crash loads than empty tubes. The deformation mode reverted from non-symmetric mode in empty tubes to axisymmetric mode in high density polyurethane foam-filled tubes.

Axial crushing behavior of the intermittent tack-welded cylindrical carbon steel tubes were investigated by Ku et al.(Ku, et al. 2001). Tube without welding, with full butt welding and with tack-welding were compressed in order to explore the effect of tube welding on crushing behavior. In the same investigation, polyurethane foam filled welded cylindrical tubes were also tested. It was shown that folding mode of empty tubes, non-symmetric (diamond) and axisymmetric mixed mode, was not affected by welding, while axisymmetric mode of deformation was found in polyurethane foam-filled tubes, mainly resulting from the circumferential stretching of filler. Continuous weld seam opening occurred in foam filled intermittent tack-welded tubes. This resulted in improvements in energy absorption capacity, by increasing load efficiency and decreasing the load amplitude, more than foam-filled fully welded tubes.

Mantena et. al. (Mantena and Mann 2003) investigated the crushing behavior of polymer foam filled cylindrical steel tubes through dynamic impact experiments and simulations. It was reported that circular tubes filled with the highest density foam was the most efficient in terms of mean load and absorbed energy. Meguid et. al. (Meguid, et al. 2004b) simulated the axial compression behavior of foam-filled columns using layered approach in which the foam filler was modeled as a series of horizontal layers. Each layer included single layers of solid elements and the layers were collocated with the nodes of the adjacent layer. Agreements between experimental and model deformation modes and mean load values were found (Figure 3.21). The discrepancy was 5.6% between experimental and simulation results at a displacement of 200 mm.

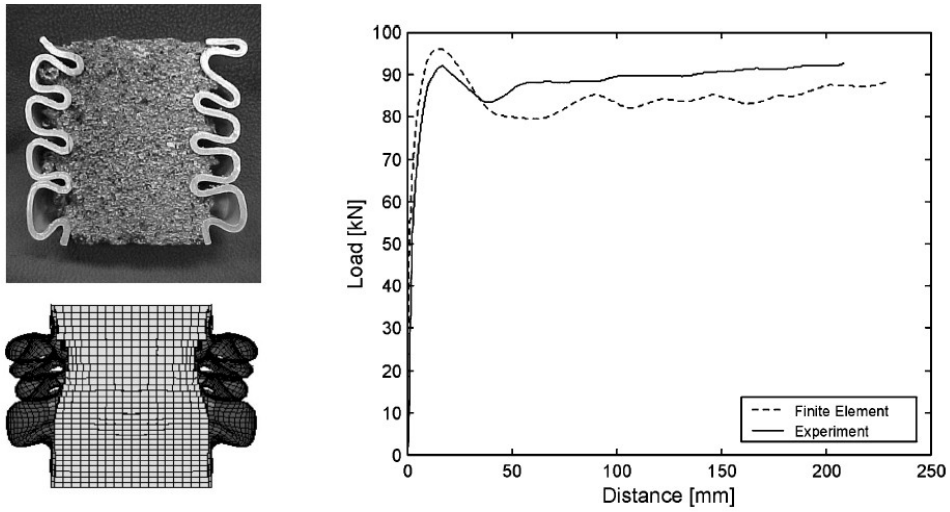

Figure 3.21. Comparison between simulation and experimental deformation modes and mean loads of polymer foam filled tubes (Source: Meguid, et al. 2004b).

The axial compression of empty and Hydro Al foam-filled 6060T4 Al circular tubes was studied by Borvik et. al. (Borvik, et al. 2003) at varying loading angles. Experimental and numerical results showed that the absorbed energy decreased with increasing loading angle. This was mainly caused by the change of the deformation mode. A progressive folding mode was observed at zero angle (axial) loading, while global bending mode became dominant at increasing loading angles. The deformation switch at increasing loading angles was also validated by the numerical simulations. Foam filled tubes further showed slightly higher SEA values than empty tubes at zero loading angle, while SEA values of empty tube increased over those of filled tube, depicted in Figure 3.22.

It was reported that the quasi-static axial crush behavior of ultralight PVC hollows foam filled aluminum circular tubes with varying wall thickness. (Meguid, et al. 2004a) The foam filler had hollows with varying diameter. Both simulations and experiments indicated that there was an optimum tube shell thickness and PVC foam filler hollow size which maximized the absorbed energy.

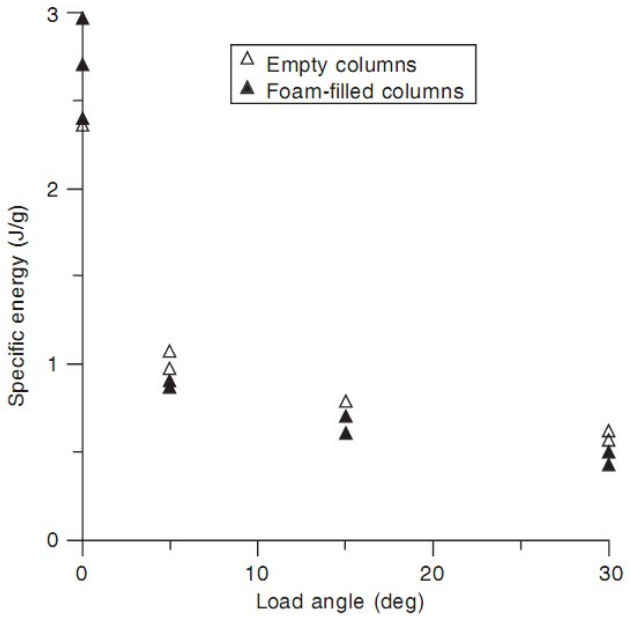

Figure 3.22. The variation of specific absorbed energy with loading angle in an empty and foam filled Al tube (Source: Borvik, et al. 2003).

The quasi-static crushing of single, bitubular and constraint square and hexagonal-packed empty and foam filled aluminum tubes were investigated experimentally and numerically (Aktay, et al. 2008, Güden and Kavi 2006). Coupled finite element methodology and smooth particle methodology were successfully implemented to simulate the foam filler (Figure 3.23). Polystyrene and aluminum foams were used as filler in bitubular and constraint packed multi-tubular structures, respectively. Although the deformation mode changed from diamond in single empty tubes to more energetic concertina mode of deformation in filled circular single tube, in multi packed foam filled tubes, the deformation mode of single tube was found not progressive due to extensive friction of the outer constraint. The SEA values of foam filled multi-tube packing were found lower than those of empty tube multi packing.

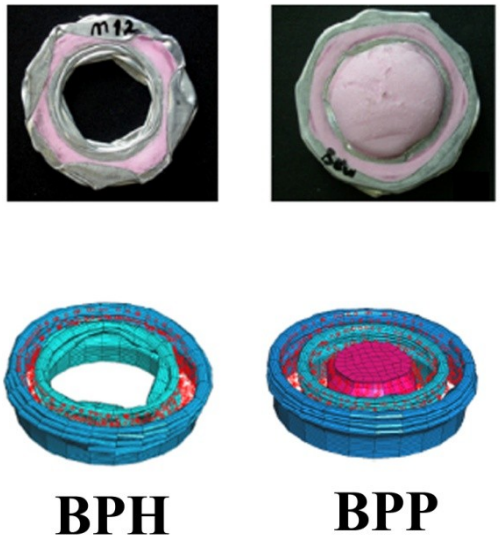

Figure 3.23. Experiment and coupled FEM/SPH simulation of the deformed shapes of bitubular polystyrene foam filling arrangements, filling only between two tubes (BPH) and filling the inner hole with polystyrene foam (BPE).(Source: Aktay, et al. 2008).

The crushing behavior of Alulight (AlMg0.6Si0.3) aluminum foam filled RSt37 and ZSt340 steel monotubal, bitubal, hexagonal and octagonal profiles were investigated (Seitzberger, et al. 2000, Seitzberger and Willminger 2001). The stroke efficiency was found to decrease with increasing foam density in all investigated profiles. The deformation mode was extensional mode in monotubal arrangement and outward and inward mode in bitubal arrangement (Figure 3.24). However the mean load efficiency and SEA increased over the empty tube with foam filling. The increase in SEA values was 30% and 60% in foam filled ZSt340 and RSt37 tubes, respectively. Although, filled hexagonal and octagonal arrangements experienced higher SEA values than empty arrangement, foam filling was found to be not effective in increasing SEA values of monotubal arrangement.

The effect of wall thickness, foam density (Alulight-AlMg1Si) and semi-apical angle on the crushing of conical steel tubes was studied numerically by Ahmad and Thambiratnam(Ahmad and Thambiratnam 2009). Al foam filling resulted in lower specific absorbed energy values than empty tubes within the investigated semi apical angle and wall thickness range (Figure 3.25). However, the foam filling found to stabilize the deformation of conical tubes and increased the number of the folds.

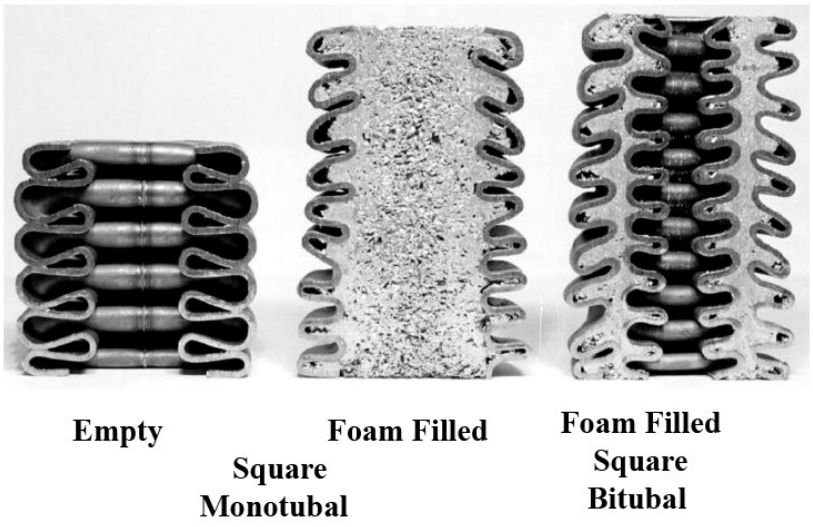

Figure 3.24. Deformation modes of empty and foam filled monotubal and bitubal square sections (Source: Seitzberger, et al. 2000).

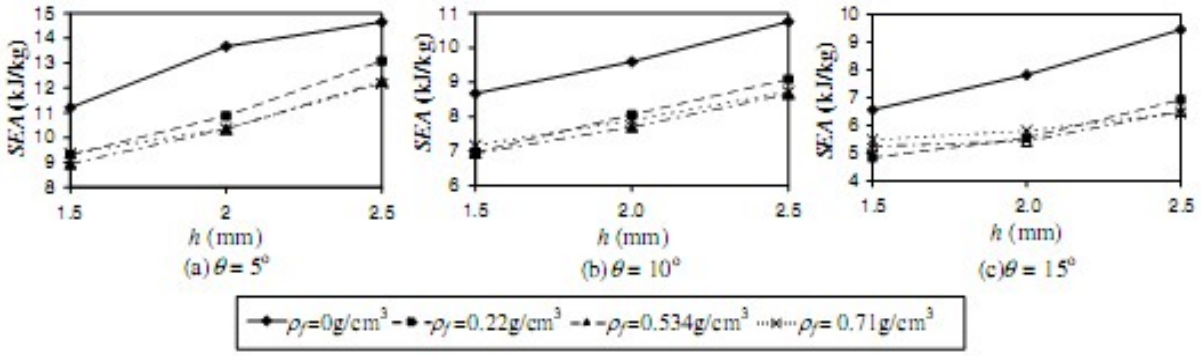

Figure 3.25. The variation of SEA values of steel conical tubes with wall thickness at three different semi apical angle (θ) and with three different foam filler density(Source: Ahmad and Thambiratnam 2009).

A comparative study of the energy absorption characteristics of foam-filled and multi-cell square columns was performed by Zhang and Cheng (Zhang and Cheng 2007). Multi-cell square columns absorbed 50-100% higher energy than foam-filled sections at same weight. This was attributed to increased numbers of folds in multi-cell square columns (Figure 3.26), as compared with foam filled columns. This also proved a higher level of interaction between internal web and square tube than that between foam filler and square tube. Al foam filled multi-cell square 6061T4 Al tubes were

investigated by Chen and Wiezbicki (Chen and Wierzbicki 2001) . Axial crushing behavior of empty and foam filled single, double and triple cell combination of square aluminum tubes were modeled by explicit finite element code PAM-CRASH. The foam filled sections were shown to exhibit higher SEA values than non filled sections (Figure 3.27). The increase in SEA values was 30% in single cell and 40% in double and triple cells. The SEA values of empty double and triple cells were 15% higher than those of single cell.

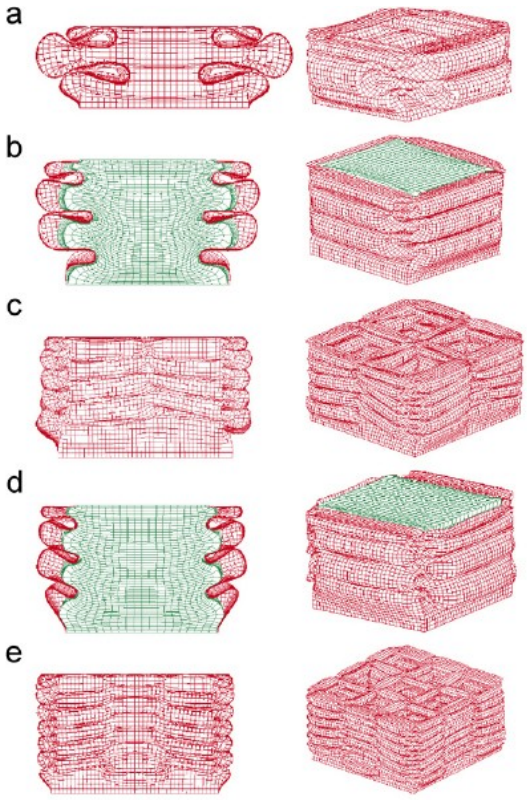

Figure 3.26. The simulated collapse modes of (a) hollow ,(b) foam-filled (0.103 g cm^{-3}), (c) 2x2 multi-cell, (d) foam-filled hollow (0.206 g cm^{-3}) (left: cut-open view right: general view) and (e) 3x3 multi-cell column (left: front view right: general view)(Source: Zhang and Chen 2007).

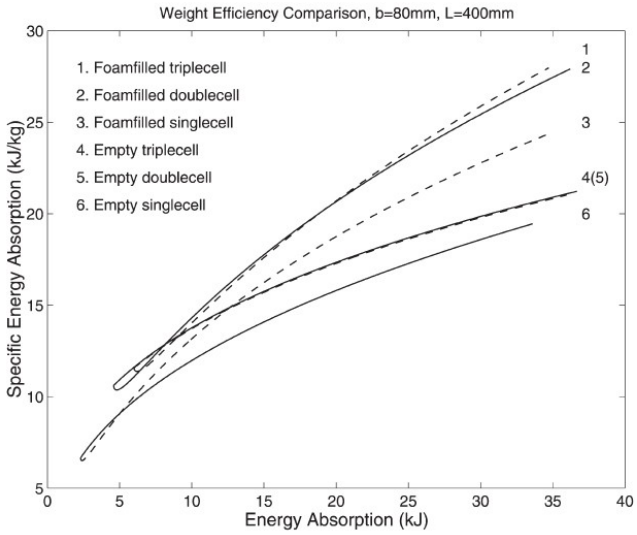

Figure 3.27. SEA values of empty and foam filled single, double and triplecell square Al sections (Source: Chen and Wierzbicki 2001)

Jones defined an energy-absorbing effectiveness factor which was based on the material properties, the cross-section of the structure, stiffeners and foam filling,(Jones In Press). Using the experimental data from literature, the energy-absorbing effectiveness factor of a 6060T4 Al tube was shown to increase with foam filler density (Figure 3.28)

The axial crushing behavior empty and foam filled square hat sections (Figure 3.29(a)) was investigated under static and dynamic loads (Altenhof, et al. 2002, Chen and Nardhi 2000, Wang, et al. 2005, Wood, et al. 2006). The SEA values of single hat filled section were higher than those of empty single hat section. While, in double hat sections, a critical filler length after which filled section became more efficient than empty section was found (Figure 3.29(b)).

The crushing behavior of empty and foam filled single, double hat HS5754 Al sections with and without center plate were determined by Chen et al. (Chen and Nardhi 2000). Several different foam filling methods including precise fitting, precompression fitting and adhesive bonding were investigated to find out the best filling method that stabilized the deformation and maximized SEA. Adhesive bonding was shown to cause less premature joint failure than precise fitting and precompression fitting. Finally, foam filled single and double hat steel square columns were shown to exhibit 20% higher SEA values than empty single and double hat columns.

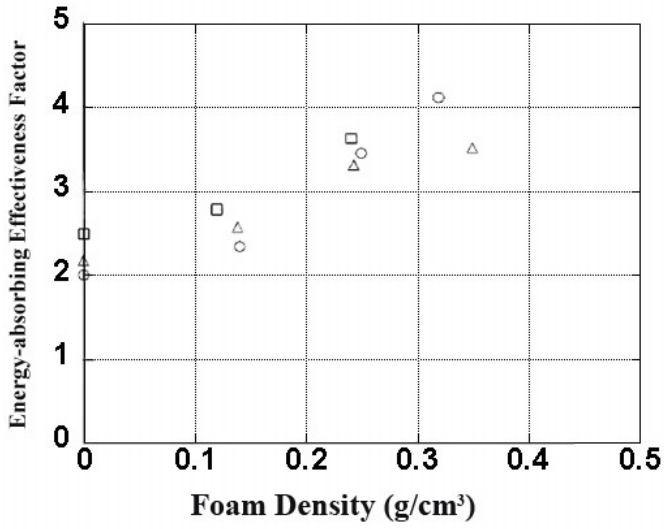

Figure 3.28. The variation of the energy-absorbing effectiveness factor of 6060T4 Al circular tube with Al foam filler density: o: t=1.40-1.42 mm, Δ : t=1.97-2.01 mm, □: t=2.35-2.46 mm (Source: Jones In Press)

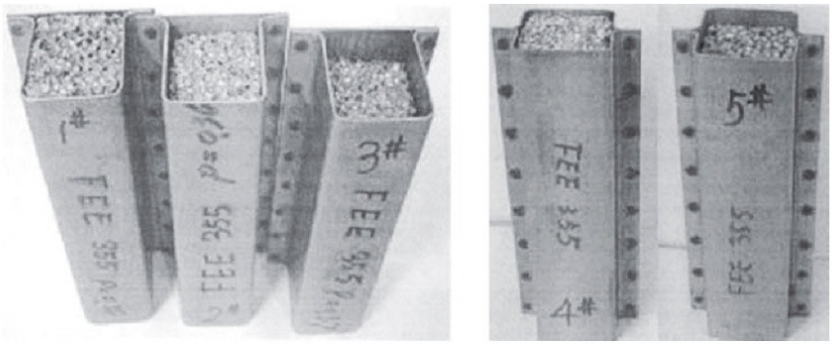

(a)

Figure 3.29. a) Aluminum foam filled single and double hat sections with various filler lengths and b) the variation of SEA values with foam filler length,(Source: Wang, et al. 2005)

(cont. on next page)

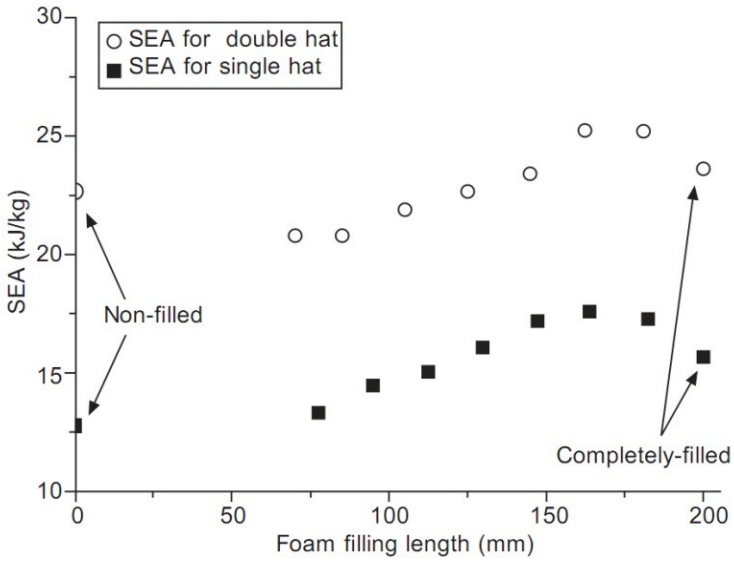

(b)

Figure 3.29. (cont.)

3.5. Motivations

Foam filling of tubular structures becomes efficient after a critical foam density and/or plateau stress (Figure 3.17). At low foam plateau stresses the specific energy absorption of filled tube is below that of empty tube because of the ineffective foam strength over total weight ratio. Filling with higher foam densities at present is however limited by an upper density, 0.4 g cm^{-3}, of the commercially available Al foams. In addition, the use of high density Al foams will increase the total cost of the crash boxes. On the other hand, the use of multi cell tubular structures was shown to improve SEA values. Similar to the use of the high strength foam filing, the use of the multiple cell tubular structures will increase the unit cost of the crash boxes. In partially foam filling in which the foam filler length is smaller than that of the column, a certain improvement in SEA was achieved (Altenhof, et al. 2002, Chen and Nardhi 2000, Wang, et al. 2005, Wood, et al. 2006). The efficiencies of foam filling depend on, besides the density of the foam filler, the geometry and the base material of the structure and the length of the foam filler. A complete analysis of the effects of tube wall thickness and base material

and foam filler density on the efficiency of Al foam filling of tubular structures is still absent in the literature.

The aims of this study is to investigate experimentally and numerically the energy absorption capabilities of the partially aluminum foam filling of the commercial available inexpensive low strength 1050H14 aluminum alloy crash boxes. The crash box selected is currently used in the frontal section of a medium class automobile. The foam filler was commercially available relatively inexpensive Alulight AlSi10 foam. The parameters investigated included foam filler density, the box geometry and wall thickness and triggering effect. The crash box crushing behavior at quasi-static and dynamic strain rates was simulated using LS-DYNA software. An optimization schedule, the response surface optimization method, was applied to the partially foam filled crash box in order to maximize the specific energy absorption in terms of foam filler density and box wall thickness. In order to determine the effect of box base material type on the energy absorption capabilities, the simulations were implemented on the filled crash boxes of steel and high strength Al alloy. Finally a cost analysis in comparison with empty crash box was made on the filled crash box with the optimized parameters.

CHAPTER 4

EXPERIMENTAL DETAILS

4.1. Compression Testing of Aluminum Foam

As received Alulight Al (AlSi10) closed cell foam panels were in 625x625x30 mm size (Figure 4.1). The panels had broadly two different densities, 426 kg m^{-3} and 512 kg m^{-3}, corresponding to the relative densities of 0.11 and 0.15, respectively. The panels accommodated relatively dense Al layer at the edges and the corners. The dense Al layer was mainly resulted from the nature of the foam production process. Before the preparation of tests samples, the dense Al regions near the edges and corners of the panels (30 mm from the edges) were removed using a decoupling machine (Figure 4.2(a)). Then, the panels were sliced into 70 mm wide and 565 mm long strips (Figure 4.2(b)). Later, cubic compression test samples with the dimension of 30x30x30mm (Figure 4.3(a)) were cut from these strips using the decoupling machine. Before compression testing, the weight of each foam test sample was measured. The uniaxial compression tests were performed at a crosshead speed of 5 mm min^{-1} through the thickness direction of the foam samples as depicted in Figure 4.3(b). The corresponding compression strain rate (the cross-head speed divided by the initial thickness of test sample) was 2.77×10^{-3} s^{-1}.

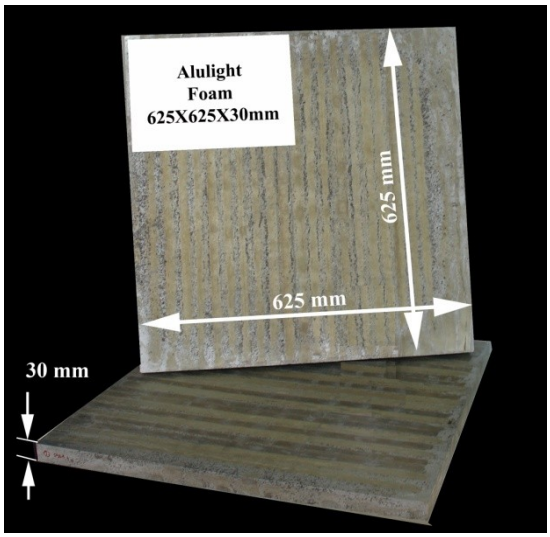

Figure 4.1. As-received Alulight Al foam panels.

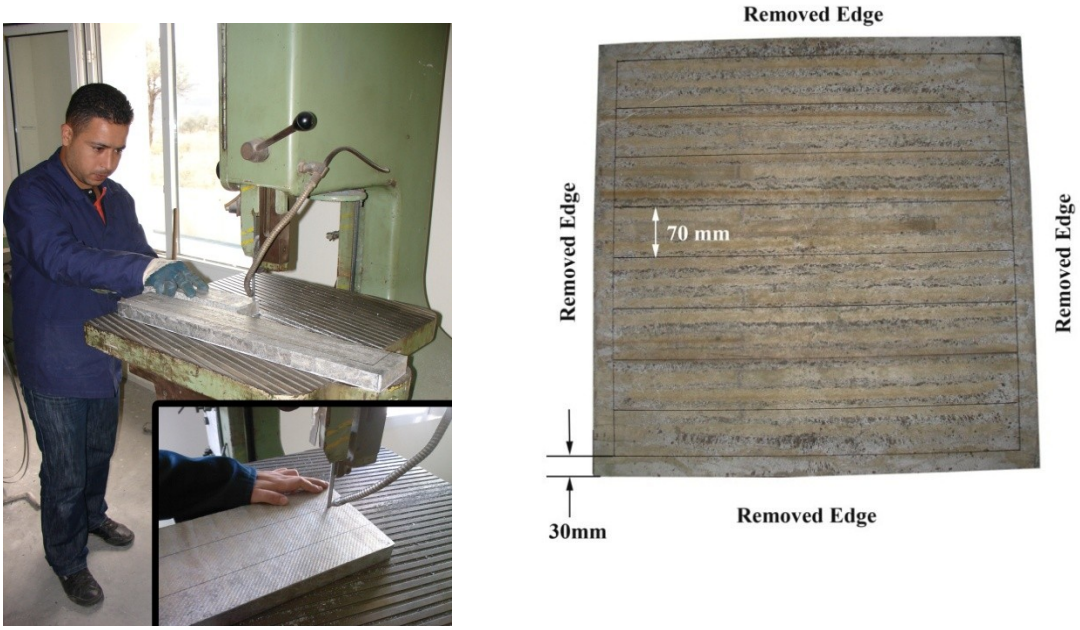

(a) (b)

Figure 4.2. a) Aluminum foam panel cutting and b) the removed dense sections.

(a)

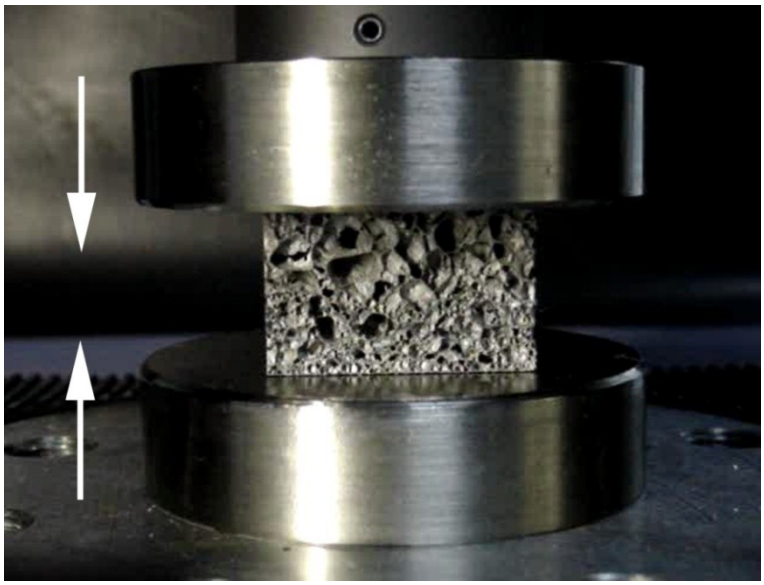

(b)

Figure 4.3.Pictures of a) foam compression test samples and b) foam sample between compression test platens.

4.2. Empty and Aluminum Foam Filled 1050Aluminum Crash Boxes

An automobile crash box consists of two major parts: a montage part which provides connection between bumper and chassis and a crash zone in which the crash energy is absorbed by plastic deformation (Figure 4.4). Depending on the specific crash

box design, various production routes including welding, bending and etc. involve in the processing stages. The manufacturing stages of the selected crash box design in this thesis are shown in Figure 4.4 and are composed of laser cutting of Al sheet metals, hydraulic press brake bending of the cut Al sheets and finally TIG welding of the edges of bent Al sheet.

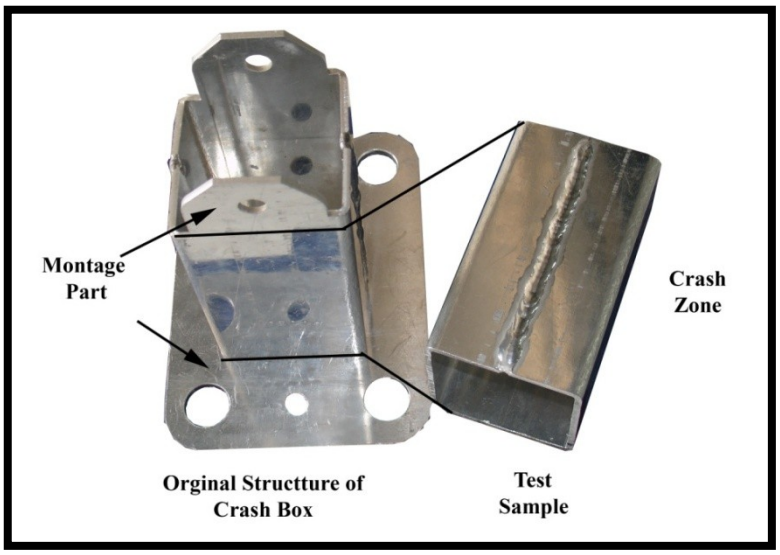

Figure 4.4. Crash box structure and crash zone.

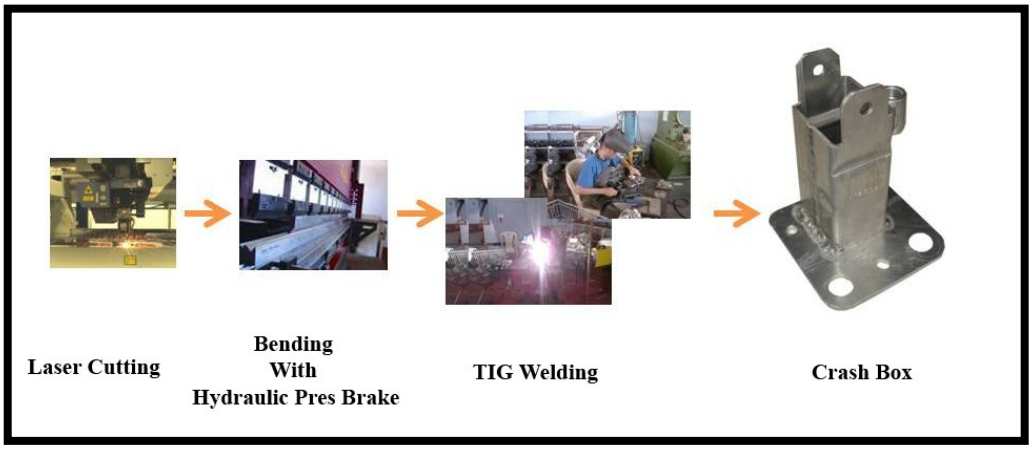

Figure 4.5. The processing stages of the tested crash boxes.

Two different sets of crash boxes with the outer dimensions of 70.6x73.2x125.2 and 60x70.4x122.6 mm were prepared and tested. The technical drawings of the crash

boxes are shown in Figure 4.6. The larger boxes with the dimensions of 70.6x73.2x125.2 mm are coded as G1 and smaller 60x70.4x122.6 mm size boxes as G2 throughout this thesis. In both geometries of the crash boxes, trigger mechanisms were made on the outer surfaces. The trigger mechanisms function to reduce the initial peak load level and induce a more uniform deformation load. In the filled box, the trigger mechanisms also allow to position the aluminum foam filler in the mid-section of the box, between the upper and lower triggers on the outer surface. Special apparatus were constructed to form the trigger mechanisms on the surface of the crash box samples. The box was first fixed on the table of the hydraulic pres and then a steel shaping roller was slid over the parallel surface of the crash box as shown in Figure 4.7. This formed a relatively thin deformed section where the folding first triggers upon loading. The trigger mechanisms were positioned at a distance of 35 mm from the top and the bottom of the crash box. After initial experimentation of the various configurations of triggers, it was decided to place 4 trigger mechanisms on the box, two of them on one surface and the other two on the opposite surface. The trigger configuration selected was found to result in a folding mechanism progressing through the filled sections, not through the compression test plates. Al foam filler section was 60 mm thick, which was approximately half of the length of the crash box. The weight of each filler was measured before filling the boxes.

Two groups of experimental crash boxes were prepared for the compression testing. In the first group boxes, the tests were performed without montage parts. For this, the montage part of the crash boxes was removed simply by cutting the montage parts (Figure 4.8(a)). In the second group, the boxes were tested with the montage plates. In this group of samples, corrugated sections, two rectangular holes of 12x12 mm in size, on each surface of the boxes were created at the upper section of the box as seen in Figure 4.8(a). Few crash boxes were tested with montage parts without corrugated sections in order to determine the effect of montage parts on the crashing behavior. The thicknesses of the boxes tested were 2, 2.5 and 3 mm (Figure 4.8 (c)).

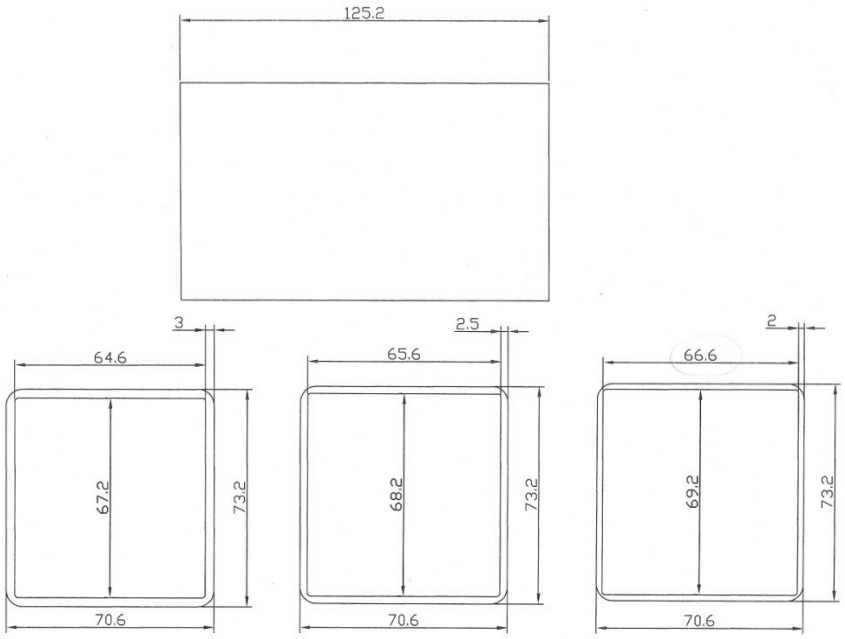

Crash BoxG1Type

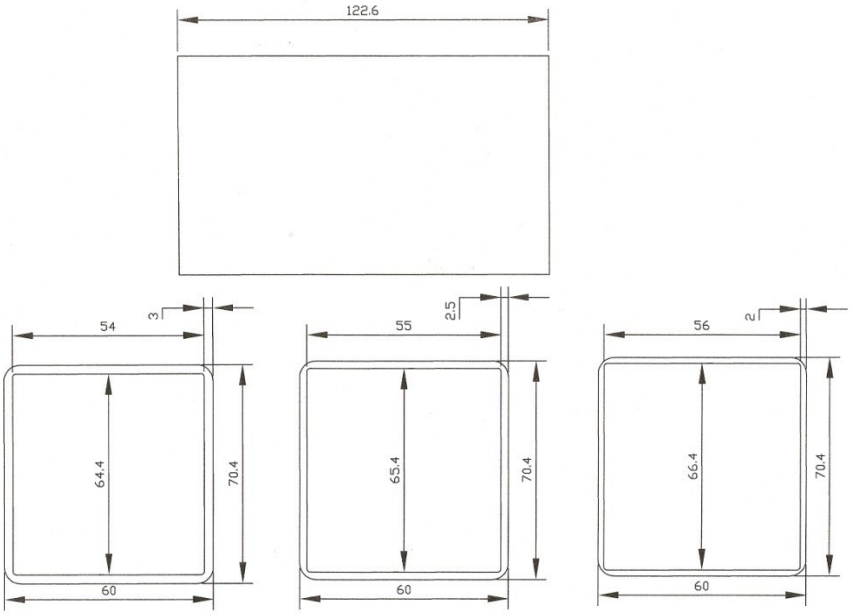

Crash Box G2 Type

Figure 4.6. Technical drawings of the tested crash boxes.

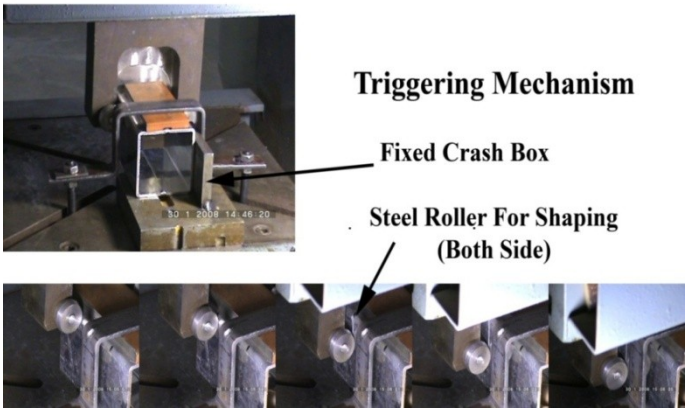

Figure 4.7. The method of trigger mechanism formation on the outer surfaces of the boxes.

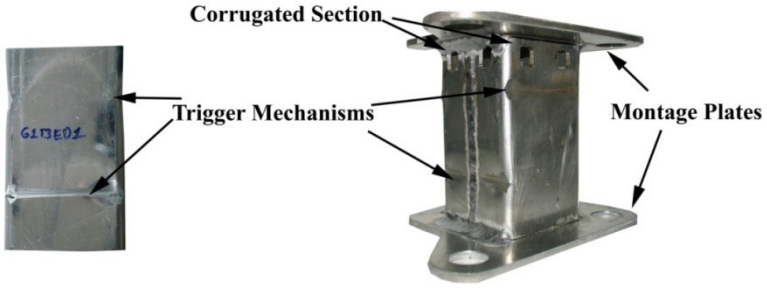

(a)

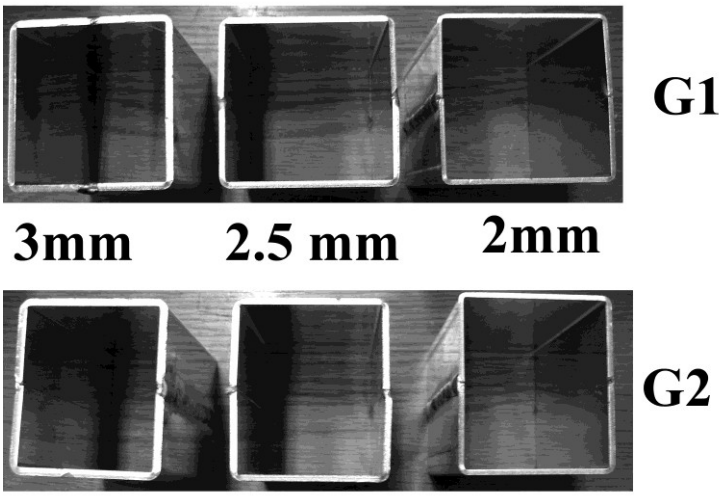

(b)

Figure 4.8. a) Experimental crash box specimens with and without montage plate and b) cross section view of the boxes of three different wall thicknesses.

4.3. Tensile Testing of 1050H14 Al

The tensile test specimens of 1050H14 Al were prepared both perpendicular and parallel to the extrusion direction. The test samples were machined according to ASTM E8/E8M-08 standard (ASTM 2001) using a electro discharge machine. The dimensions of the tested tensile test specimens are shown in Figure 4.9. 1050H14 tensile test specimens containing a weld zone at the middle were also prepared tested (Figure 4.9). The tensile tests were conducted at a cross-head speed of 5 mm min^{-1}, corresponding to a quasi-static strain rate of 1.66 x10^{-3} s^{-1}. During the tests, a video extensometer was used to measure the displacement.

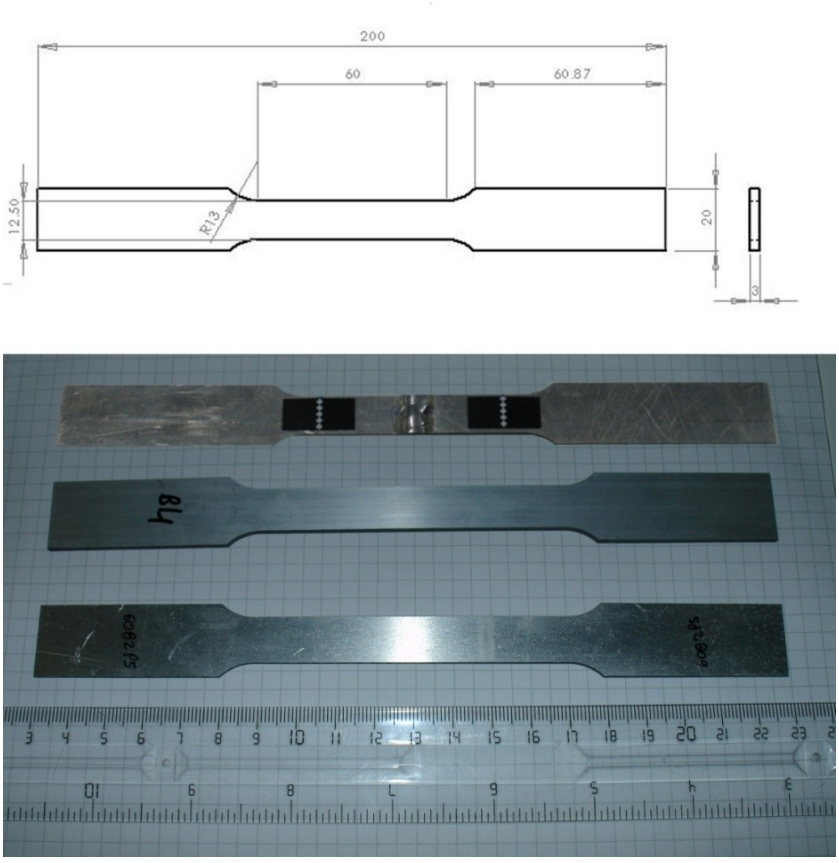

Figure 4.9. Dimensions of tensile test sample and welded and unwelded tensile test specimens.

4.4. Compression Tests of Crash Boxes

Commercially crash boxes of aluminum and steel with different geometries (Figure 4.10(a) and (b)) were purchased and quasi-statically compression tested at 5mm min^{-1} for the comparison purposes. These crash boxes are used in the automobiles of an average weight of 1100 kg . Before testing, the fixing parts were removed. In the steel crash box, flat plates were welded on the top and at the bottom in order to form a uniform crushing under uniaxial compression loads. The mean load and specific absorbed energy levels of these two commercial available crash boxes were taken as the minimum values which were used to optimize the investigated crash boxes.

(a)

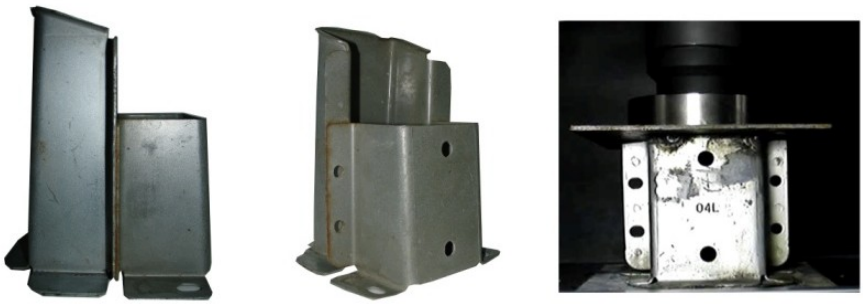

(b)

Figure 4.10. Commercially available crash boxes of a) aluminum and b) steel.

4.5. Quasi-static Compression Testing of Empty and Aluminum Foam Filled 1050Aluminum Crash Boxes

4.5.1. Uniaxial compression testing of crash boxes at different strain rates

The compression tests of empty boxes without montage plates were carried out between the tool steel plates of Schmadzu AGI 300 kN universal test machine (Figure 4.11). The surfaces of the boxes and compression test plates were lubricated before testing. Empty boxes were tested at two different displacement speeds, 5 mm min^{-1} and 500 mm min^{-1}, corresponding to the strain rates of 6.65×10^{-4} and 6.65×10^{-2} s^{-1}.

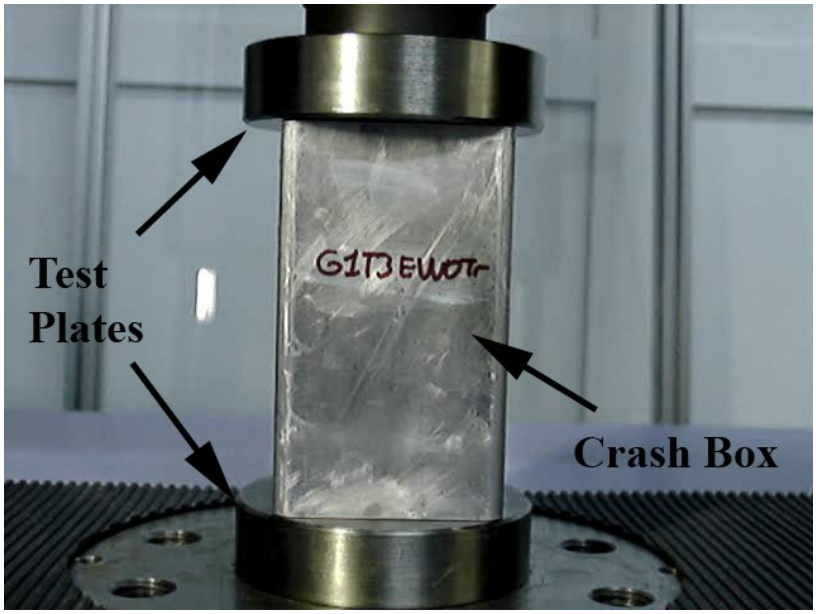

Figure 4.11. Compression testing of crash box without trigger mechanism and montage part.

4.5.2. Uniaxial Compression Testing of Empty Original Crash Boxes

The original empty crash boxes without trigger mechanism were compression tested at a loading rate of 5 mm min^{-1} (Figure 4.12 (a)). Boxes with corrugation sections were also tested under the same loading rate (Figure 4.12 (b)).

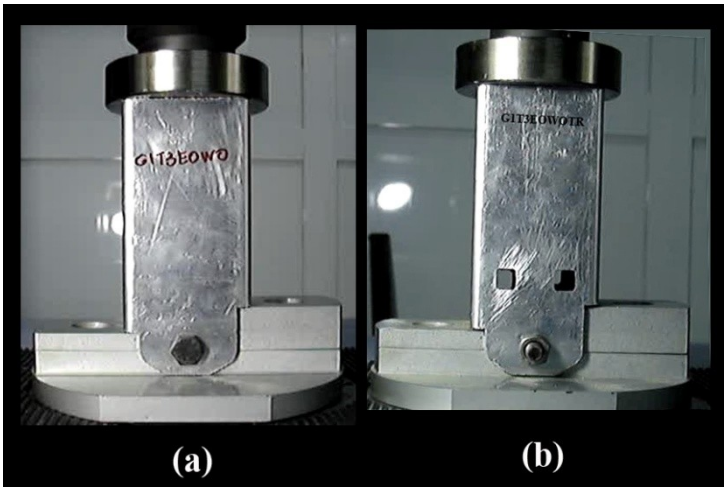

Figure 4.12. Original crash box compression testing a) without and b) with corrugation section.

4.5.3. Uniaxial Compression Testing of Empty and Partially Foam Filled Crash Box without Montage Parts

Empty and partially foam filled 1050H14 aluminum crash boxes (Figure 4.13) with trigger mechanism were tested at a deformation speed of 5 mm min^{-1} (6.65×10^{-4} s^{-1}). These boxes were filled with Al foams (0.11 and 0.15 relative density) and tested at the same deformation speed. Test sample coding and the number of compression tests are tabulated in Table 4.1.

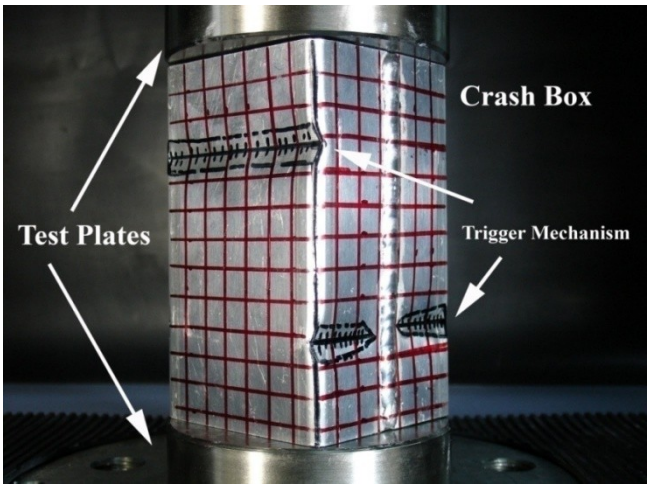

Figure 4.13. Compression testing of crash box with trigger mechanism.

Table 4.1. The coding of compression tested empty and filled boxes without montage plates.

Geometry	Thickness : T T2 : 2mm T2.5: 2.5 mm T3: 3mm	Empty : E Filled : F1, Relative Density :0.11 F2, Relative Density :0.15	Coding	Number of tests
G1	T2	E	G1T2E	3
G1	T2	F1	G1T2F1	3
G1	T2	F2	G1T2F1	3
G1	T2.5	E	G1T2.5E	3
G1	T2.5	F1	G1T2.5F1	3
G1	T2.5	F2	G1T2.5F2	3
G1	T3	E	G1T3E	3
G1	T3	F1	G1T3F1	3

(cont. on next page)

Table 4.1 (Cont.)

G1	T3	F2	G1T3F2	3
G2	T2	E	G2T2E	3
G2	T2	F1	G2T2F1	3
G2	T2	F2	G2T2F1	3
G2	T2.5	E	G2T2.5E	3
G2	T2.5	F1	G2T2.5F1	3
G2	T2.5	F2	G2T2.5F1	3
G2	T3	E	G2T3E	3
G2	T3	F1	G2T3F1	3
G2	T3	F2	G2T3F1	3

4.5.4. Uniaxial Compression Testing of Empty and Partially Foam Filled Crash Box with Montage Plates

The uniaxial compression testing of empty and partially foam filled crash box with montage plates were performed at the deformation speed, 5 mm min^{-1}. In these samples a 2 mm thick steel plate were fixed to the upper section and a thicker steel block with perfectly parallel surface was positioned at the bottom of the crash box as shown in Figure 4.14. The upper steel plate was fixed to the upper montage plate with the bolts. These tubes were also filled with two different aluminum foam relative densities, 0.11 and 0.15. The test sample coding of the tested boxes with montage plates is listed in Table 4.2.

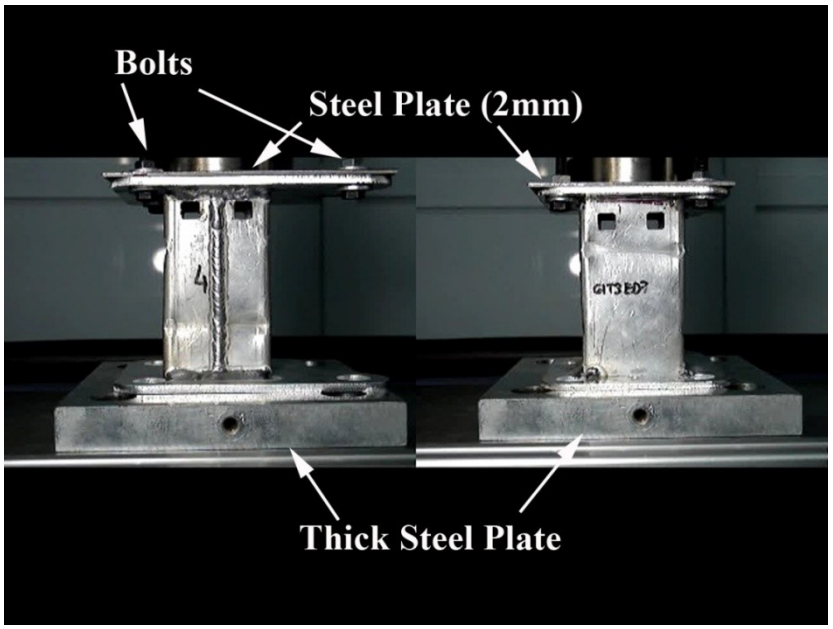

Figure 4.14. Uniaxial compression testing of empty and partially foam filled crash box with montage plates.

Table 4.2. The coding of compression tested empty and filled boxes with montage plates.

Geometry	Thickness : T T2 : 2mm T2.5: 2.5 mm T3: 3mm	With Montage Plate	Empty : E Filled : F1, Relative Density :0.11 F2, Relative Density :0.15	Coding	Number of Repetitions
G1	T2	WP	E	G1T2WPE	3
G1	T2	WP	F1	G1T2WPF1	3
G1	T2	WP	F2	G1T2WPF1	3
G1	T2.5	WP	E	G1T2.5WPE	3
G1	T2.5	WP	F1	G1T2.5WPF1	3

(cont. on next page)

Table 4.2 (Cont.)

G1	T2.5	WP	F2	G1T2.5WPF2	3
G1	T3	WP	E	G1T3WPE	3
G1	T3	WP	F1	G1T3WPF1	3
G1	T3	WP	F2	G1T3WPF2	3
G2	T2	WP	E	G2T2WPE	3
G2	T2	WP	F1	G2T2WPF1	3
G2	T2	WP	F2	G2T2WPF1	3
G2	T2.5	WP	E	G2T2.5WPE	3
G2	T2.5	WP	F1	G2T2.5WPF1	3
G2	T2.5	WP	F2	G2T2.5WPF1	3
G2	T3	WP	E	G2T3WPE	3
G2	T3	WP	F1	G2T3WPF1	3
G2	T3	WP	F2	G2T3WPF1	3

4.6. Initial Dynamic Testing of Empty and Aluminum Foam Filled 1050Aluminum Crash Boxes with Fixing Plates

The drop weight tests of empty and filled boxes were performed using Fractovis Plus drop-weight test system (Figure 4.15(a)). An apparatus (Figure 4.15(b)) that fixes the crush boxes tightly in the sample holder of drop tower were constructed. In a typical experiment, the crash box was tightly fixed to the testing apparatus with bolts and the striker head with 90kN load capacity impacted the crash box from the top (Figure 4.15(c)) with an initial velocity of 5.5 m s^{-1}. The drop-weight test system had a maximum energy capacity of 1800 J, which was unable to deform the box until the

densification displacement in a single shot; therefore, the test samples tested was hit by the striker head with several times in order to reach relatively high displacements.

(a) (b) (c)

Figure 4.15. a) Fractovis Plus drop-weight test system, b) drawing of the designed test apparatus and c) the pictures of the test sample and the sample fixture in the drop weight test.

CHAPTER 5

SIMULATION AND OPTIMIZATION OF EMPTY AND PARTIALLY ALUMINUM FOAM FILLED CRASH BOXES

5.1.Material Modeling

5.1.1. 1050H14 Base Material

Three material models are widely used in the simulations of the mechanical response of the crash box base materials. These models include the plastic kinematic model, Mat 3 in LS-DYNA (Mamalis, et al. 2003c, Wang, et al. 2005), the piece-wise linear plasticity model, Mat 24 in LS-DYNA (Mamalis, et al. 2003b, Meguid, et al. 2004b) and the anisotropic plasticity model, Mat103 in LS-DYNA (Fyllingen, et al. 2007). It was previously shown by Lademo et al. (Lademo, et al. 2008) that the processing history and anisotropy of box materials had negligible effects on the predicted load values and the deformation characteristics of the crash boxes subjected to frontal impact. Hence, it was suggested that the use of the simple piece wise or plastic kinematic model could sufficiently resemble the real crushing behavior of metallic crash boxes. In the present thesis, two material models, Mat3 and Mat24, were initially considered for the simulating of the crushing behavior of 1050H14 Al crash box. The material properties of 1050H14 Al alloy were determined from the uniaxial tension stress-strain curve of the base material.

In plastic kinematic material model, the mechanical properties are characterized by the material flow stress (σ_y), Young's modulus (E) and tangent modulus (E_t) as depicted in Figure 5.1., (Hallquist 2006)

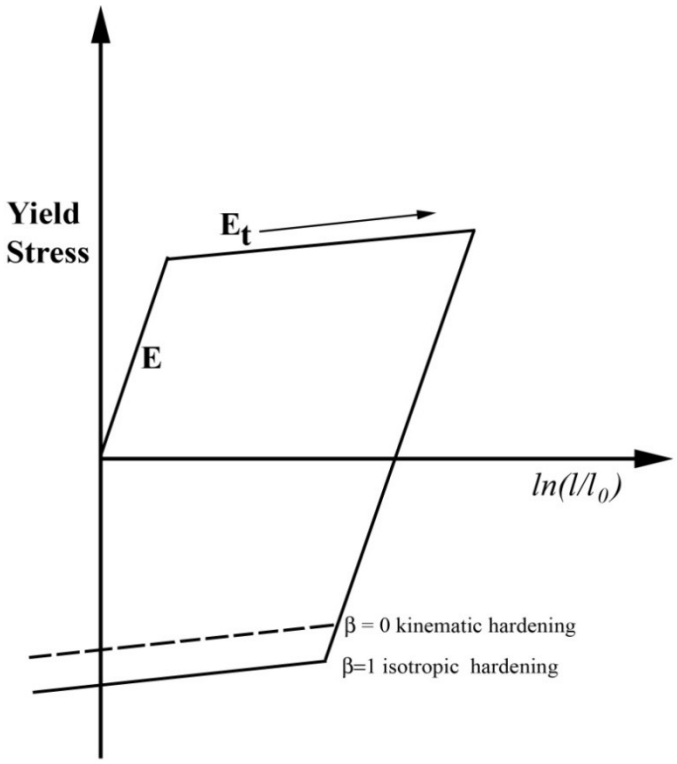

Figure 5.1. Elastic-plastic behavior with isotropic and kinematic hardening, l_0 and l are initial and final length of the tension specimen, respectively (Source: Hallquist 2006).

The yielding is defined by Von Misses yield criterion (Bathe 1996, Crisfield 1991, Hallquist 2006) as

$$f = \frac{1}{2} s_{ij} s_{ij} - \frac{\sigma_y^2}{3} = 0 \tag{5.1}$$

where, S_{ij} and σ_y are the deviatoric stress and the current radius of the yield surface. In plastic kinematic plasticity algorithm, σ_y is,

$$\sigma_y = \sigma_0 + \beta E_p \varepsilon_{eff}^p \tag{5.2}$$

where, σ_0 is the yield strength, β stands for the isotropic and kinematic of hardening, ε_{eff}^{p} is the effective plastic strain and E_p is the plastic hardening modulus given as

$$E_p = \frac{E\,E_t}{E-E_t} \tag{5.3}$$

In piece-wise linear plasticity algorithm, the current radius of yield surface is

$$\sigma_y = \beta\left(\sigma_0 + f_h\left(\varepsilon_{eff}^{p}\right)\right) \tag{5.4}$$

where, $f_h\left(\varepsilon_{eff}^{p}\right)$ is the hardening function which can be specified in tabular form. In Mat24 material model, the deviatoric stresses are updated elastically and the yield function is checked: if it is satisfied, the deviatoric stresses are accepted. If it is not satisfied, an increment in plastic strain is computed by using current plastic hardening modulus which is found from tabulated effective plastic stress-plastic strain data of the tensile test of base material (Figure 5.2). Since many Al alloys are known to show strain rate insensitive flow stresses, an strain rate insensitive material model was assigned to 1050H14 Al alloy and Alulight foam.

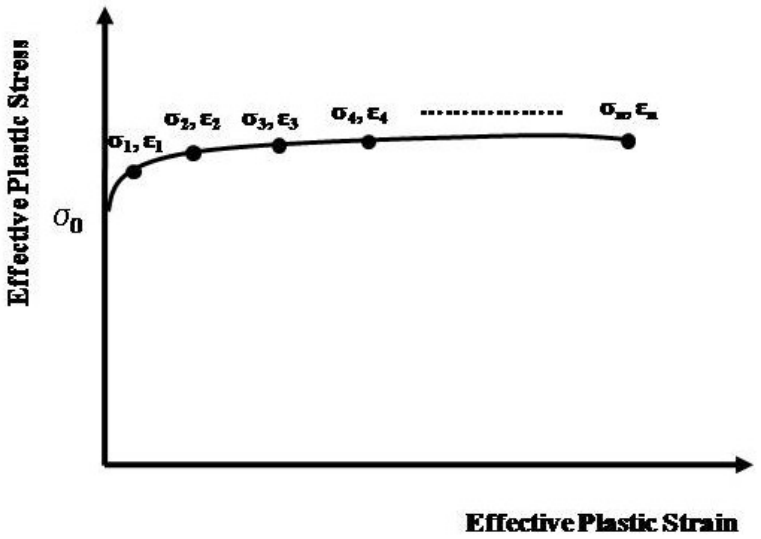

Figure 5. 2. Effective plastic stress-stain curve.

5.1.2. Aluminum Foam Modeling

Several foam models are available in LS-DYNA explicit finite element simulation program for Al closed cell foams. These models are

- Mat-26 Honeycomb model (Hanssen, et al. 2002, Meguid, et al. 2004b, Reyes, et al. 2004, Santosa and Wierzbicki 1998a),
- Mat-63 Crushable foam model (Mamalis, et al. 2008, Wang, et al. 2005),
- Mat-126 Modified Honeycomb model,(Altenhof, et al. 2002, Hanssen, et al. 2000c)
- Mat-154 Desphande and Fleck foam model(Hanssen, et al. 2006, Zhang and Cheng 2007),

Among the models listed above, the most widely used foam model namely Deshpande and Fleck foam model was used to simulate the foam filler deformation behavior in the present study. The schematic of honeycomb material geometrical model is shown in Figure 5.3. Honeycomb material model is essentially anisotropic when

considered in axial and transverse directions; therefore, material parameters are required to be determined separately for each direction.

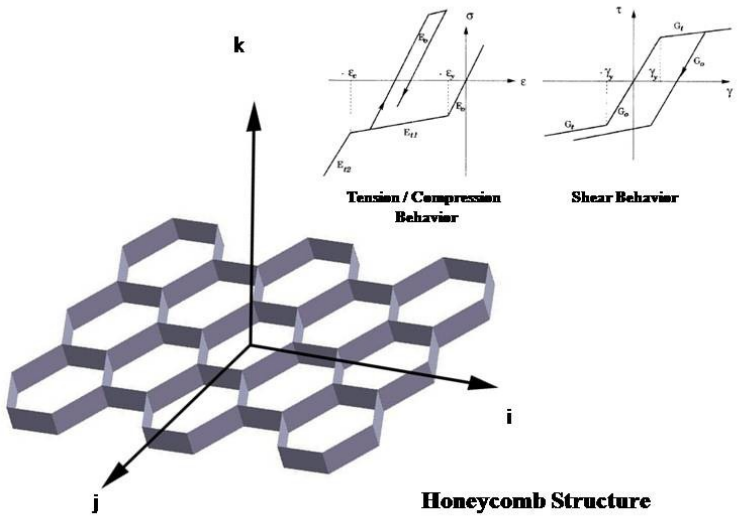

Figure 5. 3. Schematic of the honeycomb structure and tension, compression and shear behavior.

.

The material parameters of the honeycomb model are listed below (Hallquist 2006),

- E, Young modulus for the fully compacted material,
- ν, Poisson's ratio for the compacted material,
- LCA, load curve for σ_{aa} vs. volumetric strain,
- LCB, load curve for σ_{bb} vs. volumetric strain;
- LCC, load curve for σ_{cc} vs. volumetric strain,
- LCS, load curve for shear stress vs. volumetric strain,
- V_f , relative volume at which honeycomb is fully compacted,
- E_{aau} , elastic modulus in uncompressed condition,
- E_{bbu} , elastic modulus in uncompressed condition,
- E_{ccu} , elastic modulus in uncompressed condition,
- G_{aau} , elastic shear modulus in uncompressed condition,
- G_{bbu} , elastic shear modulus in uncompressed condition,
- G_{ccu} , elastic shear modulus in uncompressed condition,

- LCAB, load curve of σ_{ab} vs. volumetric strain,
- LCBC, load curve of σ_{bc} vs. volumetric strain,
- LCCA, load curve of σ_{ca} vs. volumetric strain, and
- LCSR, load curve of strain rate effects,

Al foams are usually considered nearly isotropic, showing small variations in mechanical properties in 3 directions; therefore, the mechanical properties in a, b and c direction are taken equal to each other (Santosa and Wierzbicki 1998a). Desphande and Fleck foam model yield function is defined as

$$\Phi = \hat{\sigma} - \sigma_Y \tag{5.5}$$

where, $\hat{\sigma}$ is the he equivalent stress and given as,

$$\hat{\sigma}^2 = \frac{{\sigma_{VM}}^2 + \alpha^2 {\sigma_m}^2}{1+(\alpha/3)^2} \tag{5.6}$$

where, σ_{VM} and σ_m are the von Misses effective stress and mean stress, respectively and α defines the shape of the yield surface. The following relation for α is given by Deshpande and Fleck (Deshpande and Fleck 2000b)

$$\alpha^2 = \frac{9}{2}\frac{(1-2\upsilon^p)}{(1+\upsilon^p)} \tag{5.7}$$

where, υ^p is the plastic Poisson ratio of foam. As Al foams are known to show no lateral plastic deformation under uniaxial compression, the value of υ^p is taken 0, so that α becomes equal to $\sqrt{9/2} \cong 2.12$ (Reyes, et al. 2004). σ_Y is then expressed by the following relation,

$$\sigma_y = \sigma_p + \gamma \frac{\hat{\varepsilon}}{\varepsilon_D} + \alpha_2 \ln\left(\frac{1}{1-\left(\frac{\hat{\varepsilon}}{\varepsilon_D}\right)^{\beta}}\right) \quad (5.8)$$

In Equation 5.8, ε_D is the densification strain of foam and the value is calculated using the following relation,

$$\varepsilon_D = -ln\left(\frac{\rho_f}{\rho_{f0}}\right) \quad (5.9)$$

In Equation 5.9, ρ_f and ρ_{f0} are the foam density and the density of metal from which the foam is made. The material parameters, plateau stress, γ, α_2 and β are simply determined from the uniaxial compression stress-strain curves of foam. Al foams particularly Alulight and Alcan foams are known to show strain rate insensitive mechanical behavior. So that, any strain-rate effect on the mechanical response of the studied foams is neglected in the simulations.

5.2. Quasi-static and Dynamic Simulation of Crashing Behavior of Empty and Foam Filled 1050H14 Al Crash Box

1050H14 Al alloy was modeled with 4 node Belytschko–Tsay shell elements with one point integration in the plane and five in the thickness direction. 8-node solid elements were used to model Alulight Al foam. The shell and solid element lengths were taken 3 and 6 mm, respectively. LS-DYNA is based on explicit time integration and since the quasi-static deformation occurs under relatively low deformation rates, the quasi-static modeling in LS-DYNA requires relatively long durations. To simulate the quasi-static deformations at reasonably shorter times in LS-DYNA, the mass scaling is

usually applied (Marsolek and Reimerdes 2004, Meguid, et al. 2004b). Two methods of mass scaling are as follows (Santosa, et al. 2000),

- Scaling down of the material density increases the number of time increments. The total time of solution is decreased by increasing the loading rate of quasi-static simulation.
- Second way is scaling up the mass density with very low loading rates. This is caused to very large time step with reduced the number of time step.

Quasi-static simulation of mass scaling must met two conditions. First, the total kinetic energy of entire simulation must be relatively very small as compared with the total internal energy of system. Second, the load vs. deformation behavior must be independent of deformation rate. These conditions must be satisfied in the total duration of simulation.

In the simulation of the quasi-static crushing of empty and filled boxes, the material mass density was scaled down by a factor of 1000 and the deformation speed was increased to 2 m s^{-1}. Dynamic crush simulations results of G1 geometry boxes (implemented with the montage plates) were used as inputs to the crash boxes optimization. In dynamic simulations, a planar moving force contact algorithm was used to simulate the impact of 550 kg mass with an initial deformation velocity of 10 ms^{-1}.

In the quasi-static compression simulations, the compression top and bottom plates were modeled as rigid walls. The planar forces and the geometric flat motion of rigid wall algorithms were applied to top and bottom compression plates, respectively (Figure 5.4(a)). In the modeling of the deformation of empty and partially filled aluminum crash boxes without montage plates, the planar flat rigidwall representing the bottom deformation plate was fixed, no translation and rotation, and the geometric flat motion rigid-wall representing the upper plate moved only in z direction, the motion in all other directions was restricted. In the simulation of empty and partially filled crash boxes with montage parts; however, no rigid wall algorithms were used. The top and bottom weld plates were created as separate parts and the bottom and top weld plates

were constrained. Since the width of the welding zone was measured 9 mm, the rotational motions of all nodes in a distance 6 mm from the top and bottom of tube were not allowed in all direction (Figure 5.4(b)). The translation motion of weld zone nodes was only allowed in Z direction. Similar constraints were also previously applied in the simulation of the crushing of 5018 Al tubes (Williams, et al. 2007).

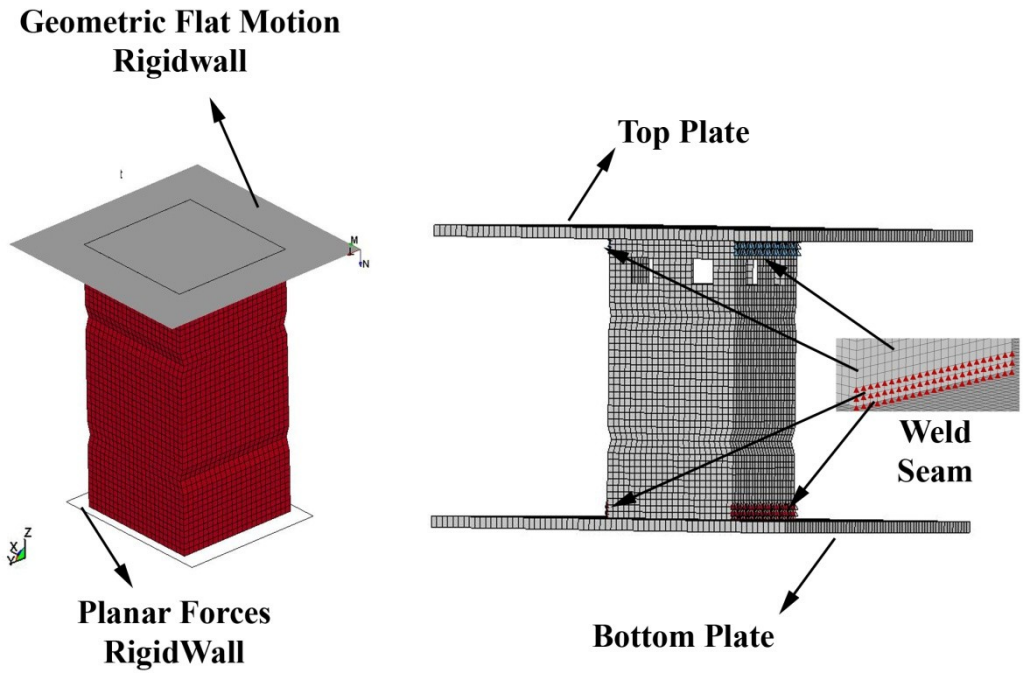

(a) (b)

Figure 5.4. The model of a) crash box without montage plates and b) crash box with montage plates.

The self contact of crush zone surfaces (contact between folds) was modeled with automatic single surface contact algorithm (Figure 5.5(a)). Automatic surface to surface contact algorithm was used to simulate the contact between foam filler and box wall and box edge and weld plates of crush boxes with montage plates (Figure 5.5(b)). The contact between crash zone and montage plates was modeled with automatic nodes to surface contact algorithm. Lastly, the static and dynamic friction coefficients were taken 0.3 and 0.2, respectively.

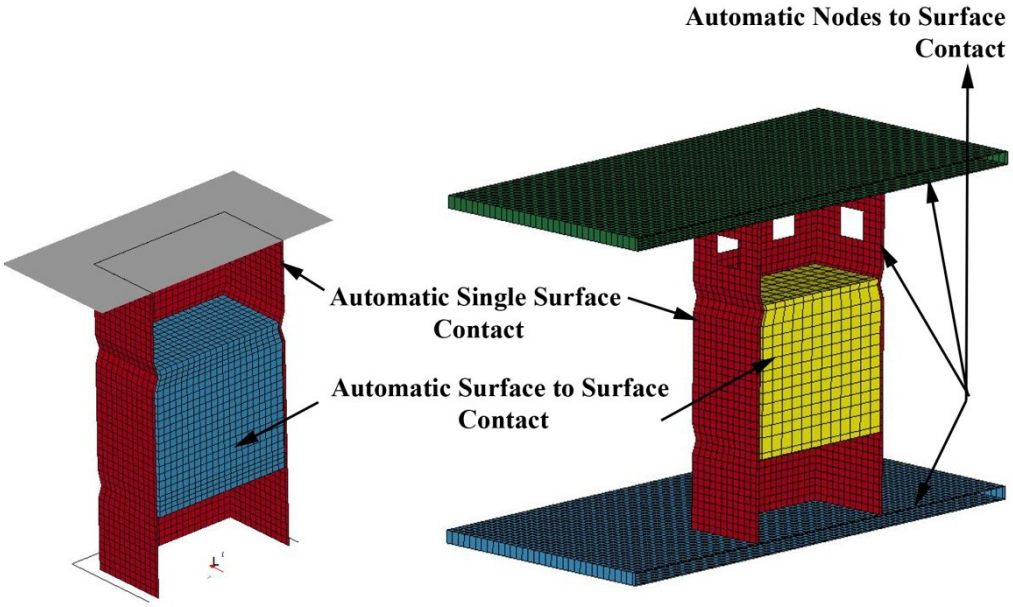

(a) (b)

Figure 5.5. Contact algorithms used in crash box modeling a) without and b) with montage plates.

5.3.The Response Surface Methodology

As stated earlier, tube G1 geometry (70.2x67.6x125.2 mm) was selected for the optimization study. The response surface algorithm was implemented in order to determine the optimum combination of 1050H14 Al and 6061 T4 Al crash box thickness and Alulight and Hydro foam filler relative density. A quadratic-polynomial objective function was selected for constraint single-objective optimization. 6061 T4 Al alloy is known to have higher strength than 1050H14 Al and Hydro foam has higher plateau stress than Alulight foam at similar relative densities. The selection of these materials was to determine the effect of box and filler material properties on the optimized crush box parameters. Response surface methodology (RSM) is a widely used method of crush box energy absorption optimization studies. RSM has three terms (Giess 1998)

Objective function: the performance measure of a structure which is to be maximized or minimized. Response/design: the variables which are directly related to the design of structure such as tube thickness, length and filler density. Constraint function: a restriction/limitation on the response or design variables of a structure.

Generally, response y depends on controllable, natural, independent variables of $\xi_1,\xi_2,\ldots\xi_k$. Then, the relationship between the response and independent variables is expressed as,

$$y = f(\xi_1, \xi_2, \ldots . \xi_k) + \varepsilon \tag{5.10}$$

where, f is the response objective function and ε is an error which represents non dependable variables e.g experimental and computational error and background noise. ε is generally treated as a statistical error and often presumed to have a normal distribution with a mean of zero (Fang, et al. 2005). Then response function (E) is rearranged as,

$$E(y) = E[f(\xi_1, \xi_2, \ldots . \xi_k)] + E(\varepsilon) \tag{5.11}$$

The response function(η) is given in terms of independent variables as,

$$\eta = f(\xi_1, \xi_2, \ldots . \xi_k) \tag{5.12}$$

Note that natural variables in above equations are expressed in the units of measurement e.g Newton per square meter and degrees of Celsius (°C). These are transformed into the coded variables ($x_1,x_2,\ldots x_k$) which are dimensionless with a mean of zero and with the same standard deviation. A coded variable is given by the following relation,

$$x_{ii} = \frac{\xi_{ii} - (max\,(\xi_{ii}) + min\,(\xi_{ii}))/2}{(max\,(\xi_{ii}) - min\,(\xi_{ii}))/2} \tag{5.13}$$

The response function in terms of coded function is then written as,

$$\eta = f(\mathrm{x}_1, \mathrm{x}_2, \ldots . \mathrm{x}_\mathrm{k}) \tag{5.14}$$

If the objective function of response function is a second order polynomial, Equation 5.11 is rewritten as,

$$\underbrace{y = \beta_0 + \beta_1 x_1 + \beta_2 x_2 + \beta_3 {x_1}^2 + \beta_4 {x_2}^2 + \beta_5 x_1 x_2}_{\eta} + \varepsilon \tag{5.15}$$

For n observations, the response equation becomes

$$y_1 = \beta_0 + \beta_1 x_{11} + \beta_2 x_{12} + \beta_3 {x_{11}}^2 + \beta_4 {x_{12}}^2 + \beta_5 x_{11} x_{12} + \varepsilon_1$$

$$y_2 = \beta_0 + \beta_1 x_{21} + \beta_2 x_{22} + \beta_3 {x_{21}}^2 + \beta_4 {x_{22}}^2 + \beta_5 x_{21} x_{22} + \varepsilon_2$$

.

.

.

$$y_n = \beta_0 + \beta_1 x_{n1} + \beta_2 x_2 + \beta_3 {x_{n1}}^2 + \beta_4 {x_{n2}}^2 + \beta_5 x_{n1} x_{n2} + \varepsilon_n \tag{5.16}$$

Equation 5.16 can also be written in the following form,

$$y = \begin{bmatrix} y_1 \\ y_2 \\ \vdots \\ y_n \end{bmatrix} = \begin{bmatrix} 1 & x_{11} & x_{12} & {x_{11}}^2 & {x_{12}}^2 & x_{11}x_{12} \\ 1 & x_{21} & x_{22} & {x_{21}}^2 & {x_{22}}^2 & x_{21}x_{22} \\ \vdots & \vdots & \vdots & \vdots & \vdots & \vdots \\ 1 & x_{n1} & x_{n2} & {x_{n1}}^2 & {x_{n2}}^2 & x_{n1}x_{n2} \end{bmatrix}, \tag{5.17}$$

$$\beta = \begin{bmatrix} \beta_0 \\ \beta_1 \\ \vdots \\ \beta_5 \end{bmatrix} \tag{5.18}$$

and

$$\varepsilon = \begin{bmatrix} \varepsilon_1 \\ \varepsilon_2 \\ \vdots \\ \varepsilon_n \end{bmatrix} \tag{5.19}$$

where, y is an nx1 vector of observation, x is an nx6 matrix of independent variables, β is a 6x1 regression vector and ε is an nx1 vector of random errors. For n observations and k number of regressor, Equation 5.16 can also be formulated as,

p=k+1

$y = X\beta + \varepsilon$, n , p (5.20)

The sum of the square of errors is

$$L = \sum_{i=1}^{n} \varepsilon_i^2 \ = \sum_{i=1}^{n} \left(y_i - \beta_0 - \sum_{j=1}^{k} \beta_j X_{ij} \right)^2 \tag{5.21}$$

or

$$L = \sum_{i=1}^{n} \varepsilon_i^2 \ = \sum_{i=1}^{n} \varepsilon' \varepsilon \ = (y - X\beta)'(y - X\beta) \tag{5.22}$$

In Equation 5.22, the function L is to be minimized with respect to $\beta_0, \beta_1, \beta_2, \ldots . \beta_k$. The least square estimators, $b = \{b_0, b_1, b_2, \ldots . b_k\}$, must satisfy the following,

$$\left. \frac{\partial L}{\partial \beta} \right|_b = -2X'y + 2X'Xb = 0 \tag{5.23}$$

The least square estimator can be calculated as,

$$b = (X'X)^{-1}X'y \tag{5.24}$$

The fitted regression model then becomes;

$$\hat{y} = Xb \tag{5.25}$$

In addition, the error is calculated using the following relation,

$$e = y - \hat{y} \tag{5.26}$$

The error sum of square (SS_E), the total sum of square (SS_T), root mean square (R^2) adjusted root mean square (R_{adj}^2), root mean square error (RMSE) are sequentially given by the following relations,

$$SS_E = y'y - b'X'y \tag{5.27}$$

$$SS_T = y'y - \frac{\left(\sum_{i=1}^{n} y_i\right)^2}{n} \tag{5.28}$$

$$R^2 = 1 - SS_E/SS_T \tag{5.29}$$

$$R_{adj}{}^2 = 1 - (1 - R^2)\frac{n-1}{n-p-1} \tag{5.30}$$

and

$$RMSE = \sqrt{\frac{SS_E}{n-p-1}} \tag{5.31}$$

Briefly, Equations 5.27-5.31 are used to validate the constructed response surface. The details of RSM can be found in references (Montgomery 1997, Myers and Montgomery 1995).

5.4. The Crashworthiness Optimization of Tubular Structures

The crushing behavior of multi-corner, thin-walled columns was previously optimized using RSM (Liu 2008a). The wall thickness and cross-section edge length were selected independent variables for the maximization of SEA. In another study, a square crush box with multi-cell sections was optimized with optimum cell numbers and cell geometrical parameters using again RMS (Hou, et al. 2008). The objective functions including linear, quadratic, cubic, quadratic and quintic polynomial were implemented, while the minimum error was accomplished by using a quadratic polynomial objective function. In a study of the multi-objective optimization of the frontal crush of an automobile chassis, RSM and radial basis function methodology were implemented together for comparison purpose (Fang, et al. 2005). Both were shown to be effective in the optimization of the intricate structure of automobile frontal section. RMS was also applied to determine the optimum thickness and radius of a cylindrical shell type tubular structure (Yamazaki and Han 2000). An orthogonal polynomial function was chosen as objective function and an orthogonal sampling array was implemented to create the response surface. Additionally, dynamic tests were carried out in order to validate objective function. The crashworthiness optimization of the circular Al tubes was studied by Zarei and Kröger, (Zarei and Kröger 2006). Various shapes of the impact side of circular tubes were investigated for the maximization of crush performance (Chiandussi and Avalle 2002). The taper length and the smallest diameter of tube were selected independent variable and the load uniformity (maximum load divided by mean load) dependent variable. The minimization of the load uniformity was applied to, in an separate study, the optimization of corrugated circular and tapered rectangular tubes (Avalle, et al. 2002).

The shape optimization of a non-uniform closed hat front crash absorber section of an automobile was studied using RSM by Y.-B Cho et al.(Cho, et al. 2006). Two different crush initiator shapes, rectangular hole-type and circular dent-type, were investigated to maximize the crush energy absorption. A cross-section shape optimization study was further performed by Giess and Tomas (Giess 1998) by implementing the average mean crushing load as an objective function. The constraint

imposed was a constant prismatic cross-section and resulted in a 91% increase in the energy absorption at an impact velocity of 48 km h^{-1}.

The minimum weight optimization of an Al foam filled S-Frame was carried out using an analytical energy absorption equation as an objective function (Kim, et al. 2002). The optimized variables, the thickness and cross-section length of the frame and the foam relative density, were validated with the finite element simulations. The simulation and optimization results showed 5% difference. Zarei and Köreger (Zarei and Kröger 2008b) worked on the optimization of Alporas Al foam-filled Al tubes to maximize SEA for the crush box applications by taking the width of cross-section and foam density as independent variables. The optimum parameters of empty square Al tubes were determined under the maximum mean load constraint of 68.5 kN. Equivalent SEA values of the optimized empty square tubes were compared with those of the optimized foam filled Al tube. Approximately, 20% increase in SEA values was found after the optimization in foam filled tubes. A similar optimization study was conducted on Al honeycomb filled Al square tubular structures (Zarei and Kröger 2008c). With respect to empty counterpart, 14.3% increase in SEA values were found in filled tube. Zhang et al.(Zhang, et al. 2008) performed an optimization study on the honeycomb filled bitubular hexagonal columns using Chebyshev's orthogonal polynomial as objective function with the independent variables of inner side length and the thickness of inner and outer wall. With the maximized average mean load, 40% increase in SEA values was found in the optimized bitubal honeycomb filled Al tubes. Single and weighted arithmetic and geometrical average methods of multi objective optimization were implemented to foam filled thin-wall structures (Hou, et al. 2009). The applied Pareto analysis showed that geometrical average method was more effective than arithmetic average method in multi objective optimization of foam filled thin-wall structures. The bending properties of Alporas Al foam filled square tubular structures were optimized by Zarei and Kröger (Zarei and Kröger 2008a). Agreements between experimental and numerical results were found under the prescribed constraints and 28.1% increase in SEA values was found in foam filled tubular structures. Square tapered mild steel tubes were optimized in terms of tube thickness and width and taper angle (Liu 2008b). Full factorial design with 27 sampling points and second order objective functions were implemented using RSM. It was shown that taper angle had a

great effect on the crushing behavior of tube. Lower values of taper angle were shown to improve SEA and mean load/maximum load values.

5.5.Optimization of 1050H14 Al Crush Box – Alulight Al Foam Filler Binary System

The optimization process was to maximize SEA of partially filled 1050H14 Al crush box (70.2X67.6X125.2 mm). The fixing parts of the box were also included in the optimization study in order to represent the real crash behavior of the box. SEA and mean load values were defined by two independent variables: box wall thickness and foam filler relative density. A quadratic (4^{th} order) polynomial objective function was used to create the response surface of filled crash box. Full factorial design, r^s, was used to generate sampling points of the response surface. The created mesh of sampling points had r points spaced intervals in each variable direction. To create an approximation of order of r, at least $(r+1)^s$ factorial designs were required. In the optimization study r and s were taken as 4 and 2, respectively. The optimization problem is defined as,

Maximize : SEA (t,ρ^*)

The constraints were:

Mean Load (t,ρ^*) < 55 kN

$1 < t < 3.0$ mm

$0 < \rho^* < 0.2$

The mesh of sampling points are shown in Figure 5.6. Total 25 simulations were run for each design set in the response surface analysis.

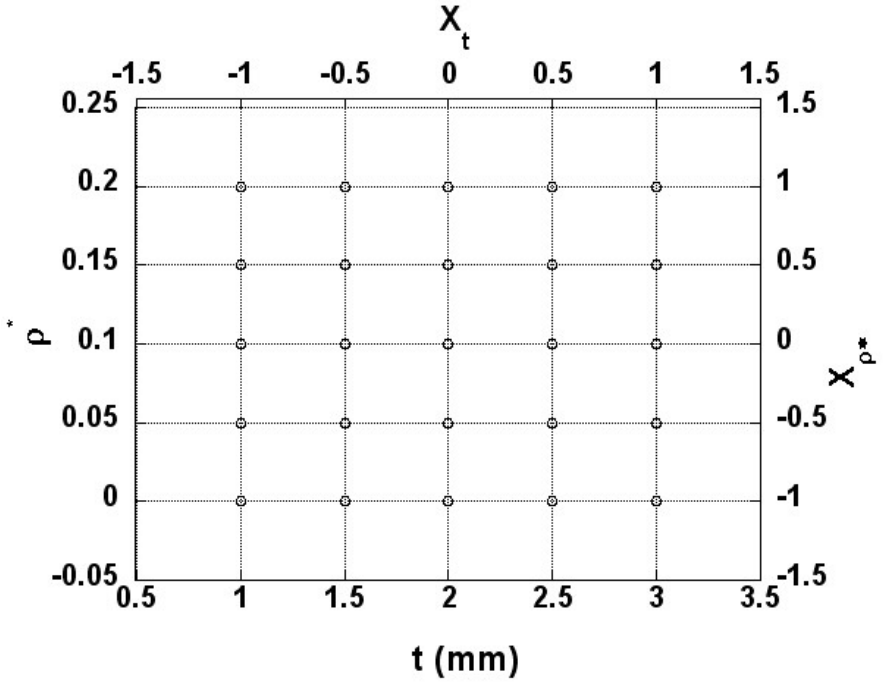

Figure 5.6. The mesh of sampling points of RSM optimization.

The fmincon command of Matlab optimization tool box was implemented to maximum SEA values at the boundaries of independent variables (box thickness and foam relative density). fmincon attempts to find a constraint minimum of a scalar function of several variables starting from an initial estimate. This is generally referred as to constraint nonlinear optimization or nonlinear programming. The details of the Matlab optimization tool box is given in reference (Arora 2004).

CHAPTER 6

EXPERIMENTAL RESULTS

6.1. Uniaxial Compression Behavior of Alulight Closed-Cell Al Foam Materials

Engineering compression stress-strain curves of Alulight closed-cell Al foams of varying relative densities are shown in Figure 6.1(a). As is seen in Figure 6.1(a), the compression stress is function of relative density: increasing foam relative density increases foam stresses. The compression curves in the same figure essentially show the characteristics of the foam/cellular metal compression deformation behavior. In compression testing, the initial elastic region is followed by a plateau region in which the stress values slightly increase with increasing strain and a densification region after which the stress values increase sharply. The plateau stress values of the foams are determined by drawing a straight line to the stress values until about 0.1 strain. The intercept of the fitted-line on the stress axis is taken as the plateau stress. Figure 6.1(b) shows the variation of plateau stress with foam relative density. In this graph, each datum point represents the average plateau stress values of three repetitive compression tests on the foams of the same relative densities. The plateau stress in Figure 6.1(a) is further fitted with the power law strengthening equation.

The foam strength model developed by Desphande and Fleck (Deshpande and Fleck 2000b, Reyes, et al. 2003) is used to determine the stress-strain behavior of the investigated Alulight Al foam. Desphande and Fleck foam model is given by the following equation,

$$\sigma = \sigma_p + \gamma \frac{\hat{\varepsilon}}{\varepsilon_D} + \alpha_2 \ln\left(\frac{1}{1-\left(\frac{\hat{\varepsilon}}{\varepsilon_D}\right)^{\beta}}\right) \tag{6.1}$$

The parameters of the foam model are determined by fitting the stress-strain curves of the foams of different relative densities with Eqn. 6.1. The determined model parameters are tabulated in Table 6.1. In the model, the plateau stresses and the material constants are function of foam density with the following relations,

$$\left\{\sigma_p, \gamma, \alpha_2, {}^{1}/_{\beta}\right\} = C_0 + C_1\left({}^{\rho_f}/_{\rho_{f0}}\right)^n \tag{6.2}$$

where, C_o, C_1 and n are the constants and ρ_f and ρ_{fo} are the foam and foam material density, respectively. The model parameters, C_o, C_1, n, and foam relative density for the studied foams are further listed in Table 6.2. The experimental and Desphande and Fleck foam model stress-strain curves at different relative densities are shown together in Figure 6.2 for comparison. The model and experimental stress-strain curves () show good agreement with each other until about relatively large strains, depicted in Figure 6.2.

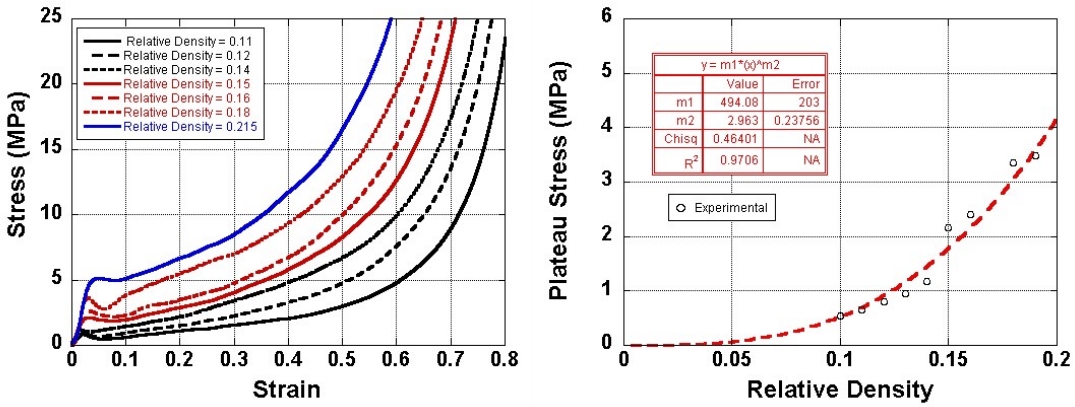

(a) (b)

Figure 6.1. (a) Compression stress-stain curves and (b) plateau stress *vs.* relative density of Al foam and.

Table 6.1. Desphande and Fleck foam model constants for Alulight Al foam.

Relative Density	Plateau Stress (MPa)	γ (MPa)	α_2 (MPa)	β
0.10	0.55	2.4423	25.568	7.2720
0.11	0.65	2.9117	29.755	6.9642
0.12	0.80	4.2377	28.172	5.3789
0.13	0.96	4.5500	39.216	6.2697
0.14	1.17	6.3561	28.164	5.3278
0.15	2.17	5.4245	39.622	5.3424
0.16	2.40	5.8326	37.086	4.5582
0.18	3.35	9.2817	38.732	4.8496
0.215	4.96	3.0435	33.705	2.9579

Table 6.2. Alulight Al foam material model parameters.

Foam Material Data Model Description :$\left\{\sigma_p, \gamma, \alpha_2, {}^1/_\beta\right\} = C_0 + C_1\left({}^{\rho_f}/_{\rho_{f0}}\right)^n$				
Model Parameters	σ_p (MPa)	γ (MPa)	α_2 (MPa)	${}^1/_\beta$
C_0	0	0	0	0.14307
C_1	494.08	298.2	125.44	97.396
N	2.963	2.0563	0.6635	4.0628

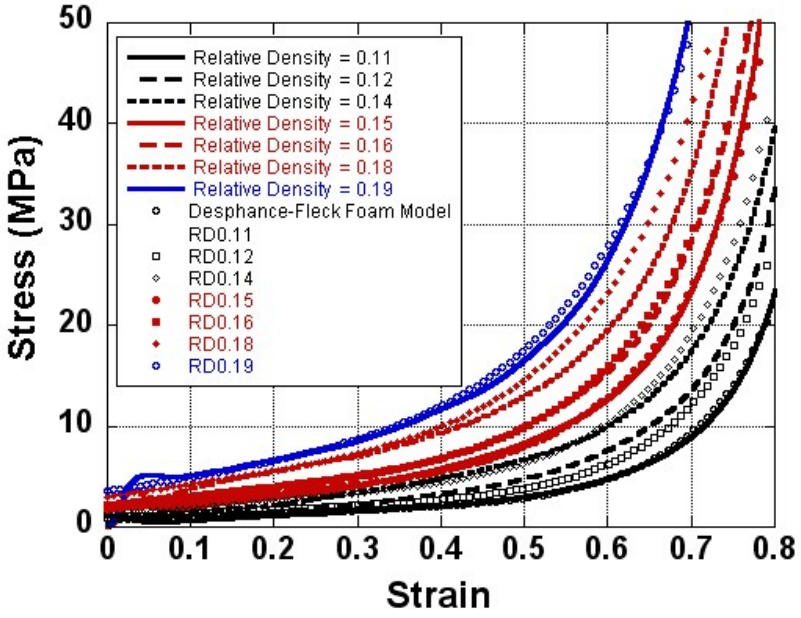

Figure 6.2. Experimental and foam model stress-strain curves of Alulight foams.

6.2. Tension Test of 1050H14 Al Crash Box Base Material

Typical tensile stress-strain curves of 1050H14 Al sheet metal, parallel and perpendicular to the extrusion direction are shown in Figure 6.3. The material shows slightly higher flow stress and lower ductility in the perpendicular to extrusion direction than in the parallel to extrusion direction. Tensile mechanical properties of the tested 1050H14 sheet Al material for both directions are further listed in Table 6.3.

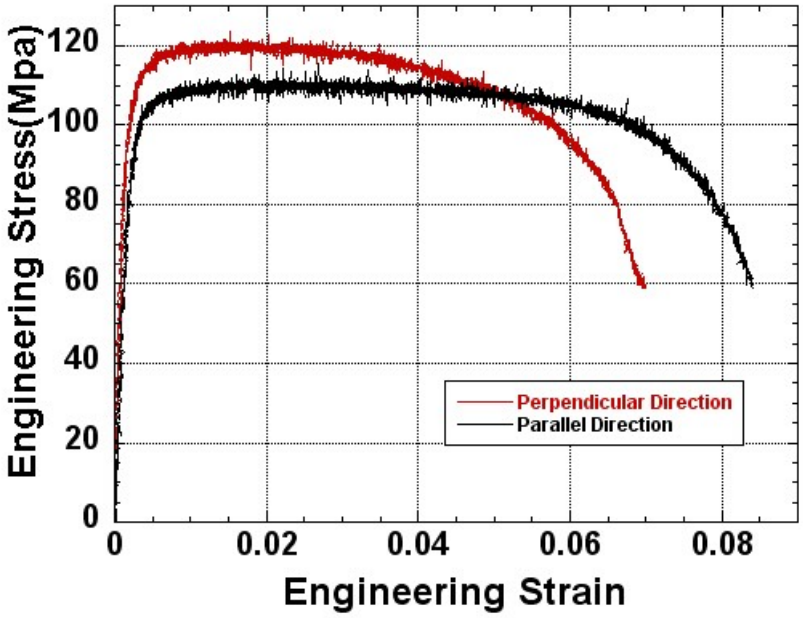

Figure 6.3.Tensile stress-strain curves of 1050H14 Al sheet material.

Table 6.3. Tensile mechanical properties of 1050H14 Al.

Direction	Young Modulus E (GPa)	Tangent Modulus E_t (MPa)	Yield Strength $\sigma_{0.2}$ (MPa)	Ultimate Strength σ_u (MPa)	Failure Strain (%)
Parallel	70	147	105	110	8.4
Perpendicular	70	117	117	123	7

6.3.Tension Test of Welded 1050H14 Al Base Crash Box Material

The stress-strain curve of welded 1050H14 Al sample is shown in Figure 6.4(a) together with that of Al sample without welding for comparison. As is seen in Figure 6.4(a), the failure strain of the welded sample is relatively low, 3%. The yield strength ($\sigma_{0.2}$) and ultimate strength of the welded sample are 70 MPa and 82 MPa, respectively.

Figure 6.4(b) shows the picture of a fractured welded Al sample in tension. The sample fractures in the heat affected zone as shown in Figure 6.4(b).

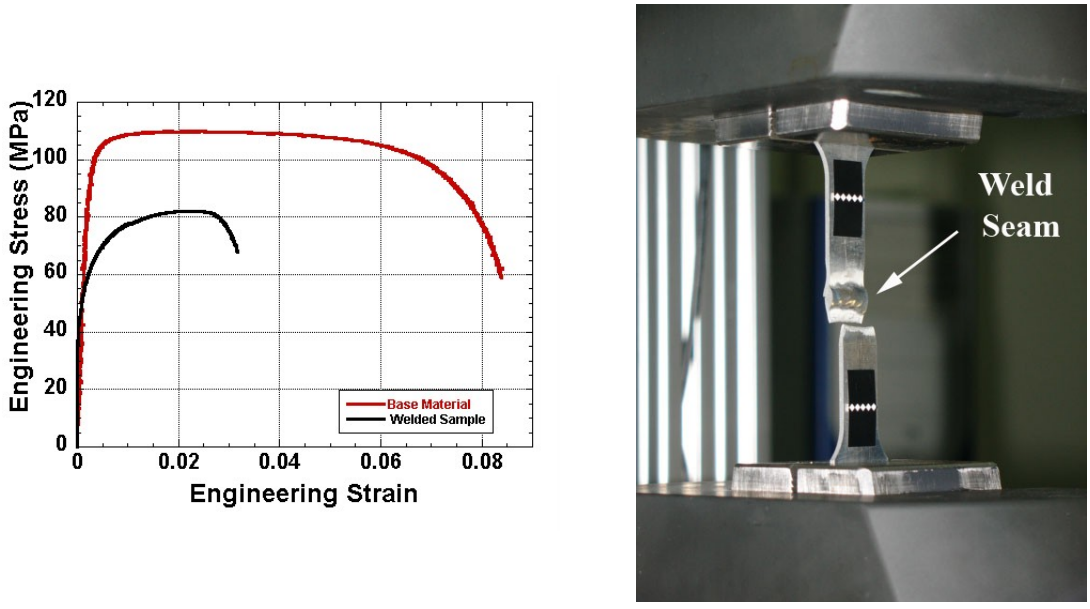

(a) (b)

Figure 6.4. (a) Tensile stress-strain curve of the welded 1050H14 Al and (b) the picture of a fractured welded Al specimen showing the failure in the heat affected zone.

6.4. Compression Testing of Commercial Crash Boxes

Figures 6.5 (a) and (b) are the deformation pictures of commercial Al and steel crash boxes at different displacements, respectively. In Al crash box, two folds form until 80 mm displacement (Figure 6.5(a)). However, in steel crash box only one fold forms until about the same displacement. The initial peak load values of both crash boxes are above 100 kN, and steel crash box shows slightly higher initial peak load values than Al crash box (110 kN) (Figure 6.6(a)). The mean load values at 50% deformation are 52 kN and 62 kN for Al and steel crash box, respectively. The SAE value of Al crash box is however higher than that of steel box, 13.1 kJ kg^{-1} for Al steel box and 5.2 kJ kg^{-1} for steel crash box at 50% deformation (Figure 6.6(b)).

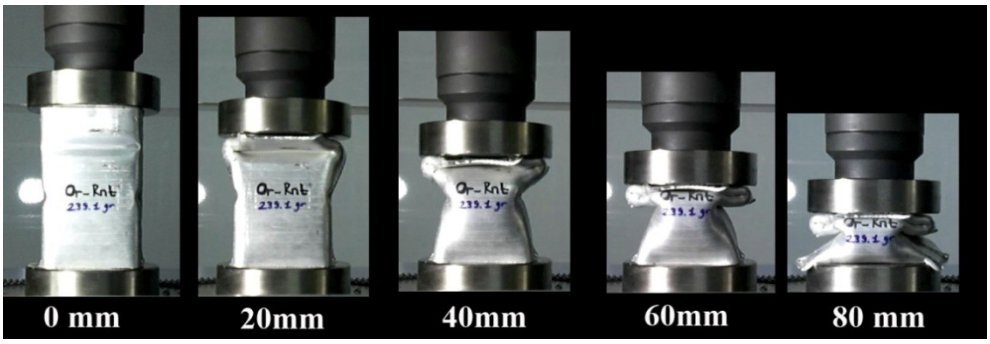

(a)

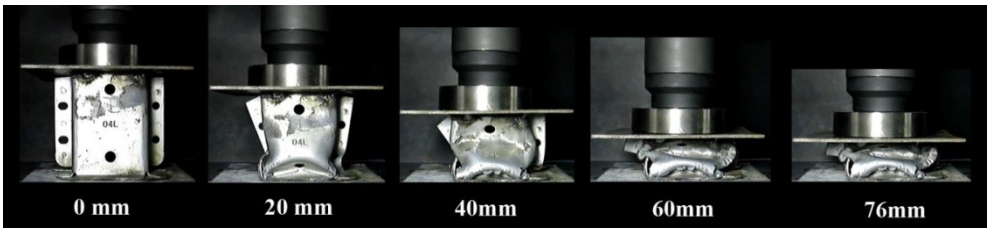

(b)

Figure 6.5. Sequential deformation pictures of (a) Al crash box (Renault) and (b) steel crash box (Honda).

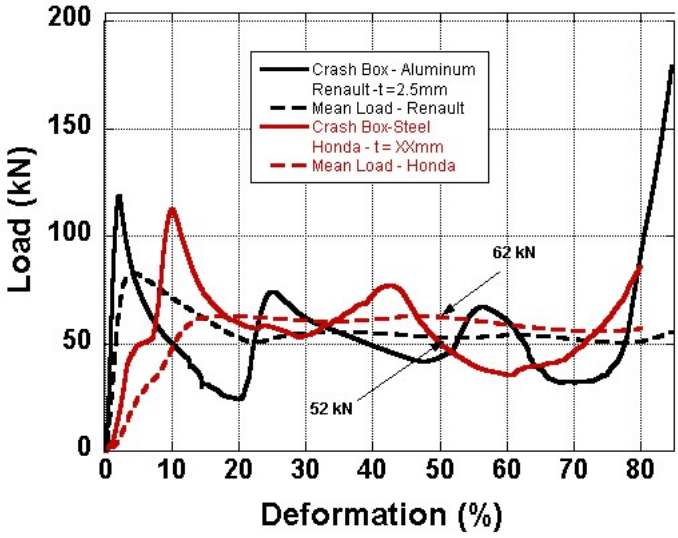

(a)

Figure 6.6. (a) load and b) SAE vs. deformation ratio (%) curves of commercial crash boxes.

(cont. on next page)

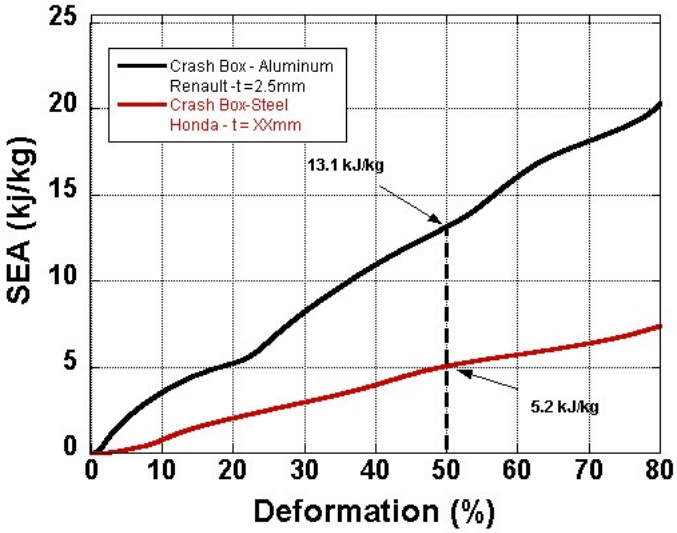

(b)

Figure 6.6.(Cont)

6.5. Quasi-static Testing of Empty and Al Foam Filled 1050Al Crash Boxes

6.5.1. Compression Tests of Empty Crash Box with and without Trigger Mechanism

The function of the trigger mechanism is to control the crash box deformation by initiating a controllable progressive energy efficient deformation in the crash box. In the present study, the trigger mechanisms are also used to position the Al foam filler in the middle of the crash box. Figures 6.7(a) and (b) show the sequential deformation pictures of G1T3E box (empty) without and with trigger, respectively. As is seen in Figures 6.7(a) and (b), the presence trigger on the empty box changes the initiation site of the folding. In empty box without trigger, the folding starts near the upper compression plate from the upper end of the box (Figure 6(a)), while in empty tubes with trigger folding starts from the trigger mechanism position just below the upper compression

plate (Figure 6(b)). The trigger is also found to affect the load and mean load values of empty boxes. Trigger decrease the initial peak and mean load values of empty boxes as shown in Figure 6.8. The initial peak and mean load values decrease from 93 kN and 38 kN (at 50% deformation) in boxes without trigger to 70 kN and 31 kN in boxes with trigger (Figure 6.8). It is also noted in Figure 6.8 that trigger induces a more uniform deformation behavior in empty box, by lowering the differences between peak and subsequent peak load values in load-displacement curve.

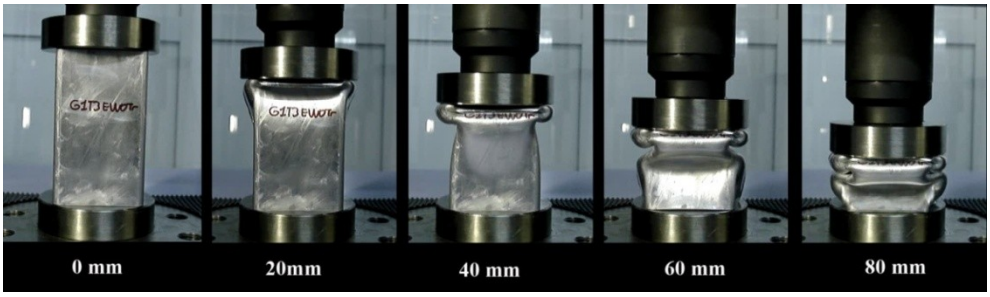

(a)

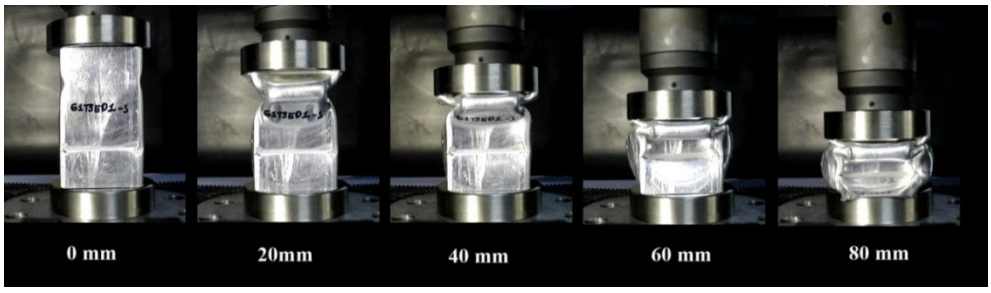

(b)

Figure 6.7. Deformation sequence pictures of G1T3E box (empty); a) without and b) with trigger mechanism.

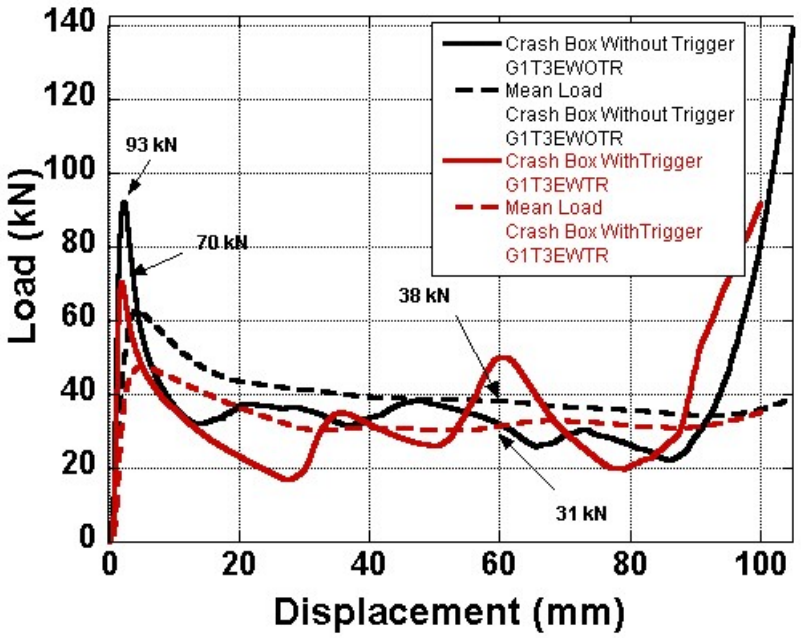

Figure 6.8. Load-displacement and mean load-displacement curves of G1T3E box (empty) with and without trigger mechanisms.

6.5.2. Compression of Empty Original Crash Box

The deformation pictures of corrugated and non-corrugated original crash box until about various displacements are shown in Figures 6.9(a) and (b), respectively. In terms of deformation mode, there seems to be no significant difference between corrugated and non-corrugated crash box and the folding starts from the fixed end of the box in both boxes. The initial peak load value of non-corrugated empty crash box is 77 kN, while this values decreases to 64 kN in corrugated crash box as depicted in Figure 6.10. Corrugation although lowers the initial peak load value, it increases the values subsequent peak load and load values. At 50% deformation, the mean load value of the box with corrugation, 39.1 kN, becomes almost equal to that of box without corrugation, 40.5 kN.

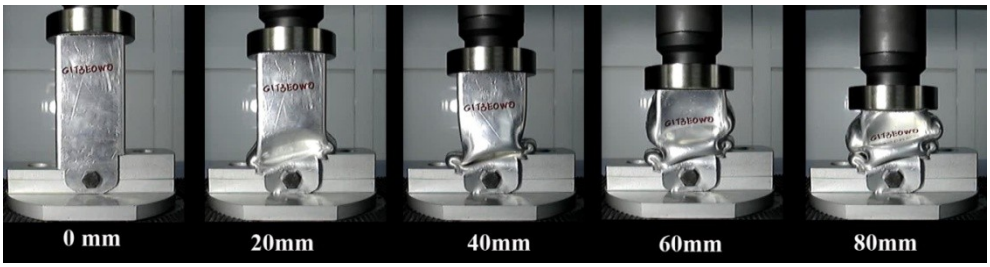

(a)

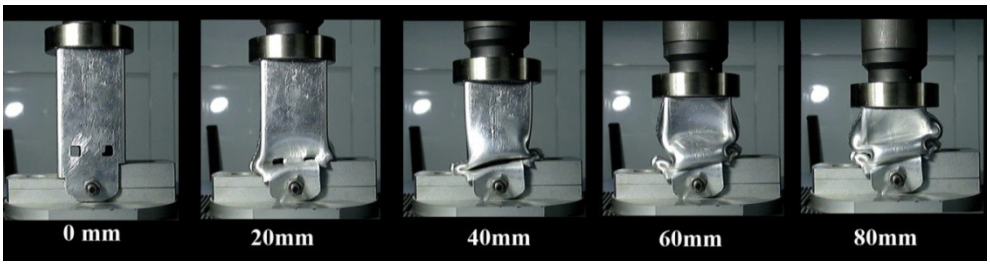

(b)

Figure 6.9. Deformation sequence pictures of fixed crash box a) without and b) with corrugation.

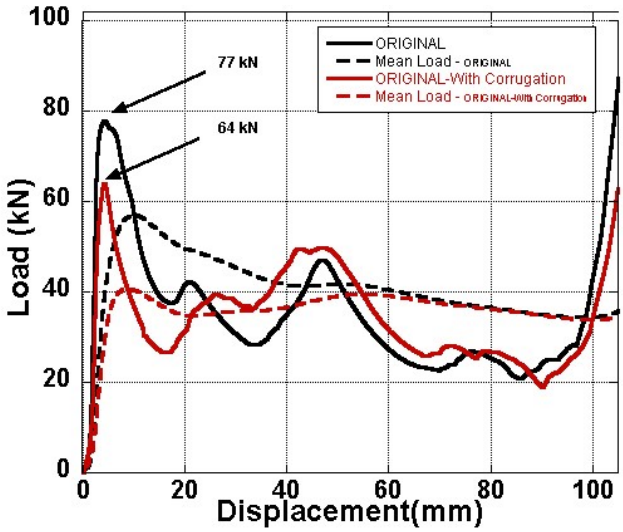

Figure 6.10. Load-displacement and mean load-displacement curves of crash boxes with and without corrugation.

Figure 6.11 shows the variation of load and mean load values of the box with and without fixing part as function of displacement. The fixing part is noted to act as a trigger, lowering the initial peak load value. The initial peak load decreases from 93 kN in empty box without fixing part to 77 kN in empty box with fixing part. The effect of

fixing part on the mean load values is however noted to be not significant in Figure 6.11.

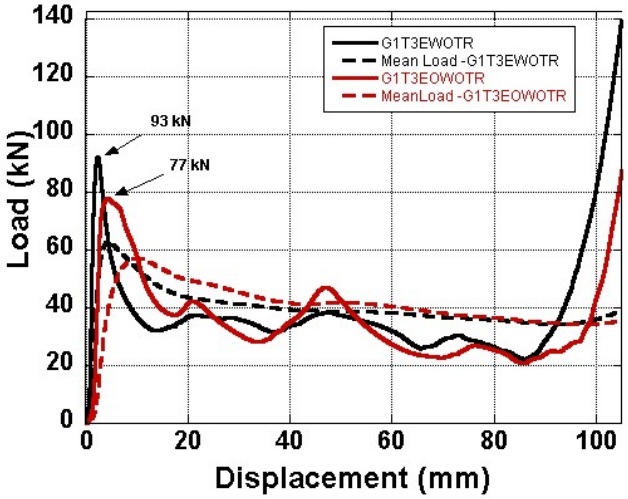

Figure 6. 11. Load-displacement and mean load-displacement curves of crash box with and without fixing part.

6.5.3. Compression Tests of Empty and Partially Foam Filled Crash Box without Montage Parts

The sequential deformation pictures of empty, F1 and F2 foam filled G1 tubes of 3, 2.5 and 2 mm wall thickness are shown in Figures 6.12-6.14, respectively. The sequential deformation pictures of empty, F1 and F2 foam filled G2 tubes of 3, 2.5 and 2 mm wall thickness are further shown in Figures 6.15-6.17, respectively. In all empty crash boxes tested, two regular symmetric folds are seen, while in all partially filled boxes three folds form (Figures 6.12-16). In filled boxes, the fold formation is observed to change from regular to irregular as the box thickness decreases. Irregular folding forms particularly in high relative density foam filled boxes, Figures 6.13, 6.15 and 6.16.

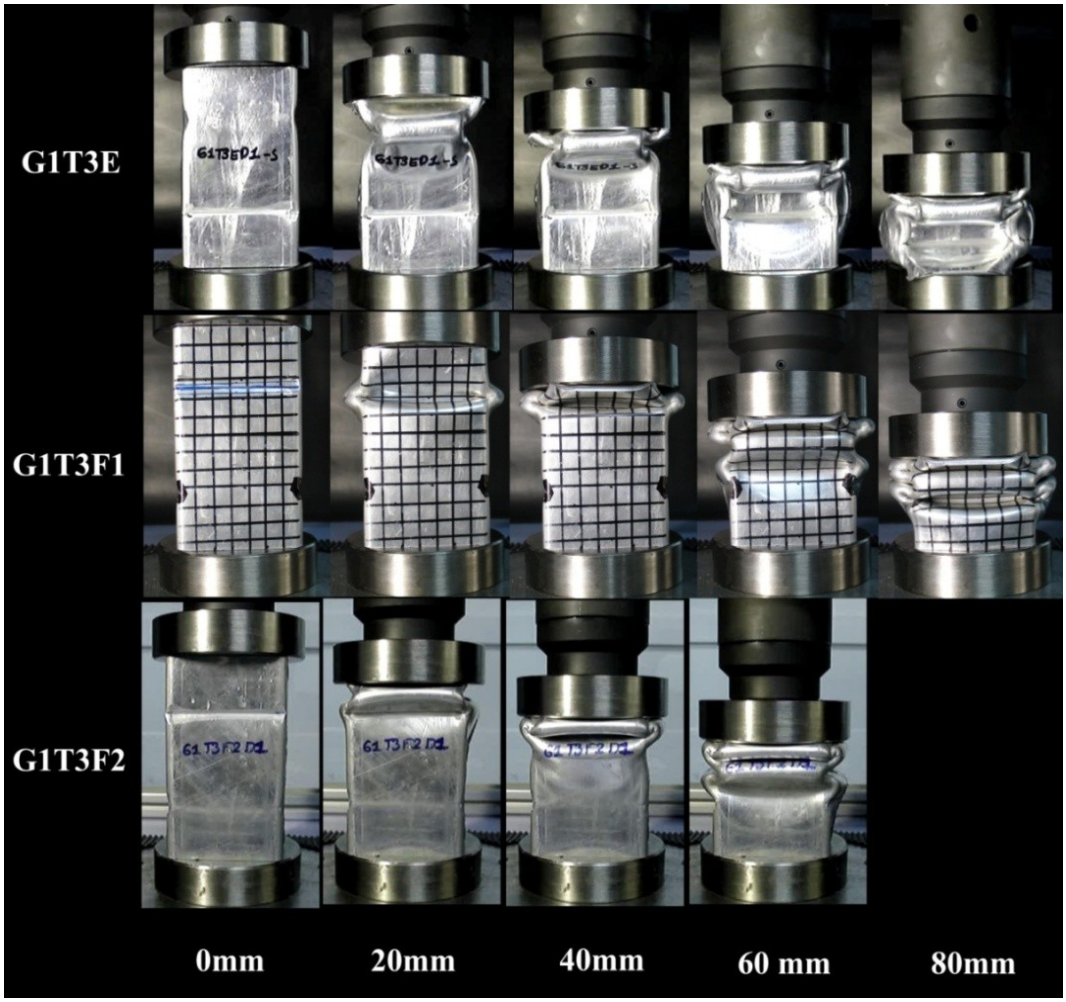

Figure 6.12. Sequential deformation photos of empty and foam filled G1 geometry crash boxes with 3 mm thickness.

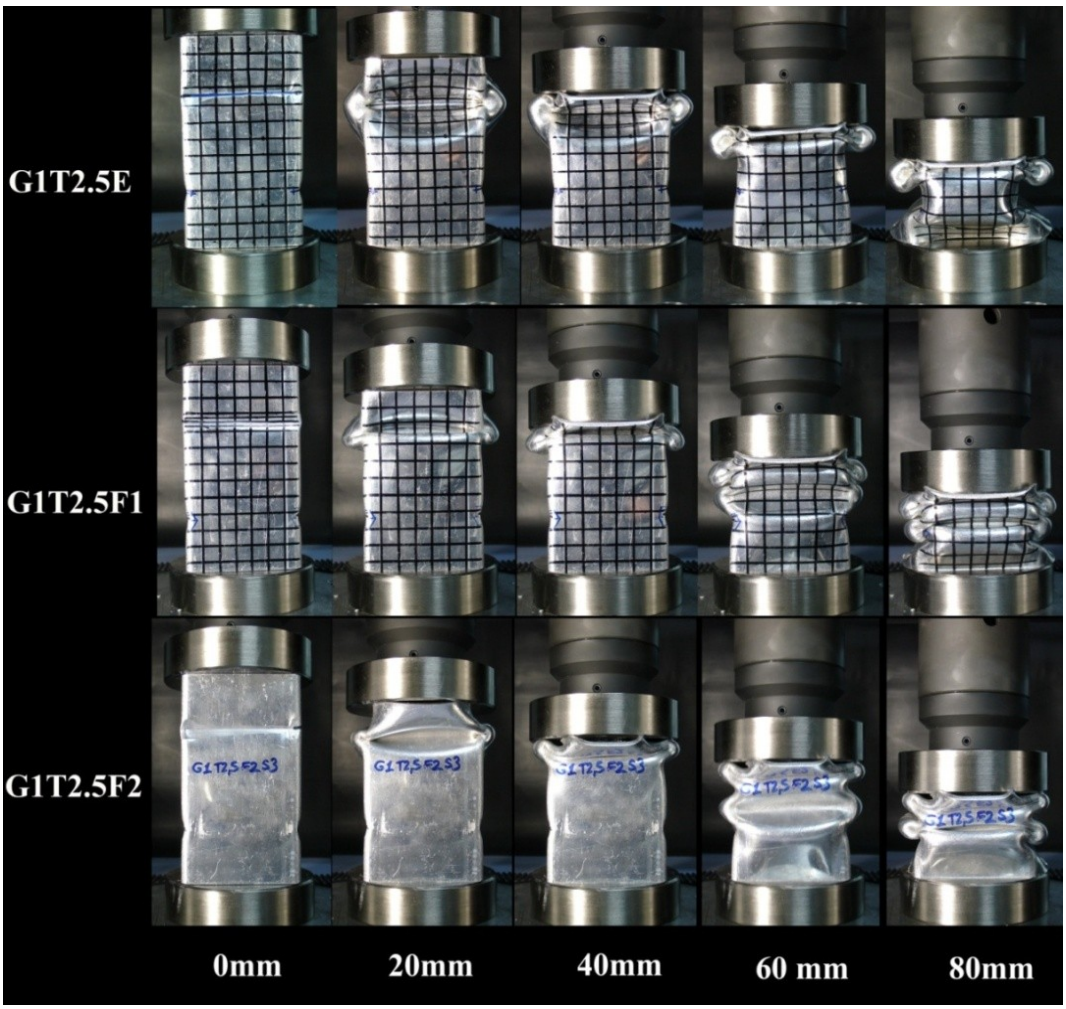

Figure 6.13. Sequential deformation photos of empty and foam filled G1 geometry crash boxes with 2.5 mm thickness.

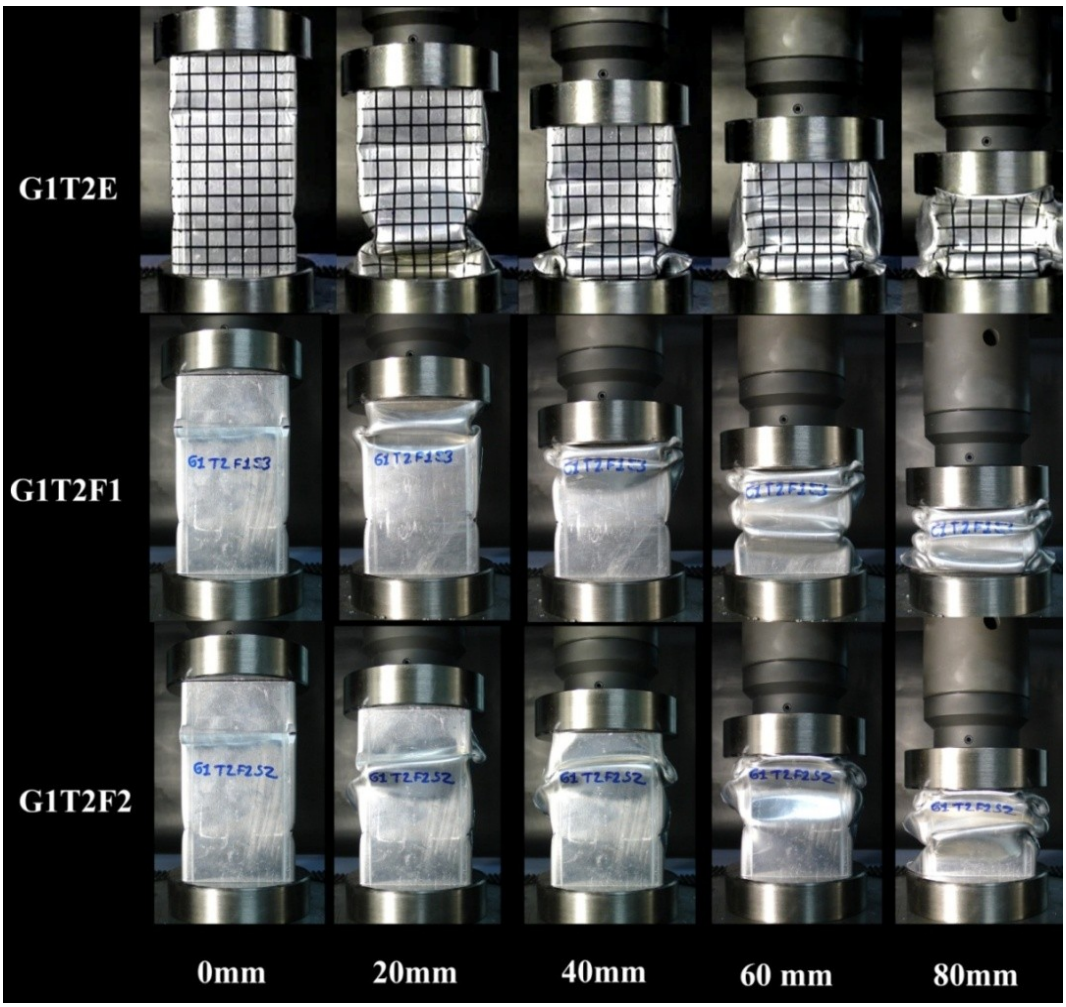

Figure 6.14. Sequential deformation photos of empty and foam filled G1 geometry crash boxes with 2 mm thickness.

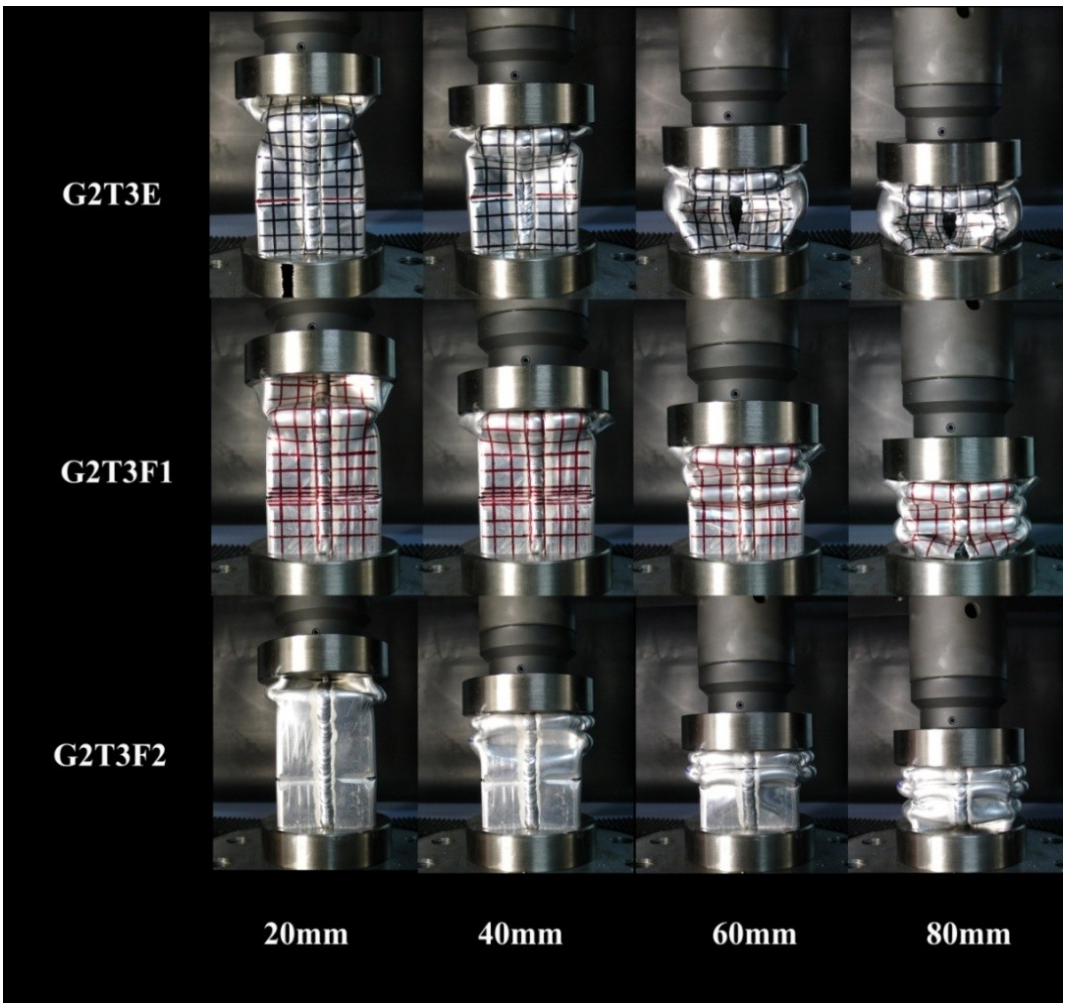

Figure 6.15. Sequential deformation photos of empty and foam filled G2 geometry crash boxes with 3 mm thickness

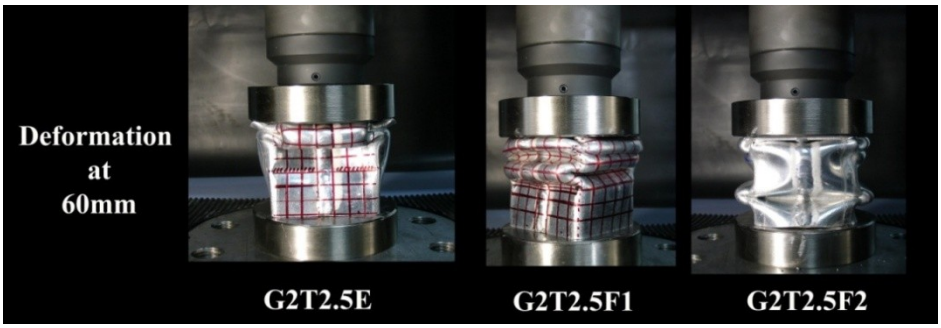

Figure 6.16. Sequential deformation photos of empty and foam filled G2 geometry crash boxes with 2.5 mm thickness at 60 mm deformation.

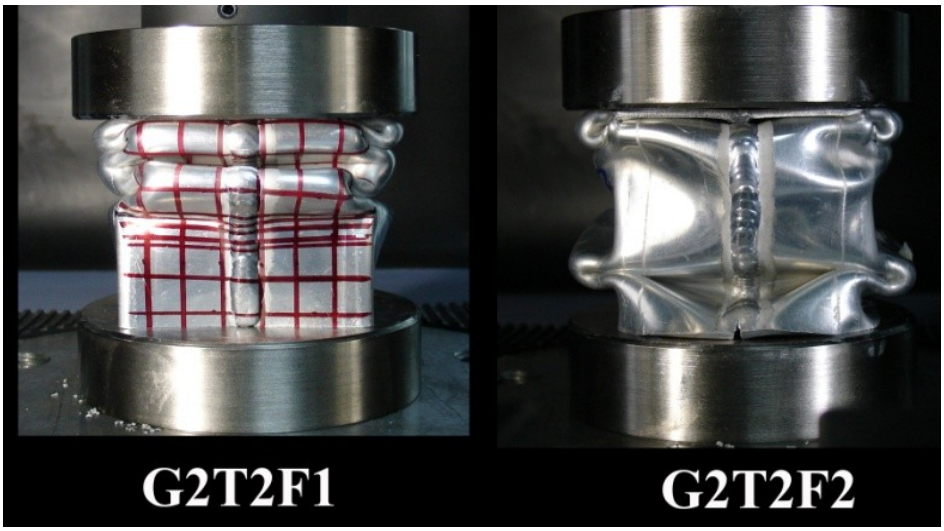

Figure 6.17. Sequential deformation photos of foam filled crash G2 geometry boxes with 2mm thickness at 60 mm deformation.

The load, mean load and SEA vs. displacement graphs for G1 and G2 box geometries are shown in Figures 6.18, 6.19 and 6.20, respectively. Partially filled 1050 H14 Al crash boxes show similar load values with empty boxes approximately up to 20 mm displacement (Figure 7.18). As seen in the same figure, the load values of filled tubes of different foam filler densities are also very close to each other. At larger deformations, above 20 mm, the load values of filled boxes start to increase rapidly over those of empty boxes. Increasing foam relative density in filled box also increases the load values as shown in Figure 6.18. The mean load values of filled boxes are also noted to be higher than that of empty boxes, while the boxes filled with higher foam density show higher mean load values as shown in Figure 6.19. The SEA values of filled crash boxes are similar to those of empty crash boxes between 20 and 40 mm

deformation in both geometries, Figure 6.20. However, the SEA values of filled boxes increase over those empty boxes after about 40 mm displacement. At 50% deformation the partially filled 1050 H14 Al crash boxes show clearly higher SEA values than empty crash boxes, except 2 mm thick G2 geometry, Figure 6.20 (c).

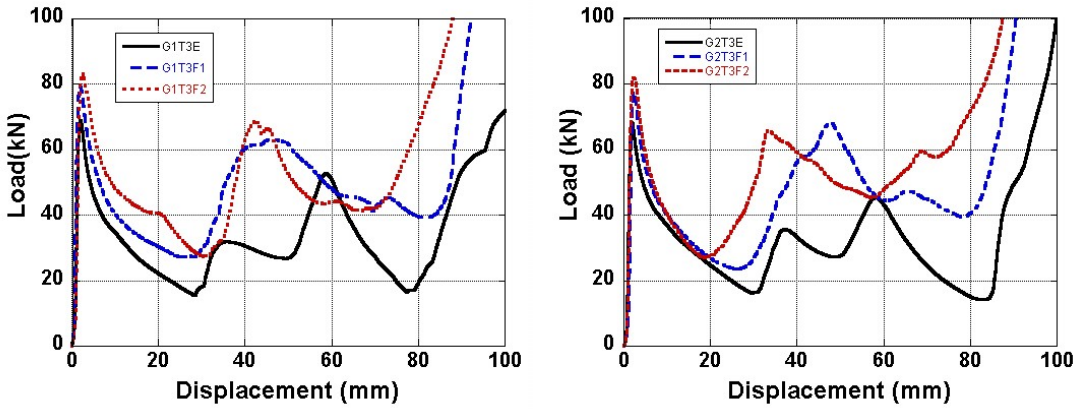

(a)

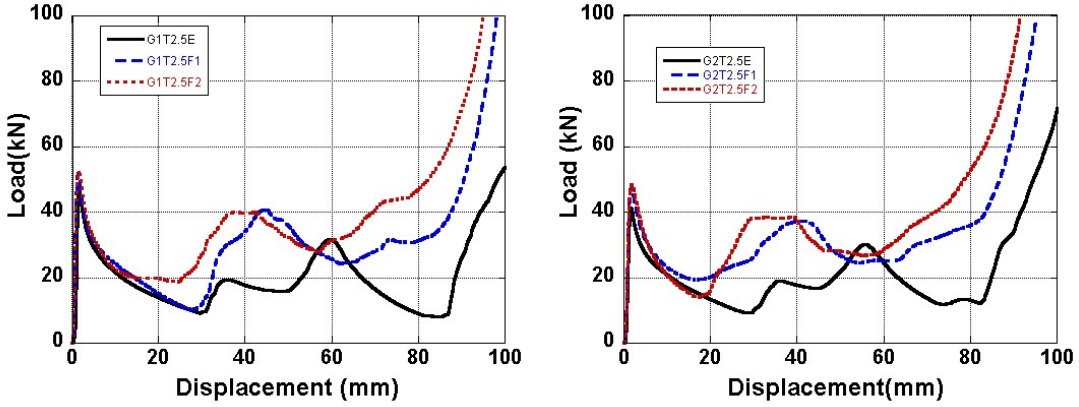

(b)

Figure 6.18. Load-displacement graphs of crash box with Geometry of G1 and G2 a) 3 mm thickness, b) 2.5 mm thickness and c) 2 mm thickness.

(cont. on next page)

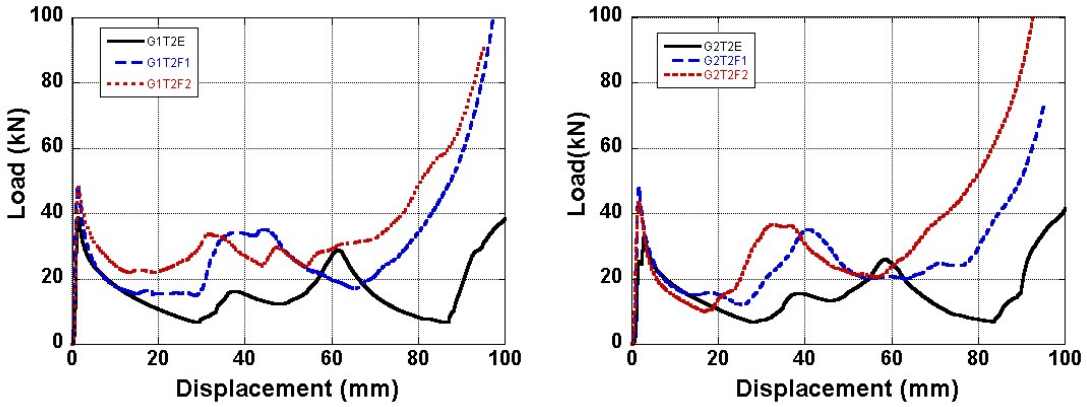

(c)

Figure 6.18. (cont.)

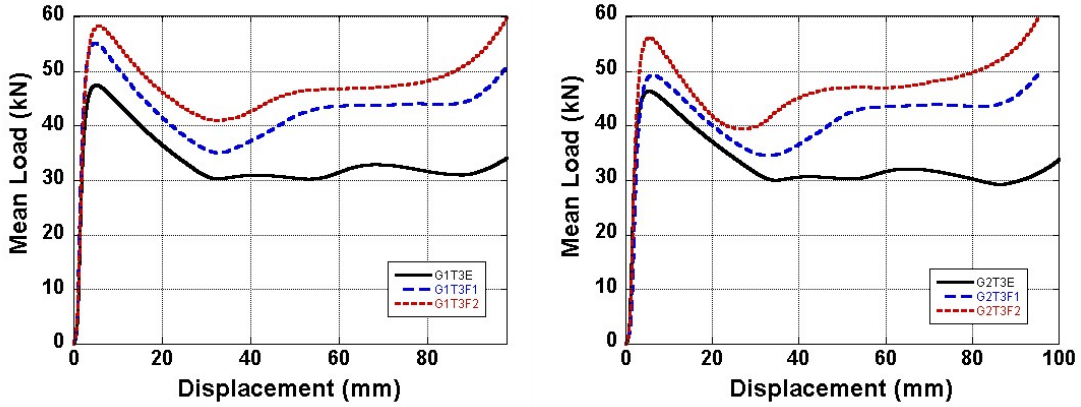

(a)

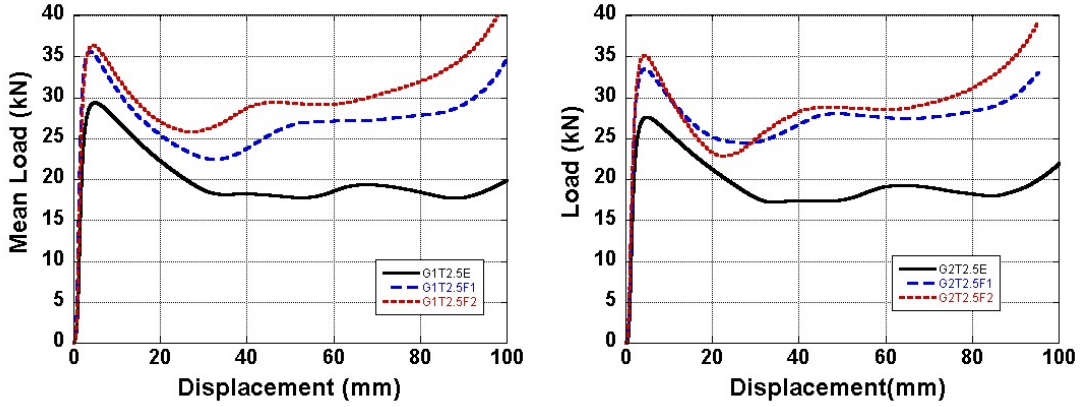

(b)

Figure 6.19. Mean load -displacement graphs of crash box with Geometry of G1 and G2 a) 3 mm thickness, b) 2.5 mm thickness and c) 2 mm thickness.

(cont. on next page)

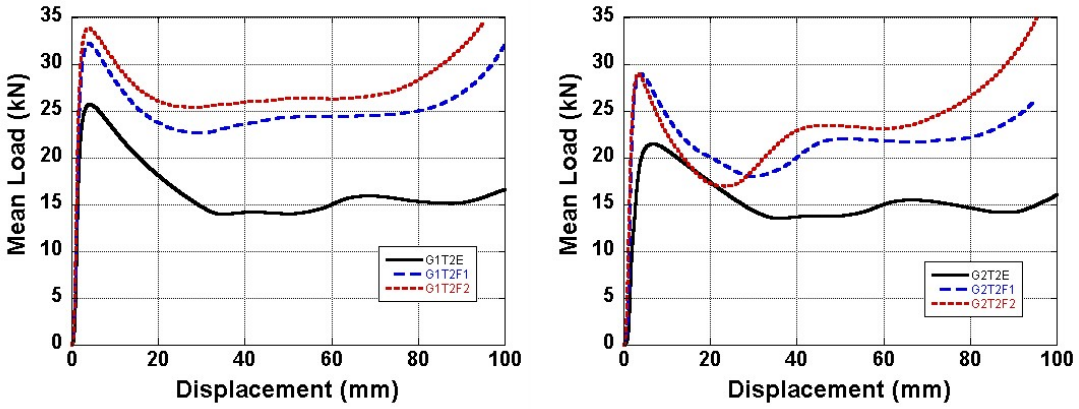

(c)

Figure 6.19.(cont.)

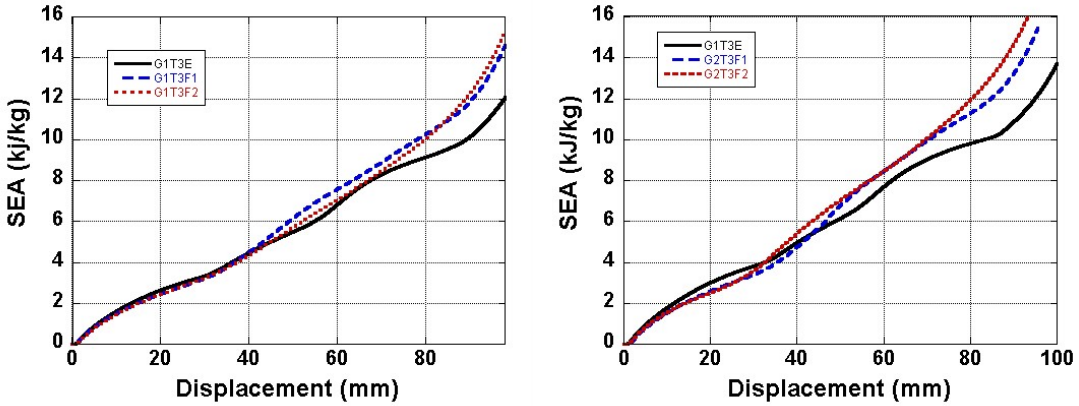

(a)

Figure 6.20. SEA vs. displacement graphs of crash box with Geometry of G1 and G2, a) 3 mm thickness, b) 2.5 mm thickness and c) 2mm thickness.

(cont. on next page)

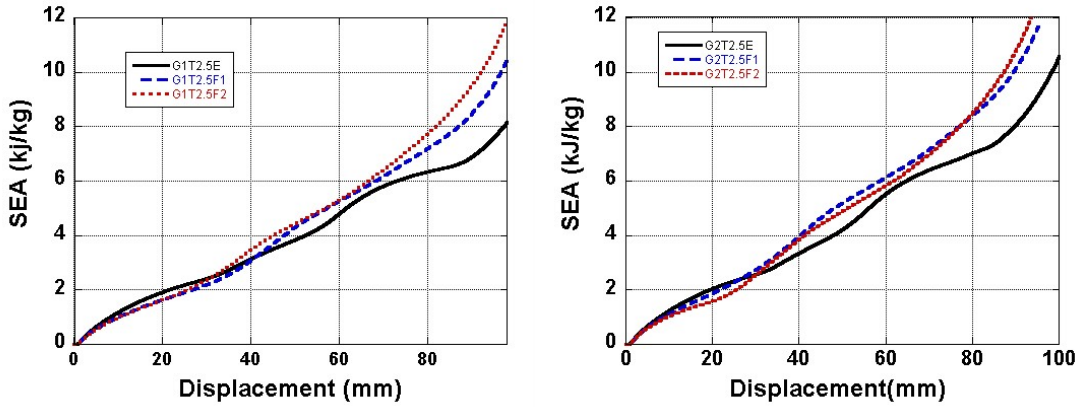

(b)

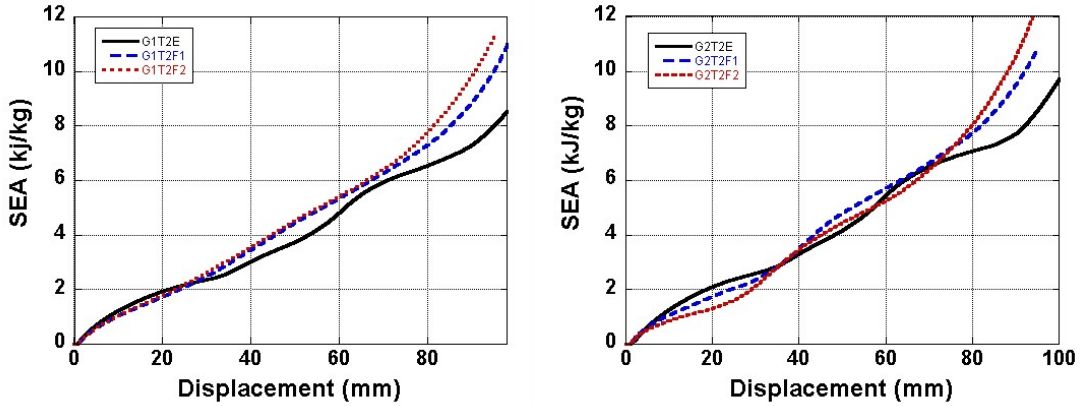

(c)

Figure 6.20.(cont.).

6.5.4. Uniaxial Compression Testing of Empty and Partially Foam Filled Crash Box with Montage Parts

The sequential deformation pictures of empty, F1 and F2 foam filled G1 and G2 tubes with montage parts (3, 2.5 and 2 mm wall thickness) are shown in Figures 6.21 and 6.22, respectively. As seen in the fallowing figures, the folding starts from the corrugated sections in all tube thicknesses and geometries. In 3 mm thick filled G1 boxes, the folding progresses through the filled section of the box following the folding of the corrugated section, while in other filled boxes, the other end of the boxes (empty) deform before the folding progresses into filled section. In both variations of empty

crash boxes, totally two folds form. The cross-section pictures of deformed empty and filled 3 mm thick 1050 H14 Al G1 geometry with montage parts are shown in Figure 6.23 together for comparison. As is seen in the same figure, the foam filler does not completely but partially enter in between the folds. However, the foam filling as shown in the same figure, increases the number of folds to 3.

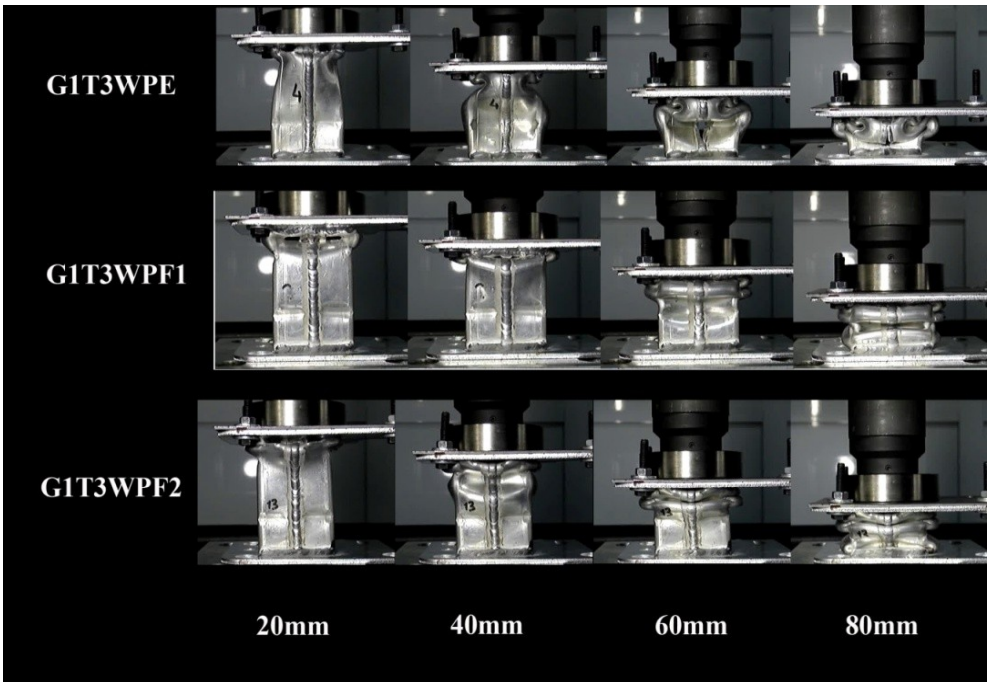

(a)

Figure 6.21. Sequential deformation pictures of empty and foam filled G1 geometry crash boxes: a) 3 mm thickness, b) 2.5 mm thickness and c) 2 mm thickness.

(cont. on next page)

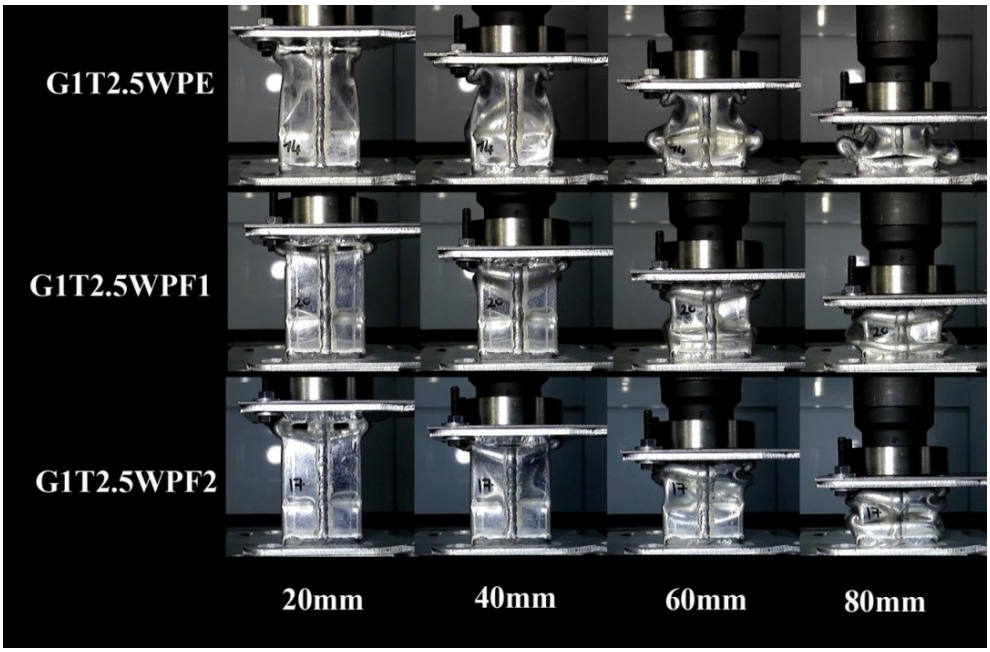

(b)

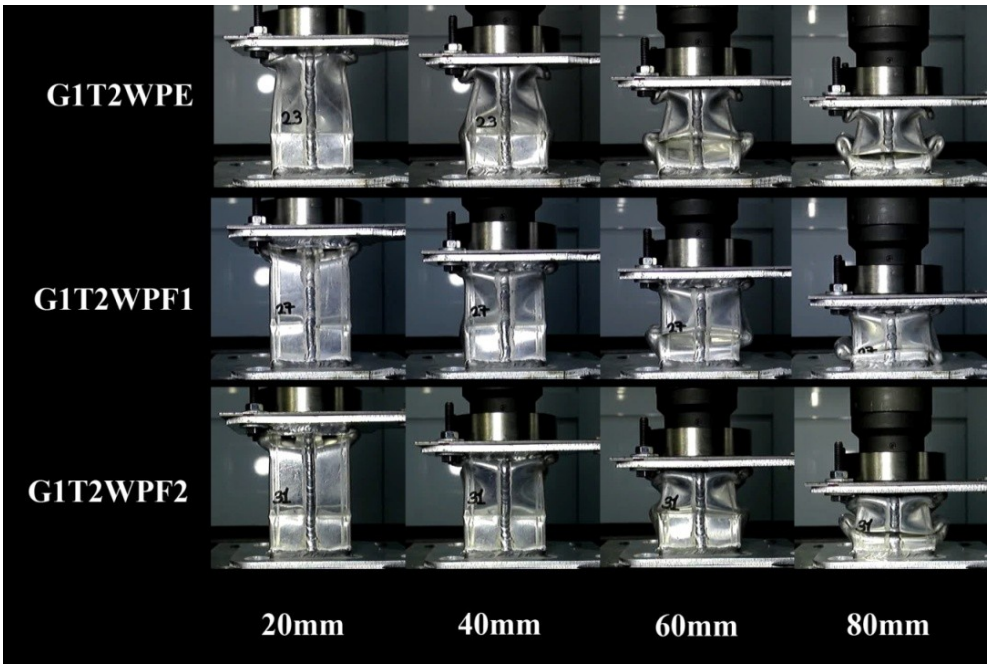

(c)

Figure 6.21.(cont.)

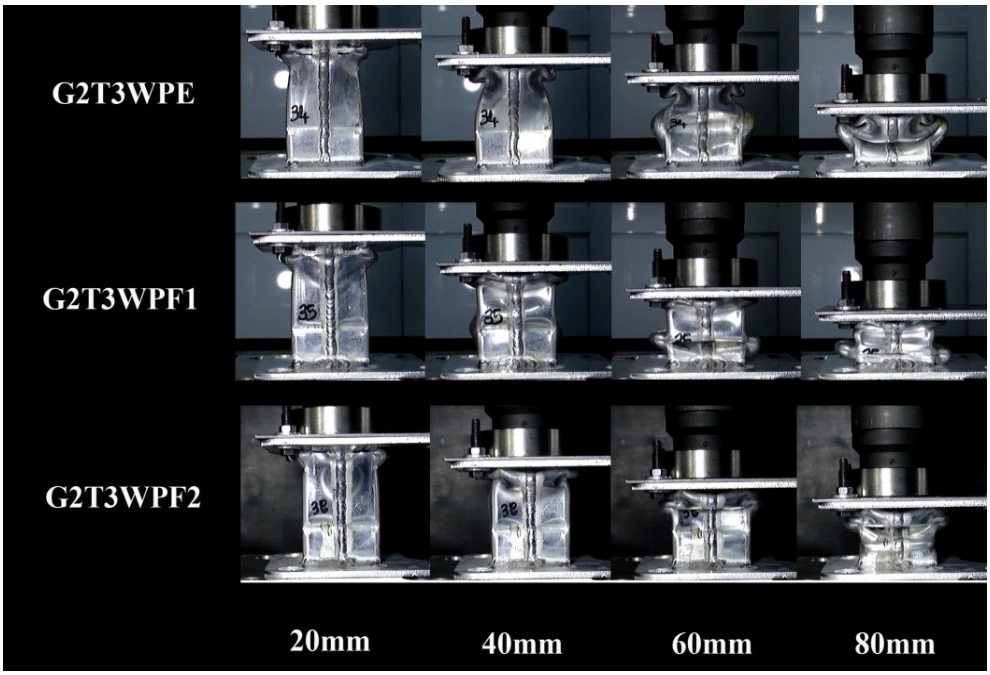

(a)

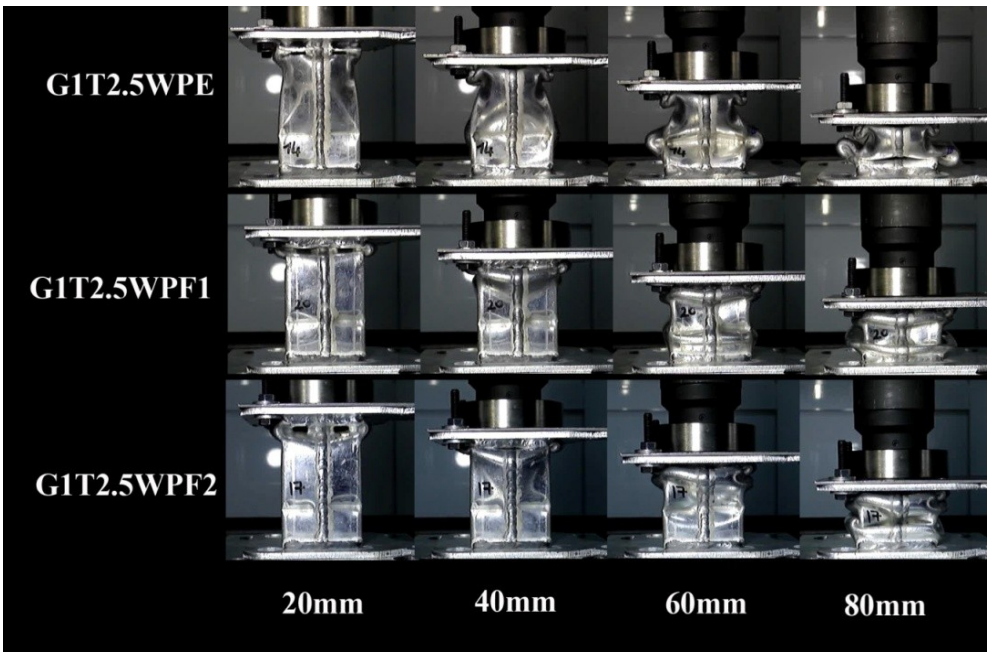

(b)

Figure 6.22. Sequential deformation pictures of empty and foam filled G2 geometry crash boxes: a) 3 mm thickness, b) 2.5 mm thickness and c) 2mm thickness.

(cont. on next page)

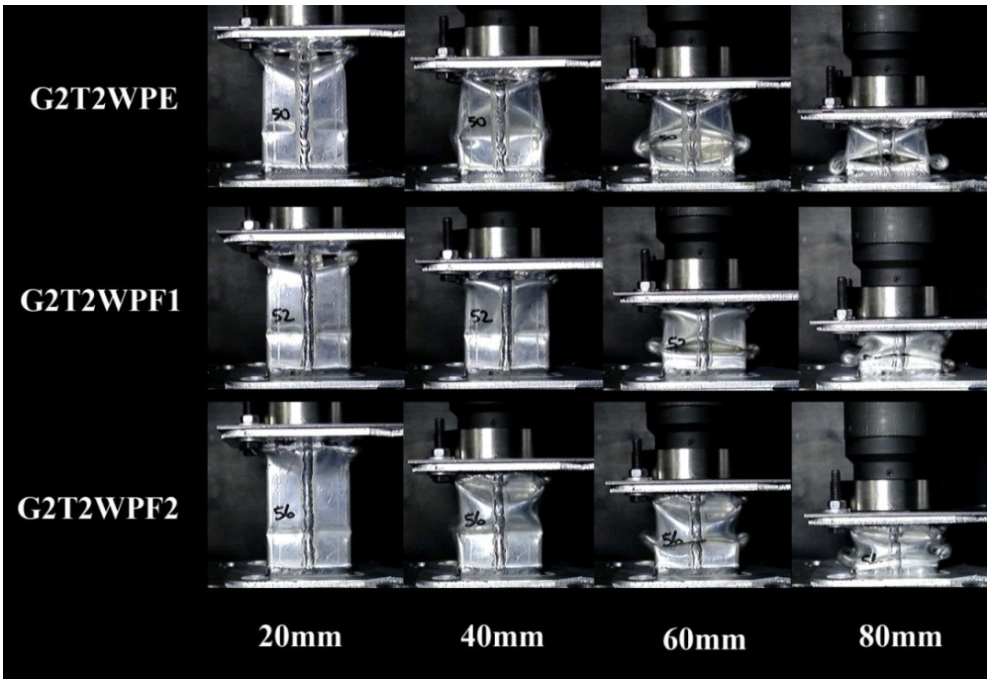

(c)

Figure 6.22.(cont.)

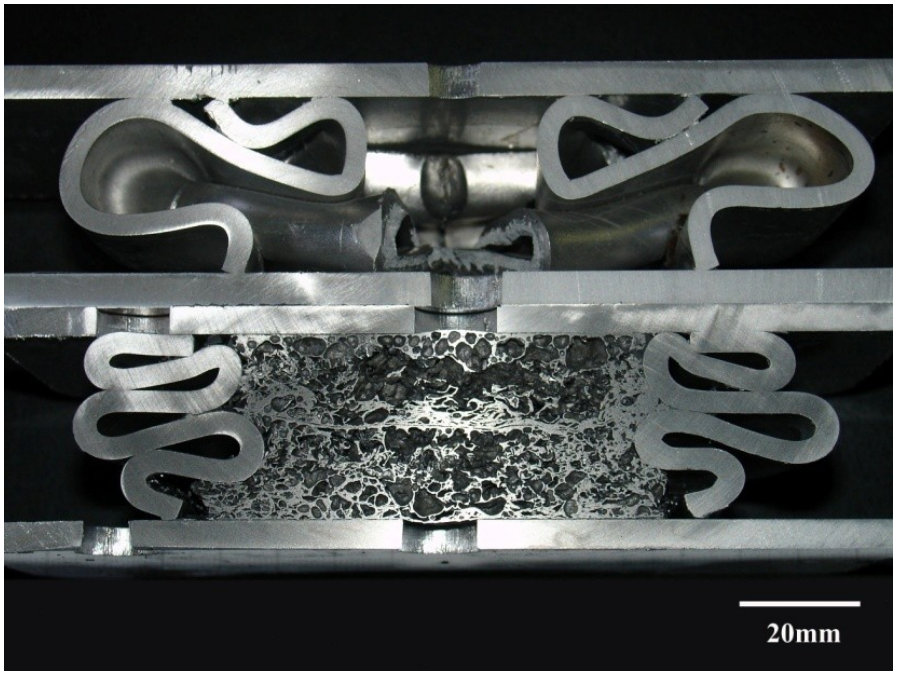

Figure 6.23. Cross-section pictures of deformed empty and F1 foam filled 1050 H14 G1 box with montage parts, t=3 mm.

Load–displacement and mean load-displacement curves of empty and G1 and G2 filled crash boxes are shown in Figures 6.24 and 6.25, respectively. It is seen in Figure 6.24 that foam filling has almost no effect on the deformation load until about the complete deformation of the corrugated section. Following the crushing of the corrugated section, partially filled crash boxes with montage parts show higher deformation loads than empty boxes. Increasing the relative density of the foam filler slightly increases the deformation load values. Similar effects of foam filling are also seen on the mean load-displacement graphs of filled boxes, Figure 6.25. Similar to the crash boxes without montage parts, the SEA values of partially filled crash boxes are lower than those of empty box until about a critical displacement (Figure 6.26). The critical displacement for both geometries is found to depend on the box thickness. The critical displacement for SEA becoming effective is about 45 mm in 3 mm thick crash box, 40 mm for 2.5 mm thick boxes and 60 mm for 2 mm thick boxes. It is further noted that the effective SEA range for boxes with montage parts is narrower than the boxes without montage parts.

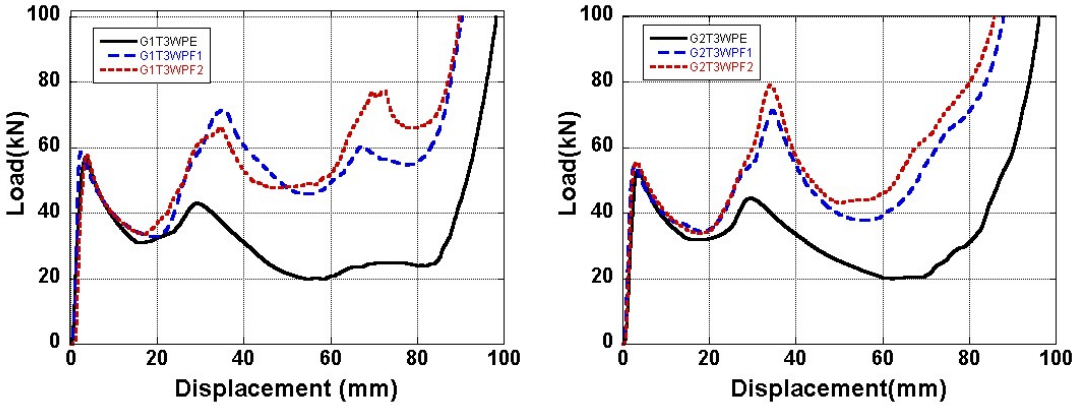

(a)

Figure 6.24. Load-displacement graphs of G1 and G2 empty and filled crash boxes with a) 3 mm, b) 2.5 mm and c) 2 mm thickness.

(cont. on next page)

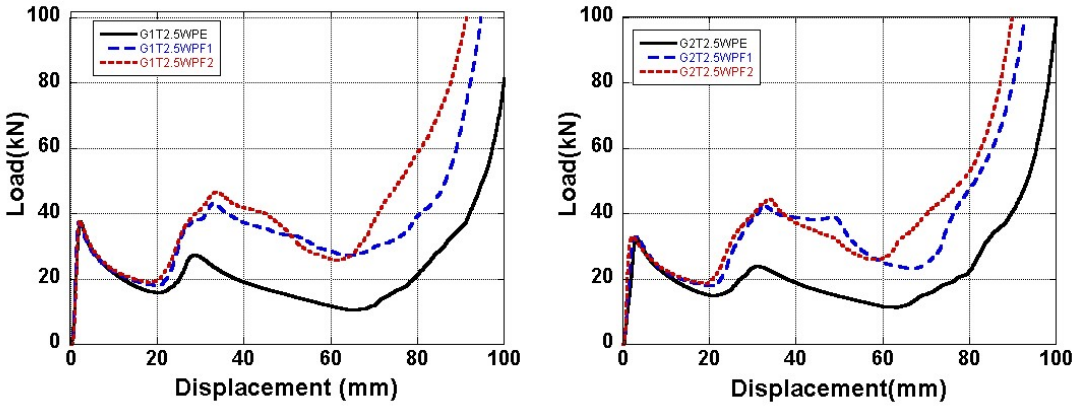

(b)

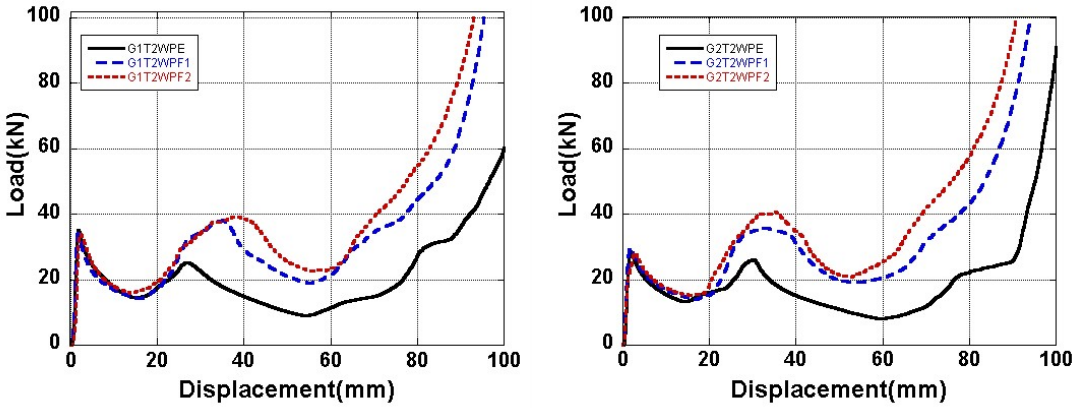

(c)

Figure 6.24.(Cont.)

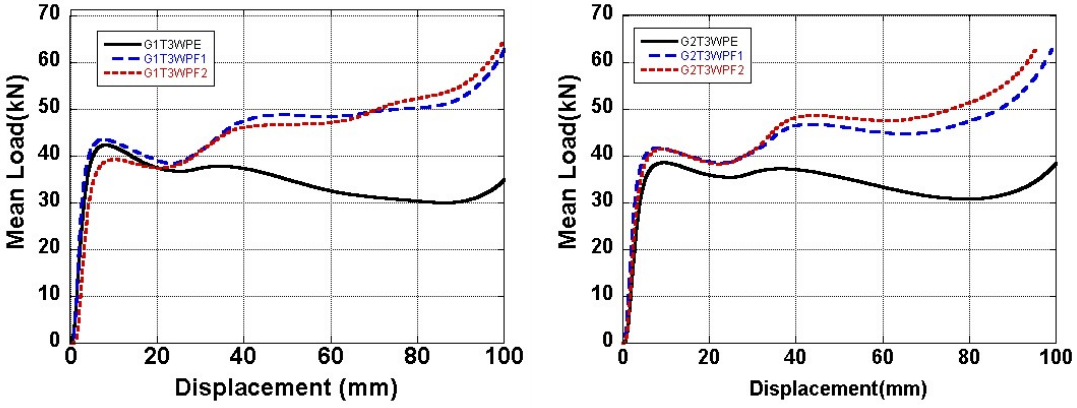

(a)

Figure 6.25. Mean load-displacement graphs of G1 and G2 empty and filled crash boxes with a) 3 mm, b) 2.5 mm and c) 2 mm thickness.

(cont. on next page)

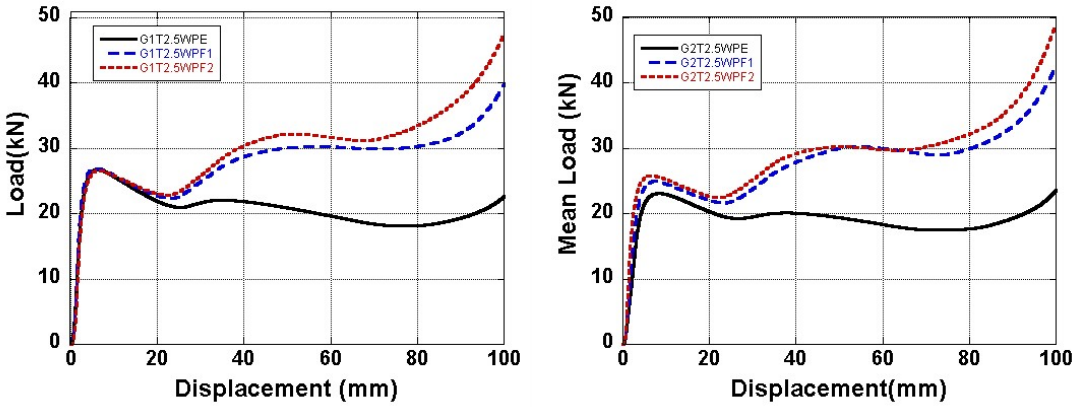

(b)

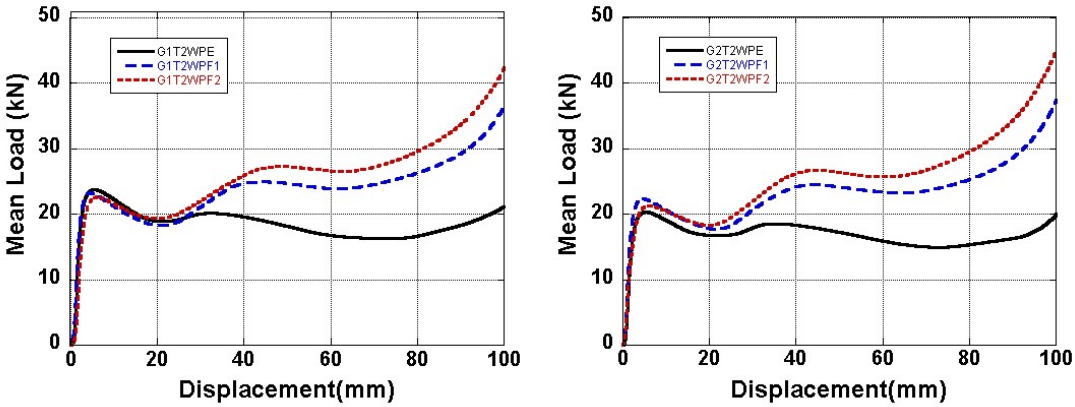

(c)

Figure 6.25.(cont.)

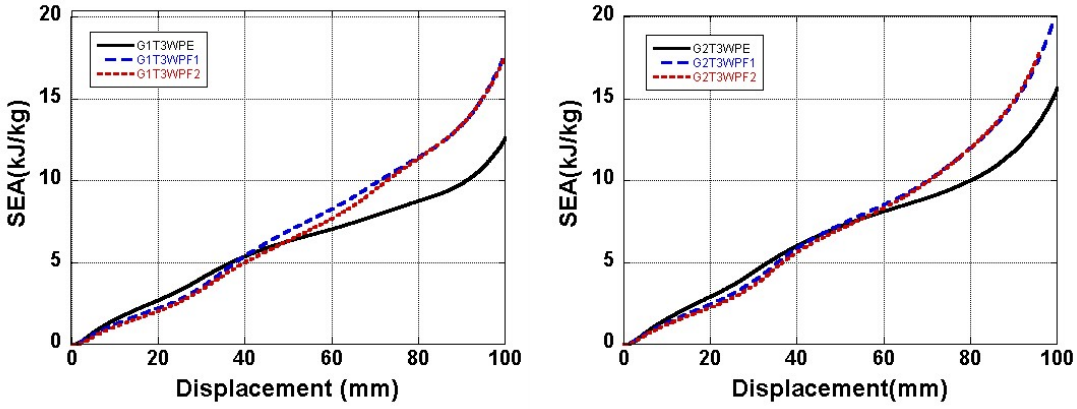

(a)

Figure 6.26. SEA-displacement graphs of G1 and G2 empty and filled crash boxes with montage parts a) 3 mm, b) 2.5 mm and c) 2 mm thickness.

(cont. on next page)

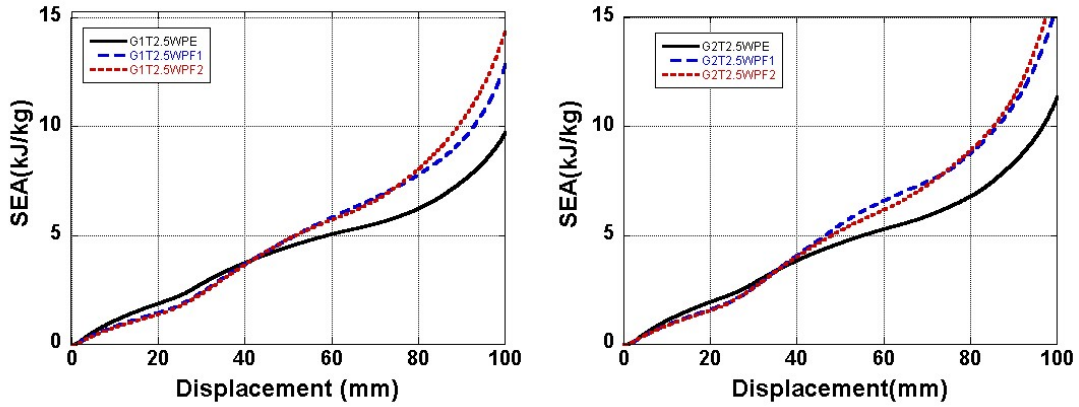

(b)

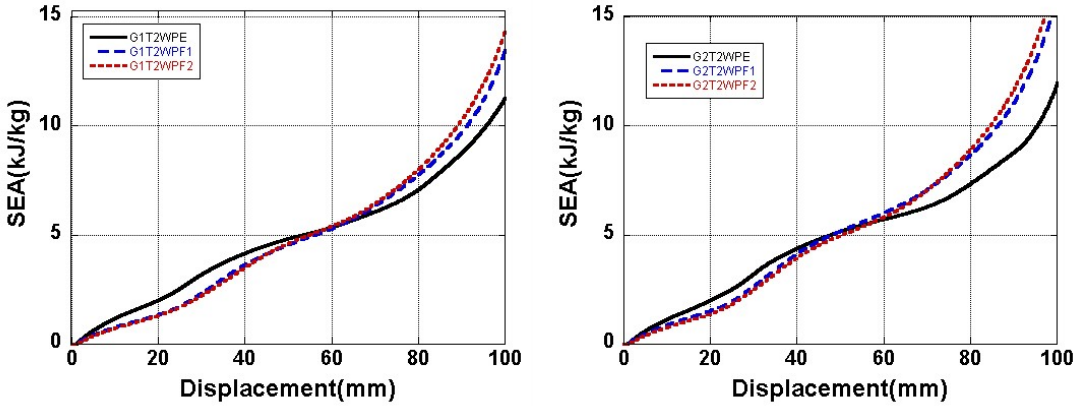

(c)

Figure 6.26.(cont.)

6.6.Dynamic Testing of Empty and Al Foam Filled 1050 Al Crash Boxes.

Empty and partially foam filled (relative density of 0.11) crash box samples with montage parts having 3 mm thickness were dynamically tested by reloading the same sample. The dynamic reloading load-displacement graphs of empty crash box are shown in Figure 6.27 (a). Because of reloading, an initial peak load is seen at beginning of each load-displacement curve as noted in the same figure. The dynamic load-displacement curves are constructed by extracting the initial part of the load-displacement curves corresponding the deformations after peak load. The reconstructed dynamic load-

displacement curve of empty tube is further shown in Figure 6.27(b) together with the quasi-static load-displacement curve. The procedure outlined above is also applied to the load-displacement curves of dynamically tested partially filled crash boxes (Figure 6.25 (c)). The initial peak load and mean load values (corresponding to 50% deformation) of quasi-statically and dynamically tested empty and filled box are tabulated in Table 6.4. As is noted in Table 6.24, although the initial load peak values of dynamically tested boxes are higher than those of quasi-statically tested boxes, the mean load values of dynamically and quasi-statically tested boxes are the almost the same in both empty and filled boxes. The deformation patterns of dynamically and quasi-statically tested empty and partially filled crash box are also found to be very similar as shown in Figure 6.28. It may be concluded that the dynamic testing has negligible effects on load values and the deformation pattern of empty and partially filled 1050H14 Al crash box.

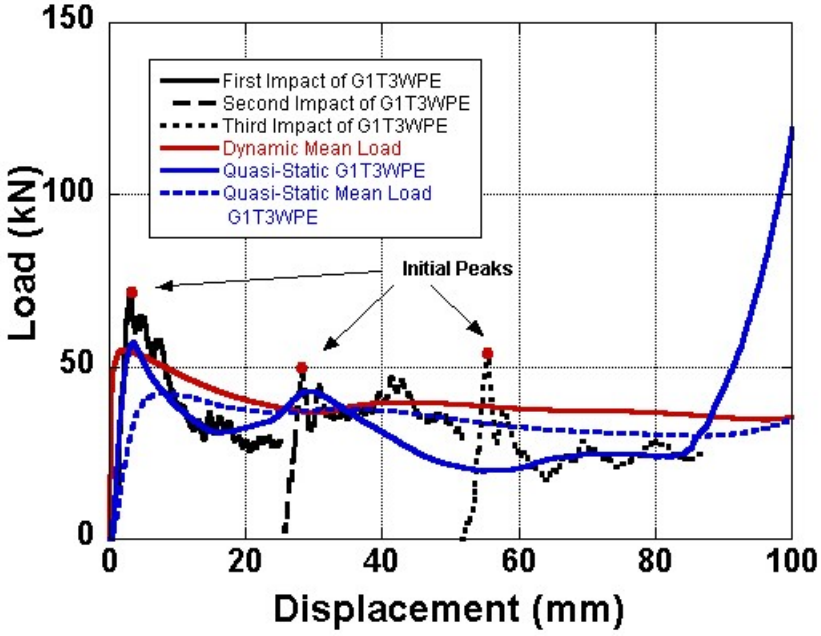

(a)

Figure 6.27. Load-displacement graphs of a) quasi-statically and dynamically tested empty crash box, b) load-displacement graphs of empty tube after reconstruction and c) load-displacement graphs of filled crash box after reconstruction.

(cont. on next page)

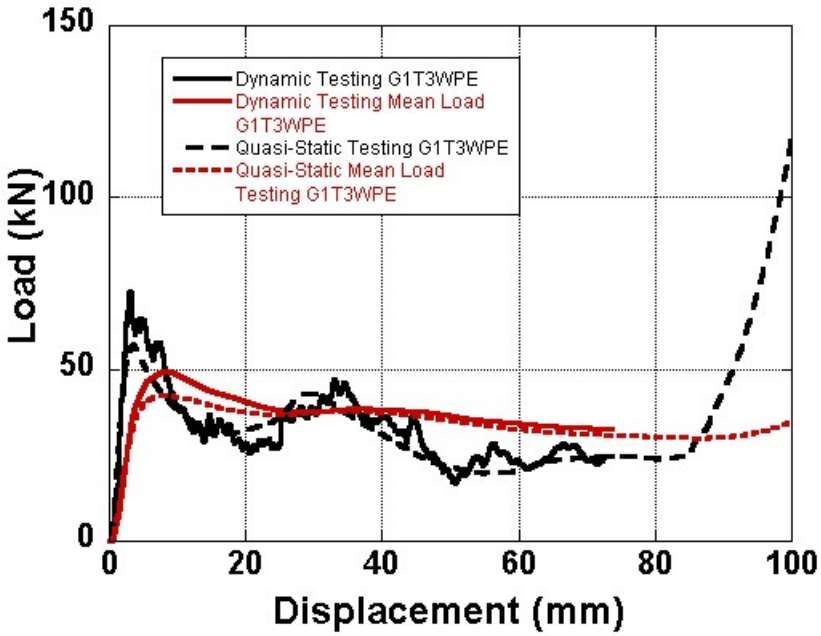

(b)

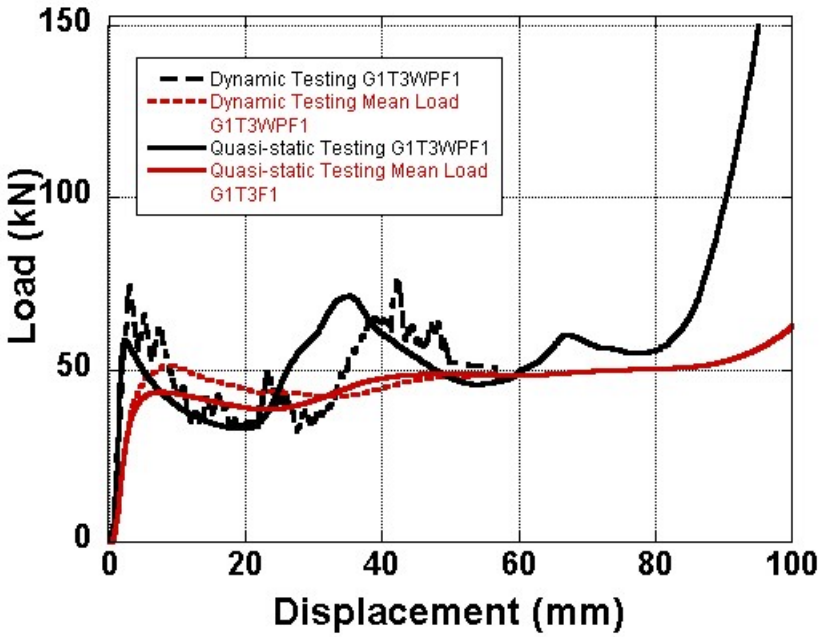

(c)

Figure 6.27. (cont.)

Table 6.4. Initial peak and mean load values of empty and filled crush box under quasi-static and dynamic loading.

Crash Box Configuration	Initial Peak Load (kN)		Mean Load at 50% Deformation (kN)	
	Quasi-static Loading	Dynamic Loading	Quasi-static Loading	Dynamic Loading
Empty G1T3WPE	58	72	32.14	33.81
Filled G1T3WPF1	59	73	48.54	48.76

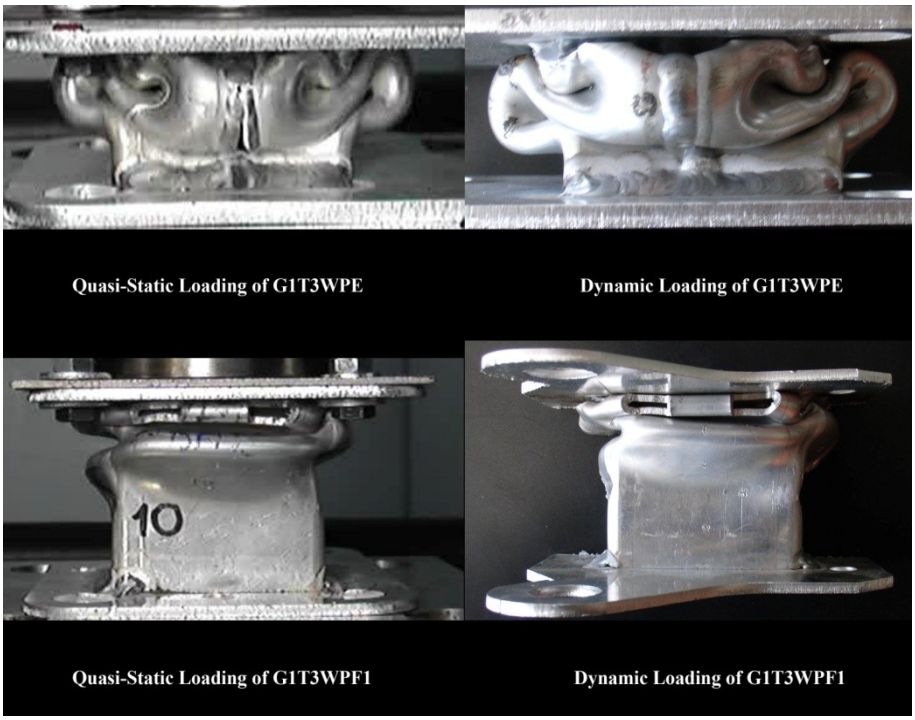

Figure.6.28. Deformation pattern of quasi-static and dynamically tested empty (G1T3WPE) and partially filled (G1T3WPF1) crash boxes.

CHAPTER 7

MODELING RESULTS OF FOAM, EMPTY AND AL FOAM FILLED CRASH BOX

7.1.Simulation Results of Al Foam Modeling

The simulation stress-strain curves of honeycomb material model (Mat26) and Desphande and Fleck Foam model (Mat154) are shown in Figure 7.1 together with the experimental stress-strain curves of 0.11 and 0.15 relative dense Alulight Al foams. Both material models stress-strain curves show good agreements with the experimental stress-strain curves, proving that both material cards are capable of simulating the deformation of partially filled crash boxes. Because of its simplicity of the implementation, Mat 26 Honeycomb material card is selected for the simulations of filled crash boxes. The Deshpande and Fleck analytical foam model parameters determined in Chapter 6 are used to construct the stress-strain curves of Alulight foams at various densities. For comparison, the experimental and Mat 26 simulation compression stress-strain curves of Alulight foams at various relative densities are shown together in Figure 7.2. The experimental foam stress-strain curves at varying relative densities shown in the same figure are well matched with the simulated stress-strain curves. This further proves the capability of the analytic model developed in predicting correct material stress-strain data for the simulations.

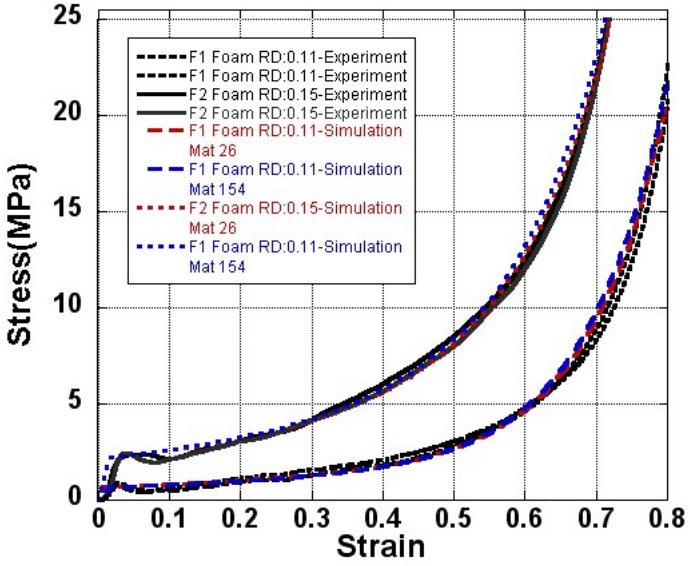

Figure 7.1. Experimental and simulation compression stress-strain curves of Alulight Al foam with relative densities of 0.11 and 0.15.

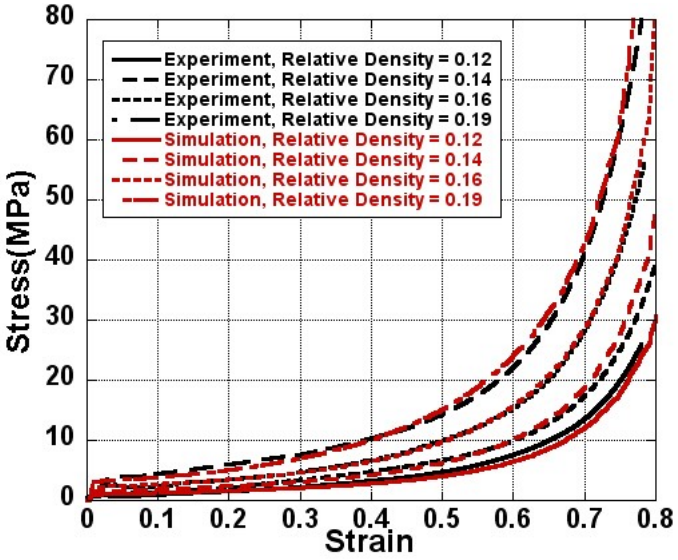

Figure 7.2. Experimental and Mat 26 Honeycomb foam model simulation compression stress-strain curves of Alulight Al foams at various relative densities.

7.2.Evaluation of the Material Models for 1050H14 Al Base Material

Two materials models namely plastic-kinematic material card (Mat 3) and piecewise linear plasticity material code (Mat 24) are implemented in LS-DYNA program for the tensile testing of the base material (Figure 7.3(a)) . The simulated and

experimental tensile stress-strain curves are shown together in Figure 7.3(b). Both models, as seen in Figure 7.3(b), adequately capture the elastic and plastic deformation regions of the experimental tensile stress-strain curve of 1050 H14 Al base material. The models cannot however correctly predict the stress values of the base material in the regions following the ultimate tensile strength, depicted in Figure 7.3(b). A ductile failure mode with the well known necking phenomenon is seen in the experimentally tested samples (Figure 7.3(a)). The shear plane cracking observed in experimental tensile test is however not observed in the simulations with both material models (Figure 7.3(a)). A similar observation was previously reported in the tensile testing simulation of a similar Al alloy (Lademo, et al. 2008). The deformation of crash boxes was however simulated in this thesis using Mat 3 card, as Mat 3 card uses shorter calculation times than Mat 24 card.

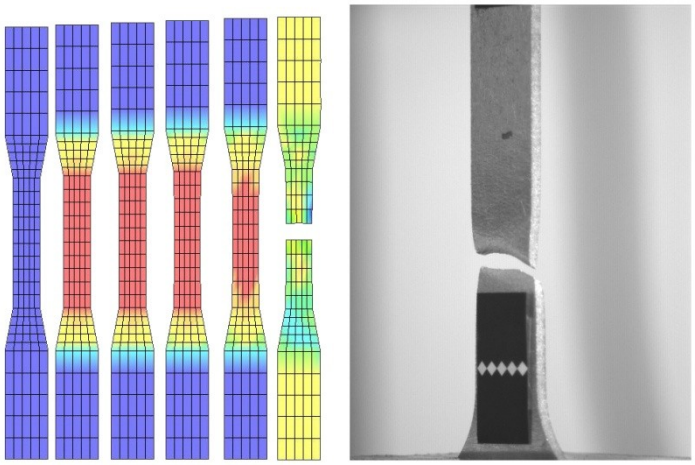

(a)

Figure 7.3. The deformation pictures of numerically tensile testes sample and fractured experimental tensile test sample and (b) experimental and numerical, Mat 3 and Mat 24, engineering stress–strain curves of 1050 H14 Al.

(cont. on next page)

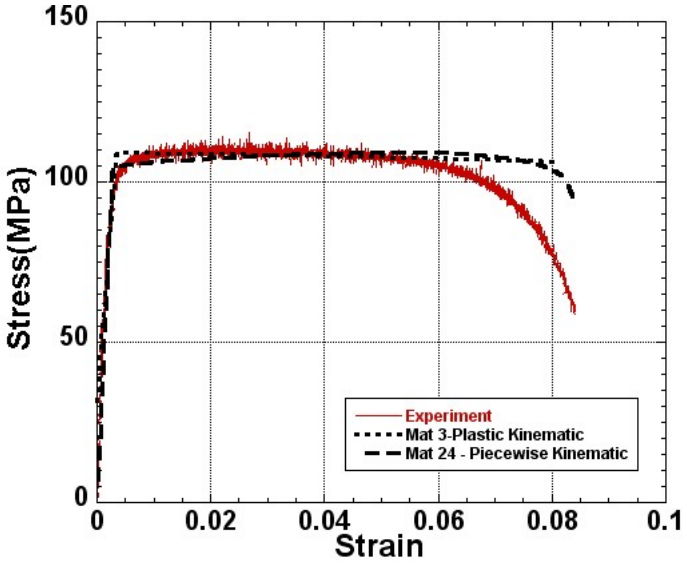

(b)

Figure 7.3. (cont.)

7.3.Simulation of Empty and Partially Foam Filled Crash Box without Montage Parts

The pictures of the deformation sequences of empty and partially Alulight foam filled 1050 H14 Al crash boxes without montage parts are shown in Figures 7.4-7.12. the simulated deformed shapes of empty and partially foam filled boxes are in good agreement with the experimental deformed shapes as shown in Figures 7.4-7.12. A quasi-inextensional deformation mode is observed in all numerically and experimentally crushed empty boxes (Figures 7.4, 7.8 and 7.11). As similar with the experiments, the numerical number of fold formation increases in partially foam filled boxes. Load and mean load-displacement curves of empty and F1 and F2 partially Alulight foam filled 1050 H14 Al crash boxes without montage parts are shown in Figures 7.13, 7.14 and 7.15, respectively. The experimental and numerical load and mean load-displacement curves essentially show good agreements in empty and filled 2 and 3 mm thick crash boxes (Figures 7.13(a) and (c), 7.14(a) and (c) and 7.15(a) and (c)), while the numerical mean load values of the 2.5 mm thick crash boxes are slightly higher than those of experiments (Figures 7.13(b), 7.14(b) and 7.15(b)). The weld seem opening is observed during the compression loading of few empty tubes as seen in Figure 7.8. However, no

significant effect of weld seem opening is detected on the load-displacement curves. The weld seam opening, as seen in Figure 7.8, occurs at a later stage of the fold formation and therefore its influence, if any, on the load values is relatively small at increasingly large displacements.

Figure 7.4. Sequential deformation photos of empty crash box without montage parts, t=3 mm (G1T3E).

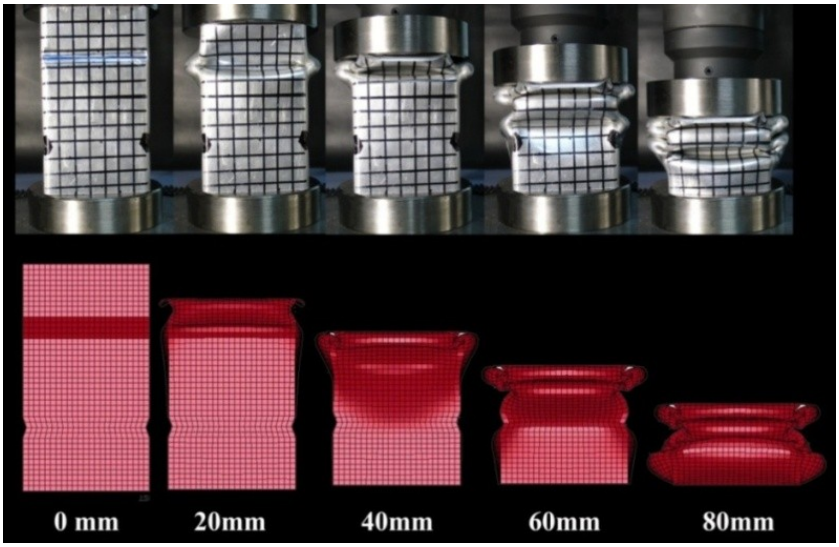

Figure 7.5. Sequential deformation photos of filled crash box without montage parts, t=3 mm (G1T3F1).

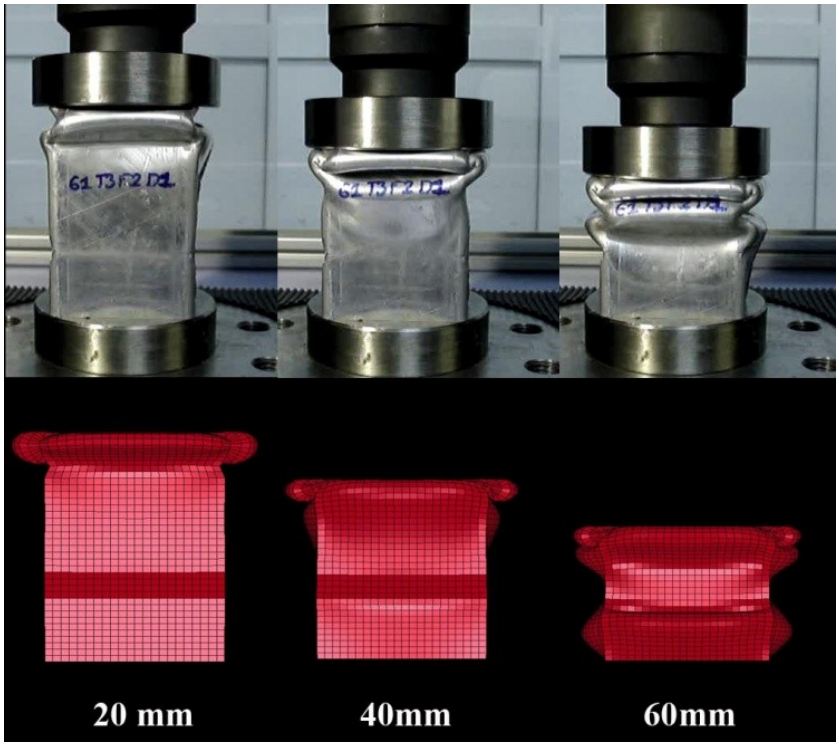

Figure 7.6. Sequential deformation photos of filled crash box without montage parts, t=3 mm (G1T3F2).

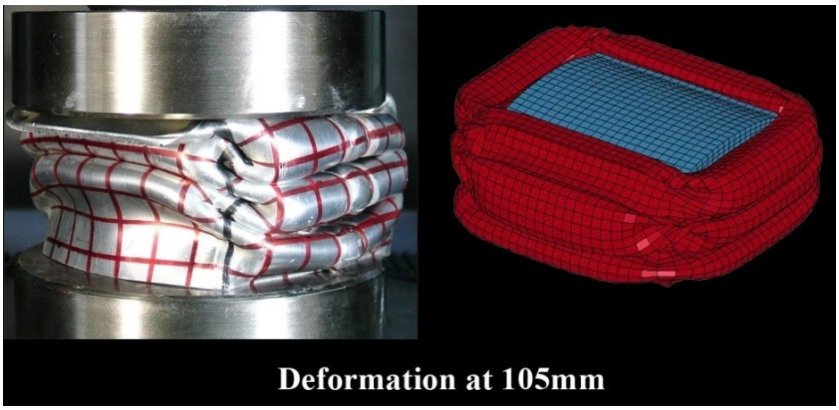

Figure 7.7. Deformation photo of filled crash box without montage parts, t=2 mm (G1T2F2).

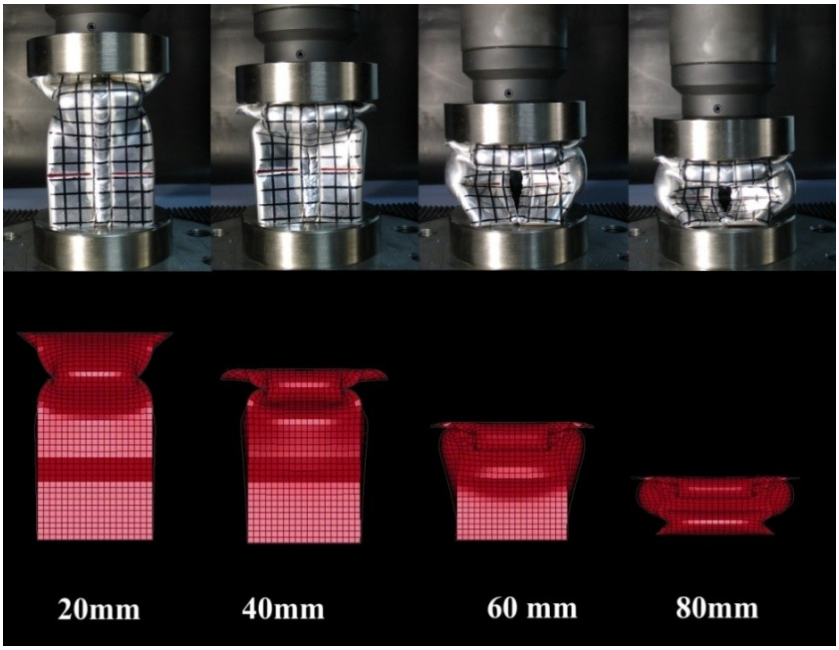

Figure 7.8. Sequential deformation photos of empty crash box without montage parts, t= 3 mm (G2T3E).

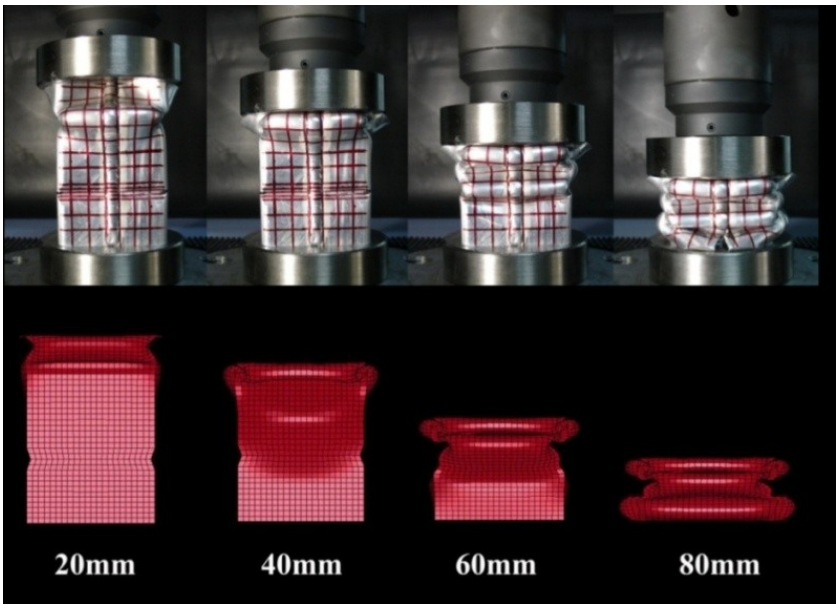

Figure 7.9. Sequential deformation photos of filled crash box without montage parts, t=3 mm (G2T3F1).

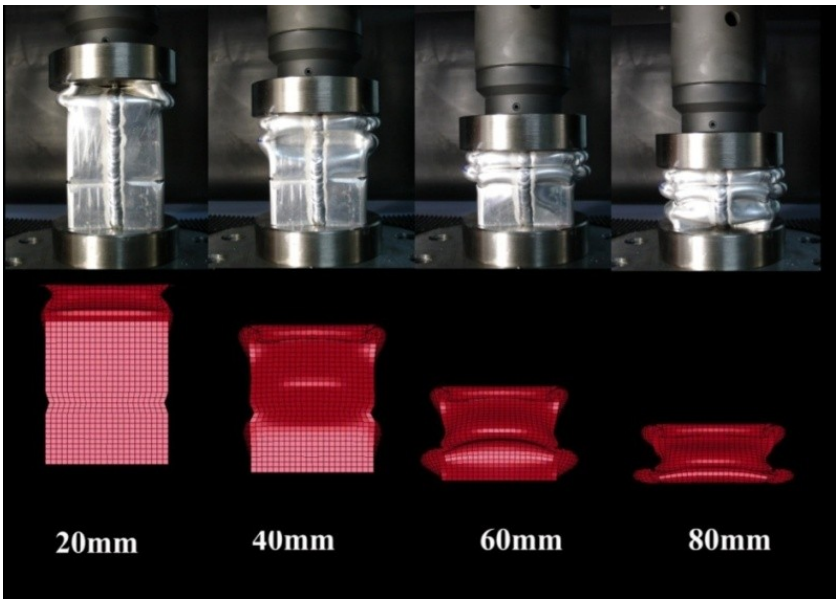

Figure 7.10. Sequential deformation photos of filled crash box without montage parts, t= 3 mm (G2T3F2).

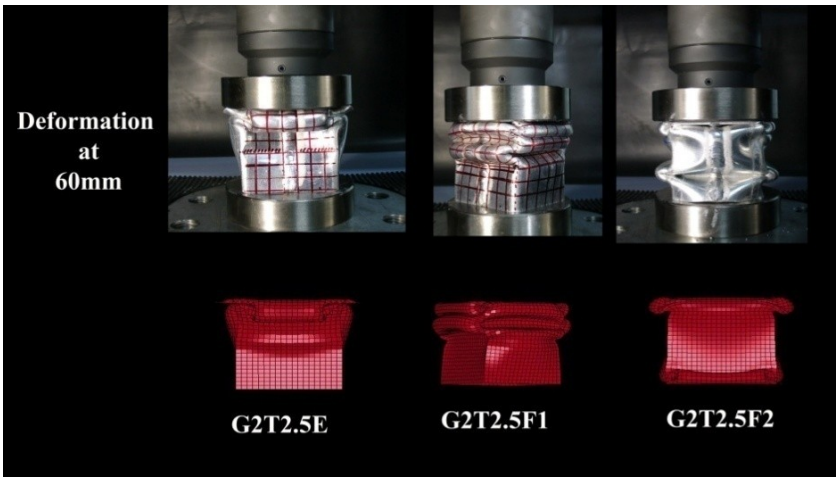

Figure 7.11. Deformation photos of empty and filled crash box without montage parts, t=2.5 mm (G2T2.5E)

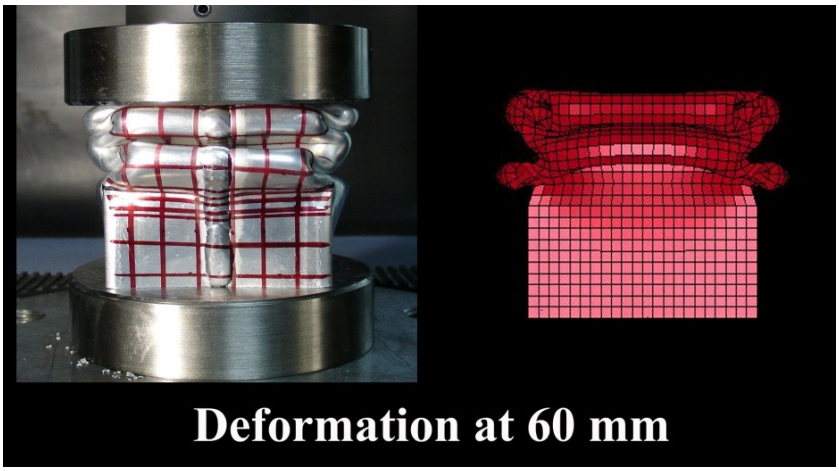

Figure 7.12. Deformation photo of filled crash box without montage parts, t= 2 mm (G2T2F1).

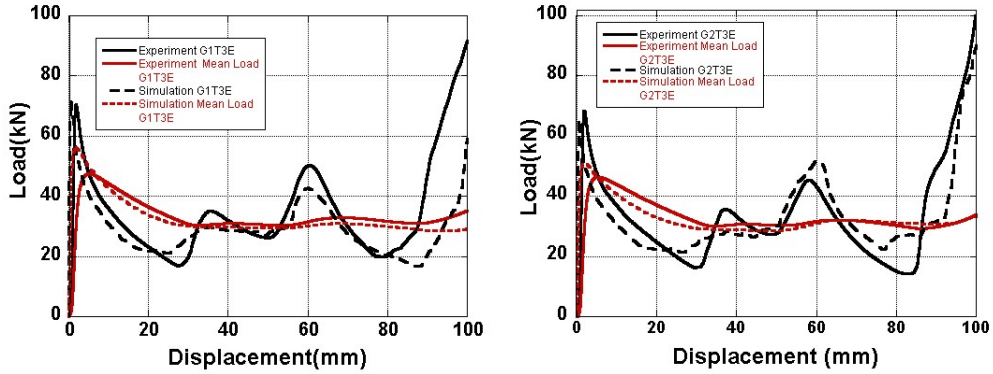

(a)

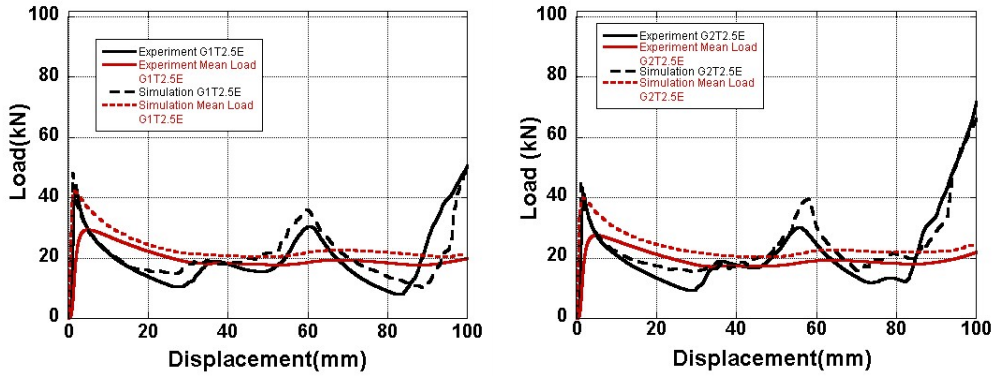

(b)

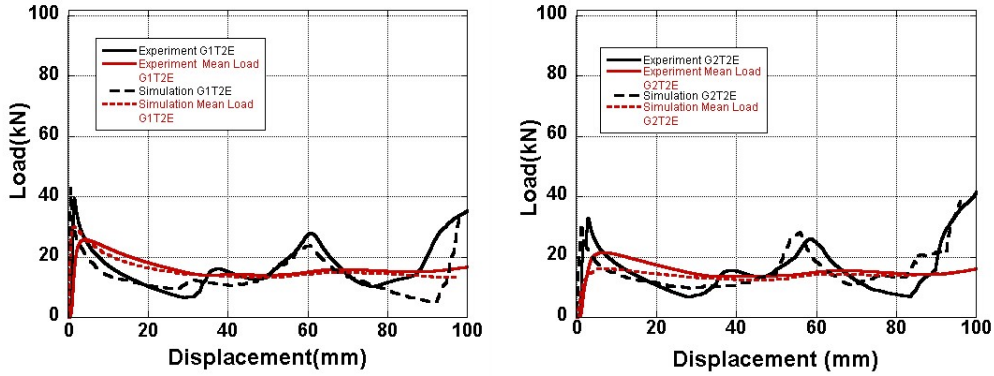

(c)

Figure 7.13. Load-displacement graphs of empty crash box without fixing parts, a) 3 mm , b) 2.5 mm and c) 2 mm thickness.

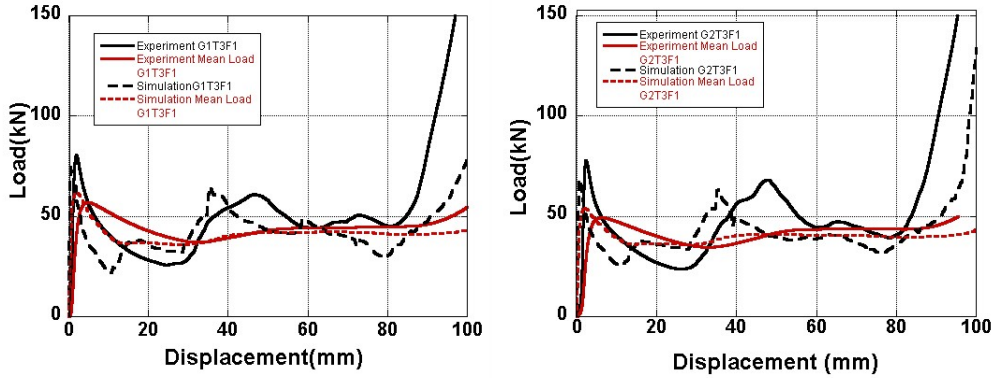

(a)

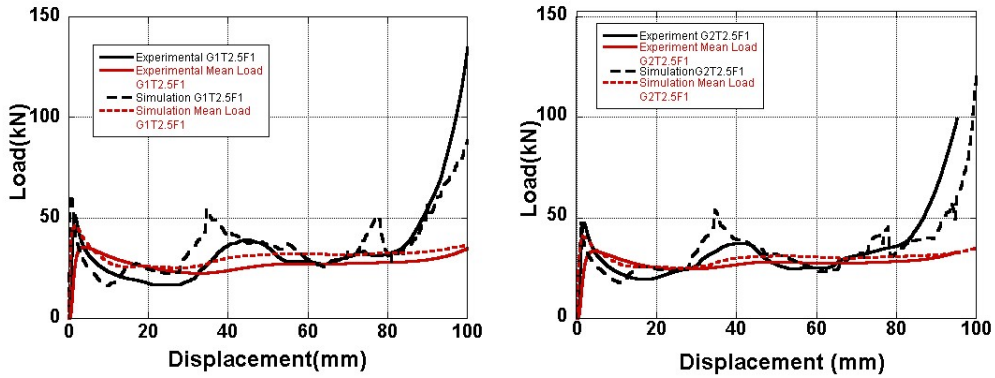

(b)

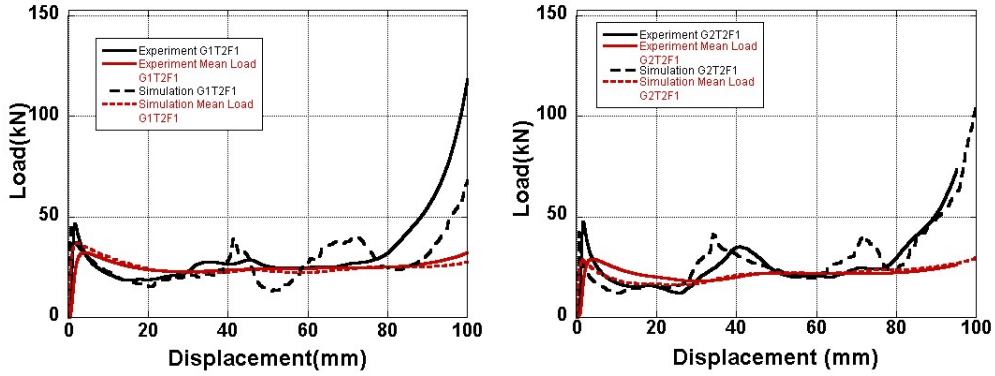

(c)

Figure 7.14. Load-displacement graphs of F1 foam filled crash box without fixing parts, a) 3 mm , b) 2.5 mm and c) 2 mm thickness.

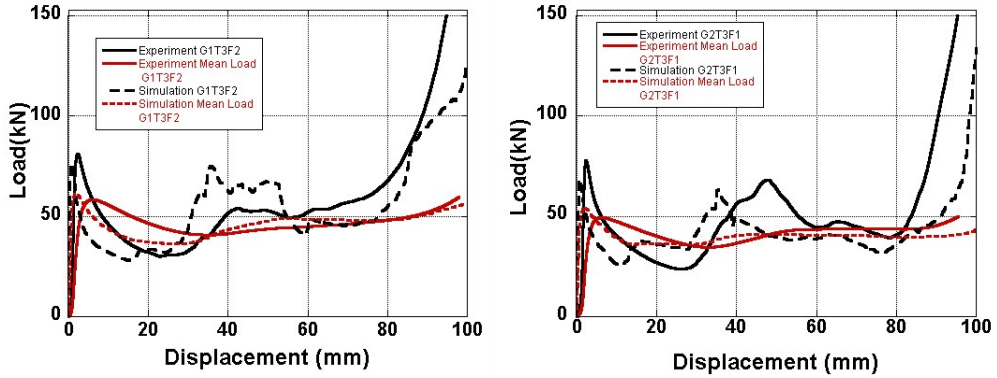

(a)

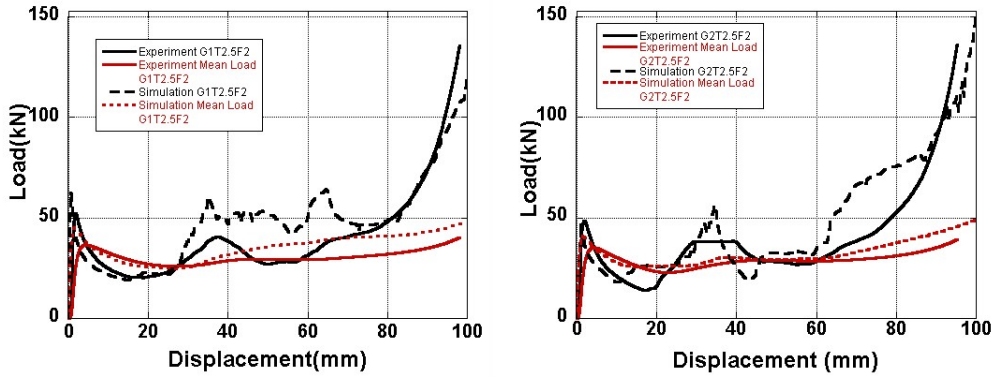

(b)

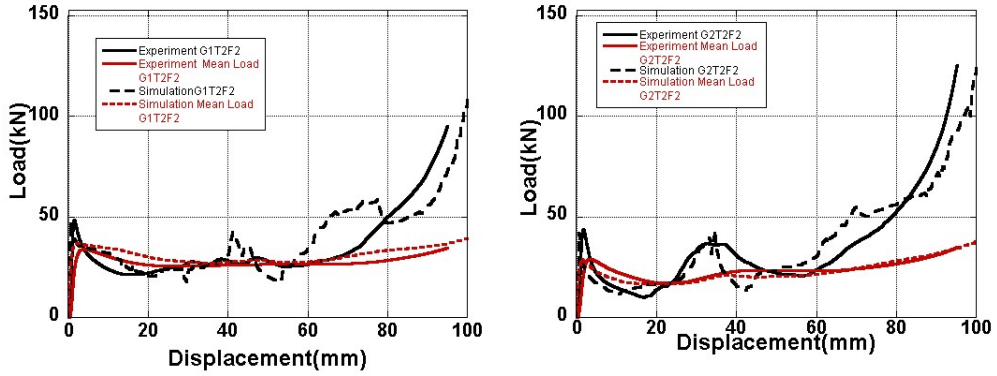

(c)

Figure 7.15. Load-displacement graphs of F2 foam filled crash box without fixing parts, a) 3 mm , b) 2.5 mm and c) 2 mm thickness.

7.4. Simulation of Empty and Partially Foam Filled Crash Box with Montage Parts

The numerical and experimental pictures of the deformation sequences of empty and partially F1 and F2 Alulight foam filled G1 geometry 3 mm, 2.5 mm and 2 mm thick 1050 H14 Al crash boxes with montage parts are shown in Figures 7.16, 7.17 and 7.18, respectively. As shown in Figure 7.16, foam filled G1 geometry boxes with 3 mm thickness deform in progressive folding mode both experimentally and numerically. G1 box geometries in 2.5 and 2 mm thickness, the deformation is non-progressive (Figures 7.17 and 7.18). The numerical and experimental pictures of the deformation sequences of empty and partially F1 and F2 Alulight foam filled G2 geometry 3 mm, 2.5 mm and 2 mm thick 1050 H14 Al crash boxes with montage parts are shown in Figures 7.19, 7.20 and 7.21, respectively. Similar to 2.5mm and 2 mm thick foam filled G1 boxes, all G2 geometry filled boxes deform in non-progressive mode. It is also noted that, the folding starts in the empty top and bottom sections of the foam filled crash boxes, followed by the folding of the foam filled section. Similar to crash boxes without montage part, foam filling in boxes with montage plates increases the total number of fold formation.

The experimental and numerical load and mean load-displacement curves of empty and partially F1 and F2 Alulight foam filled G1 and G2 geometry crash boxes with montage parts are shown in Figures 7.22, 7.23 and 7.24, respectively. As in the experimental load-displacement curves, the corrugation is noted to reduce the numerical initial peak load values in empty and filled crash box. However, the initial peak load values are still the maximum loads in empty tubes. In the filled tubes however, the second fold induces experimentally and numerically a higher peak load value than initial peak load mainly due to interaction between the foam filler and crash box. It is also note that the simulation load values show good correlation with those experiments in both empty and foam filled crash boxes. Similar to the boxes without montage plates, the numerical mean load values of the crash boxes with 2.5 thickness are higher than experimental mean load values.

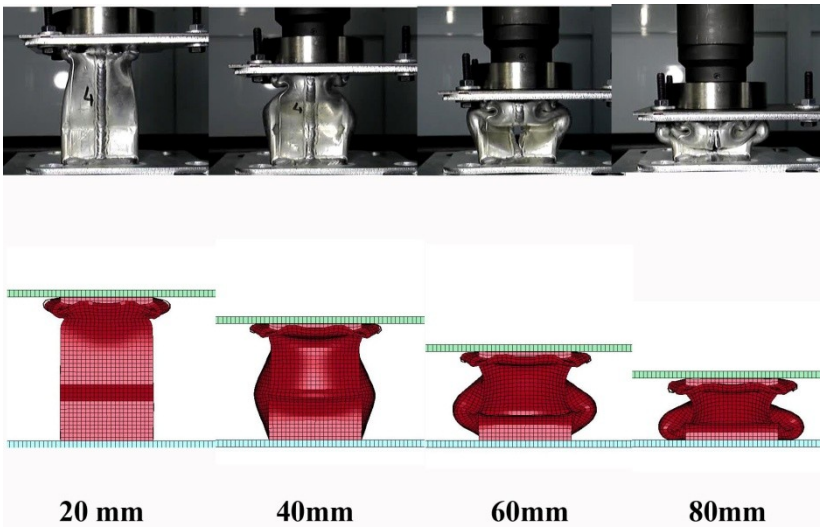

(a)

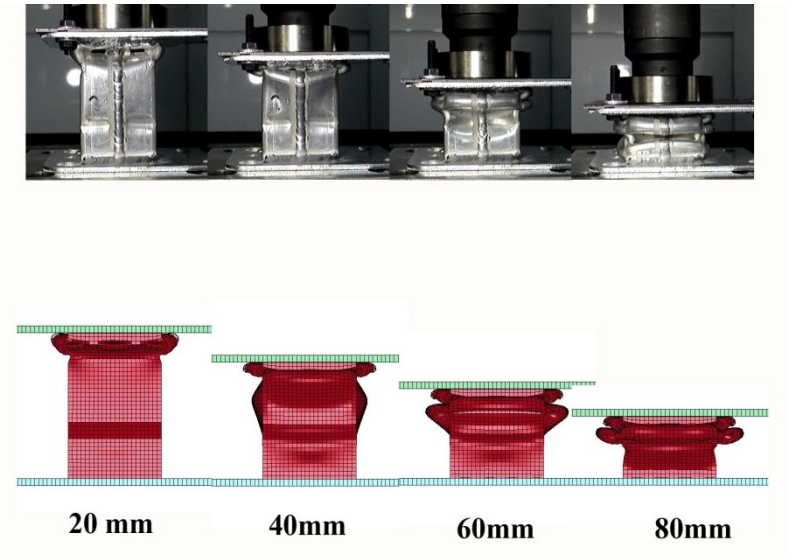

(b)

Figure 7.16. Sequential deformation pictures of crash box with montage parts a) empty, b) F1 foam filled and c) F2 foam filled (Geometry G1, t =3 mm)

(cont. on next page)

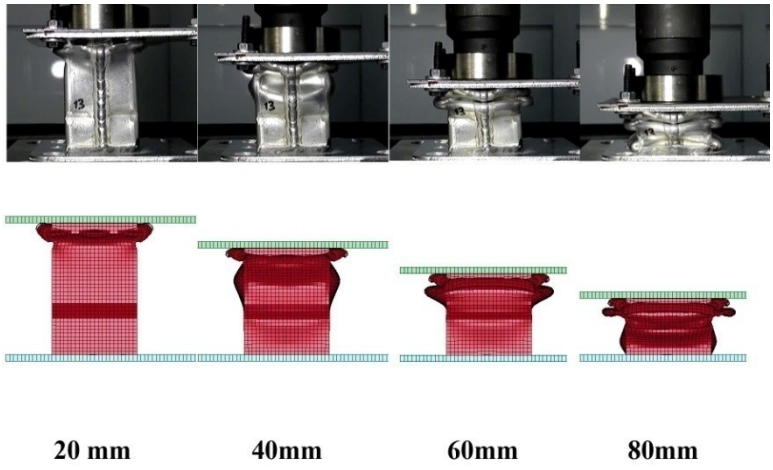

(c)

Figure 7.16. (cont.)

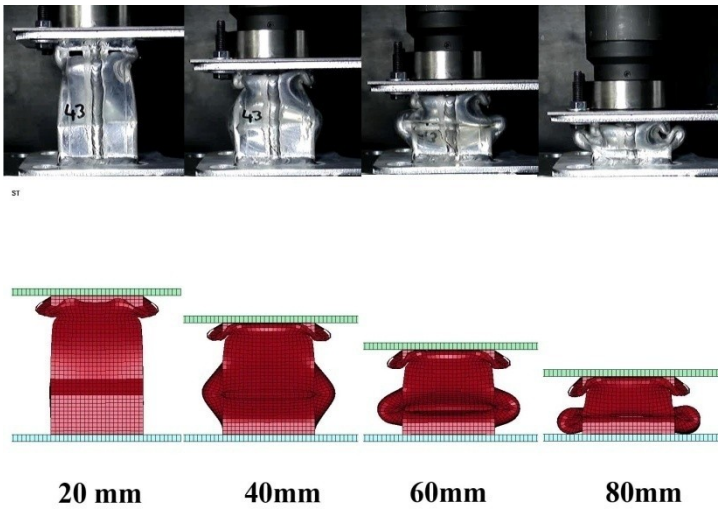

(a)

Figure 7.17. Sequential deformation pictures of crash box with montage parts a) empty, b) F1 foam filled and c) F2 foam filled (Geometry G1, t= 2.5 mm)

(cont. on next page)

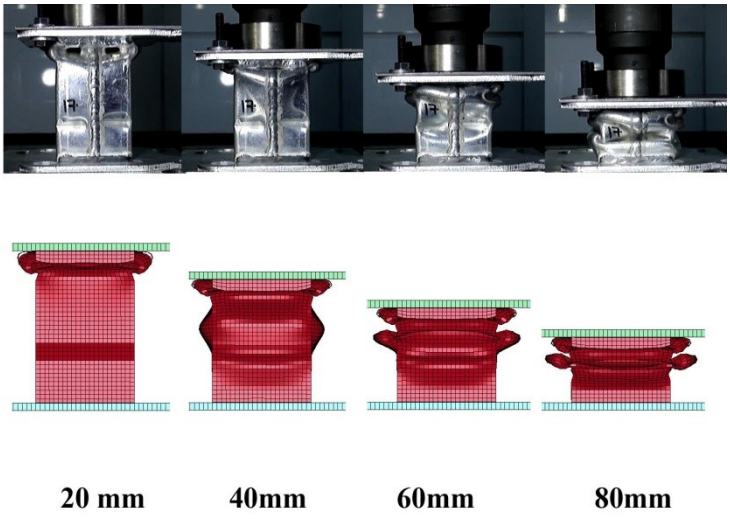

(b)

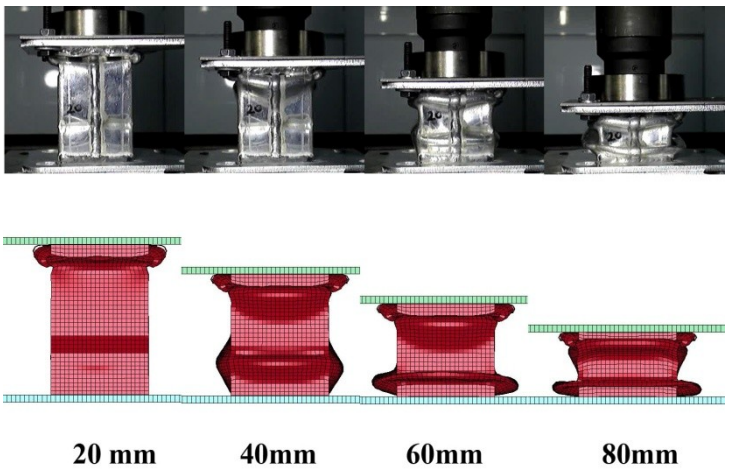

(c)

Figure 7.17. (cont.)

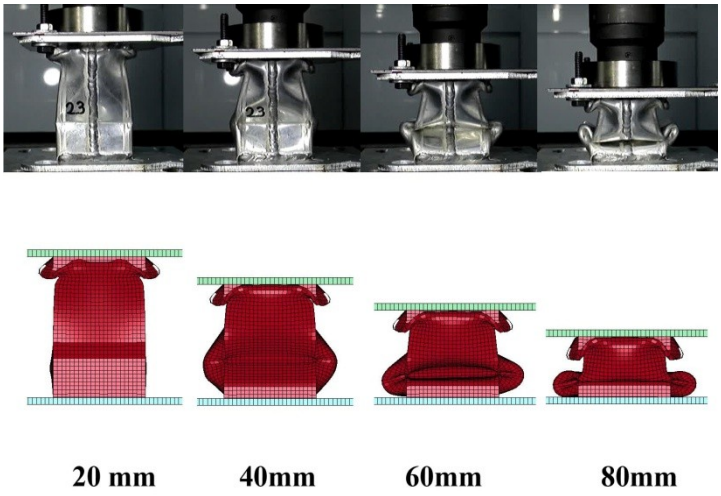

(a)

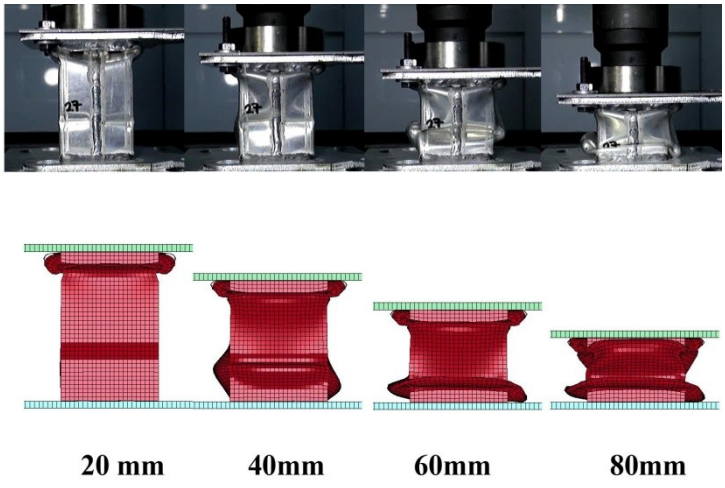

(b)

Figure 7.18. Sequential deformation pictures of crash box with montage parts a) empty, b) F1 foam filled and c) F2 foam filled (Geometry G1, t= 2 mm).

(cont. on next page)

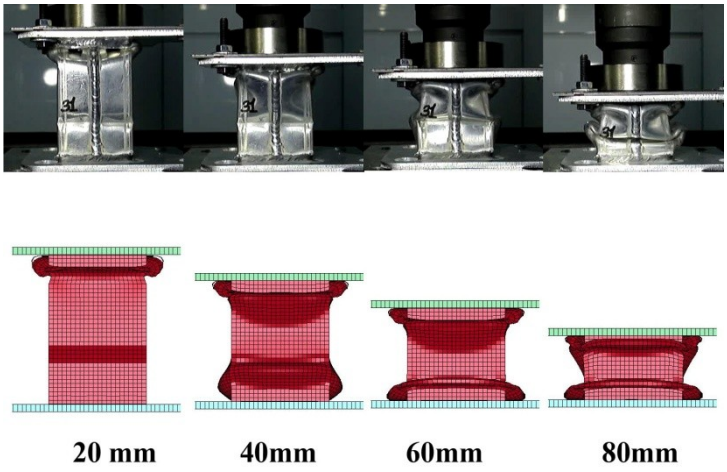

(c)

Figure 7.18. (cont.)

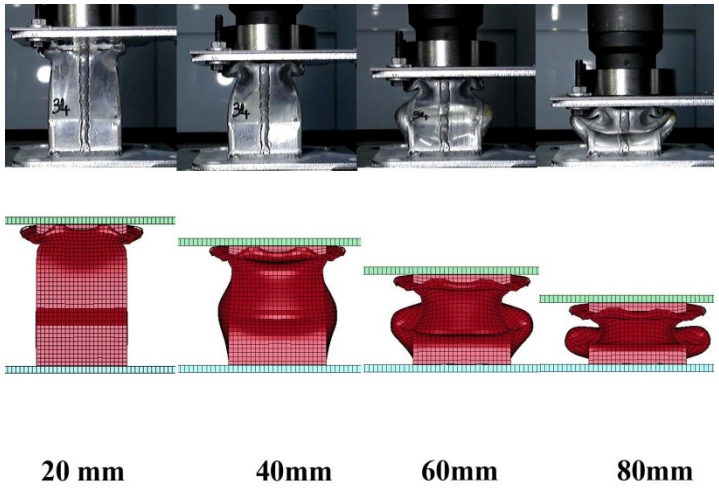

(a)

Figure 7.19. Sequential deformation pictures of crash box with montage parts a) empty, b)F1 foam filled and c) F2 foam filled (Geometry G2, t= 3 mm)

(cont. on next page)

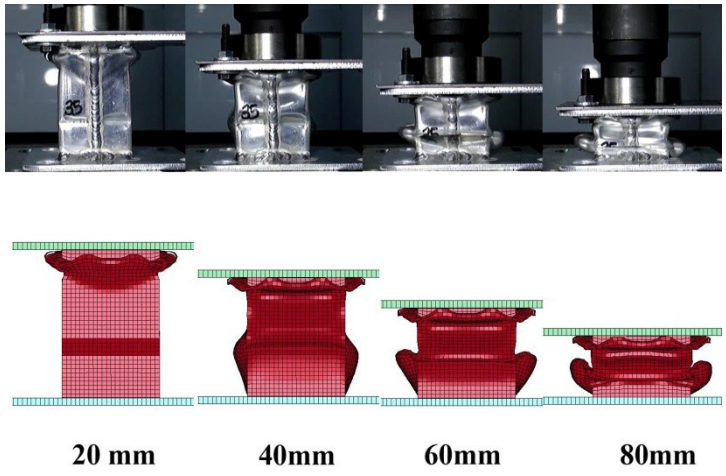

(b)

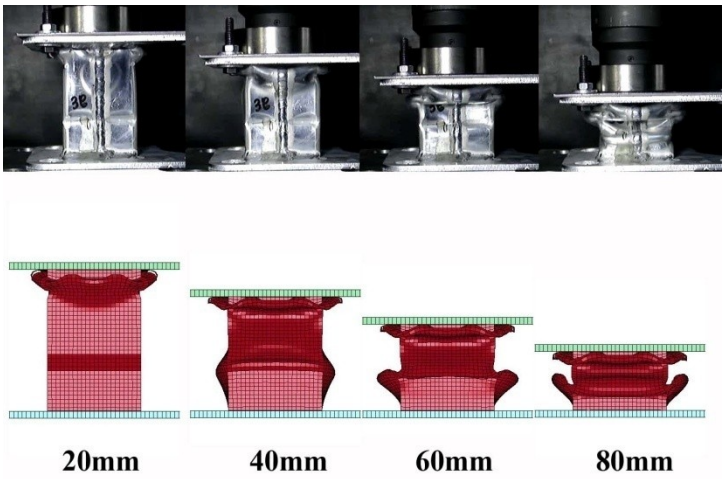

(c)

Figure 7.19. (cont.)

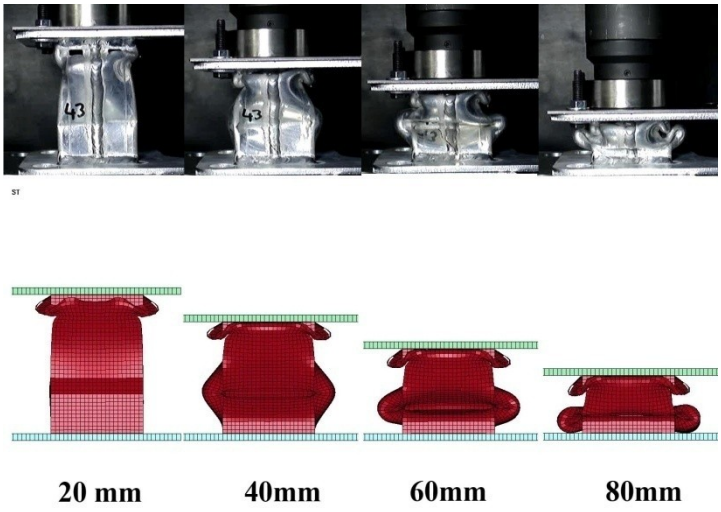

(a)

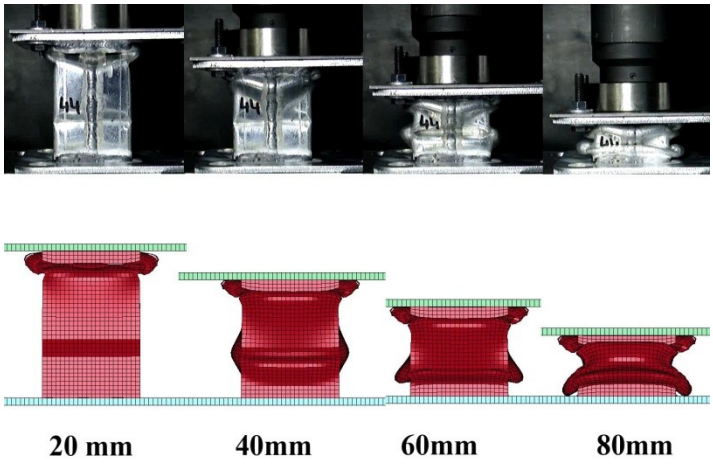

(b)

Figure 7.20. Sequential deformation pictures of crash box with montage parts a)Empty, b) F1 foam filled and c) F2 foam filled (Geometry G2, t= 2.5 mm.)

(cont. on next page)

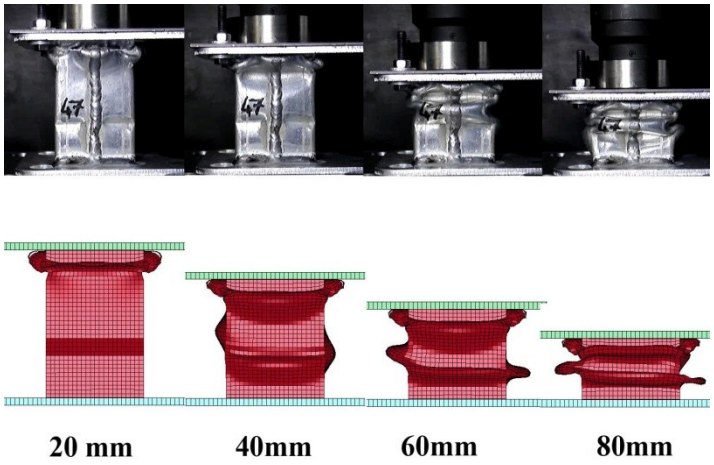

(c)

Figure 7.20. (cont.)

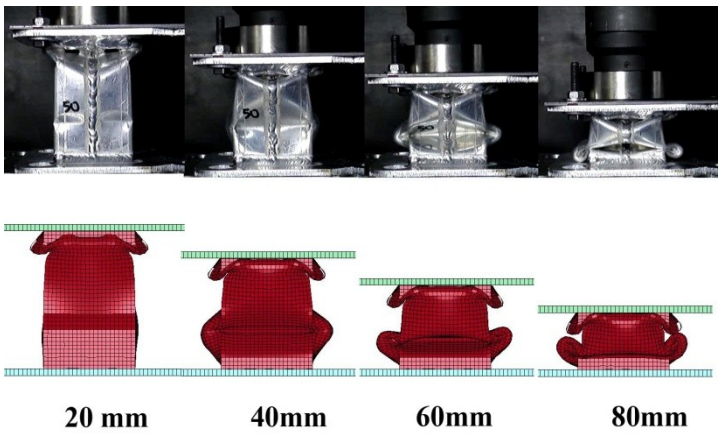

(a)

Figure 7.21. Sequential deformation pictures of crash box with montage parts a) empty, b) F1 foam filled and c) F2 foam filled (Geometry G2, t= 2 mm)

(cont. on next page)

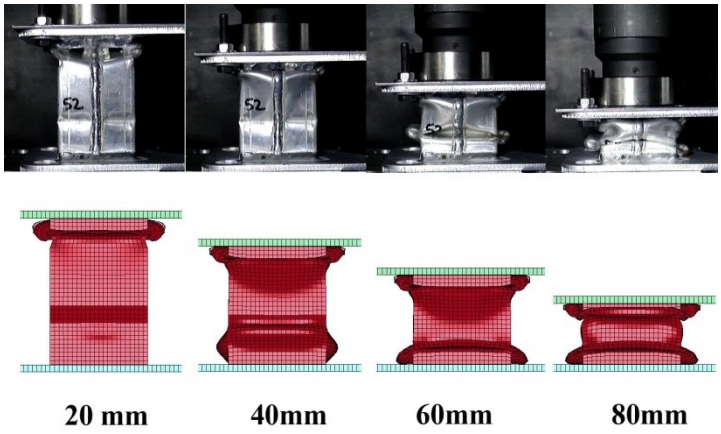

(b)

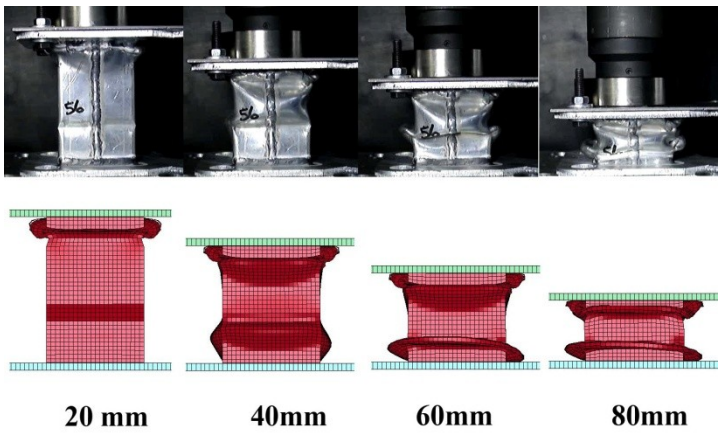

(c)

Figure 7.21.(cont.)

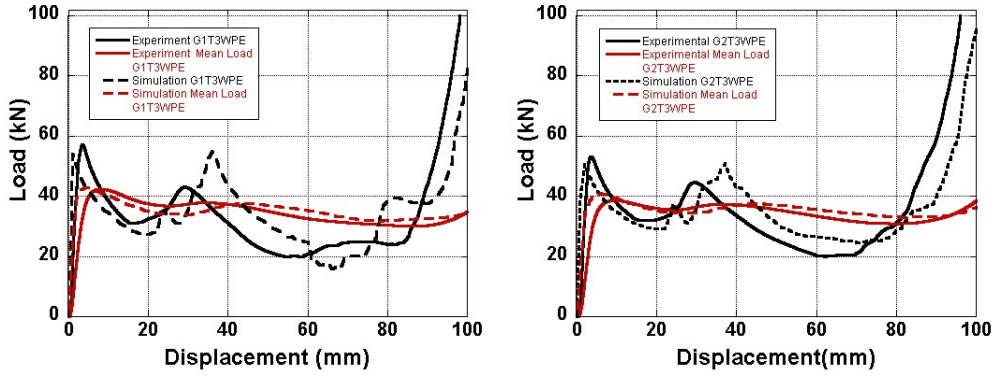

(a)

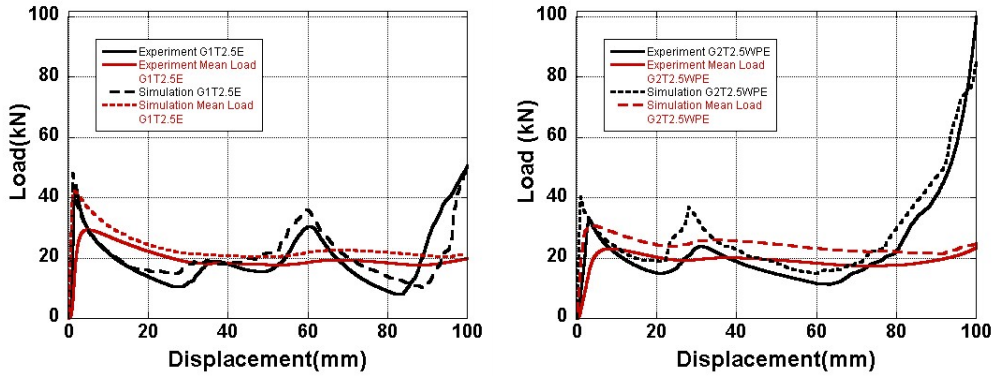

(b)

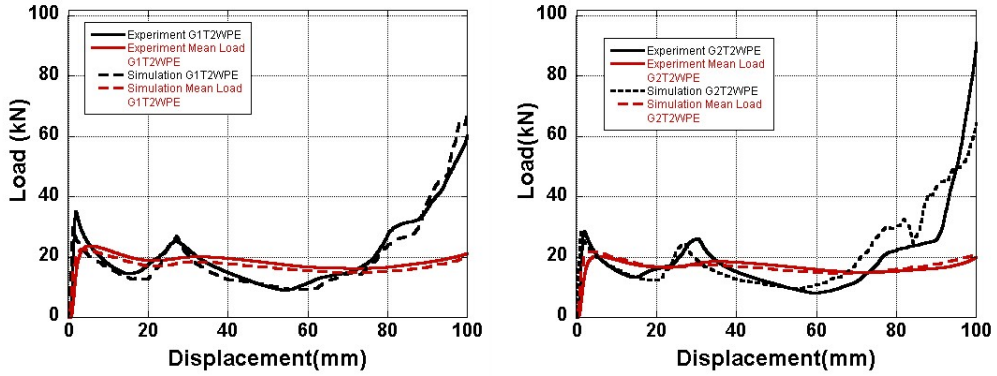

(c)

Figure 7.22. Load-displacement graphs of empty crash box with fixing parts a) 3 mm, b) 2.5 mm and c)2 mm thickness.

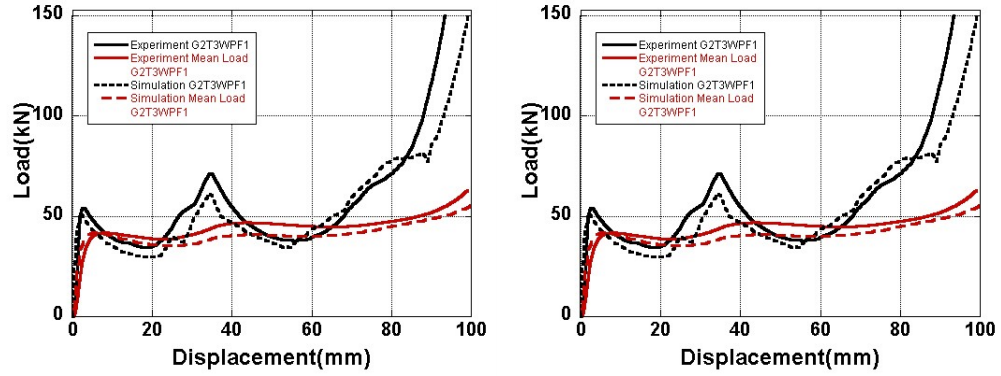

(a)

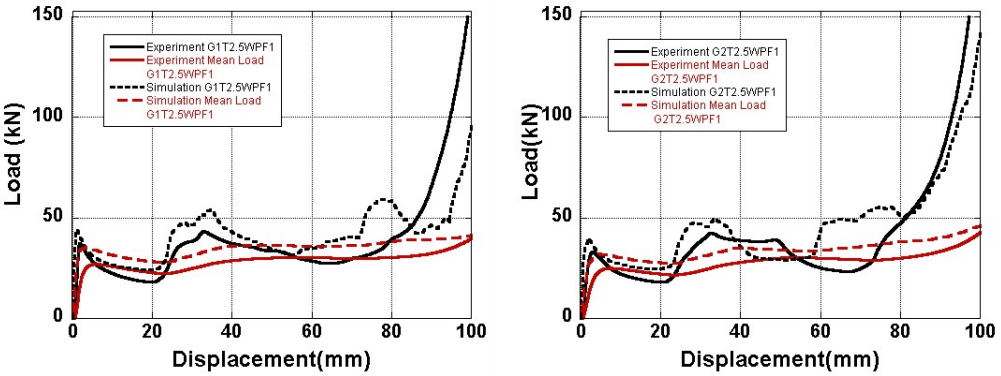

(b)

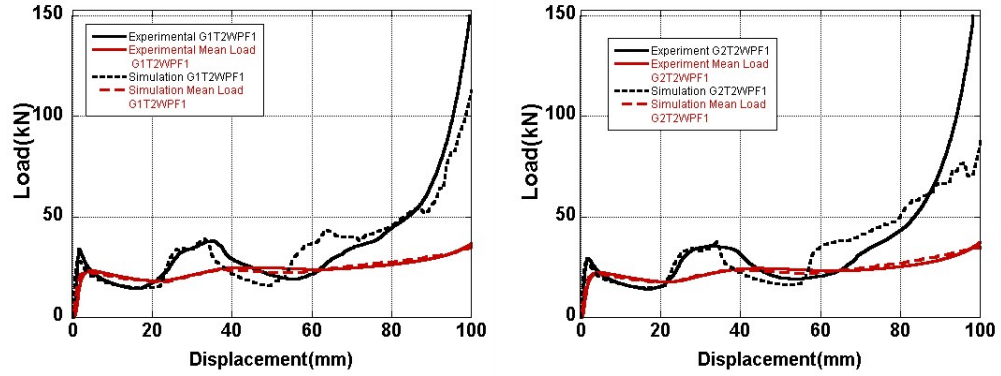

(c)

Figure 7.23. Load-displacement graphs of F1 foam filled crash box with fixing parts a) 3 mm, b) 2.5 mm and c)2 mm thickness.

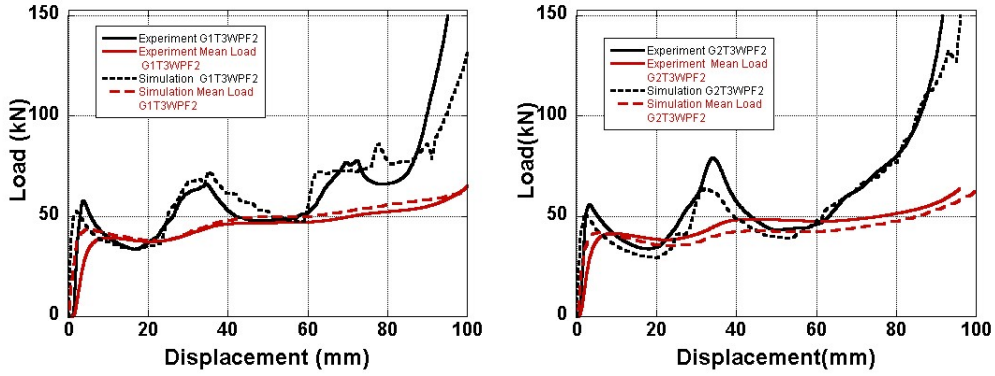

(a)

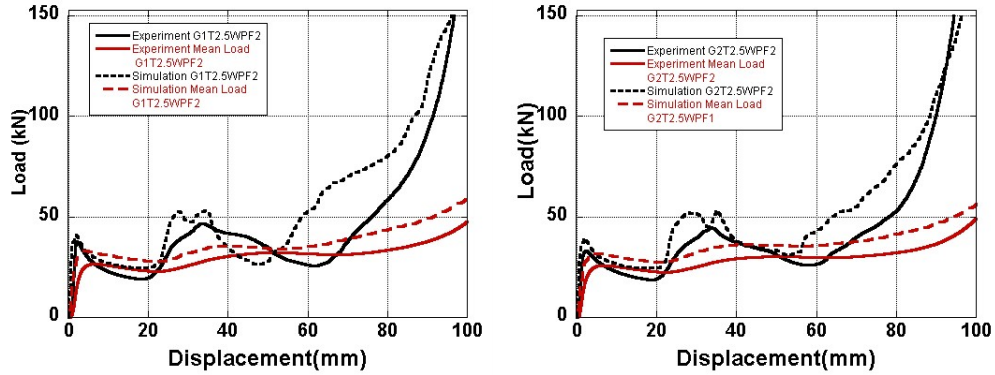

(b)

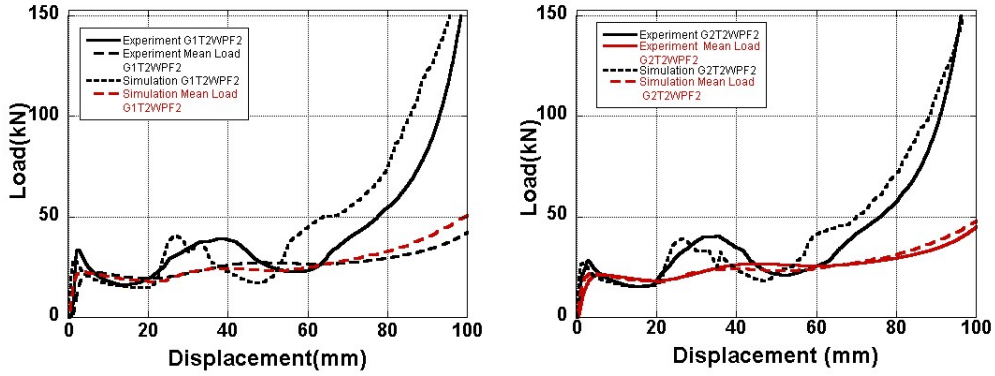

(c)

Figure 7.24. Load-displacement graphs of F2 foam filled crash box with fixing parts a) 3 mm, b) 2.5 mm and c)2 mm thickness.

7.5.Dynamic Testing of Empty and Al Foam Filled 1050Al Crash Boxes

Experimental and numerical deformation patterns of dynamically tested empty and partially filled crash boxes are shown together in Figure 7.24 for comparison. Both, numerical and experimental compression, results in very much similar deformation shapes of the crash boxes investigated as seen in the same figure. The deformation in dynamic loading starts from the corrugated section of the boxes in experiments and numerical simulations. At 50% deformation, the experimental and simulation load values are sequentially 35 kN and 38 kN for empty crash box (Figure 7.25(a)). Similarly, the experimental and simulation load values of filled crash boxes show good agreements with each other as shown in Figure 7.25(b).

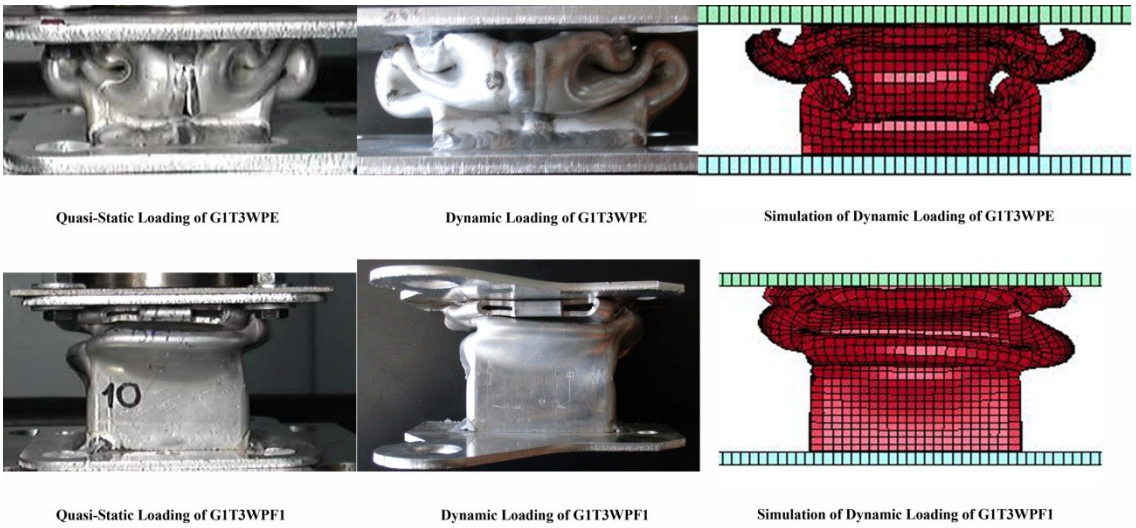

Figure 7.25. Deformations pictures of empty and filled crash boxes in quasi-static and dynamic testing and simulation.

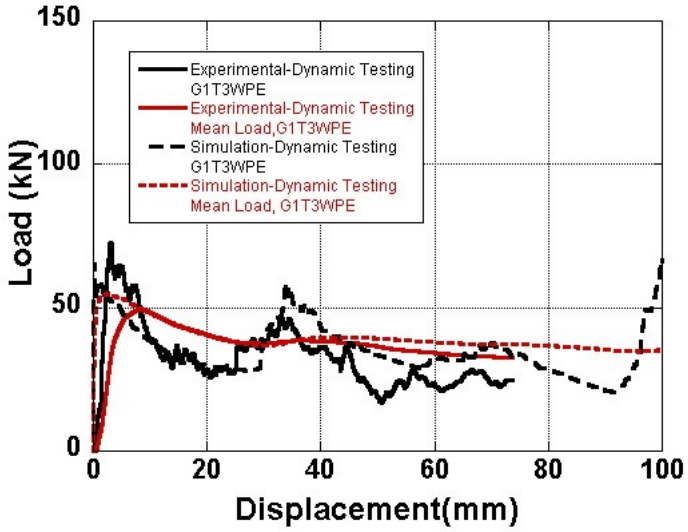

(a)

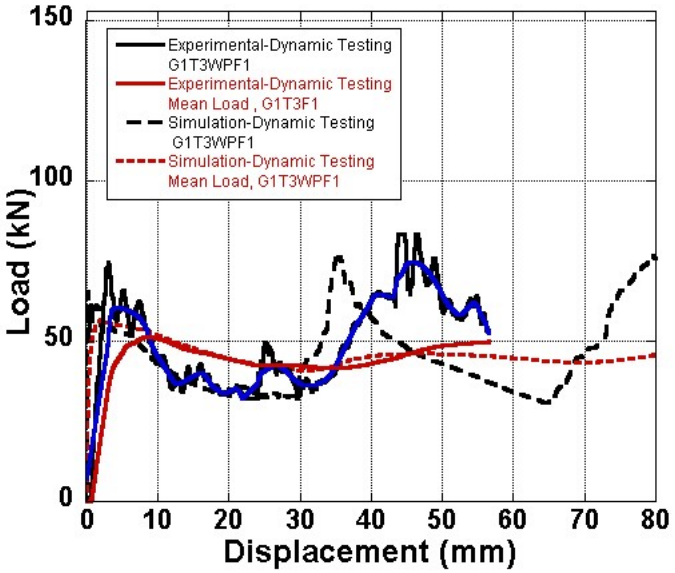

(b)

Figure 7.26. Experimental and numerical load-displacement graphs of a) empty and b) partially filled crash box.

CHAPTER 8

ALUMINUM CRUSH BOX OPTIMIZATION

8.1. Optimization Results

Representative, simulation (LS-DYNA) load-displacement and mean load-displacement curves of empty and partially filled 1.5 and 3 mm thick 1050H14 Al boxes are shown in Figure 8.1(a) and (b), respectively. The load and mean load values of filled boxes increase rapidly after about 50% deformation as the foam filler relative density increases at increasing deformation levels, particularly after the densification strain. The mean load values generally increase with increasing foam relative density, except 2 and 2.5 mm thick boxes as shown in Figure 8.2(a). After about 0.1 relative density the foam filling is shown to be not effective in increasing mean load values of 2 and 2.5 mm thick boxes. The SEA values however show a clear tendency of maximum at a foam relative density of 0.1 within the studied foam relative density range, shown in Figure 8.2 (b)

The response of 4^{th}-order polynomial function of SEA and Pm are given by the following equations,

$$\begin{aligned} SEA(t,\rho^*) = {} & -45.516t - 104.553\rho^* - 13.330t^3 + 38.790t^2 + 111.555t\rho^* \\ & + 985.596\rho^{*2} - 41.602t^2\rho^* - 326.594t\rho^{*2} - 6135.120\rho^{*3} \\ & + 4.071t^3\rho^* + 1.645t^4 + 100.271t^2\rho^{*2} - 259.786t\rho^{*3} \\ & + 16173.33\rho^{*4} + 22.298 \end{aligned} \tag{8.1}$$

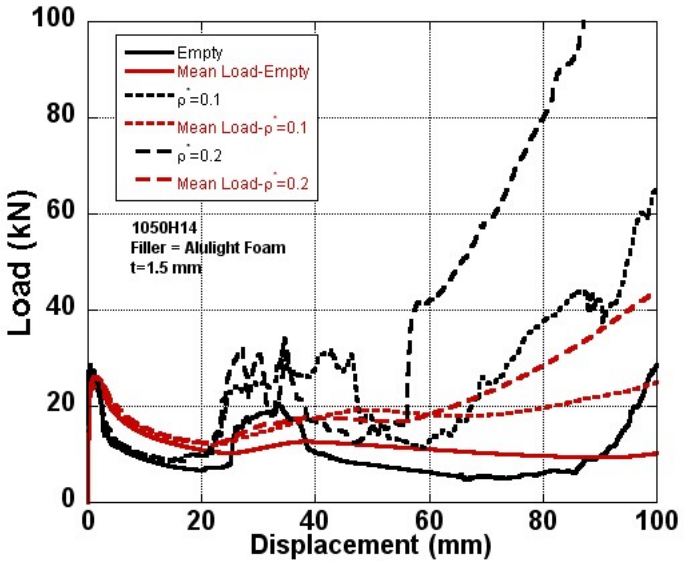

(a)

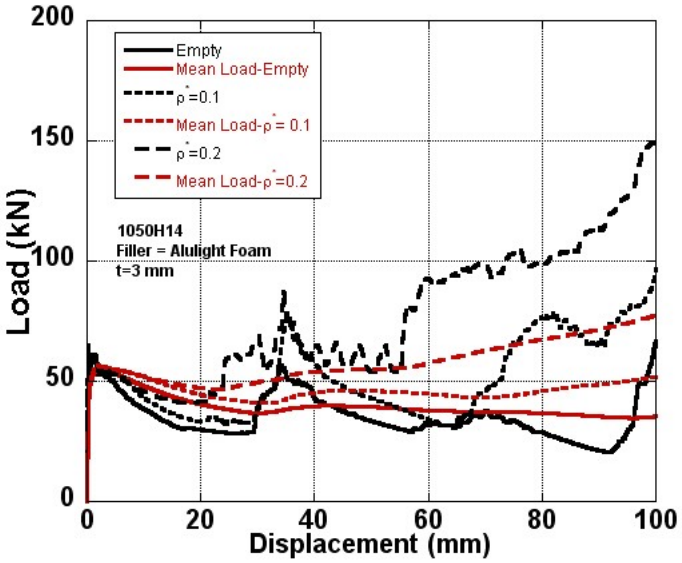

(b)

Figure 8.1. Load-displacement curves of empty and foam filled 1050H14 crush box, thicknesses of a) 1.5 mm and b) 3 mm.

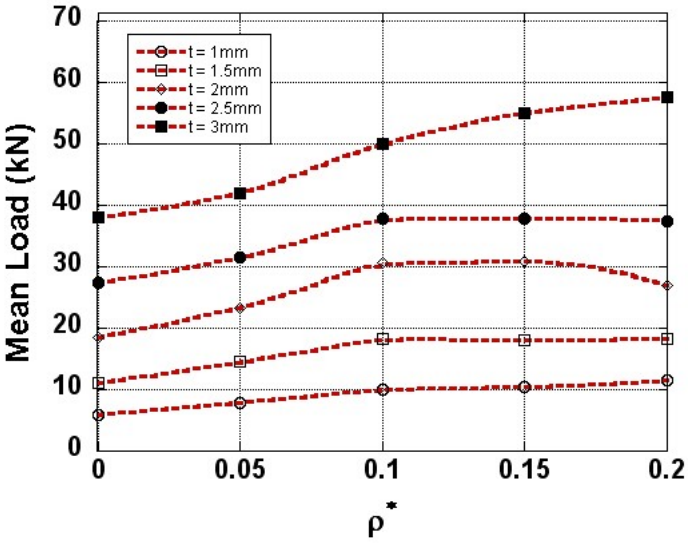

(a)

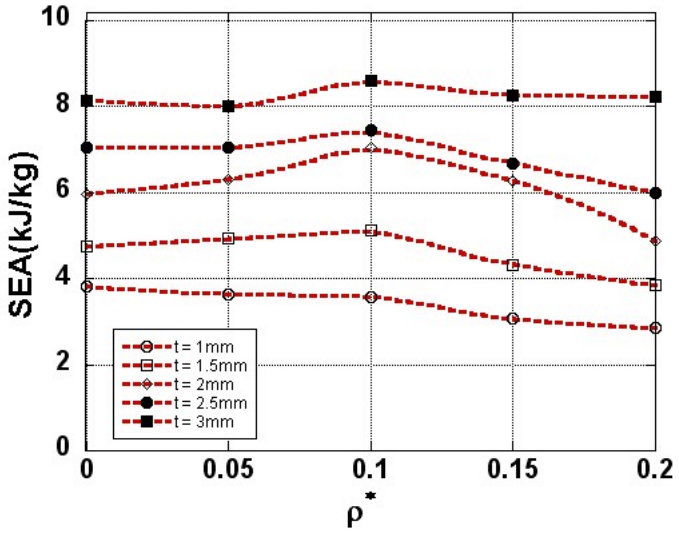

(b)

Figure 8.2. The variation of (a) mean load and (a) SEA of 1050H14 crush boxes with foam relative density and box wall thickness.

$$Pm(t,\rho^*) = -225.037t - 452.332\rho^* - 61.317t^3 + 185.170t^2 + 701.160t\rho^* + 1967.319\rho^{*2} - 274.815t^2\rho^* - 1723.313t\rho^{*2} - 5393.531\rho^{*3} + 28.844t^3\rho^* + 7.435t^4 + 618.698t^2\rho^{*2} - 2296.453t\rho^{*3} + 19852.662\rho^{*4} + 45.122 \quad (8.2)$$

The constructed response surface of mean load and SEA vs. box wall thickness and foam relative density graphs of filled 1050H14 Al boxes are shown sequentially in Figure 8.3(a) and (b). Figure 8.4(a) and (b) show the simulation and RSM mean load and SEA response surfaces, respectively. R^2, R_{adj}^2 and RMSE values of partially Alulight foam filled boxes are further listed in Table 8.1. Relatively higher values of R^2 and R_{adj}^2 and relatively smaller values of RMSE confirm the agreement between experimental and simulated response surfaces.

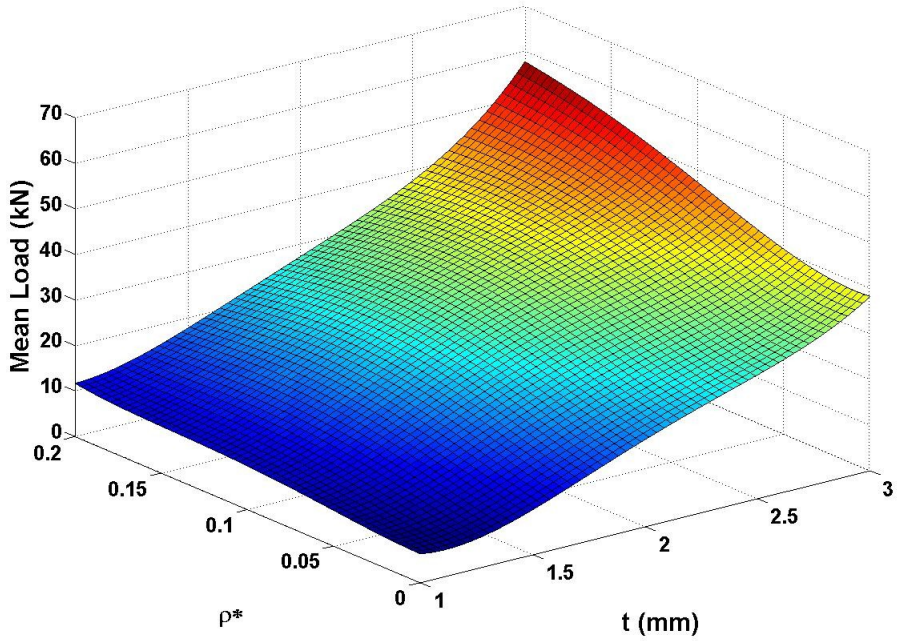

(a)

Figure 8.3. Response surface foam filled 1050H14 crush box; a) mean load and b) SEA vs. foam relative density and box thickness.

(cont. on next page)

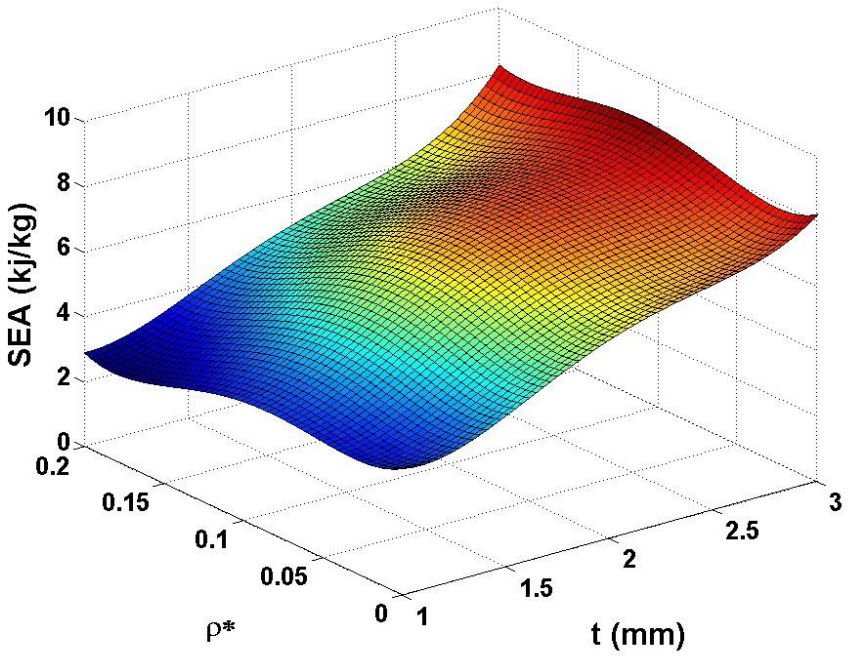

(b)

Figure 8.3. (cont.)

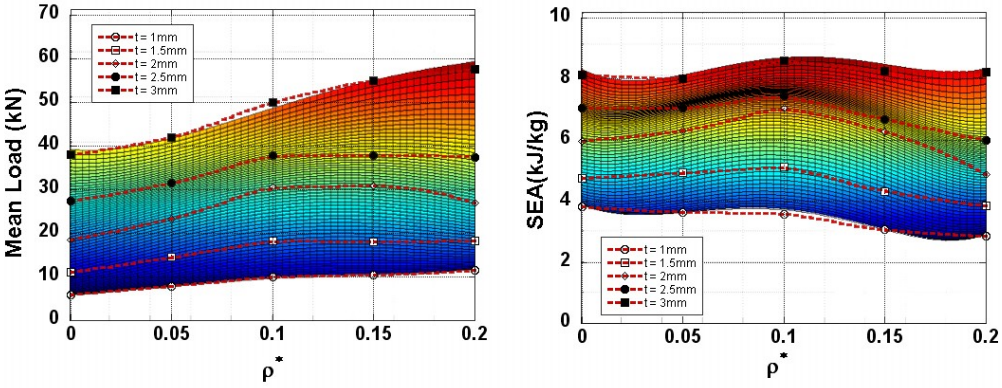

(a) (b)

Figure 8.4. Comparison between simulation and response surface analysis of a) mean load-foam relative density , b) SEA vs. foam relative density curves.

Table 8.1. R^2, R_{adj}^2 and RMSE values of RMS of partially foam filled 1050H14 crash box.

Response Function	R^2	R_{adj}^2	RMSE
Mean Load	0.9958	0.9954	0.9912
SEA	0.9966	0.9963	0.1098

8.2. Optimization of Partially Filled Crush Box with 6061T4 Al and Hydro Foam Filler

The material model data of 6061T4 Al (MAT 3) and Hydro Al foam (AlSi8Mg) used in the simulations are tabulated in Tables 8.2 and 8.3. data The plastic-kinematic hardening material model data of 6061T4 Al were taken from reference (Hou, et al. 2008), Hydro Al foam (AlSi8Mg) data from reference (Reyes, et al. 2003). The simulations of Hydro Al foam filling were performed both for 1050H14 and 6061T4 Al alloy boxes. Representative load-displacement curve of partially Hydro foam filled 2 mm thick 6061T4 Al box is shown in Figure 8.4. Similar to Alulight foam filling of 1050H14 Al boxes, Hydro foam filling of 6061T4 Al box of 2 mm thick results in higher load values than empty box, as is expected. However, the increase in load values of filled boxes after about 50 mm displacement is more pronounced in 6061T4 Al boxes than in 1050H14 Al boxes (Figure 8.5).

Table 8.2. Plastic-kinematic hardening material model (MAT 3) data of 6061T4 Al (Hou, et al. 2008).

Density ρ (kg m^{-3})	Poisson Ratio ν	Young Modulus E (GPa)	Tangent Modulus E_t (MPa)	Yield Strength σ_y (MPa)
2700	0.28	70	450	110.3

Table 8.3. Material parameters of HYDRO aluminum foam (Reyes, et al. 2003).

Foam Material Data Model Description : $\{\sigma_p, \gamma, \alpha_2, 1/\beta\} = C_0 + C_1 \left(\rho_f/\rho_{f0}\right)^n$				
	σ_p (MPa)	α_2 (MPa)	$1/\beta$	γ (MPa)
C_0	0	0	0.22	0
C_1	590	140	320	40
n	2.21	0.45	4.66	1.4

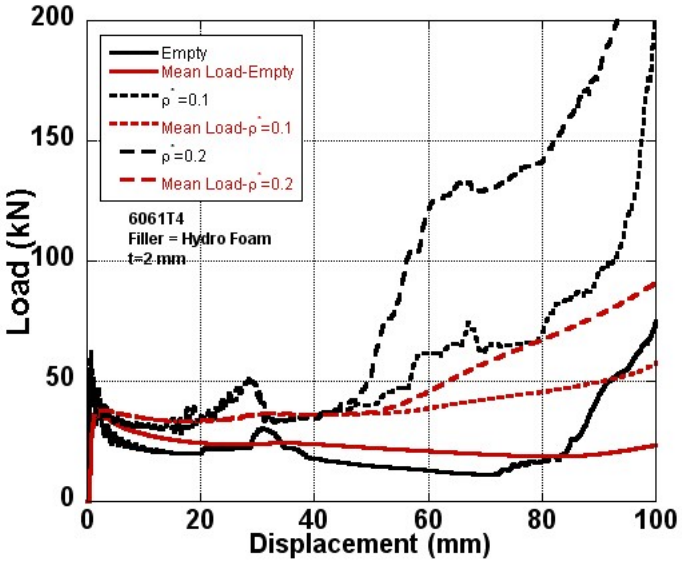

Figure 8.5. Load-displacement curves of empty and partially Hydro foam-filled 6061T4 Al crush box with a wall thickness of 2 mm.

The response of 4th-order polynomial functions of Alulight and Hydro foam partially filled 1050H14 and 6061T4 Al crash boxes are given in Appendix A.1, A.2 and A.3, respectively. The constructed response surface of mean load-box wall thickness-foam relative density graphs of Alulight and Hydro foam filled 1050H14 and 6061T4 Al boxes are sequentially shown in Figures 8.6(a) and (b). The constructed response surface of SAE-box wall thickness-foam relative density graphs of Alulight and Hydro foam filled 1050H14 and 6061T4 Al boxes are also shown sequentially in Figures 8.7(a) and (b). For both Alulight and Hydro foam filling, 6061T4 Al crash

boxes experience higher mean load and SEA values than 1050H14 Al crush box because of higher yield strength of 6061T4 Al alloy. Furthermore, Hydro foam filling is more effective than Alulight foam in increasing both mean load and SEA values of filled boxes, resulting from the higher plateau stresses of Hydro foam.

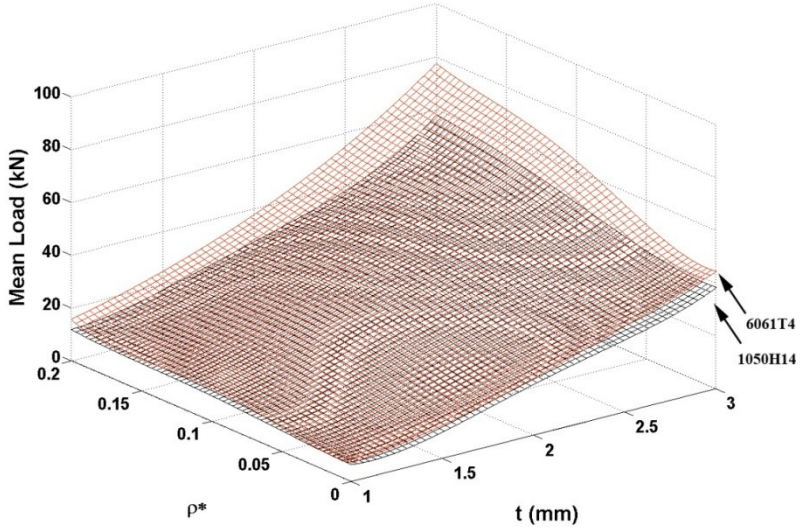

(a)

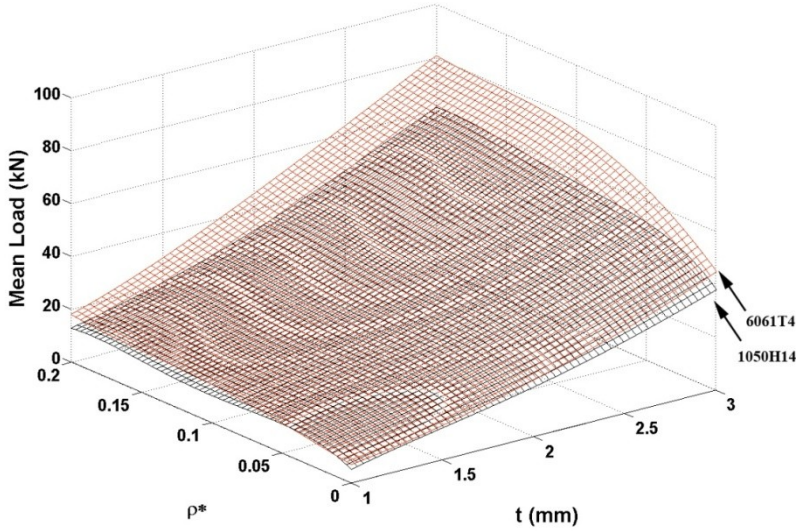

(b)

Figure 8.6. Response surface of mean load of filled boxes; a) Alulight and b) Hydro foam filling.

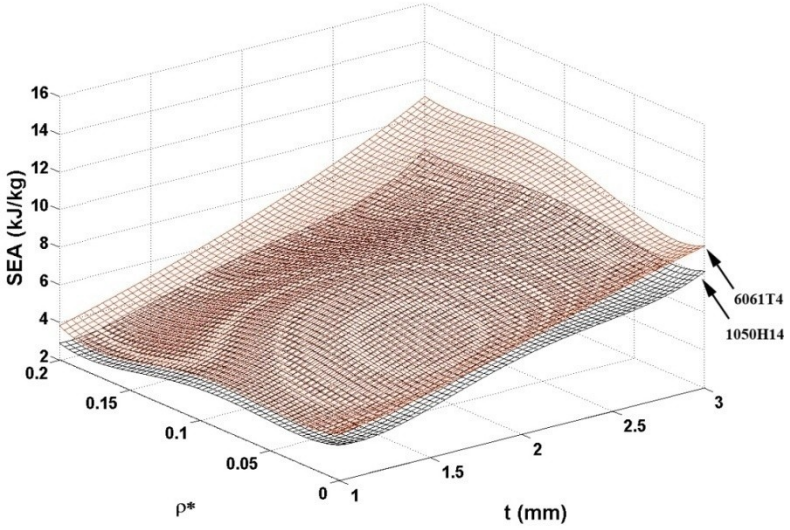

(a)

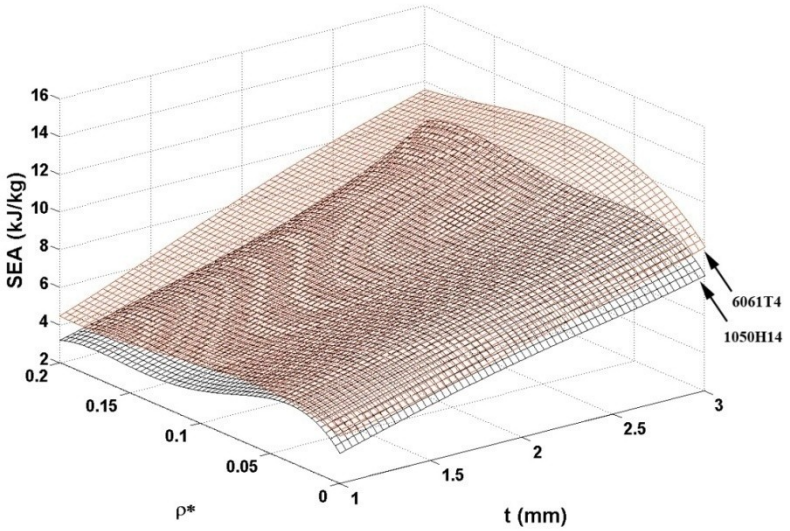

(b)

Figure 8.7. Response surface of SEA of filled boxes; a) Alulight and b) Hydro foam filling.

R^2, R_{adj}^2 and RMS values of filled box response functions are tabulated in Table 8.4. R^2 and R_{adj}^2 values listed in Table 8.4 confirm that the fitted quadratic objective functions effectively represent the mean load and SEA values of the boxes. The RMSE values of Alulight and Hydro foam filled 1050H14 Al crash boxes are higher than those of Alulight and Hydro foam filled 6061T4 Al boxes. The optimum box thickness and

foam relative density of filled boxes are tabulated in Table 8.5. It is noted in Table 8.5, higher yield strength of box material and higher plateau stresses of filler result in higher SEA values at smaller box wall thickness and foam relative densities. The highest SEA value is found in Hydro foam filled 6061T4 Al box with the optimum wall thicknesses of 2.7 mm and filler foam relative density of 0.0471.

Table 8.4. R2, R_{adj}^2 and RMSE values for RMS of partially foam filled crush box**.**

Crush Box	Response Function	R^2	R_{adj}^2	RMSE
1050H14-Alulight Foam	Mean Load	0.9958	0.9954	0.9912
	SEA	0.9966	0.9963	0.1098
6061T4-Alulight Foam	Mean Load	0.9988	0.9987	0.7193
	SEA	0.9967	0.9964	0.1400
1050H14-Hydro Foam	Mean Load	0.9964	0.9961	1.0290
	SEA	0.9896	0.9887	0.2289
6061T4-Hydro Foam	Mean Load	0.9992	0.9992	0.6379
	SEA	0.9965	0.9962	0.1630

Table 8.5. Optimum thickness and relative foam density of partially Alulight and Hydro foam filled 1050H14 and 6061T4 Al boxes.

Material Combination	**1050H14-Alulight Foam**	**6061 T4-Alulight Foam**	**1050H14-Hydro Foam**	**6061 T4-Hydro Foam**
t (mm)	3	2.8389	3	2.7659
ρ^*	0.1114	0.0878	0.0508	0.0471
SEA(kJ/kg)	8.5648	10.1439	9.8894	11.3723

The variations of mean load and SEA values empty crush box with wall thickness are shown given in Figures 8.8(a) and (b) for 1050H14 and 6061T4 Al boxes, respectively. The maximum load value, 55 kN, as shown in these curves, corresponds to

an empty tube wall thickness higher than 3 mm. Even with Hydro foam filling of 1050H14 Al crash box, SEA values are lower than that of empty 1050H14 Al crash box with a tube wall thickness of 3.88 mm. However, 3.45 mm thick 6061T4 Al crash box has lower SEA values than Hydro foam filled 6061T4 Al crash box (Figure 8.8(b)). When design range is considered, the increases in SEA values with Alulight and Hydro foam filling of 1050H14 Al crash box are about 5.6% and 21.9%, respectively. The increases in SEA values with Alulight and Hydro foam filling of 6061T4 Al are 6.7% and 19.7%, respectively.

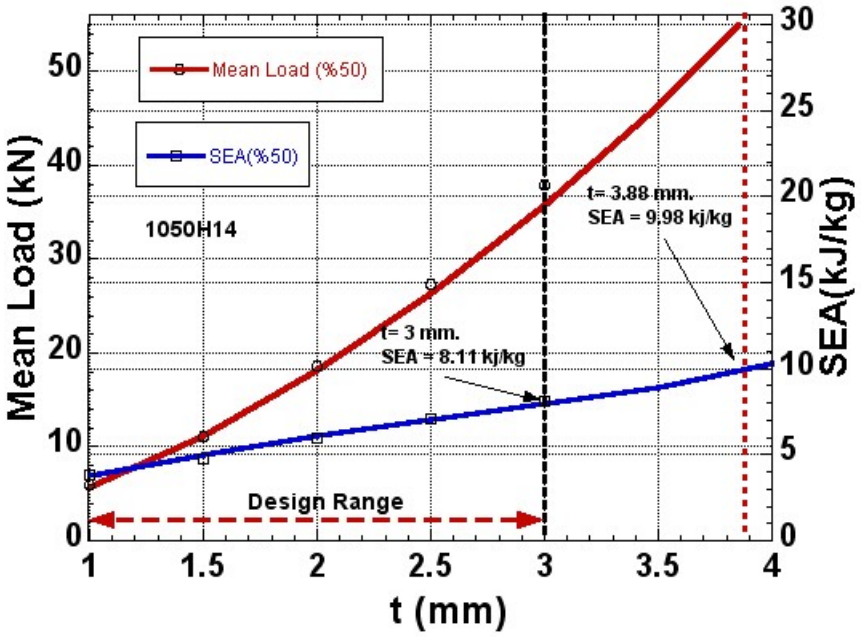

(a)

Figure 8.8. Mean load and SEA vs. empty box thickness; a) 1050H14 and b) 6061T4 Al crash box.

(cont. on next page)

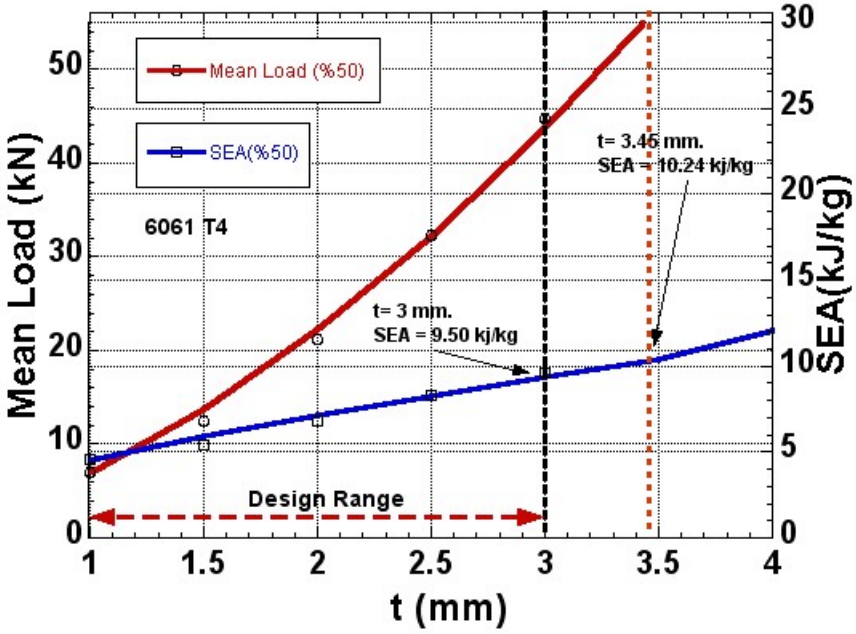

(b)

Figure 8.8. (cont.)

CHAPTER 9

DISCUSSION

9.1.Comparison of Mean Load Values

The analytical models of full foam filling generally include empty crash box mean load, foam mean load, and the interaction (between foam filler and crash box load) as in the form of

$$P_{m,,filled} = P_{m,e} + b^2\sigma_f + C_{avg}\sqrt{\sigma_f\sigma_0}\,bt \quad (9.1)$$

The interaction coefficient, C_{avg}, presents the level of interaction between wall and filler. The foam filler deformation in partially filled boxes occurs at a later stage of the deformation, starting after 40-60 mm displacement. Up to these displacements, empty tube crushing load and the friction forces between foam filler and box walls are merely effective on the deformation loads. Based on this, Equation 9.1 is rearranged, by extracting the filler crushing load, as,

$$P_{m,filled} = P_{m,e} + C_{avg}\sqrt{\sigma_f\sigma_0}\,bt \quad (9.2)$$

The empty box mean load , $P_{m,e}$, is given as,

$$P_{m,e} = K\,\sigma_0 b^{1/3} t^{5/3}, \quad (9.3)$$

where, K is a dimensionless constant and its value can be found by simply fitting Equation 9.3 with the experiment and simulation mean load values. In the calculation of the analytic mean load values for partially filled crash boxes, C_{avg} in Equation 9.2 is taken as 5.5. The fitting gives the value of K as 11.3 for the crash box without montage plates (Figures 9.1(a) and (b)). The same value of K was found previously for the empty square section Al boxes by Hanssen et al.(Hanssen, et al. 1999). However, in the study of Hanssen et al.(Hanssen, et al. 1999) the square section boxes were fully filled with Hydro Al foam without trigger mechanism.

The tested G1 and G2 box geometries without montage plates accommodate triggers at both ends of foam filled section. The mean load values of empty crash boxes with montage plates are further fitted with Equation 9.3 and the value of K is found 13.06 (Figures 9.1(c) and (d)), the same with the value reported by Abromowicz and Jones (Abramowicz and Jones 1986). The variation of mean load values of G1, G2, G1WP and G2WP crash boxes with filler relative density are shown in Figures 9.2(a), (b), (c) and (d), respectively. It is also noted in the same graphs, the fitted K values of 11.3 and 13.06 give good correlations with the experimental and simulation results. As with simulations, the analytic model overestimates the mean load values of 2.5 mm thick empty and partially filled crash boxes, depicted in Figures 9.2(a), (b), (c) and (d).

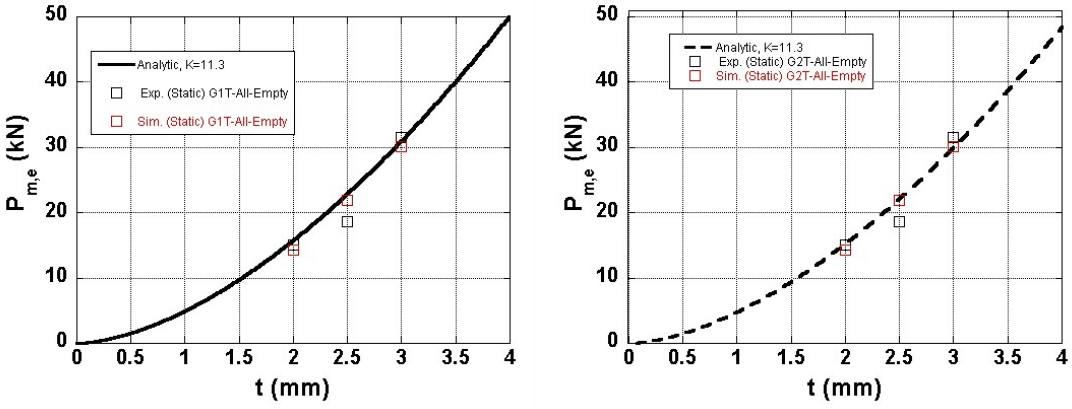

(a) (b)

Figure 9.1. $P_{m,e}$ vs. thickness graph for a) G1, b) G2, c) G1WP and d) G2WP empty crash boxes

(cont. on next page)

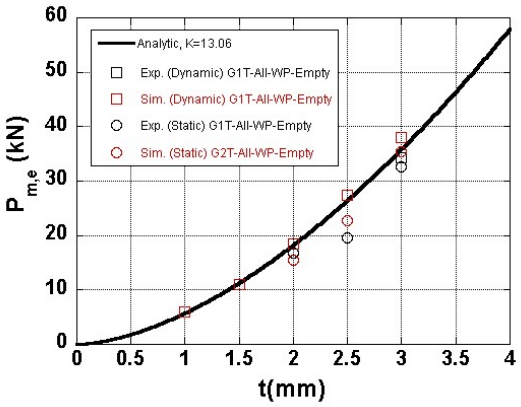

(c)

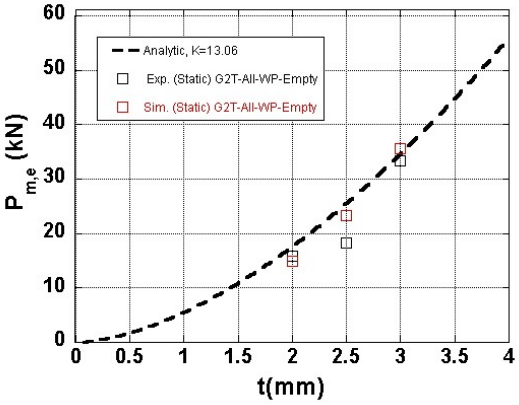

(d)

Figure 9.1. (cont.)

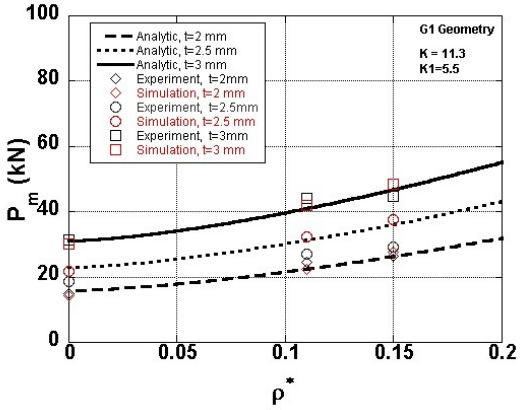

(a)

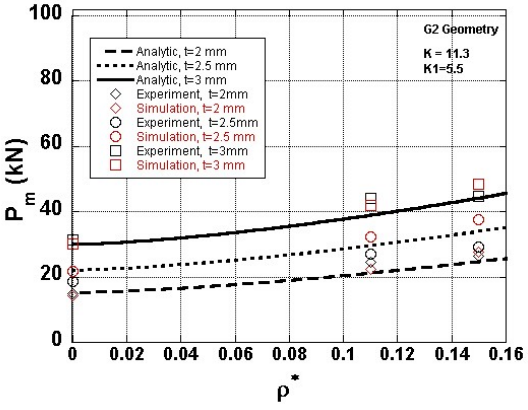

(b)

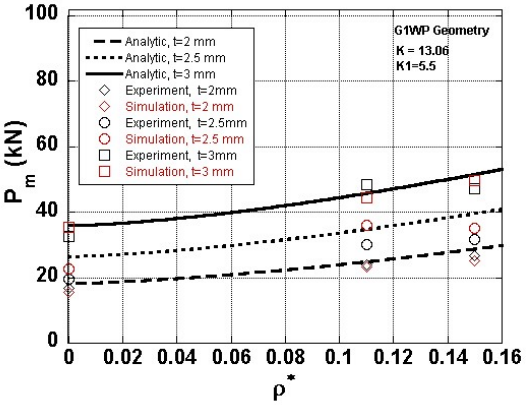

(c)

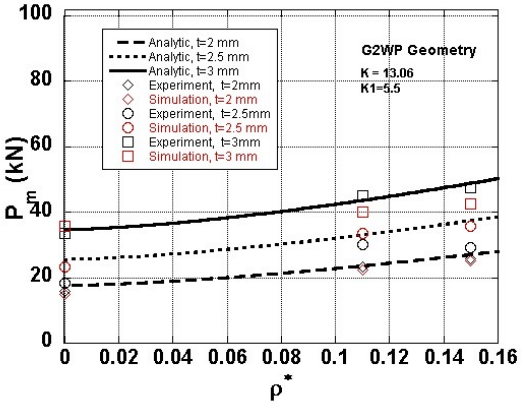

(d)

Figure 9.2. The change of P_m with filler relative density; a) G1, b) G2, c) G1WP and d) G2WP empty and partially foam filled crash boxes.

The dynamic simulation and analytical mean load values as function of filler relative density are further shown in Figure 9.3(a). In the dynamic simulation, the analytic approach for predicting mean load values is shown to found ineffective in Figure 9.3(a) since it underestimates the mean loads of the boxes with montage plates. Figure 9.3(b) shows the variation of mean load values with the box thickness and the foam filler relative density. The simulation mean load values shown in the same figure increase with increasing both thicknesses and foam filler density.

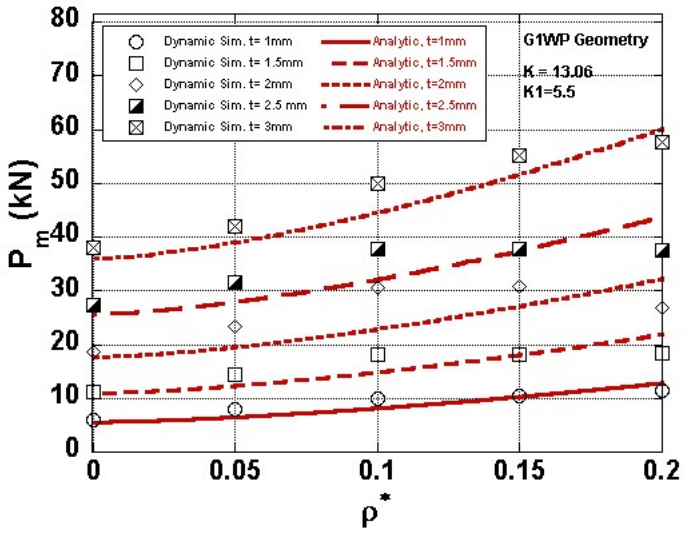

(a)

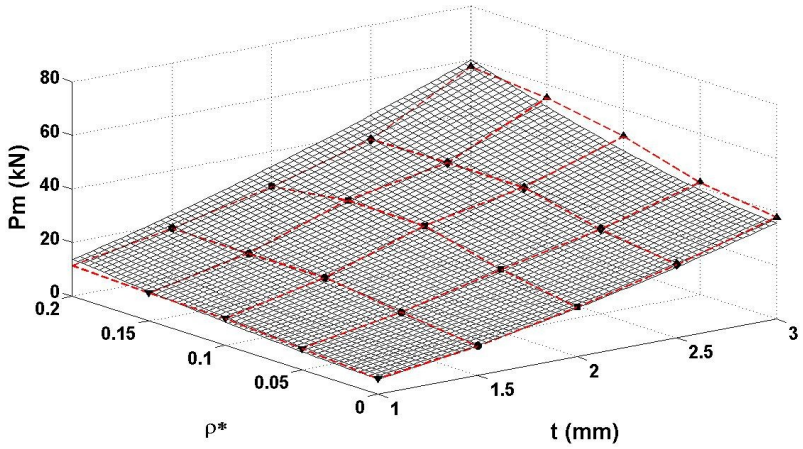

(b)

Figure 9.3. a) 2D and b) 3D representation of P_m vs. thickness graphs for dynamic simulation of G1WP.

9.2.Stroke Efficiency of Crash Boxes

In all crash boxes tested and simulated, the SE values decreases with foam filling as compared with empty boxes (Figures 9.4(a-d)). The reduction of SE values of empty boxes with foam filling was also previously reported for foam filled square Al boxes (Hanssen, et al. 2000a, Seitzberger, et al. 2000). Figure 9.5 shows further the variation of SE values with the plateau stress relative density ratio. In the same figure, the variation SE values with the plateau stress relative density ratio of Alulight foam filled square steel (RST37) and Hydro Al full foam filled square steel and Al (6060T4) tubes are also shown for comparison. It should be noted that the Alulight AlSi10 foams used in this study have lower σ_p/ρ^* ratios than those of Alulight AlMg0.6Si0.3 and Hydro AlSi8Mg foams which were previously used to fill square sections by Seitzberger et al. (Seitzberger, et al. 2000) and Hanssen et al.(Hanssen, et al. 1999), respectively. The SE values as shown in Figure 9.5 decrease slightly with increasing foam plateau stress relative density ratio and SE values reach almost a constant value of about 0.55 after a foam plateau stress relative density ratio of 30.

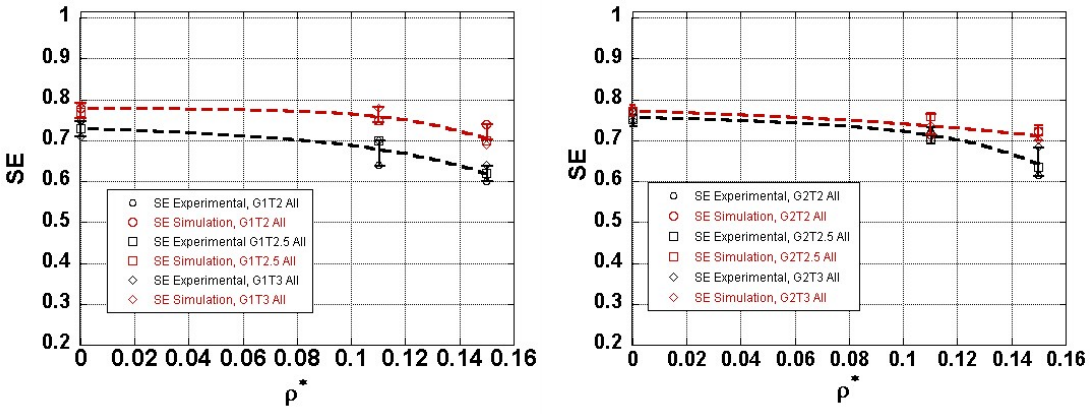

(a) (b)

Figure 9.4. Stroke efficiency vs. relative density graphs of a) G1, b)G2, c) G1WP and d)G2WP.

(cont. on next page)

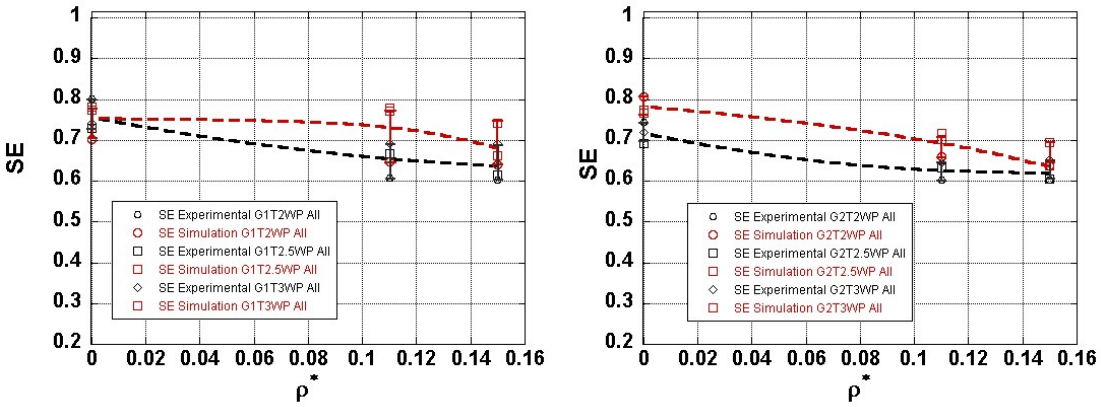

(c) (d)

Figure 9.4. (cont.)

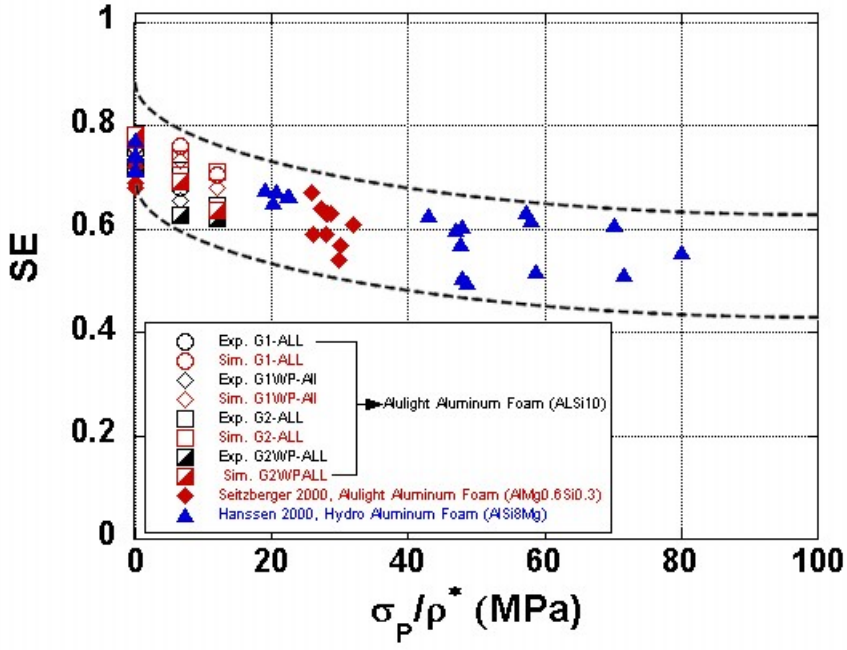

Figure 9.5. Stroke efficiency vs. plateau stress relative density change ratio.

9.3.Crush force efficiency of crash boxes

The variations of experimental and numerical force efficiency (AE) values of G1, G2, G1WP and G2WP geometry with foam filler relative density are shown sequentially in Figures 9.6(a), (b), (c) and (d). In contrast with SE values, the

experimental and numerical AE values increase with increasing foam filler relative density in all box geometries as shown in Figures 9.6(a), (b), (c) and (d) . The experimental AE values are further found to be well accord with the below equation developed by Hanssen (Hanssen, et al. 1999),

$$AE = \frac{K*\sigma_o*b^{2/3}*t^{1/3}+\sigma_p*b^2+5.5\sqrt{\sigma_o*\sigma_p}*b*t}{\frac{K}{AE_0}*\sigma_o*b^{2/3}*t^{1/3}+\sigma_p*b^2+0.6\sqrt{\sigma_o*\sigma_p}*b*t} \quad (9.4)$$

where, AE_0 is the empty crash box AE. Since Al foam plateau stress is considered to be not affect the mean deformation loads of partially filled boxes at early deformation stages, the foam crushing load term is extracted from Equation 9.4. In this case Equation 9.4 is written as,

$$AE = \frac{K*\sigma_o*b^{2/3}*t^{1/3}+5.5\sqrt{\sigma_o*\sigma_p}*b*t}{\frac{K}{AE_0}*\sigma_o*b^{2/3}*t^{1/3}+5.5\sqrt{\sigma_o*\sigma_p}*b*t} \quad (9.5)$$

The average AE_0 values of the tested empty tubes are tabulated in Table 9.1. The calculated AE_o values are inserted in Equation 9.5 and then AE values of the filled boxes are calculated. Figure 9.7(a) and (b) show the variations of the calculated AE values with plateau stress relative density of crash boxes without and with fixing plate, respectively. For comparison, the AE values of full foam filling of Hannsen et al. (Hanssen, et al. 2000b) are also shown in the same figure. AE values shown in these graphs increases with increasing plateau stress relative density ratio. Similar to SE values at increasing plateau stress relative density ratios, AE values reach a constant value as seen in Figures 9.7(a) and (b). It should be noted that AE equals to 1 for a perfect energy absorber. However, the variations of the stress values of the box and the foam filler lower the AE values below 1. As shown in Figures 9.7(a) and (b), in fully foam filled tubes, AE values increase with increasing plateau stress relative density ratio and eventually reach to a maximum value of approximately 0.90 at a plateau stress relative density ratio of 60 (Hanssen, et al. 1999). Similarly, the AE values of partially

foam filled boxes increase with increasing plateau stress relative density ratio but the increase is less pronounced in partially foam filled boxes. The slope of partially and fully foam filled boxes AE-plateau stress relative density ratio curves decrease with increasing plateau stress relative density ratios, showing a reduced effect of foam filling on the mean load values of filled structures at increasing plateau stress relative density ratios.

Table 9.1.Empty crash box crush force efficiency values.

Geometry	AE_0
G1	0.560
G1WP	0.565
G2	0.500
G2WP	0.577

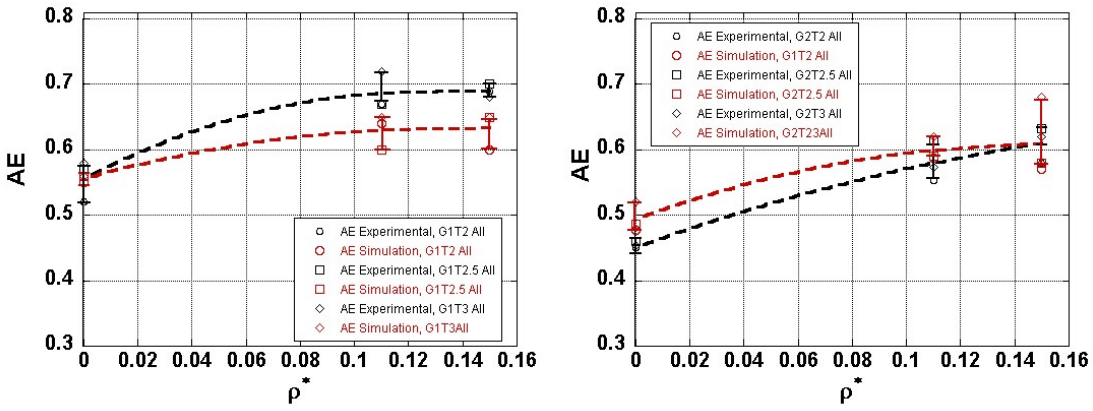

(a) (b)

Figure 9.6. Crush force efficiency vs. relative density of a) G1, b)G2, c)G1WP and d)G2WP.

(cont. on next page)

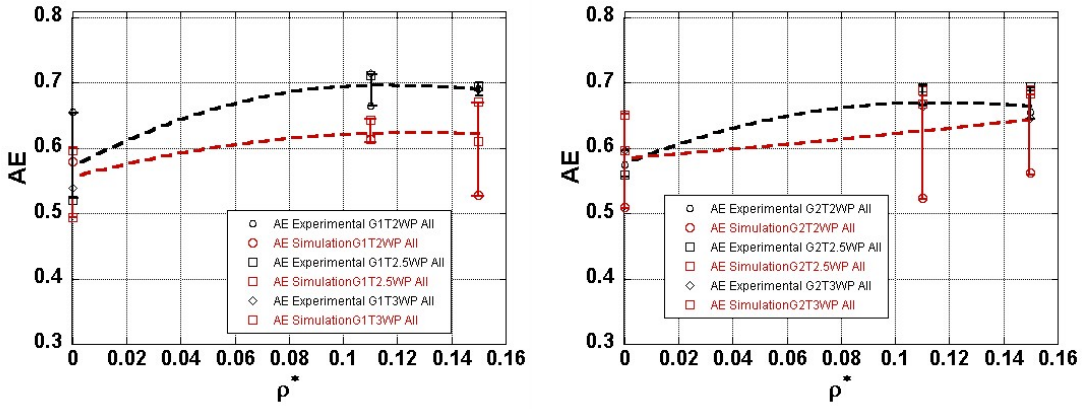

(c) (d)

Figure 9.6. (cont.)

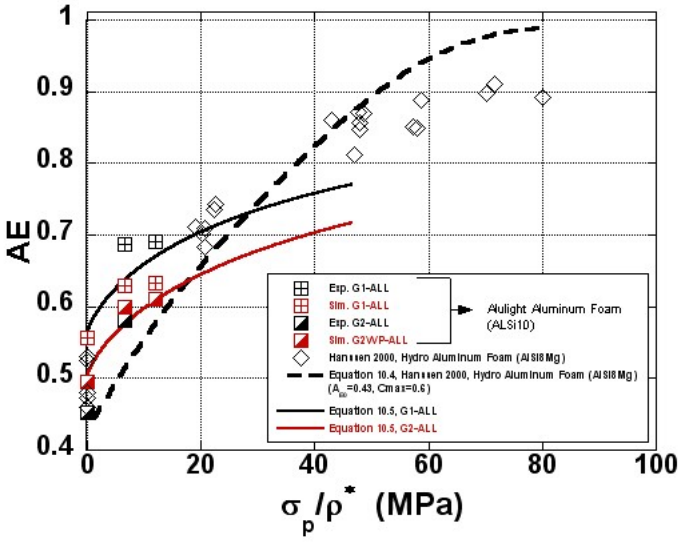

(a)

Figure 9.7. AE vs. plateau stress /relative density of crash boxes a) without and b)with fixing plate.

(cont. on next page)

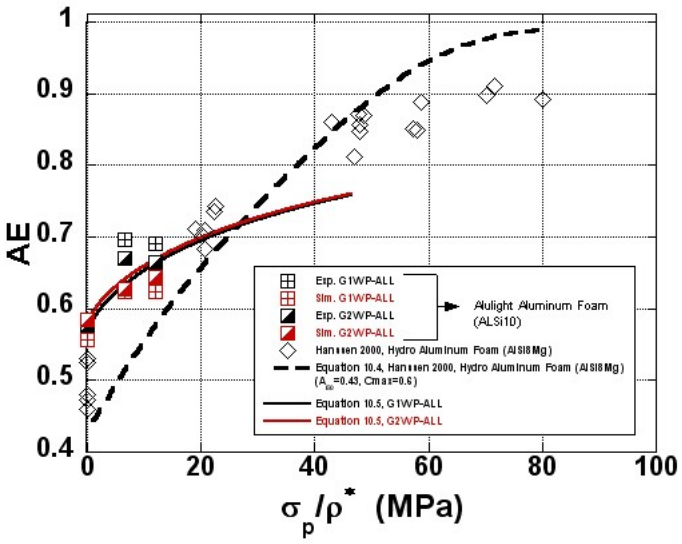

(b)

Figure 9.7.(cont.)

9.4.Total Efficiency of Crash Boxes

The variations of G1, G2, G1WP and G2WP geometries experimental numerical crush box total efficiency (TE) values with foam filler relative density are shown sequentially in Figures 9.8(a), (b), (c) and (d). The numerical and experimental TE values shown in these graphs are very similar to each other. There exists a slight increase in TE values with lower relative density foam filling, while at increasing foam filler relative densities TE values decrease. This behavior may be attributed to the relatively small increase in the man load values of filled boxes at increasing foam relative densities.

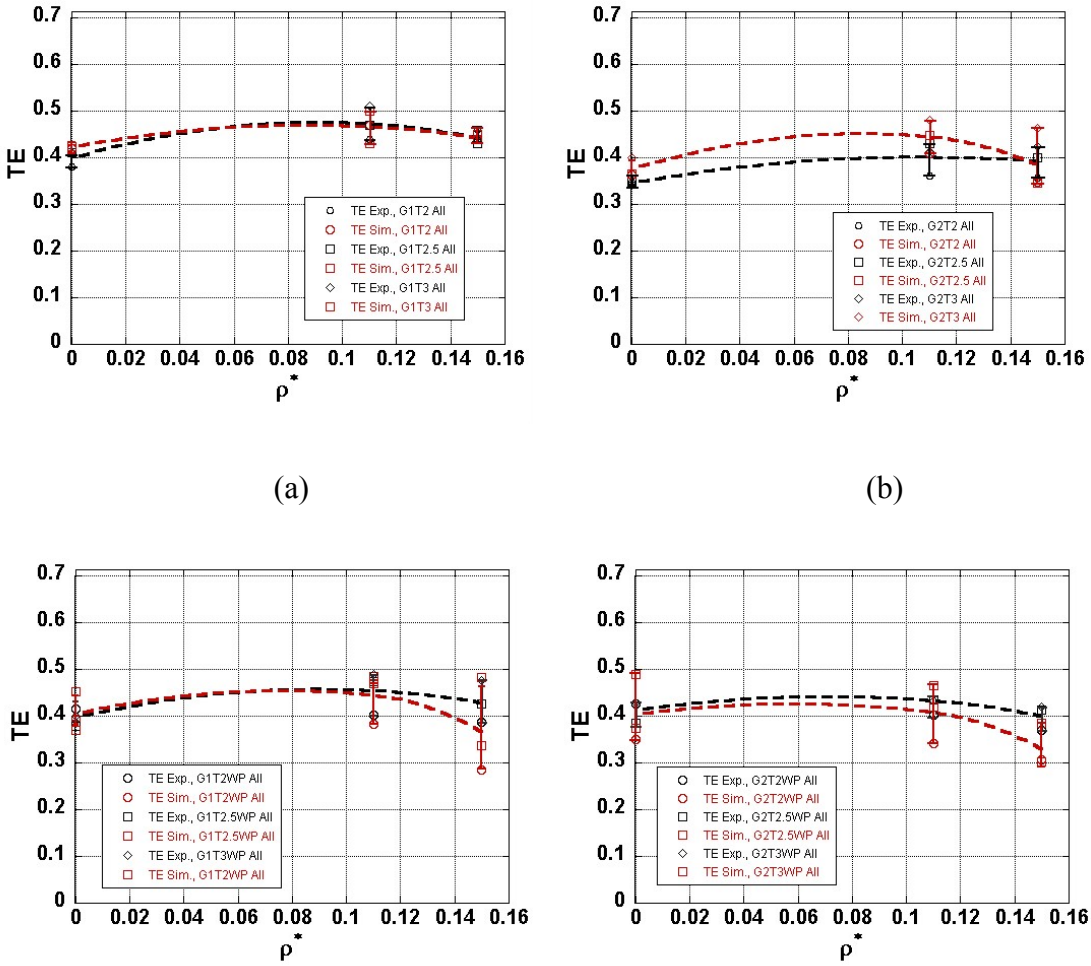

(a) (b)

(c) (d)

Figure 9.8. Total efficiency vs. relative density of a) G1, b)G2, c)G1WP and d)G2WP.

9.5.Foam filling efficiency of crash boxes

The strengthening coefficient (C) showing the effect of foam plateau strength on the mean load of filled tube (Toksoy 2003) is given as,

$$C = \frac{P_{mf} - P_{me}}{P_f} \tag{9.6}$$

where P_f is the foam filler load. Substituting Equations 9.1 and 9.2 into Equation 9.6, gives the following strengthening coefficients,

$$C = 5.5\sqrt{\frac{\sigma_0}{\sigma_f}}\frac{t}{b} \tag{9.7}$$

for partially filling and

$$C = 5.5\sqrt{\frac{\sigma_0}{\sigma_f}}\frac{t}{b} + 1 \tag{9.8}$$

for full foam filling. C values of the tested filled tubes are shown in Figure 9.9 as function of foam plateau stress relative density ratio. In same figure, C values of foam filled 6060 Al and FEE355 steel square tubes previously determined by Hanssen et al (Hanssen, et al. 1999, Hanssen, et al. 2000b) and Wang et al.(Wang, et al. 2005) are also shown for comparison. It is seen in Figure 9.9, after a critical value of foam plateau stress relative density ratio of 20, the value of C becomes constant around 2. The values of C however increase greatly with decreasing foam plateau stress relative density ratio and at very low ratios the values of C are above 10. Therefore, it can be concluded that partially foam filling are not effective in the strengthening of boxes at relatively high foam plateau stress relative density ratios as in the full foam filling.

An energy-absorbing effectiveness factor for energy absorbers was previously defined by Hsu and Jones and Jones (Hsu and Jones 2004). This factor can be used to compare the crash zone structure design parameters. The energy-absorbing effectiveness factor (ψ) is given as,

$$\Psi = \frac{\text{total elastic and plastic strain energy absorbed by a structural member}}{\text{energy absorbed in the same volume of material up to failure in tension}} \tag{9.7}$$

Equation 9.7 can also be rewritten as,

$$\Psi = \frac{\int_0^{\delta_f} P d\delta}{V \int_0^{\varepsilon_r} \sigma d\varepsilon} \tag{9.8}$$

where, P is the axial crushing load , δ is the corresponding axial crushing displacement, δ_f is the final displacement, V is the volume of the material in the crash element and ε_r and σ_0 are the uniaxial tensile engineering rupture strain and flow stress, respectively. The static and dynamic energy-absorbing effectiveness factor (ψ') can be written as,

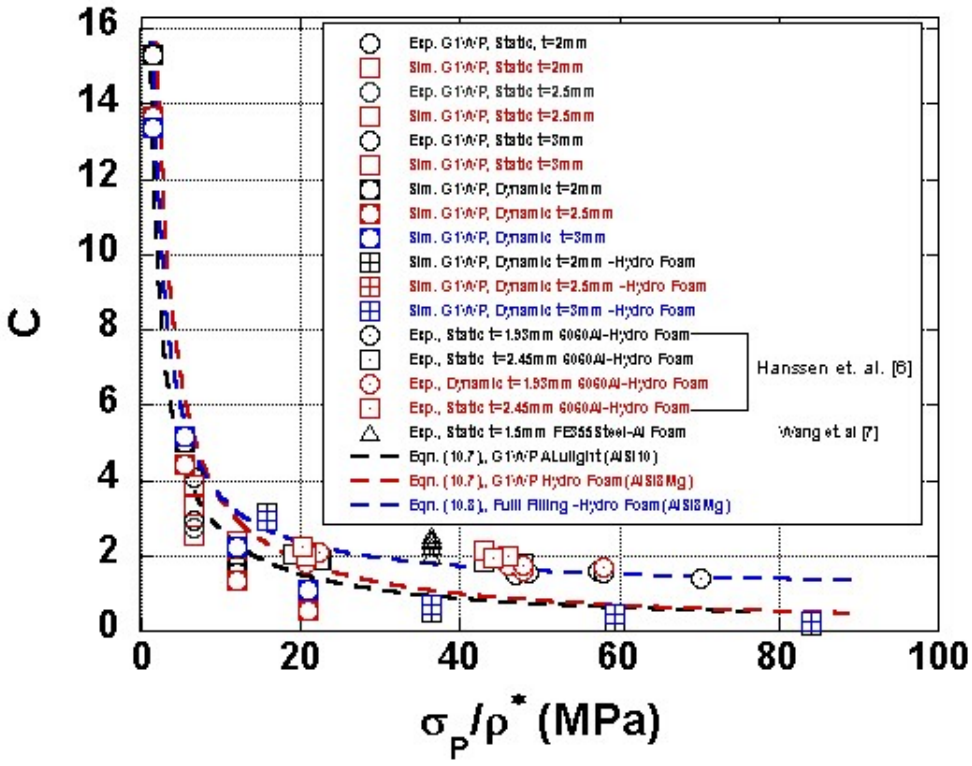

Figure 9.9. The variation of strengthening coefficient with foam plateau stress relative density ratio in fully and partially filled boxes.

$$\Psi = \frac{P_m \delta_f}{\sigma_0 A L \varepsilon_r} \tag{9.9}$$

and

$$\Psi' = \frac{GV_0^2}{2\sigma_0 AL\varepsilon_r} \tag{9.10}$$

where, G is the impacted mass, V_0 is initial velocity of the projector and L is the initial length of absorber. As an engineering approach, L can be replaced by $4/3\delta_f$ in order to reflect the axial length of an energy absorber participating to energy absorption (Jones In Press). The energy absorption of foam filler in the case of filled tube is added to the denominator of Equations 9.9 and 9.10. The energy absorption in a simple compression then becomes,

$$E_f = \sigma_p A_f \delta_f (4/3)\varepsilon_r \tag{9.11}$$

Equations 9.9 and 9.10 are rearranged with the above for static loading as

$$\Psi = \frac{3P_m}{4\varepsilon_r(\sigma_0 A_0 + \sigma_p A_f)} \tag{9.12}$$

and for dynamic loading as

$$\Psi' = \frac{GV_0^2}{8\delta_f\varepsilon_r(\sigma_0 A_0 + \sigma_p A_f)} \tag{9.13}$$

By substituting Equations 9.1 and 9.2 into Equation 9.12, energy-absorbing effectiveness factor becomes,

$$\Psi = \frac{3*\left(K\,\sigma_0 b^{1/3} t^{5/3} + b^2 \sigma_f + C_{avg}\sqrt{\sigma_f \sigma_0}\, bt\right)}{4\varepsilon_r\left(\sigma_0 A_0 + \sigma_p A_f\right)} \tag{9.14}$$

for full foam filled and

$$\Psi = \frac{3*\left(K\,\sigma_0 b^{1/3} t^{5/3} + C_{avg}\sqrt{\sigma_f \sigma_0}\, bt\right)}{4\varepsilon_r\left(\sigma_0 A_0 + \sigma_p A_f\right)} \tag{9.15}$$

for partially filled crash boxes. The energy-absorbing effectiveness factors of the tested filled boxes are shown in Figures 9.10 (a) and (b) for static and dynamic loading, respectively. On the same graphs, energy-absorbing effectiveness factor of fully Hydro foam filled 6060T4 Al square boxes (Hanssen, et al. 2000b) are also shown for comparison purpose. The static energy-absorbing effectiveness factors of partially filled boxes are higher than those of fully foam filled tubes, Figure 9.10 (a). This may be attributed to the relatively lower flow stress of 1050 H14 alloy (107.5 MPa) than 6060T4 Al alloy (118 MPa). Static and dynamic The energy-absorbing effectiveness factors in fully foam filled structures increase linearly with foam plateau stress relative density ratio as depicted in Figures 9.10(a) and (b). Somewhat similar increase in the numerical and experimental energy-absorbing effectiveness factors of the statically tested filled boxes is also seen. However, unlike fully foam filled structures, increasing plateau stress values of partially filled boxes result in reductions in the energy-absorbing effectiveness factor of dynamically tested partially filled boxes, Figure 9.10(b). The dynamic energy-absorbing effectiveness factor values start to decrease approximately after about 0.10 relative density for both Alulight and Hydro Al partially filled foam 1050H14 Al boxes. Analytic calculations on hydro foam filled 6060T4 Al crash boxes show that partially filled structures have lower energy-absorbing effectiveness factor values since the less material involves in the crash energy absorption of partially filled structures. Theoretical analysis further show that partially Alulight foam filling with relatively low plateau stress results in higher energy-absorbing effectiveness factors than partially Hydro foam filling, Figure 9.10(a).

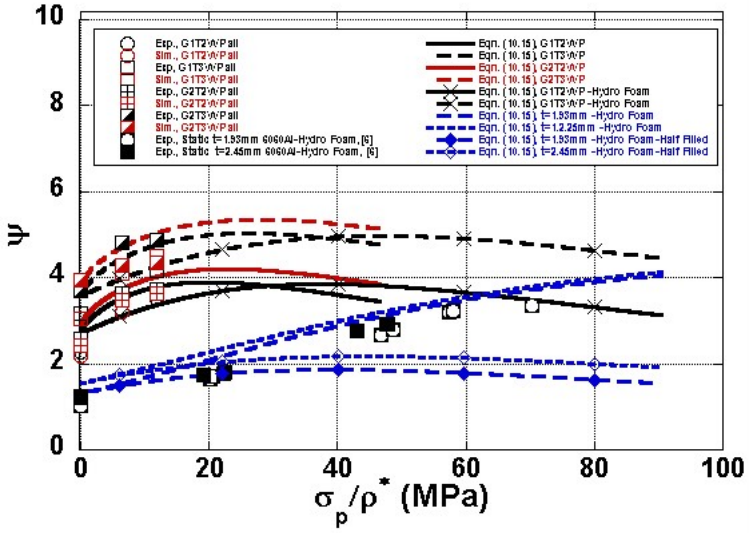

(a)

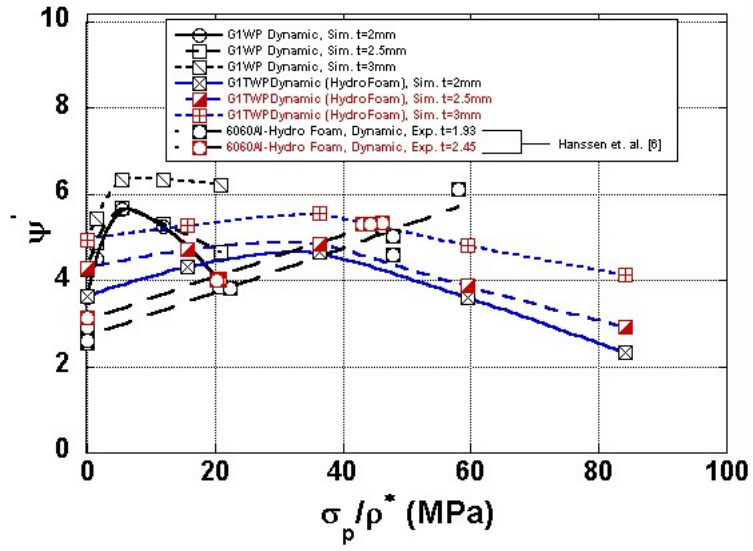

(b)

Figure 9.10. Energy-absorbing effectiveness factor for a) statically and b) dynamically tested boxes.

9.6.SEA analysis of crash boxes

SEA is defined as the absorbed energy divided by total mass of the crash element (m_t) as,

$$SEA = \frac{P_m * \delta}{m_{total}} \tag{9.14}$$

Energy absorption of filled column is generally calculated by multiplying the mean load by effective crash distance (0.75) (Santosa and Wierzbicki 1998a). Since experimental and simulation SEA values are determined at 50% deformation of empty and foam filled structures, the crash length is taken as 0.5L. Equation 9.14 can also be rewritten as,

$$SEA = \frac{\left(P_{m,e} + C_{avg}\sqrt{\sigma_f \sigma_0}\, bt\right) * 0.5 * L}{\rho_{tube} * 2bt * L + \rho_{foam} * (b-t)^2 * L_{foam}} \tag{9.15}$$

Figures 9.11(a-d) show sequentially the variations of the calculated, experimental and numerical SEA values of G1, G2, G1WP and G2WP geometries as function of foam relative density. The difference between numerical and experimental SEA values is 9.14% and between experimental analytic prediction 7.5% on the average. The optimization algorithm is run for Pm (Equation 9.1) and SEA (Equation 9.15) with the same constraints used in Chapter 9. The optimum thickness and relative density for G1WP crash box are found 3 mm and 0.1706, respectively. With these parameters, 7.13% gain in SEA values of the filled box is obtained, as compared with the empty crash box with the same thickness. Actually, the SEA values of the dynamical simulation of the partially foam filled crash boxes do not increase constantly with increasing relative density of foam filler and the analytic equation developed cannot capture this behavior. Therefore, the optimization algorithm gives higher relative density values than the response surface algorithm.

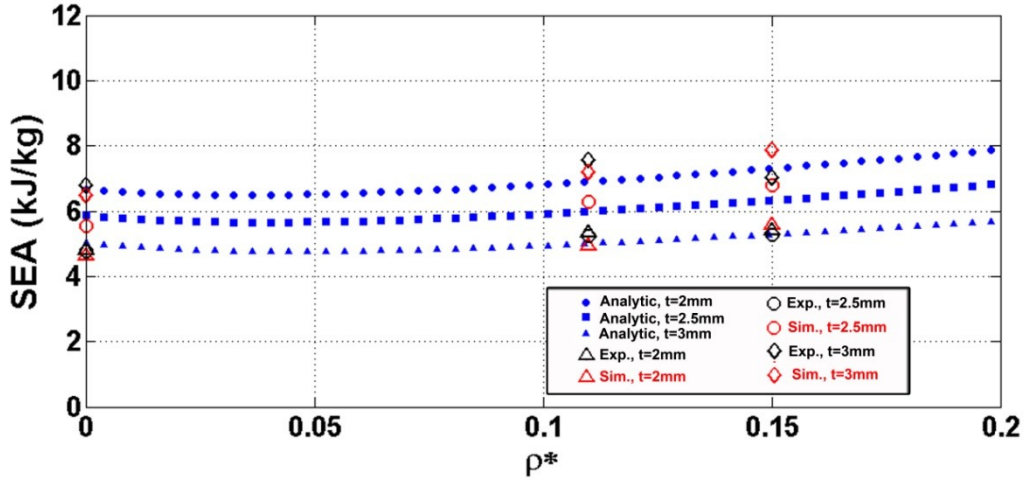

(a)

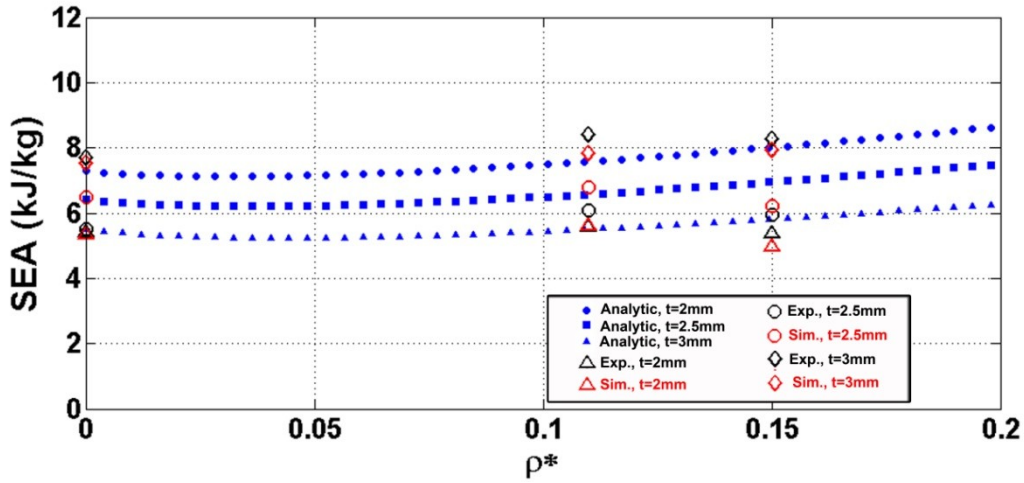

(b)

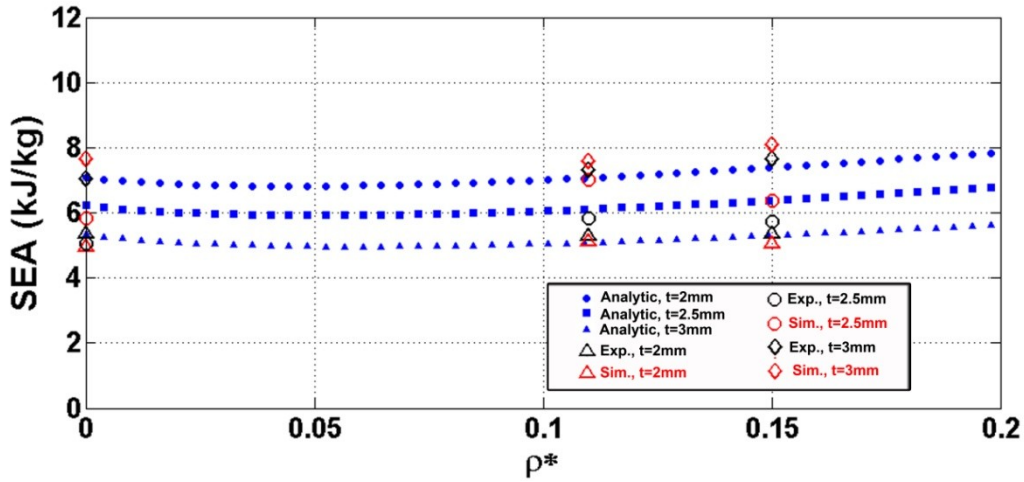

(c)

Figure 9.11. SEA vs. relative density of a) G1, b)G2, c)G1WP and d)G2WP.

(cont. on next page)

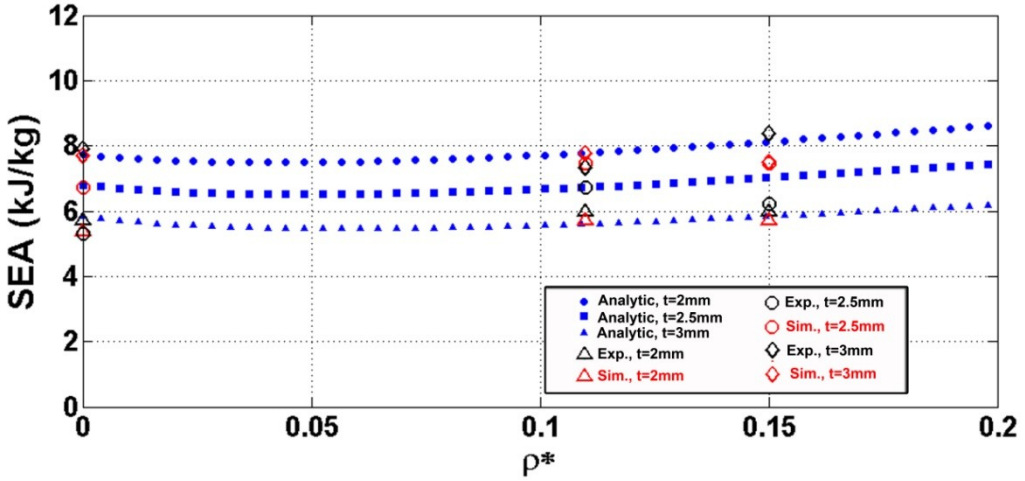

(d)

Figure 9.11. (cont.)

The variations of SEA values G1WP crash box with thickness and foam filler relative density are shown in Figure 9.12. Although, the experiments, static and dynamic simulations and response surface algorithm analysis show that the partially foam filling has higher SEA values than those of empty box within the studied box thickness and foam relative density range, analytical calculations showed that partially foam filling is efficient after a certain box thickness and foam filler density as shown in Figure 9.12.

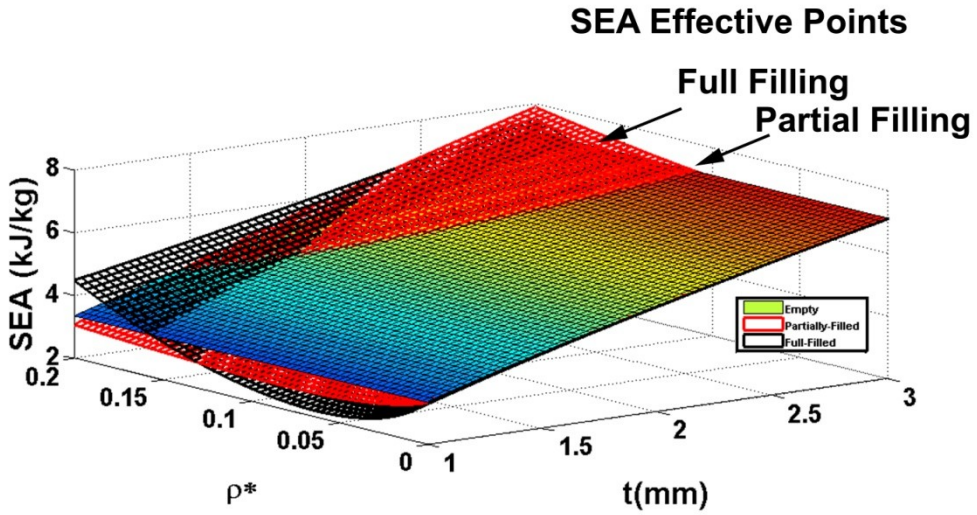

Figure 9.12. 3D plot of SEA variation with thickness and filler relative density for G1WP crash box.

CHAPTER 10

CONCLUSIONS

The present thesis focused on the optimization of the crushing behavior of partially foam filled commercial 1050H14 Al crash boxes in 2, 2.5 and 3 mm wall thickness. The boxes were partially filled, 50% of the total length of the box, with commercially available closed-cell Al foam (Alulight AlSi10) with two relative densities, 0.11 and 0.15. In the first part the thesis, empty and foam filled boxes with various configurations, with and without trigger and with and without corrugations were crushed at a quasi-static strain rate in order to determine the box crushing behavior and to provide experimental data for the subsequent modeling and optimization studies. Few filled and empty boxes were also compression tested at a relatively high velocity (5.5 mm/s) using a drop-weight impact tester. In the second part of the thesis, the quasi-static crushing of empty and filled boxes was simulated using LS-DYNA explicit finite element program. In the simulations, the box material was modeled with plastic-kinematic material card (Mat 3) and the foam filler with the Honeycomb model (Mat26). To simulate quasi-static crushing, the material mass density was scaled down by a factor of 1000 and the deformation speed was increased to 2 m/s. The final part of the thesis focused on the optimization of partially foam filled 1050H14 Al crash box crushing using the response surface methodology to maximize the specific energy absorption. A full factorial design was used to create the sample mesh. Dynamic test simulations were also run in accord with the design points of the sampling mesh. In the optimization, the wall thickness and foam filler relative density were selected as independent variables, while a mean crushing load of less than 55 kN, a box wall thickness between 1 and 3 mm and a foam filler density ranging between 0 and 0.2 were considered as constraints. The used optimization methodology was also applied to the boxes made of a stronger Al alloy, 6061T4 Al, and filled with a higher strength Al foam, Hydro Al closed cell foam, in order to clarify the effect of box material and foam filler strength on the crush behavior of the filled boxes. Finally, the benefits of partially

foam filling were evaluated. The results of crash analysis of the studied 1050H14 Al boxes were also compared with those of commercially available other boxes made from 6061T4 Al and steel. Following conclusions can be made based on the experimental, simulation and optimization studies on the partially filled crash boxes:

1. Honeycomb model of Alulight AlSi10 aluminum foam was successively captured the foam compression behavior at varying foam relative densities and also the deformation of the foam filler in the filled boxes.
2. The triggers and corrugations formed/machined on the box surface and the montage plate changed the folding initiation site on the box wall. The folding started from one of the ends of the box near the compression plate in the boxes without triggers and corrugations, while the folding started from the triggers and /or corrugations in the boxes with triggers and corrugations. The triggers, corrugations and the montage plate decreased the initial peak load and mean load values of empty boxes. The trigger induced a more uniform folding in empty box, by lowering the differences between initial peak load and the subsequent peak load values in the load-displacement curves.
3. In the filled boxes without montage plates, the fold formation was observed to change from regular to irregular as the box thickness decreased and the foam filler relative density increased. The SEA values of filled crash boxes were similar to those of empty crash boxes between 20 and 40 mm displacement; however, the SEA values of filled boxes increased over those of empty boxes after about 40 mm displacement.
4. Similar to the crash boxes without montage parts, the SEA values of partially filled crash boxes increased over those of empty boxes after about displacement between 40-60 mm.
5. In empty crash boxes tested without and with montage plates, two regular symmetric folds formed. Although, the foam filler microscopically was found to not completely enter in between the folds, it increased the number of folds to 3 in the filled boxes both with and without montage plates.
6. The initial peak load values of dynamically tested boxes were found to be higher than those of quasi-statically tested boxes. However, the mean load values of dynamically and quasi-statically tested empty and filled boxes were almost the

same. The deformation patterns of dynamically and quasi-statically tested empty and partially filled crash boxes were also found to be very similar.

7. The simulation load values showed good correlation with experimental load values in both 2 and 3 mm thick empty and foam filled crash boxes with and without montage parts. The numerical mean load values of the crash boxes with 2.5 thickness were however slightly higher than experimental mean load values in the boxes with and without montage parts.
8. Experimental and numerical deformation patterns and load values of dynamically tested empty and partially filled crash boxes were found very much similar to each other. This further proved the validity of the rate insensitivity of the foam and box base material model used in the dynamic crash simulations. This also showed that the micro inertial effects, if any, had negligible effects on the load-displacement curves of empty and filled boxes.
9. Within the investigated tube thickness and foam relative density range, the energy absorption of 1050 H14 Al boxes was optimized at 3 mm box wall thickness and 0.1114 (Alulight) and 0.0508 (Hydro foam) foam filler relative density. The corresponding specific energy values of 1050 H14 Al boxes with these optimized parameters were however lower than that of empty box at 55 kN mean load.
10. Increasing box material strength however decreased the optimum tube wall thickness and foam relative density and increased the SEA. Increasing foam plateau stress provided further reduction in the values of the optimum parameters and increase in specific energy absorption.
11. The increases in SEA values with Alulight and Hydro foam filling of 1050H14 Al crash box were about 5.6% and 21.9%, respectively. The increases in SEA values with Alulight and Hydro foam filling of 6061T4 Al were however higher, 6.7% and 19.7%, respectively.
12. In all crash boxes tested and simulated, the stroke efficiency values decreased with foam filling below those of empty boxes. Based on the experimental and simulation results, it was shown that the stroke efficiency in filled boxes reached almost a constant value at about 0.55 after a foam plateau stress relative density ratio of 30. The crash efficiency of partially foam filled boxes also increased with increasing foam plateau stress- foam relative density ratio but the increase was shown to be less pronounced as compared with fully foam filling.

13. The interaction between foam filler and tube wall increased with decreasing foam plateau stress-relative density ratio. It was concluded that partially foam filling was not effective in the strengthening of the boxes at relatively high foam plateau stress-foam relative density ratios as in the fully foam filling.
14. An energy absorbing effectiveness factor was calculated for the investigated filled boxes. The static energy-absorbing effectiveness factors of partially filled boxes were shown to be higher than those of fully foam filled tubes. Theoretical analysis further showed that partially Alulight foam filling with relatively low plateau stress resulted in higher energy absorbing effectiveness factor than partially Hydro foam filling.
15. A design criterion was developed for the foam filling of boxes. At relatively low foam densities partially and fully foam filled boxes were energetically less efficient than empty boxes, while at increasing foam filler densities fully foam filing became the most efficient. Partially foam filling became the most efficient at relatively high foam filler densities and box wall thicknesses.
16. Present study clearly showed that in the designing with the crash boxes, the foam filler plateau stress and box base material strength should be high for higher energy absorptions. The selection of the fully and partially foam filling must be considered based on the foam filler density and tube wall thicknesses used.

REFERENCES

Abedrabbo, N., Mayer, R., Thompson, A., Salisbury, C., Worswick, M. J. and Van Riemsdijk, I., 2009, Crash response of advanced high-strength steel tubes: Experiment and model. International Journal of Impact Engineering. **36**(8): p. 1044-1057.

Abramowicz, W. and Jones, N., 1986, Dynamic progressive buckling of circular and square tubes. International Journal of Impact Engineering. **4**(4): p. 243-270.

Abramowicz, Wlodzimierz and Jones, Norman, 1984, Dynamic axial crushing of square tubes. International Journal of Impact Engineering. 2(2): p. 179-208.

Ahmad, Z. and Thambiratnam, D. P., 2009, Dynamic computer simulation and energy absorption of foam-filled conical tubes under axial impact loading. Computers & Structures. 87(3-4): p. 186-197.

Aktay, L., Kröplin, B. H., Toksoy, A. K. and Güden, M., 2008, Finite element and coupled finite element/smooth particle hydrodynamics modeling of the quasi-static crushing of empty and foam-filled single, bitubular and constraint hexagonal- and square-packed aluminum tubes. Materials & Design. 29(5): p. 952-962.

Alexander, J.M., 1960, An approximate analysis of collapse of thin cylindrical shells under axial loading. Quarterly Journal of Mechanics and Applied Mechanics. 13: p. 10-15.

Allen, B. C., Mote, M.W. and Sabroff, A. M.,1963,Method of making foamed metal

Andrews, E. W., Gibson, L. J. and Ashby, M. F., 1999a, The creep of cellular solids. Acta Materialia. 47(10): p. 2853-2863.

Andrews, E. W., Gioux, G., Onck, P. and Gibson, L. J., 2001, Size effects in ductile cellular solids. Part II: experimental results. International Journal of Mechanical Sciences. 43(3): p. 701-713.

Andrews, E. W., Huang, J. S. and Gibson, L. J., 1999b, Creep behavior of a closed-cell aluminum foam. Acta Materialia. 47(10): p. 2927-2935.

Andrews, K. R. F., England, G. L. and Ghani, E., 1983, Classification of the axial collapse of cylindrical tubes under quasi-static loading. International Journal of Mechanical Sciences. 25(9-10): p. 687-696.

Arora, J. S.,2004,Introduction to Optimum Design,Elsevier Academic Press

Asavavisithchai, S. and Kennedy, A. R., 2006, The effect of compaction method on the expansion and stability of aluminium foams. Advanced Engineering Materials. 8(9): p. 810-815.

Ashby, M. F., Evans, A. G., Fleck, N. A., Gibson, L. J., Hutchinson, J. W. and Wadley, H.N.G., 2000, Metal Foams : A Design Guide.

ASTM,2001, E8/E8M-08, Standard test methods for tension testing of metallic materials,www.astm.org, (accesed November 2009)

Avalle, M., Chiandussi, G. and Belingardi, G., 2002, Design optimization by response surface methodology: application to crashworthiness design of vehicle structures. Structural and Multidisciplinary Optimization. 24(4): p. 325-332.

Baccouche, M. Ridha and Wagner, David A., 2001, Crash strength and energy management of axially loaded extruded aluminium components reinforced with epoxy-based Terocore Foam. International Journal of Crashworthiness. 6(4): p. 539-552.

Bambach, M. R., Elchalakani, M. and Zhao, X. L., 2009, Composite steel-CFRP SHS tubes under axial impact. Composite Structures. 87(3): p. 282-292.

Banhart, J., 2000, Manufacturing routes for metallic foams. JOM Journal of the Minerals, Metals and Materials Society. 52(12): p. 22-27.

Banhart, J., 2001, Manufacture, characterisation and application of cellular metals and metal foams. Progress in Materials Science. 46(6): p. 559-632.

Banhart, J.,2007,Metal Foams—from Fundamental Research to Applications, Universities Press (India) Limited, India

Banhart, J. , 2005, Aluminium foams for lighter vehicles. International Journal of Vehicle Design 37(2/3): p. 114-125.

Bardi, F. C., Yun, H. D. and Kyriakides, S., 2003, On the axisymmetric progressive crushing of circular tubes under axial compression. International Journal of Solids and Structures. 40(12): p. 3137-3155.

Bathe, Klaus-Jürgen,1996,Finite Element Procedures,Prentice Hall, Inc

Baumgärtner, F., Duarte, I. and Banhart, J., 2000, Industrialization of Powder Compact Toaming Process. Advanced Engineering Materials. 2(4): p. 168-174.

Bonaccorsi, L. and Proverbio, E., 2006, Powder compaction effect on foaming behavior of uniaxial pressed PM precursors. Advanced Engineering Materials. 8(9): p. 864-869.

Borvik, T., Hopperstad, O. S., Reyes, A., Langseth, M., Solomos, G. and Dyngeland, T., 2003, Empty and foam-filled circular aluminium tubes subjected to axial and oblique quasistatic loading. International Journal of Crashworthiness. 8(5): p. 481-494.

Campana, Francesca and Pilone, Daniela, 2008, Effect of wall microstructure and morphometric parameters on the crush behaviour of Al alloy foams. Materials Science and Engineering: A. 479(1-2): p. 58-64.

Chen, W. and Nardhi, D., 2000, Experimental study of crush behaviour of sheet aluminium foam-filled sections. International Journal of Crashworthiness. 5(4): p. 447-468.

Chen, W. and Wierzbicki, T., 2001, Relative merits of single-cell, multi-cell and foam-filled thin-walled structures in energy absorption. Thin-Walled Structures. 39(4): p. 287-306.

Chiandussi, G. and Avalle, M., 2002, Maximisation of the crushing performance of a tubular device by shape optimisation. Computers & Structures. 80(27-30): p. 2425-2432.

Chirwa, E. C., Latchford, J. and Clavell, P., 2003, Carbon skinned aluminium foam nose cones for high performance circuit vehicles. International Journal of Crashworthiness. 8(1): p. 107-114.

Cho, Y-B., Bae, C-H., Suh, M-W. and Sin, H-C., 2006, A vehicle front frame crash design optimization using hole-type and dent-type crush initiator. Thin-Walled Structures. 44(4): p. 415-428.

Crisfield, M. A.,1991,Non-Linear Finite Element Analysis of Solids and Structures,John Wiley & Sons

Czekanski, A., Attia, M. S., Meguid, S. A. and Elbestawi, M. A., 2005a, On the use of a new cell to model geometric asymmetry of metallic foams. Finite Elements in Analysis and Design. 41(13): p. 1327-1340.

Czekanski, A., Elbestawi, M. and Meguid, S., 2005b, On the FE Modeling of Closed-cell Aluminum Foam. International Journal of Mechanics and Materials in Design. 2(1): p. 23-34.

Dannemann, K. A. and Lankford, J., 2000, High strain rate compression of closed-cell aluminium foams. Materials Science and Engineering A. 293(1-2): p. 157-164.

Degischer, H., Kriszt, B.,2002,Handbook of Cellular Metals, Production, Processing, Applications,Wiley-VCH Verlag GmbH

Deqing, W. and Chengxin, S., 2008, Simulation of aluminum foam formation and distribution uniformity. Journal of Materials Science. 43(8): p. 2825-2832.

Deqing, W., Weiwei, X., Xiangjun, M. and Ziyuan, S., 2005, Cell structure and compressive behavior of an aluminum foam. Journal of Materials Science. 40(13): p. 3475-3480.

Deshpande, V. S. and Fleck, N. A., 2000a, High strain rate compressive behaviour of aluminium alloy foams. International Journal of Impact Engineering. 24(3): p. 277-298.

Deshpande, V. S. and Fleck, N. A., 2000b, Isotropic constitutive models for metallic foams. Journal of the Mechanics and Physics of Solids. 48(6-7): p. 1253-1283.

DiPaolo, B. P., Monteiro, P. J. M. and Gronsky, R., 2004, Quasi-static axial crush response of a thin-wall, stainless steel box component. International Journal of Solids and Structures. 41(14): p. 3707-3733.

DiPaolo, B. P. and Tom, J. G., 2006, A study on an axial crush configuration response of thin-wall, steel box components: The quasi-static experiments. International Journal of Solids and Structures. 43(25-26): p. 7752-7775.

Duwe, J and Kopp, G,2009,SuperLIGHT-CAR: lightly towards the car of the future,http://www.dlr.de/en/desktopdefault.aspx/tabid-12/114_read-18596/, (accesed November 2009)

EAA, European Aluminum Association, 2008, Aluminum in cars, http://www.eaa.net/upl/4/en/doc/Aluminium_in_cars_Sept2008.pdf, (accesed November 2009)

EC ,European Commission 1998, Directive 98/69/EC of the European Parliament and of the Council of 13 October 1998 relating to measures to be taken against air pollution by emissions from motor vehicles and amending Council Directive,70/220/EEC,http://ec.europa.eu/environment/air/transport/road.htm, (accesed November 2009)

EPA -United States of America Environmental Protection Agency, 2000,Tier 2 Vehicle & Gasoline Sulfur Program,http://www.epa.gov/tier2/, (accesed November 2009)

Fang, H., Rais-Rohani, M., Liu, Z. and Horstemeyer, M. F., 2005, A comparative study of metamodeling methods for multiobjective crashworthiness optimization. Computers & Structures. 83(25-26): p. 2121-2136.

Fyllingen, Ø, Hopperstad, O. S. and Langseth, M., 2007, Stochastic simulations of square aluminium tubes subjected to axial loading. International Journal of Impact Engineering. 34(10): p. 1619-1636.

Galib, D. Al and Limam, A., 2004, Experimental and numerical investigation of static and dynamic axial crushing of circular aluminum tubes. Thin-Walled Structures. 42(8): p. 1103-1137.

Galib, D. Al, Limam, A. and Combescure, A., 2006, Influence of damage on the prediction of axial crushing behavior of thin-walled aluminum extruded tubes. International Journal of Crashworthiness. 11(1): p. 1 - 12.

Gameiro, C. P. and Cirne, J., 2007, Dynamic axial crushing of short to long circular aluminium tubes with agglomerate cork filler. International Journal of Mechanical Sciences. 49(9): p. 1029-1037.

Gibson, L. J. and Ashby, M. F.,1997,Cellular Solids,Cambridge University Press

Guillow, S. R., Lu, G. and Grzebieta, R. H., 2001, Quasi-static axial compression of thin-walled circular aluminium tubes. International Journal of Mechanical Sciences. 43(9): p. 2103-2123.

Güden, M. and Kavi, H., 2006, Quasi-static axial compression behavior of constraint hexagonal and square-packed empty and aluminum foam-filled aluminum multi-tubes. Thin-Walled Structures. 44(7): p. 739-750.

Haag, M., Wanner, A., Clemens, H., Zhang, P., Kraft, O. and Arzt, E., 2003, Creep of aluminum-based closed-cell foams. Metallurgical and Materials Transactions A. 34(12): p. 2809-2817.

Hall, I. W., Ebil, O., Guden, M. and Yu, C. J., 2001, Quasi-static and dynamic crushing of empty and foam-filled tubes. Journal of Materials Science. 36(24): p. 5853-5860.

Hall, I. W., Guden, M. and Claar, T. D., 2002, Transverse and longitudinal crushing of aluminum-foam filled tubes. Scripta Materialia. 46(7): p. 513-518.

Hall, I. W., Guden, M. and Yu, C. J., 2000, Crushing of aluminum closed cell foams: density and strain rate effects. Scripta Materialia. 43(6): p. 515-521.

Hallquist, J. O.,2006,LsDyna Theory Manual,

Han, Fusheng, Zhu, Zhengang and Gao, Junchang, 1998, Compressive deformation and energy absorbing characteristic of foamed aluminum. Metallurgical and Materials Transactions A. 29(10): p. 2497-2502.

Hanssen, A. G., Hopperstad, O. S. and Langseth, M., 2001a, Design of aluminium foam-filled crash boxes of square and circular cross-sections. International Journal of Crashworthiness. 6(2): p. 177-188.

Hanssen, A. G., Hopperstad, O. S., Langseth, M. and Ilstad, H., 2002, Validation of constitutive models applicable to aluminium foams. International Journal of Mechanical Sciences. 44(2): p. 359-406.

Hanssen, A. G., Langseth, M. and Hopperstad, O. S., 1999, Static crushing of square aluminium extrusions with aluminium foam filler. International Journal of Mechanical Sciences. 41(8): p. 967-993.

Hanssen, A. G., Langseth, M. and Hopperstad, O. S., 2000a, Static and dynamic crushing of circular aluminium extrusions with aluminium foam filler. International Journal of Impact Engineering. 24(5): p. 475-507.

Hanssen, A. G., Langseth, M. and Hopperstad, O. S., 2000b, Static and dynamic crushing of square aluminium extrusions with aluminium foam filler. International Journal of Impact Engineering. 24(4): p. 347-383.

Hanssen, A. G., Langseth, M. and Hopperstad, O. S., 2001b, Optimum design for energy absorption of square aluminium columns with aluminium foam filler. International Journal of Mechanical Sciences. 43(1): p. 153-176.

Hanssen, A. G., Lorenzi, L., Berger, K. K., Hopperstad, O. S. and Langseth, M., 2000c, A demonstrator bumper system based on aluminium foam filled crash boxes. International Journal of Crashworthiness. 5(4): p. 381-392.

Hanssen, A. G., Stabener, K., Rausch, G., Langseth, M. and Keller, H., 2006, Optimisation of energy absorption of an A-pillar by metal foam insert. International Journal of Crashworthiness. 11(3): p. 231-242.

Hou, S., Li, Q., Long, S., Yang, X. and Li, W., 2008, Multiobjective optimization of multi-cell sections for the crashworthiness design. International Journal of Impact Engineering. 35(11): p. 1355-1367.

Hou, S., Li, Q., Long, S., Yang, X. and Li, W., 2009, Crashworthiness design for foam filled thin-wall structures. Materials & Design. 30(6): p. 2024-2032.

Hsu, S. S. and Jones, N., 2004, Quasi-static and dynamic axial crushing of thin-walled circular stainless steel, mild steel and aluminium alloy tubes. International Journal of Crashworthiness. 9(2): p. 195-217.

Huang, X., 2003, Axisymmetric progressive crushing of circular tubes. International Journal of Crashworthiness. 8(1): p. 87-95.

Jensen, A., Hopperstad, O. S. and Langseth, M., 2005, Transition from progressive to global buckling of aluminium extrusions a numerical study. International Journal of Crashworthiness. 10(6): p. 609-620.

Jensen, A., Langseth, M. and Hopperstad, O. S., 2004, Experimental investigations on the behaviour of short to long square aluminium tubes subjected to axial loading. International Journal of Impact Engineering. 30(8-9): p. 973-1003.

Jones, N.,1989,Structural Impact,Cambridge University Press

Jones, N., In Press, Energy-absorbing effectiveness factor. International Journal of Impact Engineering. In Press, Corrected Proof.

Kathuria, Y., 2001a, Physical processes in laser-assisted aluminum foaming. Journal of Materials Engineering and Performance. 10(4): p. 429-434.

Kathuria, Y. P., 2001b, Laser assisted aluminum foaming. Surface and Coatings Technology. 142-144: p. 56-60.

Kathuria, Y. P., 2003a, Nd-YAG laser assisted aluminum foaming. Journal of Materials Processing Technology. 142(2): p. 466-470.

Kathuria, Y. P., 2003b, A preliminary study on laser assisted aluminum foaming. Journal of Materials Science. 38(13): p. 2875-2881.

Kavi, H.,2004,Investigation of compression mechanical behaviour of aluminum foam filled metal tubes Master Thesis,İzmir Instutue of Technology

Kavi, H., Toksoy, A. K. and Guden, M., 2006, Predicting energy absorption in a foam-filled thin-walled aluminum tube based on experimentally determined strengthening coefficient. Materials & Design. 27(4): p. 263-269.

Kim, D-K. and Lee, S., 1999, Impact energy absorption of 6061 aluminum extruded tubes with different cross-sectional shapes. Materials & Design. 20(1): p. 41-49.

Kim, H. S., Chen, W. and Wierzbicki, T., 2002, Weight and crash optimization of foam-filled three-dimensional "S" frame. Computational Mechanics. 28(5): p. 417-424.

Kitazono, K., Sato, E. and Kuribayashi, K., 2004, Novel manufacturing process of closed-cell aluminum foam by accumulative roll-bonding. Scripta Materialia. 50(4): p. 495-498.

Kitazono, K. and Takiguchi, Y., 2006, Strain rate sensitivity and energy absorption of Zn-22Al foams. Scripta Materialia. 55(6): p. 501-504.

Kormi, K., Webb, D. C. and Johnson, W., 1993, The crash response of circular tubes under general applied loading. International Journal of Impact Engineering. 13(2): p. 243-257.

Ku, J. H., Seo, K. S., Park, S. W. and Kim, Y. J., 2001, Axial crushing behavior of the intermittent tack-welded cylindrical tubes. International Journal of Mechanical Sciences. 43(2): p. 521-542.

Lademo, O. G., Berstad, T., Eriksson, M., Tryland, T., Furu, T., Hopperstad, O. S. and Langseth, M., 2008, A model for process-based crash simulation. International Journal of Impact Engineering. 35(5): p. 376-388.

Langseth, M. and Hopperstad, O. S., 1997, Local buckling of square thin-walled Aluminium extrusions. Thin-Walled Structures. 27(1): p. 117-126.

Langseth, M., Hopperstad, O. S. and Hanssen, A. G., 1998, Crash behaviour of thin-walled aluminium members. Thin-Walled Structures. 32(1-3): p. 127-150.

Lee, S., Hahn, C., Rhee, M. and Oh, J-E., 1999, Effect of triggering on the energy absorption capacity of axially compressed aluminum tubes. Materials & Design. 20(1): p. 31-40.

Liu, Y., 2008a, Crashworthiness design of multi-corner thin-walled columns. Thin-Walled Structures. 46(12): p. 1329-1337.

Liu, Y., 2008b, Design optimization of tapered thin-walled square tubes. International Journal of Crashworthiness. 13(5): p. 543-550.

Lopatnikov, S. L., Gama, B. A. and Gillespie, J. W., 2007, Modeling the progressive collapse behavior of metal foams. International Journal of Impact Engineering. 34(3): p. 587-595.

Lopatnikov, S. L., Gama, B. A., Haque, M. J., Krauthauser, C. and Gillespie, J. W., 2004, High-velocity plate impact of metal foams. International Journal of Impact Engineering. 30(4): p. 421-445.

Ma, G. W., Ye, Z. Q. and Shao, Z. S., 2009, Modeling loading rate effect on crushing stress of metallic cellular materials. International Journal of Impact Engineering. 36(6): p. 775-782.

Ma, Liqun and Song, Zhenlun, 1998, Cellular structure control of aluminium foams during foaming process of aluminium melt. Scripta Materialia. 39(11): p. 1523-1528.

Maine, E. and Ashby, M. F., 2000, Cost Estimation and the Vialibity of Metal Foams. Advanced Engineering Materials. 2(4): p. 205-209.

Mamalis, A. G., Manolakos, D. E., Ioannidis, M. B., Chronopoulos, D. G. and Kostazos, P. K., 2009, On the crashworthiness of composite rectangular thin-walled tubes internally reinforced with aluminium or polymeric foams: Experimental and numerical simulation. Composite Structures. 89(3): p. 416-423.

Mamalis, A. G., Manolakos, D. E., Ioannidis, M. B. and Kostazos, P. K., 2003a, Crushing of hybrid square sandwich composite vehicle hollow bodyshells with reinforced core subjected to axial loading: numerical simulation. Composite Structures. 61(3): p. 175-186.

Mamalis, A. G., Manolakos, D. E., Ioannidis, M. B. and Kostazos, P. K., 2005, Numerical simulation of thin-walled metallic circular frusta subjected to axial loading. International Journal of Crashworthiness. 10(5): p. 505-513.

Mamalis, A. G., Manolakos, D. E., Ioannidis, M. B., Kostazos, P. K. and Dimitriou, C., 2003b, Finite element simulation of the axial collapse of metallic thin-walled tubes with octagonal cross-section. Thin-Walled Structures. 41(10): p. 891-900.

Mamalis, A. G., Manolakos, D. E., Ioannidis, M. B., Kostazos, P. K. and Kastanias, S. N., 2003c, Numerical modelling of the axial plastic collapse of externally grooved steel thinwalled tubes. International Journal of Crashworthiness. 8(6): p. 583-590.

Mamalis, A. G., Manolakos, D. E., Ioannidis, M. B., Kostazos, P. K. and Papapostolou, D. P., 2002, Axial collapse of hybrid square sandwich composite tubular components with corrugated core: numerical modelling. Composite Structures. 58(4): p. 571-582.

Mamalis, A. G., Manolakos, D. E., Ioannidis, M. B. and Papapostolou, D. P., 2006, The static and dynamic axial collapse of CFRP square tubes: Finite element modelling. Composite Structures. 74(2): p. 213-225.

Mamalis, A. G., Manolakos, D. E., Ioannidis, M. B., Spentzas, K. N. and Koutroubakis, S., 2008, Static axial collapse of foam-filled steel thin-walled rectangular tubes: experimental and numerical simulation. International Journal of Crashworthiness. 13(2): p. 117-126.

Mantena, P. R. and Mann, R., 2003, Impact and dynamic response of high-density structural foams used as filler inside circular steel tube. Composite Structures. 61(4): p. 291-302.

Marsolek, J. and Reimerdes, H. G., 2004, Energy absorption of metallic cylindrical shells with induced non-axisymmetric folding patterns. International Journal of Impact Engineering. 30(8-9): p. 1209-1223.

McCullough, K. Y. G., Fleck, N. A. and Ashby, M. F., 1999a, Toughness of aluminium alloy foams. Acta Materialia. 47(8): p. 2331-2343.

McCullough, K. Y. G., Fleck, N. A. and Ashby, M. F., 1999b, Uniaxial stress-strain behaviour of aluminium alloy foams. Acta Materialia. 47(8): p. 2323-2330.

Meguid, S. A., Attia, M. S. and Monfort, A., 2004a, On the crush behaviour of ultralight foam-filled structures. Materials & Design. 25(3): p. 183-189.

Meguid, S. A., Cheon, S. S. and El-Abbasi, N., 2002, FE modelling of deformation localization in metallic foams. Finite Elements in Analysis and Design. 38(7): p. 631-643.

Meguid, S. A., Stranart, J. C. and Heyerman, J., 2004b, On the layered micromechanical three-dimensional finite element modelling of foam-filled columns. Finite Elements in Analysis and Design. 40(9-10): p. 1035-1057.

Miller, R. E., 2000, A continuum plasticity model for the constitutive and indentation behaviour of foamed metals. International Journal of Mechanical Sciences. 42(4): p. 729-754.

Miyoshi, T., Itoh, M., Mukai, T., Kanahashi, H., Kohzu, H., Tanabe, S. and Higashi, K., 1999, Enhancement of energy absorption in a closed-cell aluminum by the modification of cellular structures. Scripta Materialia. 41(10): p. 1055-1060.

Montgomery, D. C.,1997,Design of Experiments,John Wiley & Sons Inc.

Mukai, T., Kanahashi, H., Miyoshi, T., Mabuchi, M., Nieh, T. G. and Higashi, K., 1999, Experimental study of energy absorption in a close-celled aluminum foam under dynamic loading. Scripta Materialia. 40(8): p. 921-927.

Mukai, T., Miyoshi, T., Nakano, S., Somekawa, H. and Higashi, K., 2006, Compressive response of a closed-cell aluminum foam at high strain rate. Scripta Materialia. 54(4): p. 533-537.

Myers, H. R. and Montgomery, D. C,1995,Response surface methodology: process and product optimization using designed experiments,John Wiley & Sons

Onck, P. R., Andrews, E. W. and Gibson, L. J., 2001, Size effects in ductile cellular solids. Part I: modeling. International Journal of Mechanical Sciences. 43(3): p. 681-699.

Park, C. and Nutt, S. R., 2002, Strain rate sensitivity and defects in steel foam. Materials Science and Engineering A. 323(1-2): p. 358-366.

Paul, A. and Ramamurty, U., 2000, Strain rate sensitivity of a closed-cell aluminum foam. Materials Science and Engineering A. 281(1-2): p. 1-7.

M. Peden, R. Scurfield, D. Sleet, D. Mohan, A. A. Hyder, E. Jarawan and C. Mathers,2004,World report on road traffic injury prevention,

Peroni, L., Avalle, M. and Belingardi, G., 2009, Comparison of the energy absorption capability of crash boxes assembled by spot-weld and continuous joining techniques. International Journal of Impact Engineering. 36(3): p. 498-511.

Peroni, L., Avalle, M. and Peroni, M., 2008, The mechanical behaviour of aluminium foam structures in different loading conditions. International Journal of Impact Engineering. 35(7): p. 644-658.

Pipkorn, B. and Hayland, Y., 2005, Proposed variable stiffness of vehicle longitudinal frontal members. International Journal of Crashworthiness. 10(6): p. 603-608.

Proa-Flores, P.M. and Drew, R. A. , 2008, Production of Aluminum Foams with Ni-coated TiH2 Powder. Advanced Engineering Materials. 10(9): p. 830-834.

Pugsley, A. G. and Macaulay, M., 1960, The large scale crumpling of thin cylindrical columns. Quarterly Journal of Mechanics and Applied Mechanics. 13(1): p. 1-9.

Qiao, J. S., Chen, J. H. and Che, H. Y., 2006, Crashworthiness assessment of square aluminum extrusions considering the damage evolution. Thin-Walled Structures. 44(6): p. 692-700.

Rajendran, R., Moorthi, A. and Basu, S., 2009a, Numerical simulation of drop weight impact behaviour of closed cell aluminium foam. Materials & Design. 30(8): p. 2823-2830.

Rajendran, R., Prem Sai, K., Chandrasekar, B., Gokhale, A. and Basu, S., 2009b, Impact energy absorption of aluminium foam fitted AISI 304L stainless steel tube. Materials & Design. 30(5): p. 1777-1784.

Reyes, A., Hopperstad, O. S., Berstad, T., Hanssen, A. G. and Langseth, M., 2003, Constitutive modeling of aluminum foam including fracture and statistical variation of density. European Journal of Mechanics - A/Solids. 22(6): p. 815-835.

Reyes, A., Hopperstad, O. S., Hanssen, A. G. and Langseth, M., 2004, Modeling of material failure in foam-based components. International Journal of Impact Engineering. 30(7): p. 805-834.

Ruan, D., Lu, G., Chen, F. L. and Siores, E., 2002, Compressive behaviour of aluminium foams at low and medium strain rates. Composite Structures. 57(1-4): p. 331-336.

Santosa, S. P., Wierzbicki, T., Hanssen, A. G. and Langseth, M., 2000, Experimental and numerical studies of foam-filled sections. International Journal of Impact Engineering. 24(5): p. 509-534.

Santosa, S. and Wierzbicki, T., 1998a, Crash behavior of box columns filled with aluminum honeycomb or foam. Computers & Structures. 68(4): p. 343-367.

Santosa, S. and Wierzbicki, T., 1998b, On the modeling of crush behavior of a closed-cell aluminum foam structure. Journal of the Mechanics and Physics of Solids. 46(4): p. 645-669.

Schwingel, D., Seeliger, H-W., Vecchionacci, C., Alwes, D. and Dittrich, J., Aluminium foam sandwich structures for space applications. Acta Astronautica. 61(1-6): p. 326-330.

Seitzberger, M., Rammerstorfer, F., Degischer, H. and Gradinger, R., 1997, Crushing of axially compressed steel tubes filled with aluminium foam. Acta Mechanica. 125(1): p. 93-105.

Seitzberger, M., Rammerstorfer, F. G., Gradinger, R., Degischer, H. P., Blaimschein, M. and Walch, C., 2000, Experimental studies on the quasi-static axial crushing of steel columns filled with aluminium foam. International Journal of Solids and Structures. 37(30): p. 4125-4147.

Seitzberger, M. and Willminger, S., 2001, Application of plastic collapse mechanisms for the axial crushing analysis of tubular steel structures filled with aluminium foam. International Journal of Crashworthiness. 6(2): p. 165 - 176.

Singace, A. A., 2000, Collapse behaviour of plastic tubes filled with wood sawdust. Thin-Walled Structures. 37(2): p. 163-187.

Singace, A. A. and El-Sobky, H., 2000, Interplay of factors influencing collapse modes in axially crushed tubes. International Journal of Crashworthiness. 5(3): p. 279-298.

Singace, A. A. and Elsobky, H., 1996, Further experimental investigation on the eccentricity factor in the progressive crushing of tubes. International Journal of Solids and Structures. 33(24): p. 3517-3538.

Singace, A. A., Elsobky, H. and Reddy, T. Y., 1995, On the eccentricity factor in the progressive crushing of tubes. International Journal of Solids and Structures. 32(24): p. 3589-3602.

Solorzano, E., Rodríguez-Perez, M. A, Reglero, J. A and deSaja, J. A, 2007, Mechanical Behaviour of Internal Reinforced Aluminium Foams. Advanced Engineering Materials. 9(11): p. 955-958.

Song, Z-l., Zhu, J-S., Ma, L-Q. and He, D-P., 2001, Evolution of foamed aluminum structure in foaming process. Materials Science and Engineering A. 298(1-2): p. 137-143.

Song, Z. and Nutt, S., 2005, Energy of Compressed Aluminum Foam. Advanced Engineering Materials. 7(1-2): p. 73-77.

Sridhar, I. and Fleck, N. A., 2005, The multiaxial yield behaviour of an aluminium alloy foam. Journal of Materials Science. 40(15): p. 4005-4008.

Stöbener, K. and Rausch, G., 2009, Aluminium foam–polymer composites: processing and characteristics. Journal of Materials Science. 44(6): p. 1506-1511.

T. Miyoshi, M. Itoh S. Akiyama A. Kitahara, 2000, ALPORAS Aluminum Foam: Production Process, Properties, and Applications. Advanced Engineering Materials. 2(4): p. 179-183.

Talonen, J. and Hanninen, H., 2006, Effect of tensile properties on the energy-absorbing capacity of weld-bonded austenitic stainless steel profiles. International Journal of Crashworthiness. 11(4): p. 371-378.

Tasdemirci, A., 2008, The effect of tube end constraining on the axial crushing behavior of an aluminum tube. Materials & Design. 29(10): p. 1992-2001.

Toksoy, A. K. ,2003,Quasi-static axial compression behavior of empty and polystyrene foam filled aluminum tubes,Master of Science,Izmir Institute of Technology

Toksoy, A. K. and Güden, M., 2005, The strengthening effect of polystyrene foam filling in aluminum thin-walled cylindrical tubes. Thin-Walled Structures. 43(2): p. 333-350.

Toksoy, A. K., Tanoglu, M., Guden, M. and Hall, I. W., 2004, Effect of adhesive on the strengthening of aluminum foam-filled circular tubes. Journal of Materials Science. 39(4): p. 1503-1506.

Turkish Statistical Institute, 2007,Turkey's Statistical Yearbook,

Wallentowitz, H. and Adam, H., 1996, Predicting the crashworthiness of vehicle structures made by lightweight design materials and innovative joining methods. International Journal of Crashworthiness. 1(2): p. 163-180.

Wang, B. and Lu, G., 2002, Mushrooming of circular tubes under dynamic axial loading. Thin-Walled Structures. 40(2): p. 167-182.

Wang, Q., Fan, Z. and Gui, L., 2006, A theoretical analysis for the dynamic axial crushing behaviour of aluminium foam-filled hat sections. International Journal of Solids and Structures. 43(7-8): p. 2064-2075.

Wang, Q., Fan, Z., Song, H. and Gui, L., 2005, Experimental and numerical analyses of the axial crushing behaviour of hat sections partially filled with aluminium foam. International Journal of Crashworthiness. 10(5): p. 535-543.

Webb, D. C., Webster, J. and Kormi, K., 2001, Finite Element Simulation of Energy Absorption Devices under Axial Static Compressive and Impact Loading. International Journal of Crashworthiness. 6(3): p. 399-424.

Wen, C. E., Yamada, Y., Shimojima, K., Chino, Y., Hosokawa, H. and Mabuchi, M., 2004, Compressibility of porous magnesium foam: dependency on porosity and pore size. Materials Letters. 58(3-4): p. 357-360.

Wierzbicki, T. and Abramowicz, W., 1983, On the Crushing Mechanics of Thin-Walled Structures. Journal of Applied Mechanics. 50: p. 727-734.

Wierzbicki, T., Bhat, S. U., Abramowicz, W. and Brodkin, D., 1992, Alexander revisited--A two folding elements model of progressive crushing of tubes. International Journal of Solids and Structures. 29(24): p. 3269-3288.

Williams, B. W., Oliveira, D. A., Simha, C. H. M., Worswick, M. J. and Mayer, R., 2007, Crashworthiness of straight section hydroformed aluminium tubes. International Journal of Impact Engineering. 34(8): p. 1451-1464.

Yamazaki, K. and Han, J., 2000, Maximization of the crushing energy absorption of cylindrical shells. Advances in Engineering Software. 31(6): p. 425-434.

Zarei, H. R. and Kröger, M., 2006, Multiobjective crashworthiness optimization of circular aluminum tubes. Thin-Walled Structures. 44(3): p. 301-308.

Zarei, H. R. and Kröger, M., 2008a, Bending behavior of empty and foam-filled beams: Structural optimization. International Journal of Impact Engineering. 35(6): p. 521-529.

Zarei, H. R. and Kröger, M., 2008b, Optimization of the foam-filled aluminum tubes for crush box application. Thin-Walled Structures. 46(2): p. 214-221.

Zarei, Hamidreza and Kröger, Matthias, 2008c, Optimum honeycomb filled crash absorber design. Materials & Design. 29(1): p. 193-204.

Zhang, X. and Cheng, G., 2007, A comparative study of energy absorption characteristics of foam-filled and multi-cell square columns. International Journal of Impact Engineering. 34(11): p. 1739-1752.

Zhang, X., Cheng, G., Wang, B. and Zhang, H., 2008, Optimum design for energy absorption of bitubal hexagonal columns with honeycomb core. International Journal of Crashworthiness. 13(1): p. 99-107.

Zhang, X. W., Su, H. and Yu, T. X., 2009, Energy absorption of an axially crushed square tube with a buckling initiator. International Journal of Impact Engineering. 36(3): p. 402-417.

Zhao, H., Elnasri, I. and Girard, Y., 2007, Perforation of aluminium foam core sandwich panels under impact loading--An experimental study. International Journal of Impact Engineering. 34(7): p. 1246-1257.

Zhao, H., Elnasri, I. and Li, H. J., 2006, The mechanism of strength enhancement under impact loading of cellular materials. Advanced Engineering Materials. 8(9): p. 877-883.

APPENDIX

OBJECTIVE FUNCTIONS FOR PARTIALLY ALULIGHT AND HYDRO FOAM FILLED 1050H14 AND 6061T4 AL CRASH BOXES

The response surface functions of SEA and Pm in of 4th-order polynomial function are as follows;

1050H14-Hydro foam aluminum filler:

$$\begin{aligned} SEA(t,\rho^*) = {} & +0.075t + 97.960\rho^* - 1.311t^3 + 2.928t^2 + 0.224t\rho^* - 2036.358\rho^{*2} \\ & - 6.466t^2\rho^* + 120.152t\rho^{*2} + 13103.186\rho^{*3} + 1.988t^3\rho^* + 0.187t^4 \\ & - 0.230t^2\rho^{*2} - 465.773t\rho^{*3} - 27255.065\rho^{*4} + 1.709 \end{aligned} \quad \text{(A.1a)}$$

$$\begin{aligned} Pm(t,\rho^*) = {} & 59.713t + 390.723\rho^* + 12.259t^3 - 37.299t^2 - 184.974t\rho^* \\ & - 5292.376\rho^{*2} + 111.801t^2\rho^* + 59.986t\rho^{*2} + 35557.133\rho^{*3} \\ & - 12.248t^3\rho^* - 1.338t^4 - 138.656t^2\rho^{*2} + 866.880t\rho^{*3} \\ & - 81302.001\rho^{*4} - 83.225 \end{aligned} \quad \text{(A.1b)}$$

6061T4-Alulight foam aluminum filler:

$$\begin{aligned} SEA(t,\rho^*) = {} & -4.937t - 68.912\rho^* - 1.031t^3 + 4.461t^2 + 58.529t\rho^* + 856.235\rho^{*2} \\ & - 25.378t^2\rho^* - 18.019t\rho^{*2} - 7167.666\rho^{*3} + 3.001t^3\rho^* + 0.075t^4 \\ & + 48.833t^2\rho^{*2} - 649.093t\rho^{*3} + 20563.066\rho^{*4} + 5.939 \end{aligned} \quad \text{(A.2a)}$$

$$Pm(t,\rho^*) = -31.747t - 217.251\rho^* - 5.809t^3 + 26.452t^2 + 243.319t\rho^* + 3289.574\rho^{*2} - 117.976t^2\rho^* + 324.400t\rho^{*2} - 30467.143\rho^{*3} + 17.352t^3\rho^* + 0.501t^4 + 189.425t^2\rho^{*2} - 3803.093t\rho^{*3} + 90729.216\rho^{*4} - 37.330$$

(A.2b)

6061T4-Hydro Foam foam aluminum filler:

$$SEA(t,\rho^*) = -4.256t + 4.696\rho^* - 1.428t^3 + 4.721t^2 + 26.314t\rho^* - 237.432\rho^{*2} + 1.382t^2\rho^* - 129.821t\rho^{*2} + 981.239\rho^{*3} - 0.421t^3\rho^* + 0.162t^4 - 6.834t^2\rho^{*2} + 250.093t\rho^{*3} - 836.399\rho^{*4} + 5.307$$

(A.3a)

$$Pm(t,\rho^*) = -19.052t + 36.671\rho^* - 5.913t^3 + 21.199t^2 + 33.001t\rho^* + 924.112\rho^{*2} + 85.674t^2\rho^* - 256.652t\rho^{*2} - 9310.077\rho^{*3} - 8.129t^3\rho^* + 0.749t^4 - 211.154t^2\rho^{*2} + 1962.373t\rho^{*3} + 21981.861\rho^{*4} - 44.992$$

(A.3b)

VITA

Ahmet Kaan TOKSOY

(13.07.1978) İzmir

Education

- ✓ B. Sc : (1999) Department of Mechanical Engineering, Dokuz Eylül University, Turkey (1+4) (in Turkish)
- ✓ M. Sc : (2003) Department of Mechanical Engineering, Izmir Institute of Technology, Turkey, (in English)
- ✓ PhD : (2009) Department of Mechanical Engineering, Izmir Institute of Technology, Turkey, (in English)

Grants

- ✓ Elginkan Foundation, Technology Awards-2009, Production and Development of Engineering Application of Foam and Porous Metal Structures, Güden, M., Taşdemirci, A., Toksoy, A. K., Dizlek, M. E., Ergönenç, Ç.
- ✓

Selected Publications

- ✓ Aktay, L., Kröplin, B.-H., Toksoy, A.K., Güden, M., Finite element and coupled finite element/smoothparticle hydrodynamics modeling of the quasi-static crushing of empty and foam-filled single, bitubular and constraint hexagonal- and square-packed aluminum tubes, Material Design, 29(2008) 952-962
- ✓ Aktay, L., Johnson, A.F., Toksoy, A.K., Kröplin, B.-H., Güden, M., Modeling the progressive axial crushing of foam-filled aluminum tubes using smooth particle hydrodynamics and coupled finite element model/smooth particle hydrodynamics, Material Design, 29(2008) 569-575
- ✓ Guden, M., Toksoy, A. K., Kavi, H., Experimental investigation of interaction effects in foam-filled thin-walled aluminum tubes,J. Mater. Sci, 41(2006) 6417-6424.
- ✓ Toksoy, A.K., Güden, M.,The strengthening effect of polystyrene foam filling in aluminum thin-walled cylindrical tubes, Thin-Walled Structures 43 (2005) 333–350